MATERIAL AND STRUCTURAL DESIGNS FOR METAL ION ENERGY STORAGE DEVICES

EDITED BY: Hongsen Li, Jun Zhang, Ping Wu, Yu Ding and Pan Xiong
PUBLISHED IN: Frontiers in Chemistry

frontiers Research Topics

ISSN 1664-8714
ISBN 978-2-88976-991-9
DOI 10.3389/978-2-88976-991-9

About Frontiers

Frontiers is more than just an open-access publisher of scholarly articles: it is a pioneering approach to the world of academia, radically improving the way scholarly research is managed. The grand vision of Frontiers is a world where all people have an equal opportunity to seek, share and generate knowledge. Frontiers provides immediate and permanent online open access to all its publications, but this alone is not enough to realize our grand goals.

Frontiers Journal Series

The Frontiers Journal Series is a multi-tier and interdisciplinary set of open-access, online journals, promising a paradigm shift from the current review, selection and dissemination processes in academic publishing. All Frontiers journals are driven by researchers for researchers; therefore, they constitute a service to the scholarly community. At the same time, the Frontiers Journal Series operates on a revolutionary invention, the tiered publishing system, initially addressing specific communities of scholars, and gradually climbing up to broader public understanding, thus serving the interests of the lay society, too.

Dedication to Quality

Each Frontiers article is a landmark of the highest quality, thanks to genuinely collaborative interactions between authors and review editors, who include some of the world's best academicians. Research must be certified by peers before entering a stream of knowledge that may eventually reach the public - and shape society; therefore, Frontiers only applies the most rigorous and unbiased reviews.
Frontiers revolutionizes research publishing by freely delivering the most outstanding research, evaluated with no bias from both the academic and social point of view. By applying the most advanced information technologies, Frontiers is catapulting scholarly publishing into a new generation.

What are Frontiers Research Topics?

Frontiers Research Topics are very popular trademarks of the Frontiers Journals Series: they are collections of at least ten articles, all centered on a particular subject. With their unique mix of varied contributions from Original Research to Review Articles, Frontiers Research Topics unify the most influential researchers, the latest key findings and historical advances in a hot research area! Find out more on how to host your own Frontiers Research Topic or contribute to one as an author by contacting the Frontiers Editorial Office: frontiersin.org/about/contact

MATERIAL AND STRUCTURAL DESIGNS FOR METAL ION ENERGY STORAGE DEVICES

Topic Editors:
Hongsen Li, Qingdao University, China
Jun Zhang, Zhejiang University of Technology, China
Ping Wu, Nanjing Normal University, China
Yu Ding, University of Texas at Austin, United States
Pan Xiong, Nanjing University of Science and Technology, China

Citation: Li, H., Zhang, J., Wu, P., Ding, Y., Xiong, P., eds. (2022). Material and Structural Designs for Metal Ion Energy Storage Devices. Lausanne: Frontiers Media SA. doi: 10.3389/978-2-88976-991-9

Table of Contents

05 ***Editorial: Material and Structural Designs for Metal Ion Energy Storage Devices***
Fengkai Zuo, Yu Ding, Jun Zhang, Pan Xiong, Ping Wu and Hongsen Li

07 ***Supercritical CO_2 Synthesis of Freestanding $Se_{1-x}S_x$ Foamy Cathodes for High-Performance Li-$Se_{1-x}S_x$ Battery***
Chengwei Lu, Ruyi Fang, Kun Wang, Zhen Xiao, G. Gnana kumar, Yongping Gan, Xinping He, Hui Huang, Wenkui Zhang and Yang Xia

14 ***A Three-Dimensional Electrospun $Li_{6.4}La_3Zr_{1.4}Ta_{0.6}O_{12}$–Poly (Vinylidene Fluoride-Hexafluoropropylene) Gel Polymer Electrolyte for Rechargeable Solid-State Lithium Ion Batteries***
Donghuang Wang, Dan Cai, Yu Zhong, Zhao Jiang, Shengzhao Zhang, Xinhui Xia, Xiuli Wang and Jinagping Tu

22 ***Nitrogen-Doped Carbon Encapsulated Partial Zinc Stannate Nanocomposite for High-Performance Energy Storage Materials***
Jiage Yu, Zhijie Liu, Xian Zhang, Yu Ding, Zhengbing Fu and Feng Wang

30 ***The Synergetic Effect Induced High Electrochemical Performance of CuO/Cu_2O/Cu Nanocomposites as Lithium-Ion Battery Anodes***
Lin-Hui Wang, Shang Gao, Long-Long Ren, En-Long Zhou and Yu-Feng Qin

39 ***One-Pot Synthesized Amorphous Cobalt Sulfide With Enhanced Electrochemical Performance as Anodes for Lithium-Ion Batteries***
Long-Long Ren, Lin-Hui Wang, Yu-Feng Qin and Qiang Li

49 ***Regulation of the Interfaces Between Argyrodite Solid Electrolytes and Lithium Metal Anode***
Bo Pang, Yongping Gan, Yang Xia, Hui Huang, Xinping He and Wenkui Zhang

56 ***Architecting Hierarchical WO_3 Agglomerates Assembled With Straight and Parallel Aligned Nanoribbons Enabling High Capacity and Robust Stability of Lithium Storage***
Xiaotong Dong, Yongshuai Liu, Shikai Zhu, Yike Ou, Xiaoyu Zhang, Wenhao Lan, Haotian Guo, Cunliang Zhang, Zhaoguo Liu, Shuai Ju, Yuan Miao, Yongcheng Zhang and Hongsen Li

65 ***Hydrothermal Preparation and High Electrochemical Performance of NiS Nanospheres as Anode for Lithium-Ion Batteries***
Lin-Hui Wang, Long-Long Ren, Yu-Feng Qin and Qiang Li

74 ***Energy-Saving Synthesis of Functional CoS_2/rGO Interlayer With Enhanced Conversion Kinetics for High-Performance Lithium-Sulfur Batteries***
Junan Feng, Yahui Li, Jinshi Yuan, Yuling Zhao, Jianmin Zhang, Fengyun Wang, Jie Tang and Jianjun Song

84 ***Research Progresses and Challenges of Flexible Zinc Battery***
Yunfei Xu, Xin Xu, Mei Guo, Guoxin Zhang and Yaqun Wang

104 ***Recent Developments of Cathode Materials for Thermal Batteries***
Renyi Li, Wei Guo and Yumin Qian

112 ***Hollow CoS/C Structures for High-Performance Li, Na, K Ion Batteries***
Yan Liu, Xiangkun Li, Fengling Zhang, Leqing Zhang, Tao Zhang, Changshuan Li, Zhicheng Jin, Yueying Wu, Zhongyu Du, Huiwen Jiao, Ying Jiang, Yuliang Yan, Qiang Li and Weijin Kong

121 ***Synthesis and Modification of Tetrahedron*** $Li_{10.35}Si_{1.35}P_{1.65}S_{12}$ **via** ***Elemental Doping for All-Solid-State Lithium Batteries***
Yuanzhong Lin, Jian Chen, Jiawei Yan, Yanhua Zhuang, Hengyi Lu and Chenyang Zhao

frontiers | Frontiers in Chemistry

EDITORIAL
published: 08 August 2022
doi: 10.3389/fchem.2022.952440

Editorial: Material and Structural Designs for Metal Ion Energy Storage Devices

Fengkai Zuo[1], Yu Ding[2], Jun Zhang[3]*, Pan Xiong[4]*, Ping Wu[5]* and Hongsen Li[1]**

[1]Center for Marine Observation and Communications, College of Physics, Qingdao University, Qingdao, China, [2]College of Engineering and Applied Sciences, Nanjing University, Nanjing, China, [3]College of Materials Science and Engineering, Zhejiang University of Technology, Hangzhou, China, [4]Key Laboratory for Soft Chemistry and Functional Materials of Ministry Education, School of Chemistry and Chemical Engineering, Nanjing University of Science and Technology, Nanjing, China, [5]Jiangsu Key Laboratory of New Power Batteries, School of Chemistry and Materials Science, Nanjing Normal University, Nanjing, China

Keywords: electrode materials, structural design, metal-ion energy storage device, high energy densities, electrochemical performance

OPEN ACCESS

Edited and reviewed by:
Xifei Li,
Xi'an University of Technology, China

****Correspondence:***
Hongsen Li
hsli@qdu.edu.cn
Yu Ding
utdingyu@gmail.com
Pan Xiong
pan.xiong@njust.edu.cn
Jun Zhang
zhangjun@zjut.edu.cn
Ping Wu
zjuwuping@njnu.edu.cn

Specialty section:
This article was submitted to
Electrochemistry,
a section of the journal
Frontiers in Chemistry

Received: *25 May 2022*
Accepted: *31 May 2022*
Published: *08 August 2022*

Citation:
Zuo F, Ding Y, Zhang J, Xiong P, Wu P and Li H (2022) Editorial: Material and Structural Designs for Metal Ion Energy Storage Devices.
Front. Chem. 10:952440.
doi: 10.3389/fchem.2022.952440

Editorial on the Research Topic

Material and Structural Designs for Metal Ion Energy Storage Devices

Driven by the increasing demand for portable electronics, grid-scale storage, and electric vehicles, intensive research on electrochemical energy storage (EES) devices with high performance that are cost-efficient and environmentally friendly is at the forefront of energy science and technology. Rechargeable metal-ion energy storage devices are considered to be promising candidates for sustainable large smart grids and renewable electrochemical energy storage technologies, owing to their high specific energy density, affordable cost, and long charge/discharge cycle life. The electrochemical properties and performance of these devices are intimately dependent on the physicochemical nature of their electrode materials, the critical component of an energy storage system, and the main redox species for electrochemical reactions. Further innovations and breakthroughs in electrode materials, rather than incremental changes are key to a new generation of energy storage devices. For these reasons, researchers have been highly motivated toward improving energy storage performance, exploring the fundamental properties of novel electrode materials with well-designed structures. Hence, this Research Topic of *Material and Structural Designs for Metal Ion Energy Storage Devices* focuses on the design of rational materials in different metal-ion-based energy storage devices.

In this Research Topic, representative types of materials design strategies are discussed in detail to provide reasonable solutions to compound problems and enable competitive performance for various real metal ion energy storage devices. They range from Lithium-ion batteries (LIBs) (Yu et al.; Ren et al.; Dong et al.; Wang et al.) to Sodium/Potassium ion batteries (Liu et al.) and solid-state Lithium batteries (Wang et al.; Lin et al.), and lithium-sulfur/selenium batteries (Lu et al.; Feng et al.). In addition to the 10 original research articles published here, our Research Topic also contains three review articles. Xu et al. review recent research progress in flexible rechargeable Zinc batteries. They discuss the distinction between different cathode, anode materials, and electrolytes, and in doing so, introduce the differences in preparation methods of electrode materials and their corresponding effect on flexible Zinc batteries. Li et al. provide a comprehensive overview of recent research on conversion-type thermal battery cathode materials. They generalize the preparation and characterization of numerous cathode materials and the performance testing of thermal cells. After that, the electrochemical behavior, properties, and problems occurring at the argyrodite solid-state electrolyte (SSE)/Li metal anode interface are summarized by Pang et al., who discuss strategies to stabilize interfaces and resolve interface problems in recent years and conclude the review with a brief future outlook for argyrodite SSEs. Their review papers highlight that this Research Topic is far from over and conclude by discussing fundamental issues and recommendations for future research trends.

Yu et al. provide a reliable route for the preparation of bimetal oxide materials, tailoring a core-shell structure for developing high-performance energy storage devices. They successfully obtained a core-shell $ZnSnO_3$@ nitrogen-doped carbon (ZSO@ NC) nanocomposite by *in-situ* polymerization of $ZnSnO_3$ with polypyrrole (PPy) under ice bath conditions, finding it exhibits excellent electrochemical performance for lithium storage thanks to the unique compact structure.

Also exploring the field of LIBs, Wang et al. investigated the energy storage performance of the $CuO/Cu_2O/Cu$ nanocomposites and illustrate the advantages of multi-component synergy. Qin et al. demonstrated that the large-scale synthesis of NiS as an anode material for LIBs is promising due to its superior electrochemical performance and facile preparation method. Ren et al. indicated that the amorphous cobalt sulfide electrodes, with more structure defects, isotropy, and numerous grain boundaries, exhibit remarkable electrochemical performance. Dong et al. fabricated the well-designed hierarchical WO_3 agglomerates and evaluated them as anode material of LIBs, which displays excellent potential for practical application in the field of high-energy-power LIBs.

Another work further transitions to other alkali metal ion battery systems, Liu et al. exploited a zeolitic imidazolate framework (ZIF)-derived hollow structures CoS/C for alkali ion (Li, Na, and K) battery anodes. There is also some work focusing on Solid-state electrolyte (SSE) lithium-ion batteries. Wang et al. utilized the electrospinning technique to prepare a three-dimensional $Li_{6.4}La_3Zr_{1.4}Ta_{0.6}O_{12}$-Poly (Vinylidene Fluoride-Hexafluoropropylene) Gel Polymer Electrolyte, a potential candidate for safer and more stable solid-state lithium batteries. Lin et al. also gave an overview and discussed the effect of Si^{4+} concentration adjustment and elemental doping in obviously enhancing the ionic conductivity of tetrahedron $Li_{10.35}Si_{1.35}P_{1.65}S_{12}$. Their strategy can be easily extended to types of sulfide SSEs, thereby opening up previously unexplored opportunities in developing high-safety, high-performance, and long-life solid-state energy storage devices for practical applications.

Moving to the lithium-sulfur/selenium batteries, Lu et al. proposed a novel freestanding $Se_{1-x}S_x$ foamy cathodes assisted by supercritical CO_2 technology for high-performance Li-$S_{1-x}S_x$ batteries. They not only provided a new strategy to prepare high-energy-density cathodes, but also a new method of fabricating free-standing cathodes for practical applications of next-generation recharge batteries. Feng et al. used the porous conductive reduced graphene oxide (rGO) loading polar CoS_2 nanoparticles to mitigate the shuttle effect of polysulfides and speed up the electron/ion transfer. Thus, it was found that the Li-S cell with CoS_2/rGO functional diaphragm exhibits enhanced electrochemical kinetics and high performance.

Although the papers collected here present significant insights, several problems and challenges need to be overcome in this field of research. Lower costs are one of the most prioritized considerations for the practical application of rechargeable energy storage devices, and further insights into the design of inexpensive electrode materials with promising electrochemical performance. It would also be significant to reveal the correlation between novel electrode designs and the charge storage mechanism, which will effectively guide the development of next-generation energy storage systems. Furthermore, the exploration of the electrolyte-electrode interface reaction mechanism creates room for corresponding electrode designs, which will advance the exploitation of cutting-edge characterization and analysis tools, while facilitating the development of new energy storage systems, especially those utilizing metal anodes or multivalent ions.

We thank all the authors for their meaningful work and would also like to thank all the reviewers for their insightful suggestions and constructive comments. It is hoped that this Research Topic will stimulate future research on the discovery and design of novel electrodes and drive the intensive ongoing development of high-energy-density rechargeable energy storage devices. We anticipate that these endeavors will pave the way for achieving green growth and stainable development.

AUTHOR CONTRIBUTIONS

FZ: writing and review. YD, JZ, PX, PW, and HL: co-drafting and editing. All authors have made a substantial, direct, and intellectual contribution and approved the submitted version.

Conflict of Interest: The authors declare that the research was conducted in the absence of any commercial or financial relationships that could be construed as a potential conflict of interest.

frontiers in Chemistry

ORIGINAL RESEARCH
published: 28 July 2021
doi: 10.3389/fchem.2021.738977

Supercritical CO_2 Synthesis of Freestanding $Se_{1-x}S_x$ Foamy Cathodes for High-Performance Li-$Se_{1-x}S_x$ Battery

*Chengwei Lu[1], Ruyi Fang[1], Kun Wang[1], Zhen Xiao[2], G. Gnana kumar[3], Yongping Gan[1], Xinping He[1], Hui Huang[1], Wenkui Zhang[1] and Yang Xia[1]**

[1]College of Materials Science and Engineering, Zhejiang University of Technology, Hangzhou, China, [2]Institute of Optoelectronic Materials and Devices, China Jiliang University, Hangzhou, China, [3]Department of Physical Chemistry, School of Chemistry, Madurai Kamaraj University, Madurai, India

Selenium-sulfur solid solutions ($Se_{1-x}S_x$) are considered to be a new class of promising cathodic materials for high-performance rechargeable lithium batteries owing to their superior electric conductivity than S and higher theoretical specific capacity than Se. In this work, high-performance Li-$Se_{1-x}S_x$ batteries employed freestanding cathodes by encapsulating $Se_{1-x}S_x$ in a N-doped carbon framework with three-dimensional (3D) interconnected porous structure (NC@SWCNTs) are proposed. $Se_{1-x}S_x$ is uniformly dispersed in 3D porous carbon matrix with the assistance of supercritical CO_2 (SC-CO_2) technique. Impressively, NC@SWCNTs host not only provides spatial confinement for $Se_{1-x}S_x$ and efficient physical/chemical adsorption of intermediates, but also offers a highly conductive framework to facilitate ion/electron transport. More importantly, the Se/S ratio of $Se_{1-x}S_x$ plays an important role on the electrochemical performance of Li- $Se_{1-x}S_x$ batteries. Benefiting from the rationally designed structure and chemical composition, NC@SWCNTs@$Se_{0.2}S_{0.8}$ cathode exhibits excellent cyclic stability (632 mA h g−1 at 200 cycle at 0.2 A g^{-1}) and superior rate capability (415 mA h g^{-1} at 2.0 A g^{-1}) in carbonate-based electrolyte. This novel NC@SWCNTs@$Se_{0.2}S_{0.8}$ cathode not only introduces a new strategy to design high-performance cathodes, but also provides a new approach to fabricate freestanding cathodes towards practical applications of high-energy-density rechargeable batteries.

Keywords: Se1-xSx, N-doped carbon foam, supercritical CO2, high areal capacity, Li-Se1-xSx batteries

Edited by:
Ping Wu,
Nanjing Normal University, China

Reviewed by:
Yongfeng Yuan,
Zhejiang Sci-Tech University, China
Wenjia Zhao,
Nanjing Agricultural University, China

***Correspondence:**
Yang Xia
nanoshine@zjut.edu.cn

Specialty section:
This article was submitted to Electrochemistry, a section of the journal Frontiers in Chemistry

Received: *09 July 2021*
Accepted: *19 July 2021*
Published: *28 July 2021*

Citation:
Lu C, Fang R, Wang K, Xiao Z, kumar GG, Gan Y, He X, Huang H, Zhang W and Xia Y (2021) Supercritical CO_2 Synthesis of Freestanding $Se_{1-x}S_x$ Foamy Cathodes for High-Performance Li-$Se_{1-x}S_x$ Battery. Front. Chem. 9:738977. doi: 10.3389/fchem.2021.738977

INTRODUCTION

Lithium-sulfur (Li-S) batteries are considered as promising next-generation electrochemical energy-storage systems in view of their high theoretical energy density (2600 W h kg^{-1}), environmental friendliness and natural richness of sulfur (Yao et al., 2017; Zheng et al., 2020; Yuan et al., 2021a; Yuan et al., 2021b; Sun et al., 2021). Although great progress has been made, the widespread practical application of Li-S battery is still facing issues of the insulation property of natural sulfur (5×10^{-30} S m^{-1}, 25°C), the serious volume effect in the cycle process, and the dissolution of the intermediate polysulfide, leading to the low sulfur utilization, fast capacity decay and poor cycle stability (Zhang et al., 2020).

As a congener of element S, Se has similar chemical properties with S, such as high theoretical volumetric capacity (3,253 mA h cm^{-3}, $\rho = 4.81$ g cm^{-3}), which is suitable for mobile devices and

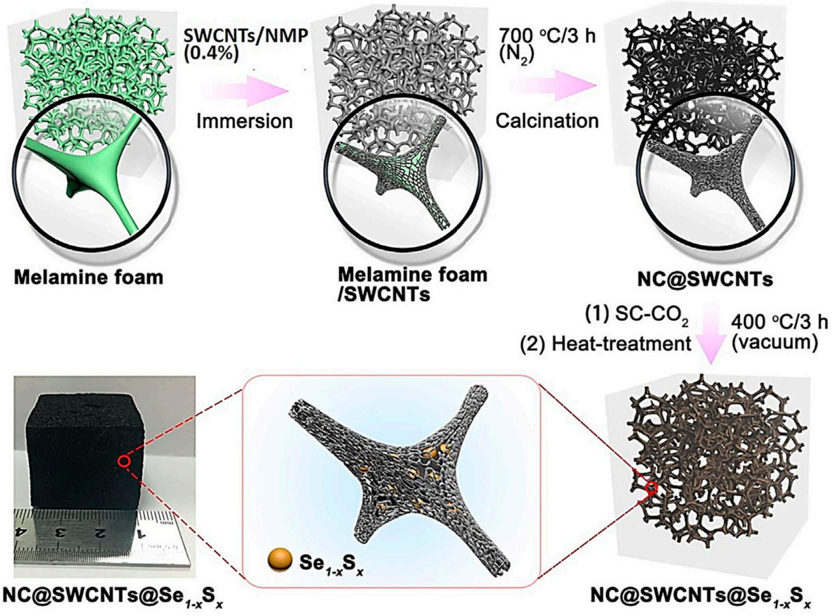

FIGURE 1 | Schematic illustration of the synthetic process of NC@SWCNTs@$Se_{1-x}S_x$.

hybrid electric vehicles with strict restrictions on battery volume (Lin et al., 2021; Sun et al., 2021). Meanwhile, selenium is a semiconductor with much higher electronic conductivity (1×10^{-3} S m^{-1}) than sulfur, which is conducive to excellent kinetic behavior (Zhang et al., 2020). Nevertheless, in the current research stage of Li-Se batteries, there are still many problems in Se cathode materials, such as relatively unfavorable higher cost and lower gravimetric capacity (675 mA h g^{-1}) when compared to Li-S batteries (1,675 mA h g^{-1}) (Fang et al., 2018b). In order to offset the drawbacks of Se and S and complement each other's advantages, a solid solution of Se and S ($Se_{1-x}S_x$, $0 < x < 1$) has been proposed as high-performance cathode materials for lithium storage. $Se_{1-x}S_x$ is a class of chemical compounds with different Se-S ratios, which not only owns a higher theoretical capacity than pure Se, but also has increased electronic conductivity and accelerated reaction kinetics than pristine S (Abouimrane et al., 2012; Wei et al., 2016; Xu et al., 2019).

However, similar to S, $Se_{1-x}S_x$ cathode materials also suffer from poor cycle lifespan and low Coulombic efficiency due to the dissolution and shuttling of intermediates (Chen et al., 2019; Du et al., 2020). Since $Se_{1-x}S_x$ cathode materials exhibit similar electrochemical behaviors to S, the strategies of immobilizing S should also be effective for $Se_{1-x}S_x$ (Luo et al., 2014). At present, the main host materials of $Se_{1-x}S_x$ are carbonaceous materials (Sun et al., 2021), such as hollow carbon spheres (Xu et al., 2015; Hu et al., 2020), mesoporous carbon (Han et al., 2019), carbon nanotubes (Fan et al., 2018; Guan et al., 2019; Shen et al., 2020), carbon fiber (Chen et al., 2014; Zhang et al., 2017), graphene (Tang et al., 2016; Chen et al., 2019) and carbonized polyacrylonitrile (Li et al., 2018). Generally, expect serving as hosts for $Se_{1-x}S_x$, these carbonaceous materials play another dual role of establishing conductive frameworks to facilitate ions/electrons transport and inhibiting the shuttle effect (Hu et al., 2020). Nevertheless, the physical adsorption ability of nonpolar pristine carbon materials to polar intermediates is too weak to effectively prevent the dissolution and diffusion of intermediate (Sun et al., 2016; Nazarian-Samani et al., 2021). Research shows heteroatom-doped (B, N, O, *etc.*) carbon hosts can effectively improve the electrochemical performance of Li-$Se_{1-x}S_x$ batteries due to the strong chemical affinity of polarized carbon surface, which can significantly trap the soluble intermediates to inhibit the shuttle effect and side reactions in the electrolyte (Guo et al., 2016; Zhang et al., 2017; Fan et al., 2018; He et al., 2018; Sun et al., 2021).

Herein, a series of $Se_{1-x}S_x$ cathode materials with optimized Se/S ratio are incorporated into N-doped three-dimensional (3D) porous carbon matrix to form novel freestanding $Se_{1-x}S_x$ foamy cathodes (NC@SWCNTs@$Se_{1-x}S_x$) with the assistance of supercritical CO_2 fluid (**Figure 1**). In carbonate-based electrolyte, NC@SWCNTs@$Se_{1-x}S_x$ cathodes exhibit single-phase transformation during charge/discharge. Benefiting from the rationally designed structure and chemical composition, NC@SWCNTs@$Se_{1-x}S_x$ cathodes with high conductivity and strong adsorption present superior electrochemical performance.

EXPERIMENTAL SECTION

Preparation of NC@SWCNTs

Melamine foam (3 cm × 3 cm × 3 cm) was washed with anhydrous ethanol and dried in an oven at 80°C for 12 h, then immersed in SWCNTs/NMP suspension (0.4%). After 6 h, the melamine foam impregnated with SWCNTs/NMP suspension was taken out and dried in a vacuum oven at 80°C for 24 h to obtain the precursor of melamine/SWCNTs. The above precursor was calcined at 700°C under flowing N_2 atmosphere for 3 h to obtain NC@SWCNTs host.

Preparation of NC@SWCNTs@$Se_{1-x}S_x$

NC@SWCNTs@$Se_{1-x}S_x$ composites were prepared with the help of supercritical CO_2 (SC-CO_2) fluid, which is reported in our previous works (Fang et al., 2018a; Fang et al., 2018b; Fang et al., 2020). Firstly, S and Se powders with different molar ratios (S:Se = 7:3, 8:2, 9:1) were put into stainless-steel milling jars, respectively. The pre-mixed Se and S mixture was obtained after ball milling (500 rpm) for 12 h. Subsequently, 0.6 g pre-mixed Se and S mixture and a piece of NC@SWCNTs (3 cm × 3 cm × 3 cm, ~0.4 g) were put into a stainless-steel jar. Then, CO_2 was pumped into the jar until the gaseous pressure reached 8.5 MPa. After the jar was kept at 32°C for 24 h, NC@SWCNTs@$Se_{1-x}S_x$ precursor was obtained by rapidly releasing CO_2. Then, NC@SWCNTs@$Se_{1-x}S_x$ precursor was sealed in a quartz glass tube under vacuum. Finally, the sealed quartz glass tube was heated to 400°C for 3 h to obtain NC@SWCNTs@$Se_{1-x}S_x$. The samples with different Se/S molar ratios were labeled as NC@SWCNTs@$Se_{0.3}S_{0.7}$, NC@SWCNTs@$Se_{0.2}S_{0.8}$ and NC@SWCNTs@$Se_{0.1}S_{0.9}$, respectively. For comparison, NC@SWCNTs hosts impregnated with Se or S were prepared by using the same SC-CO_2 method and named NC@SWCNTs@Se and NC@SWCNTs@S, respectively.

Materials Characterizations

The morphologies and microstructures of samples were observed on field-emission scanning electron microscopy (FE-SEM, Hitachi S-4800) and transmission electron microscopy (TEM, FEI Tecnai G2 F30) equipped with an energy-dispersive spectroscopy (EDS) detector. X-ray diffraction (XRD) patterns were recorded on Rigaku Ultima IV powder X-ray diffractometer by using Cu Kα radiation (λ = 0.15418 nm). Raman spectra were performed by Renishaw In*Via* Raman spectrometer (λ = 532 nm). Thermogravimetric analysis (TGA) was conducted on SDT Q600 analyzer (TA Instruments) under a flowing Ar atmosphere.

Electrochemical Measurements

NC@SWCNTs@$Se_{1-x}S_x$ cathodes were cut into disks of 15 mm in diameter and 2 mm in height. CR2025 coin-type cells were assembled in an Ar-filed glove box (MIKROUNA, moisture <1.0 ppm, oxygen <1.0 ppm) with NC@SWCNTs@$Se_{1-x}S_x$ composites as cathodes, commercial microporous polypropylene membrane (Celgard 2400) as separator, and lithium metal as anode. A solution of 1.0 M $LiPF_6$ in a co-solvent of ethylene carbonate (EC) and dimethyl carbonate (DMC) (1:1, volume ratio) was used as electrolyte. The dosage of electrolyte in coin-type cells is 15 μl mg^{-1} (based on the mass of $Se_{1-x}S_x$). Li-$Se_{1-x}S_x$ cells were cycled in the voltage range of 1.0–3.0 V on a battery testing system (Shenzhen Neware Technology Co. Ltd.). Cyclic voltammetry (CV) was performed on a CHI650B electrochemical workstation (Chenhua, Shanghai, China).

RESULTS AND DISCUSSION

The morphology and microstructure of NC@SWCNTs host are characterized by SEM and TEM as illustrated in **Figure 2**. As vividly depicted in **Figure 2A** and **Supplementary Figure S1**, NC@SWCNTs host exhibits a 3D honeycombed network structure, fully inheriting the 3D interconnected framework of melamine foam. Local magnification SEM images (**Figures 2B,C**) demonstrate that numerous interlaced SWCNTs are covered the surface of melamine foam derived carbon skeletons, as well as SWCNTs are formed into small sheets between carbon skeletons. This unique interconnecting structure not only endows NC@SWCNTs a highly conductive 3D network to accelerate the electron/ion transport, but also effectively enhances the mechanical strength and flexibility of NC@SWCNTs host. Moreover, TEM results (**Figure 2D**) further indicate that SWCNTs are crisscrossed in carbon skeletons, forming an intertwined 3D network structure. On the basis of EDS results (**Figure 2E**), the main elements in NC@SWCNTs are C, O and N, which are uniformly distributed in NC@SWCNTs. Notably, N signal is derived from melamine foam since melamine has high content of N. According to the above analysis, NC@SWCNTs host has a typical 3D network structure that is composed of SWCNTs-coated N-doped carbon skeleton derived from melamine foam and wafery sheets interwoven by SWCNTs. The pores and layer gaps in NC@SWCNTs host are conducive to loading more $Se_{1-x}S_x$ active materials. Meanwhile, the 3D interconnected conductive network framework can not only effectively promote redox kinetics, but also endow NC@SWCNTs host with strong mechanical properties to buffer the volume expansion during cycling. Additionally, the doped N is also beneficial to the adsorption of intermediates.

After $Se_{1-x}S_x$ impregnation, compared to NC@SWCNTs host, NC@SWCNTs@$Se_{1-x}S_x$ composites well maintain the original morphology of NC@SWCNTs (**Supplementary Figure S2**). Moreover, no discernible $Se_{1-x}S_x$ particles can be found at the surface of NC@SWCNTs. Additionally, according to EDS mapping results, the C, N, Se and Se signals are overlapped well, suggesting $Se_{1-x}S_x$ composites are uniformly permeated into the pores and layer gaps of NC@SWCNTs host with the assistance of SC-CO_2 due to the good permeability, excellent diffusivity and high solubility of SC-CO_2. Furthermore, elemental analyses (**Supplementary Table S1**) of NC@SWCNTs@$Se_{1-x}S_x$ show that molar ratios of Se to S in NC@SWCNTs@$Se_{1-x}S_x$ conform to the design values.

NC@SWCNTs@$Se_{1-x}S_x$ composites are further revealed by XRD and Raman analysis. As illustrated in **Figure 3A**, all the samples have a wide peak in 2θ ranging from 15 to 40°, corresponding to the existence of NC@SWCNTs. Meanwhile, the characteristic diffraction peaks of Se and S are clearly observed in NC@SWCNTs@Se and NC@SWCNTs@S samples, respectively. With the introduction of Se, no characteristic diffraction peak of Se is detected in NC@SWCNTs@$Se_{1-x}S_x$ composites. However, some characteristic diffraction peaks of S with low intensity can be still observed, indicating a small amount of Se may occupy S position and further form $Se_{1-x}S_x$ in NC@SWCNTs host (Yao et al., 2017). To further investigate the bond between Se and S, Raman spectra were depicted in **Figure 3B**. Apparently, all the samples have three characteristic peaks located at 260, 375 and 470 cm^{-1}, respectively, which are assigned to Se-Se, Se-S and S-S

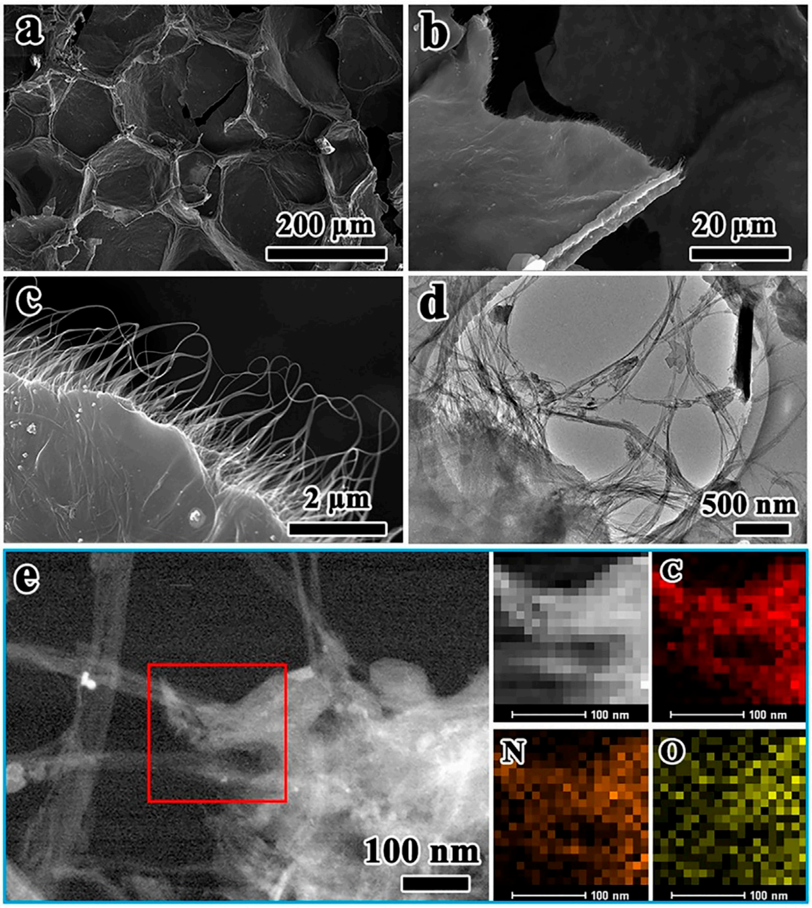

FIGURE 2 | (A–C) SEM images and **(D)** TEM image of NC@SWCNTs. **(E)** STEM image of NC@SWCNTs and the corresponding mapping images.

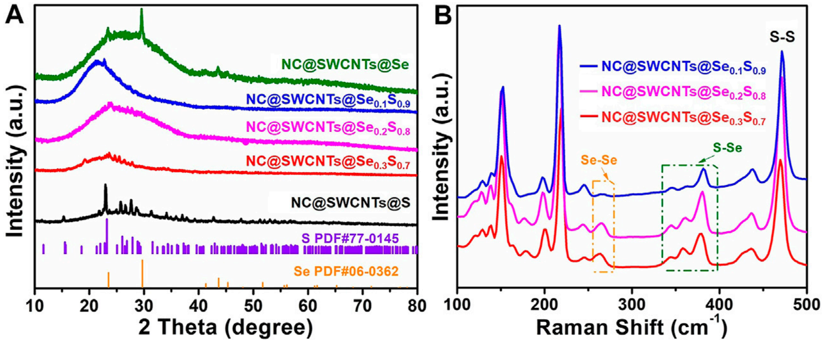

FIGURE 3 | (A) XRD patterns of NC@SWCNTs@S, NC@SWCNTs@$Se_{0.3}S_{0.7}$, NC@SWCNTs@$Se_{0.2}S_{0.8}$, NC@SWCNTs@$Se_{0.1}S_{0.9}$ and NC@SWCNTs@Se. **(B)** Raman spectra of NC@SWCNTs@$Se_{0.3}S_{0.7}$, NC@SWCNTs@$Se_{0.2}S_{0.8}$ and NC@SWCNTs@$Se_{0.1}S_{0.9}$.

stretching vibrations, (Chen et al., 2019; Pham et al., 2019). With increasing Se content in $Se_{1-x}S_x$, the strength of Se-Se and Se-S bonds are simultaneously increased, whereas the strength of S-S bonds are gradually decreased. Thus, it could be concluded that $Se_{1-x}S_x$ composites are successfully synthesized.

To further inspect the $Se_{1-x}S_x$ content and thermal stability of NC@SWCNTs@$Se_{1-x}S_x$ composites, TGA tests are performed as shown in **Supplementary Figure S3**. According to TG results, NC@SWCNTs@S and NC@SWCNTs@Se exhibit the lowest and highest onset decomposition temperatures of ~130 and ~300°C,

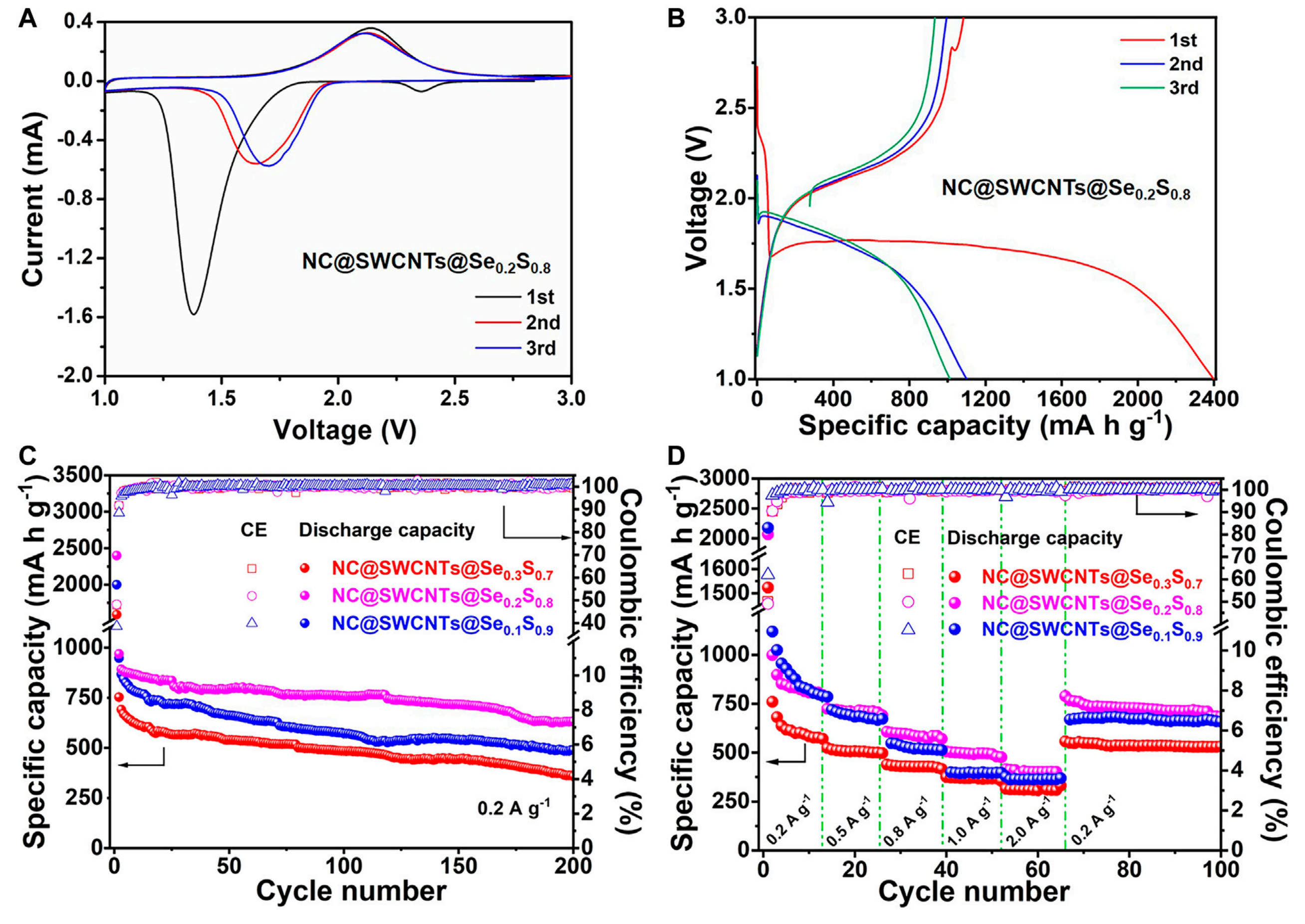

FIGURE 4 | (A) CV curves of the NC@SWCNTs@$Se_{0.2}S_{0.8}$ cathode. **(B)** Charge/discharge curves of the NC@SWCNTs@$Se_{0.2}S_{0.8}$ cathode at 0.2 A g^{-1}. **(C)** Cycle performances and **(D)** rate performances of NC@SWCNTs@$Se_{1\text{-}x}S_x$ cathodes.

respectively. Meanwhile, the onset decomposition temperatures of NC@SWCNTs@$Se_{0.3}S_{0.7}$, NC@SWCNTs@$Se_{0.2}S_{0.8}$, and NC@SWCNTs@$Se_{0.1}S_{0.9}$ are between NC@SWCNTs@S and NC@SWCNTs@Se samples, and gradually increase with increasing Se content in $Se_{1\text{-}x}S_x$. It is because the thermal stability of Se is higher than that of S, the higher the content of Se in $Se_{1\text{-}x}S_x$, the higher the thermal stability of solid solution. Moreover, the distinct weight losses exist in all the samples, corresponding to the active material in samples. Therefore, the actual contents of S, $Se_{0.3}S_{0.7}$, $Se_{0.2}S_{0.8}$, $Se_{0.1}S_{0.9}$, and Se in NC@SWCNTs@S, NC@SWCNTs@$Se_{0.3}S_{0.7}$, NC@SWCNTs@$Se_{0.2}S_{0.8}$, NC@SWCNTs@$Se_{0.1}S_{0.9}$, and NC@SWCNTs@Se are 54.8, 58.7, 52.5, 58.4, and 56.8%, respectively, which are close to the design value of ~60%.

In order to evaluate the electrochemical performance of NC@SWCNTs@$Se_{1\text{-}x}S_x$ composites, NC@SWCNTs@$Se_{1\text{-}x}S_x$ composites are employed as freestanding cathodes in Li-$Se_{1\text{-}x}S_x$ batteries with carbonate-based electrolyte ($LiPF_6$-EC/DMC). **Figure 4A** and **Supplementary Figure S4** show initial three cyclic voltammetry (CV) curves of NC@SWCNTs@$Se_{1\text{-}x}S_x$ cathodes at a scanning rate of 0.1 mV s^{-1} in the potential window from 1.0 to 3.0 V versus Li/Li^+. At the initial scan, a sharp reduction peak at ~1.38 V, a small reduction peak at ~2.37 V, and a broadened oxidation peak at ~2.14 V are clearly observed. The small reduction peak at ~2.37 V disappears after the first scan, while the sharp reduction peak at ~1.38 V shifts to ~1.7 V during the subsequent scan. The peak shift indicates the activation process during the first lithification process, and the polarization is effectively reduced thereafter (Luo et al., 2014; Zhu et al., 2018). The subsequent CV curves are well overlapped after the first scan, indicating the good cyclability and reversibility of NC@SWCNTs@$Se_{0.2}S_{0.8}$ cathode (Guo et al., 2019). It should be mentioned that the CV curves of NC@SWCNTs@$Se_{1\text{-}x}S_x$ cathodes are obviously different from S cathode, indicating the introduction of Se changes the electrochemical reaction process of S that is conducive to its stable work in carbonate-based electrolytes. Moreover, galvanostatic charge-discharge curves (**Figure 4B** and **Supplementary Figure S5**) of NC@SWCNTs@$Se_{1\text{-}x}S_x$ cathodes are consistent with CV results. During the first discharge process, there are two plateaus: one is an extremely short plateau at ~2.38 V, and another is a long plateau at ~1.75 V. In the subsequent cycles, the short plateau at ~2.38 V disappears, while the long plateau at ~1.75 V becomes a little steeper and shifts to ~1.88 V. The short plateau at ~2.38 V is attributed to the transformation of $Se_{0.2}S_{0.8}$ to polysulfides/polyselenides intermediates. And the disappearance of the short plateau is probably due to the dissolution of intermediates into the electrolyte (Li et al., 2015). Meanwhile, the long plateau at 1.75–1.88 V is assigned to the conversion of polysulfides/polyselenides to Li_2S/Li_2Se (Luo et al., 2014). During the charge process, there is only one sloping plateau at ~2.12 V, corresponding to the conversion of Li_2Se/Li_2S to $Se_{0.2}S_{0.8}$.

Figure 4C shows the cyclic performance of NC@SWCNTs@$Se_{1-x}S_x$ cathodes with different Se/S ratios at a current density of 0.2 A g^{-1}. NC@SWCNTs@$Se_{0.2}S_{0.8}$ cathode delivers the highest initial discharge capacity (2,398.5 mA h g^{-1}) among NC@SWCNTs@$Se_{0.3}S_{0.7}$, NC@SWCNTs@$Se_{0.2}S_{0.8}$ and NC@SWCNTs@$Se_{0.1}S_{0.9}$ samples. The initial discharge capacity exceeds the theoretical capacity may be attributed to side reactions and the formation of SEI layer on the surface of electrode (Luo et al., 2014). After 200 cycles, the reversible capacities of NC@SWCNTs@$Se_{0.3}S_{0.7}$, NC@SWCNTs@$Se_{0.2}S_{0.8}$ and NC@SWCNTs@$Se_{0.1}S_{0.9}$ samples are 490, 632 and 360 mA h g^{-1} with the corresponding capacity retentions of 51.7, 65.3 and 47.9%, respectively. Obviously, NC@SWCNTs@$Se_{0.2}S_{0.8}$ cathode exhibits the superior cyclic stability. In addition, the rate capabilities of NC@SWCNTs@$Se_{1-x}S_x$ cathodes at different current densities are presented in **Figure 4D**. Compare to other samples, NC@SWCNTs@$Se_{0.2}S_{0.8}$ cathode demonstrates the best rate performance. The reversible rate capacities of NC@SWCNTs@$Se_{0.2}S_{0.8}$ cathode are 998.4, 723.7, 606.8, 506.1, and 415.0 mA h g^{-1} at the current density of 0.2, 0.5, 0.8, 1.0 and 2.0 A g^{-1}, respectively. When the current density switches back to 0.5 A g^{-1}, the reversible discharge capacity of NC@SWCNTs@$Se_{0.2}S_{0.8}$ cathode reverts to the initial value. Moreover, as shown in **Supplementary Table S2** and **Supplementary Figure S4**, NC@SWCNTs@$Se_{0.2}S_{0.8}$ cathode with Se loading of as high as 4.4 mg cm^{-2} (a relevant areal capacity of as high as 2.78 mA h cm^{-2}) can surpass most reported $Se_{1-x}S_x$ cathodes (Luo et al., 2014; Li et al., 2015; Guo et al., 2016; Wei et al., 2016; Li et al., 2017; Yao et al., 2017; Zhang et al., 2017; Hu et al., 2018; Li et al., 2018; Zhu et al., 2018). Such remarkable electrochemical performance of NC@SWCNTs@$Se_{0.2}S_{0.8}$ cathode mainly is due to the following reasons: 1) Se and S in $Se_{0.2}S_{0.8}$ solid solution play different roles: Se can significantly improve the electrical conductivity, while S can greatly enhance capacity. 2) N-doped 3D porous carbon matrix and interlaced SWCNTs not only provide storage space for $Se_{1-x}S_x$, but also effectively reinforce the structural stability, and further promote the cycling stability of NC@SWCNTs@$Se_{1-x}S_x$ cathodes.

CONCLUSION

In summary, a series of rationally designed freestanding NC@SWCNTs@$Se_{1-x}S_x$ cathodes with 3D interconnected porous structure are developed with the assistance of supercritical CO_2 fluid. NC@SWCNTs host with 3D network structure serves as an effective matrix for encapsulating $Se_{1-x}S_x$ as well as facilitating ion/electron transport and redox kinetics. Benefiting from the rationally designed structure and optimized chemical composition, NC@SWCNTs@$Se_{0.2}S_{0.8}$ cathode exhibits excellent cycling stability (632 mA h g^{-1} at 0.2 A g^{-1} at 200 cycle) and remarkable rate performance (415 mA h g^{-1} at 2 A g^{-1}) in carbonate-based electrolyte. This work offers a feasible approach to develop high-performance $Se_{1-x}S_x$ cathodes for advanced Li-$Se_{1-x}S_x$ batteries.

DATA AVAILABILITY STATEMENT

The original contributions presented in the study are included in the article/**Supplementary Material**, further inquiries can be directed to the corresponding author.

AUTHOR CONTRIBUTIONS

CL: materials preparation, data analysis and manuscript writing; RF: materials preparation and data analysis; KW: manufacture and result analysis of battery; ZX: materials characterization and data analysis; GK: material properties analysis and discussion; YG: electrochemical performance test and results discussion; XH: electrochemical performance test and materials characterization; HH: data analysis and discussion; WZ: data analysis and discussion; YX: experimental design and manuscript revision. All authors contributed to the article and approved the submitted version.

FUNDING

This research was supported by Zhejiang Provincial Natural Science Foundation of China (LY21E020005), China Postdoctoral Science Foundation (2020M671785 and 2020T130597), National Natural Science Foundation of China (U20A20253) and Zhejiang Provincial Special Support Program for High-level Talents (2020R51004).

SUPPLEMENTARY MATERIAL

The Supplementary Material for this article can be found online at: https://www.frontiersin.org/articles/10.3389/fchem.2021.738977/full#supplementary-material

REFERENCES

Abouimrane, A., Dambournet, D., Chapman, K. W., Chupas, P. J., Weng, W., and Amine, K. (2012). A New Class of Lithium and Sodium Rechargeable Batteries Based on Selenium and Selenium-Sulfur as a Positive Electrode. *J. Am. Chem. Soc.* 134, 4505–4508. doi:10.1021/ja211766q

Chen, X., Peng, L., Wang, L., Yang, J., Hao, Z., Xiang, J., et al. (2019). Ether-compatible Sulfurized Polyacrylonitrile Cathode with Excellent Performance Enabled by Fast Kinetics via Selenium Doping. *Nat. Commun.* 10, 1021. doi:10.1038/s41467-019-08818-6

Chen, Y., Li, X., Park, K.-S., Hong, J., Song, J., Zhou, L., et al. (2014). Sulfur Encapsulated in Porous Hollow CNTs@CNFs for High-Performance Lithium-Sulfur Batteries. *J. Mater. Chem. A.* 2, 10126–10130. doi:10.1039/C4TA01823K

Du, H., Feng, S., Luo, W., Zhou, L., and Mai, L. (2020). Advanced Li-Se S Battery System: Electrodes and Electrolytes. *J. Mater. Sci. Technol.* 55, 1–15. doi:10.1016/j.jmst.2020.01.001

Fan, H.-N., Chen, S.-L., Chen, X.-H., Tang, Q.-L., Hu, A.-P., Luo, W.-B., et al. (2018). 3D Selenium Sulfide@carbon Nanotube Array as Long-Life and High-Rate Cathode Material for Lithium Storage. *Adv. Funct. Mater.* 28, 1805018. doi:10.1002/adfm.201805018

Fang, R., Liang, C., Xia, Y., Xiao, Z., Huang, H., Gan, Y., et al. (2018a). Supercritical CO2 Mediated Incorporation of Sulfur into Carbon Matrix as Cathode Materials Towards High-Performance Lithium-Sulfur Batteries. *J. Mater. Chem. A.* 6, 212–222. doi:10.1039/C7TA08768C

Fang, R., Lu, C., Zhong, Y., Xiao, Z., Liang, C., Huang, H., et al. (2020). Puffed rice Carbon with Coupled Sulfur and Metal Iron for High-Efficiency Mercury Removal in Aqueous Solution. *Environ. Sci. Technol.* 54, 2539–2547. doi:10.1021/acs.est.9b07385

Fang, R., Xia, Y., Liang, C., He, X., Huang, H., Gan, Y., et al. (2018b). Supercritical CO2-assisted Synthesis of 3D Porous SiOC/Se Cathode for Ultrahigh Areal Capacity and Long Cycle Life Li-Se Batteries. *J. Mater. Chem. A.* 6, 24773–24782. doi:10.1039/C8TA09758E

Guan, B., Zhang, Y., Fan, L., Wu, X., Wang, M., Qiu, Y., et al. (2019). Blocking Polysulfide with Co2B@CNT via "Synergetic Adsorptive Effect" toward Ultrahigh-Rate Capability and Robust Lithium-Sulfur Battery. *ACS Nano* 13, 6742–6750. doi:10.1021/acsnano.9b01329

Guo, B., Yang, T., Du, W., Ma, Q., Zhang, L.-Z., Bao, S.-J., et al. (2019). Double-walled N-Doped carbon@NiCo2S4 Hollow Capsules as SeS2 Hosts for Advanced Li-SeS2 Batteries. *J. Mater. Chem. A.* 7, 12276–12282. doi:10.1039/C9TA02695A

Guo, S.-P., Li, C.-X., Chi, Y., Ma, Z., and Xue, H.-G. (2016). Novel 3-D Network SeS/NCPAN Composites Prepared by One-Pot *In-Situ* Solid-State Method and its Electrochemical Performance as Cathode Material for Lithium-Ion Battery. *J. Alloys Compd.* 664, 92–98. doi:10.1016/j.jallcom.2015.12.208

Han, B., Li, X., Zhou, Y., Gao, X., Qu, W., Zhang, S., et al. (2019). "Bubble-linking-bubble" Hybrid Fibers Filled with Ultrafine TiN: a Robust and Efficient Platform Achieving Fast Kinetics, strong Ion Anchoring and High Areal Loading for Selenium Sulfide. *J. Mater. Chem. A.* 7, 18404–18416. doi:10.1039/C9TA05527D

He, J., Lv, W., Chen, Y., Xiong, J., Wen, K., Xu, C., et al. (2018). Direct Impregnation of SeS2 into a MOF-Derived 3D Nanoporous Co-N-C Architecture towards superior Rechargeable Lithium Batteries. *J. Mater. Chem. A.* 6, 10466–10473. doi:10.1039/C8TA02434K

Hu, J., Ren, Y., and Zhang, L. (2020). Dual-confined SeS2 Cathode Based on Polyaniline-Assisted Double-Layered Micro/mesoporous Carbon Spheres for Advanced Li-SeS2 Battery. *J. Power Sourc.* 455, 227955. doi:10.1016/j.jpowsour.2020.227955

Hu, J., Zhong, H., Yan, X., and Zhang, L. (2018). Confining Selenium Disulfide in 3D Sulfur-Doped Mesoporous Carbon for Rechargeable Lithium Batteries. *Appl. Surf. Sci.* 457, 705–711. doi:10.1016/j.apsusc.2018.06.296

Li, X., Liang, J., Zhang, K., Hou, Z., Zhang, W., Zhu, Y., et al. (2015). Amorphous S-Rich S1−xSex/C (X ≤ 0.1) Composites Promise Better Lithium-Sulfur Batteries in a Carbonate-Based Electrolyte. *Energy Environ. Sci.* 8, 3181–3186. doi:10.1039/C5EE01470K

Li, Z., Zhang, J., Lu, Y., and Lou, X. W. (2018). A Pyrolyzed Polyacrylonitrile/selenium Disulfide Composite Cathode with Remarkable Lithium and Sodium Storage Performances. *Sci. Adv.* 4, eaat1687. doi:10.1126/sciadv.aat1687

Li, Z., Zhang, J., Wu, H. B., and Lou, X. W. D. (2017). An Improved Li-SeS2 Battery with High Energy Density and Long Cycle Life. *Adv. Energ. Mater.* 7, 1700281. doi:10.1002/aenm.201700281

Lin, S., Chen, Y., Wang, Y., Cai, Z., Xiao, J., Muhmood, T., et al. (2021). Three-dimensional Ordered Porous Nanostructures for Lithium-Selenium Battery Cathodes that Confer superior Energy-Storage Performance. *ACS Appl. Mater. Inter.* 13, 9955–9964. doi:10.1021/acsami.0c21065

Luo, C., Zhu, Y., Wen, Y., Wang, J., and Wang, C. (2014). Carbonized Polyacrylonitrile-Stabilized SeSxCathodes for Long Cycle Life and High Power Density Lithium Ion Batteries. *Adv. Funct. Mater.* 24, 4082–4089. doi:10.1002/adfm.201303909

Nazarian-Samani, M., Haghighat-Shishavan, S., Nazarian-Samani, M., Kashani-Bozorg, S. F., Ramakrishna, S., and Kim, K.-B. (2021). Perforated Two-Dimensional Nanoarchitectures for Next-Generation Batteries: Recent Advances and Extensible Perspectives. *Prog. Mater. Sci.* 116, 100716. doi:10.1016/j.pmatsci.2020.100716

Pham, V. H., Boscoboinik, J. A., Stacchiola, D. J., Self, E. C., Manikandan, P., Nagarajan, S., et al. (2019). Selenium-sulfur (SeS) Fast Charging Cathode for Sodium and Lithium Metal Batteries. *Energ. Storage Mater.* 20, 71–79. doi:10.1016/j.ensm.2019.04.021

Shen, C., Wang, T., Xu, X., and Tian, X. (2020). 3D Printed Cellular Cathodes with Hierarchical Pores and High Mass Loading for Li-SeS2 Battery. *Electrochimica Acta* 349, 136331. doi:10.1016/j.electacta.2020.136331

Sun, F., Cheng, H., Chen, J., Zheng, N., Li, Y., and Shi, J. (2016). Heteroatomic SenS8-N Molecules Confined in Nitrogen-Doped Mesoporous Carbons as Reversible Cathode Materials for High-Performance Lithium Batteries. *ACS Nano* 10, 8289–8298. doi:10.1021/acsnano.6b02315

Sun, J., Du, Z., Liu, Y., Ai, W., Wang, K., Wang, T., et al. (2021). State-Of-The-Art and Future Challenges in High Energy Lithium-Selenium Batteries. *Adv. Mater.* 33, 2003845. doi:10.1002/adma.202003845

Tang, C., Li, B.-Q., Zhang, Q., Zhu, L., Wang, H.-F., Shi, J.-L., et al. (2016). CaO-templated Growth of Hierarchical Porous Graphene for High-Power Lithium-Sulfur Battery Applications. *Adv. Funct. Mater.* 26, 577–585. doi:10.1002/adfm.201503726

Wei, Y., Tao, Y., Kong, Z., Liu, L., Wang, J., Qiao, W., et al. (2016). Unique Electrochemical Behavior of Heterocyclic Selenium-Sulfur Cathode Materials in Ether-Based Electrolytes for Rechargeable Lithium Batteries. *Energ. Storage Mater.* 5, 171–179. doi:10.1016/j.ensm.2016.07.005

Xu, F., Tang, Z., Huang, S., Chen, L., Liang, Y., Mai, W., et al. (2015). Facile Synthesis of Ultrahigh-Surface-Area Hollow Carbon Nanospheres for Enhanced Adsorption and Energy Storage. *Nat. Commun.* 6, 7221. doi:10.1038/ncomms8221

Xu, Q.-T., Xue, H.-G., and Guo, S.-P. (2019). Status and Prospects of SexSy Cathodes for Lithium/sodium Storage. *Inorg. Chem. Front.* 6, 1326–1340. doi:10.1039/C9QI00278B

Yao, Y., Zeng, L., Hu, S., Jiang, Y., Yuan, B., and Yu, Y. (2017). Binding S0.6 Se0.4 in 1D Carbon Nanofiber with C-S Bonding for High-Performance Flexible Li-S Batteries and Na-S Batteries. *Small* 13, 1603513. doi:10.1002/smll.201603513

Yuan, Y. F., Chen, Q., Zhu, M., Cai, G. S., and Guo, S. Y. (2021a). Nano Tube-In-Tube CNT@void@TiO2@C with Excellent Ultrahigh Rate Capability and Long Cycling Stability for Lithium Ion Storage. *J. Alloys Compd.* 851, 156795. doi:10.1016/j.jallcom.2020.156795

Yuan, Y. F., Zhao, W. C., Chen, L., Cai, G. S., and Guo, S. Y. (2021b). CoO Hierarchical Mesoporous nanospheres@TiO2@C for High-Performance Lithium-Ion Storage. *Appl. Surf. Sci.* 556, 149810. doi:10.1016/j.apsusc.2021.149810

Zhang, J., Li, Z., and Lou, X. W. D. (2017). A Freestanding Selenium Disulfide Cathode Based on Cobalt Disulfide-Decorated Multichannel Carbon Fibers with Enhanced Lithium Storage Performance. *Angew. Chem. Int. Ed.* 56, 14107–14112. doi:10.1002/ange.20170810510.1002/anie.201708105

Zhang, W., Li, S., Wang, L., Wang, X., and Xie, J. (2020). Insight into Sulfur-Rich Selenium Sulfide/pyrolyzed Polyacrylonitrile Cathodes for Li-S Batteries. *Sustain. Energ. Fuels* 4, 3588–3596. doi:10.1039/D0SE00512F

Zheng, Y. Q., Yuan, Y. F., Tong, Z. W., Yin, H., Yin, S. M., and Guo, S. Y. (2020). Watermelon-like TiO2 Nanoparticle (P25)@microporous Amorphous Carbon Sphere with Excellent Rate Capability and Cycling Performance for Lithium-Ion Batteries. *Nanotechnology* 31, 215407. doi:10.1088/1361-6528/ab73be

Zhu, T., Pang, Y., Wang, Y., Wang, C., and Xia, Y. (2018). S0.87Se0.13/CPAN Composites as High Capacity and Stable Cycling Performance Cathode for Lithium Sulfur Battery. *Electrochimica Acta* 281, 789–795. doi:10.1016/j.electacta.2018.06.026

Conflict of Interest: The authors declare that the research was conducted in the absence of any commercial or financial relationships that could be construed as a potential conflict of interest.

frontiers in Chemistry

ORIGINAL RESEARCH
published: 04 October 2021
doi: 10.3389/fchem.2021.751476

A Three-Dimensional Electrospun $Li_{6.4}La_3Zr_{1.4}Ta_{0.6}O_{12}$–Poly (Vinylidene Fluoride-Hexafluoropropylene) Gel Polymer Electrolyte for Rechargeable Solid-State Lithium Ion Batteries

*Donghuang Wang[1,2†], Dan Cai[1†], Yu Zhong[1], Zhao Jiang[1], Shengzhao Zhang[1], Xinhui Xia[1], Xiuli Wang[1] and Jinagping Tu[1]**

[1]*State Key Laboratory of Silicon Materials, Key Laboratory of Advanced Materials and Applications for Batteries of Zhejiang Province, and School of Materials Science and Engineering, Zhejiang University, Hangzhou, China,* [2]*Yangtze Delta Region Institute (Huzhou), University of Electronic Science and Technology of China, Huzhou, China*

Edited by:
Jun Zhang,
Zhejiang University of Technology, China

Reviewed by:
Yongqi Zhang,
University of Electronic Science and Technology of China, China
Zhujun Yao,
Zhejiang Sci-Tech University, China

***Correspondence:**
Jinagping Tu
tujp@zju.edu.cn

†These authors have contributed equally to this work

Specialty section:
This article was submitted to Electrochemistry, a section of the journal Frontiers in Chemistry

Received: *01 August 2021*
Accepted: *25 August 2021*
Published: *04 October 2021*

Citation:
Wang D, Cai D, Zhong Y, Jiang Z, Zhang S, Xia X, Wang X and Tu J (2021) A Three-Dimensional Electrospun $Li_{6.4}La_3Zr_{1.4}Ta_{0.6}O_{12}$–Poly (Vinylidene Fluoride-Hexafluoropropylene) Gel Polymer Electrolyte for Rechargeable Solid-State Lithium Ion Batteries. Front. Chem. 9:751476. doi: 10.3389/fchem.2021.751476

Developing high-quality solid-state electrolytes is important for producing next-generation safe and stable solid-state lithium-ion batteries. Herein, a three-dimensional highly porous polymer electrolyte based on poly (vinylidenefluoride-hexafluoropropylene) (PVDF-HFP) with $Li_{6.4}La_3Zr_{1.4}Ta_{0.6}O_{12}$ (LLZTO) nanoparticle fillers (PVDF-HFP-LLZTO) is prepared using the electrospinning technique. The PVDF-HFP-LLZTO gel polymer electrolyte possesses a high ionic conductivity of 9.44×10^{-4} S cm^{-1} and a Li-ion transference number of 0.66, which can be ascribed that the 3D hierarchical nanostructure with abundant porosity promotes the liquid electrolyte uptake and wetting, and LLZTO nanoparticles fillers decrease the crystallinity of PVDF-HFP. Thus, the solid-state lithium battery with $LiFePO_4$ cathode, PVDF-HFP-LLZTO electrolyte, and Li metal anode exhibits enhanced electrochemical performance with improved cycling stability.

Keywords: poly (vinylidenefluoride-hexafluoropropylene), $Li_{6.4}La_3Zr_{1.4}Ta_{0.6}O_{12}$ nanoparticles, three-dimensional, solid-state batteries, gel polymer electrolyte

INTRODUCTION

Nowadays, there has been a strong demand for developing rechargeable lithium batteries with high energy density and high safety for many applications, such as portable electronic devices, electric vehicles, and grid storage of electricity (Thangadurai et al., 2014; Manthiram et al., 2017; Zhao et al., 2020). The lithium metal batteries are extensively considered as the most promising candidates for next-generation rechargeable energy storage devices due to their high energy density (Fergus, 2010; Fan et al., 2018; Nair et al., 2019). However, the lithium metal batteries with flammable liquid organic electrolytes suffer severe safety issues of fire or explosion caused by lithium dendrite growth (Quartarone and Mustarelli, 2011; Fu et al., 2016; Mauger et al., d2017). Solid-state electrolytes (SSEs) can solve the safety issue raising from liquid electrolytes as they are nonflammable and have good mechanical strength to effectively suppress the lithium dendrite growth (Bachman et al., 2016; Li et al., 2020; Wang et al., 2020; Zhao et al., 2021).

In general, SSEs can be categorized into two major types: inorganic solid electrolytes (ISEs) and polymer solid electrolytes (PSEs) (Gao et al., 2018; Tan et al., 2020; Yuan et al., 2021). ISEs usually have excellent thermodynamic stability, wide electrochemical window, and high ionic conductivity

(Li et al., 2018; Jiang et al., 2020). However, the high interfacial resistance between ISEs and electrodes caused by their rigid nature still impedes their application. PSEs alleviate drawbacks of ISEs as they possess high flexibility and good interfacial compatibility (Hazama et al., 2015; Cui et al., 2017; Jiang et al., 2018). The gel polymer electrolytes (GPEs), one type of the PSEs, have been a research hotpot, such as poly (ethylene oxide) (PEO) (Wu et al., 2018), poly (acrylonitrile) (PAN) (Zhou et al., 2015), poly (methyl methacrylate) (PMMA) (Liu et al., 2016), and poly (vinylidenefluoride-hexafluoropropylene) (PVDF-HFP) (Deng et al., 2018). Among the abovementioned polymer electrolytes, PVDF-HFP has attracted much attention due to its good thermal stability and mechanical strength (Fasciani et al., 2015). Nevertheless, PVDF-HFP usually suffers from low lithium-ion transference number and low ionic conductivity caused by the crystallization of polymer at room temperature.

To solve the stubborn problems, it is an effective and simple strategy to improve the absorbing ability of liquid electrolyte. A promising way is to directly introduce inorganic nanoparticles into the polymer matrix to decrease the crystallinity and facilitate the segment motion. Many inorganic fillers (such as SiO_2, Al_2O_3, and TiO_2) (Cao et al., 2013; Pandey et al., 2015; Blake et al., 2017) were doped into PVDF-HFP–based gel polymer electrolytes to improve the ionic conductivities with percolation effect. But these doping inert ceramic fillers may block the lithium-ion conducting routes because they cannot transfer the lithium ions. It is a feasible way to replace the inert ceramic fillers by some lithium ion conductors, such as $Li_{1.3}Al_{0.3}Ti_{1.7}(PO_4)_3$ (LATP) (Xia et al., 2017), $Li_{0.33}La_{0.557}TiO_3$ (LLTO) (Le et al., 2016), and $Li_7La_3Zr_2O_{12}$ (LLZO) (Liang et al., 2018). Among these lithium ion conductors, garnet LLZO has attracted much attention due to its outstanding stability with lithium metal anode and superior ionic conductivity (Zhang X. et al., 2017; Zhou et al., 2020). Another way is to prepare porous GPE membranes to improve the absorbing ability of liquid electrolyte (Wang et al., 2017; Zhang D. et al., 2017). However, the GPE membranes only own few holes synthesized by the traditional blade casting method, which leads to a bottleneck in forming fast ion channels (Farooqui et al., 2017; Shen et al., 2019). By contrast, electrospinning is a facile and effective method to prepare a porous nanofiber membrane, which constructs a three-dimensional (3D) network to uptake liquid electrolyte (Prasanth et al., 2014; Huang et al., 2015; Zhou et al., 2017). Li et al. prepared novel electrospun single-ion conducting polymer electrolytes, in which the single-ion conductive mechanism can facilitate the Li-ion transfer speed and obtain a high Li-ion transference number (Li et al., 2019).

Herein, we prepare a three-dimensional highly porous polymer electrolyte based on PVDF-HFP with $Li_{6.4}La_3Zr_{1.4}Ta_{0.6}O_{12}$ (LLZTO) nanoparticle fillers by the electrospinning technique. This unique 3D hierarchical nanostructure possesses abundant porosity that promotes the liquid electrolyte uptake and wetting and favors the Li-ion transfer between the electrodes and electrolyte. In addition, the LLZTO nanoparticle fillers decrease the crystallinity of PVDF-HFP, thus improving the ionic conductivity and Li-ion transference number and ensuring the cycling stability and high rate performance.

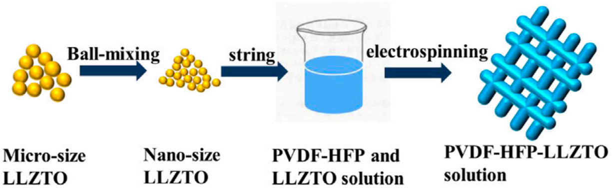

FIGURE 1 | Schematic illustration of the synthesis of PVDF-HFP-LLZTO gel polymer electrolyte.

RESULT AND DISCUSSION

The PVDF-HFP-LLZTO gel polymer electrolyte was prepared by electrospinning, as shown in **Figure 1**. The microsize LLZTO powder was synthesized through a solid-state reaction and then was ball-milled into nanoparticles. And a proper amount of LLZTO was added into PVDF-HFP solution that was dissolved in *N*, *N*-dimethylformamide (DMF) with continuous stirring to form a uniform PVDF-HFP-LLZTO solution. The PVDF-HFP-LLZTO membrane was obtained by electrospinning and was activated by soaking the commercial liquid electrolyte.

Comparison on the morphologies of the different samples is analyzed by SEM. As shown in **Figures 2A,B**, the LLZTO particles are in a diameter of about 5–10 μm before ball-milling. The LLZTO particles decrease to ~50 nm after ball-milling. And the SEM images of PVDF-HFP and PVDF-HFP-LLZTO nanofiber membranes are shown in **Figures 2C,E**. It can be seen that tens of nanofibers with a diameter of ~200 nm construct a three-dimension framework, which ensures a microporous architecture with sufficient void space to uptake liquid electrolyte. The PVDF-HFP-LLZTO membrane shows a similar morphology with the PVDF-HFP membrane, indicating that LLZTO nanoparticles have been doped into the nanofibers and the doping has no impact on the structure of the membranes. **Figures 2D,F** show a cross-sectional SEM image of PVDF-HFP and PVDF-HFP-LLZTO nanofiber membranes, and the thickness of the membranes is about 50 μm.

The phases and crystallinities of PVDF-HFP and PVDF-HFP-LLZTO membranes are investigated by XRD. As shown in **Figure 3**, three typical broad peaks of both samples were located at 18°, 20°, and 35°. In comparison, the PVDF-HFP-LLZTO membrane demonstrates weak diffraction peaks of LLZTO (JCPDS No. 80-0457), indicating that the LLZTO nanoparticles have been doped into the PVDF-HFP nanofibers (Ren et al., 2016). Additionally, the diffraction peaks of the PVDF-HFP-LLZTO membrane at 18°–20° are broadened than that of the PVDF-HFP membrane, which suggests that the crystallinity of PVDF-HFP decreases and the amorphous region expand, which can be ascribed to the introduction of LLZTO nanoparticles that disorder the regular long chain of PVDF-HFP (Le et al., 2016; Guo et al., 2017; Zhang X. et al.,

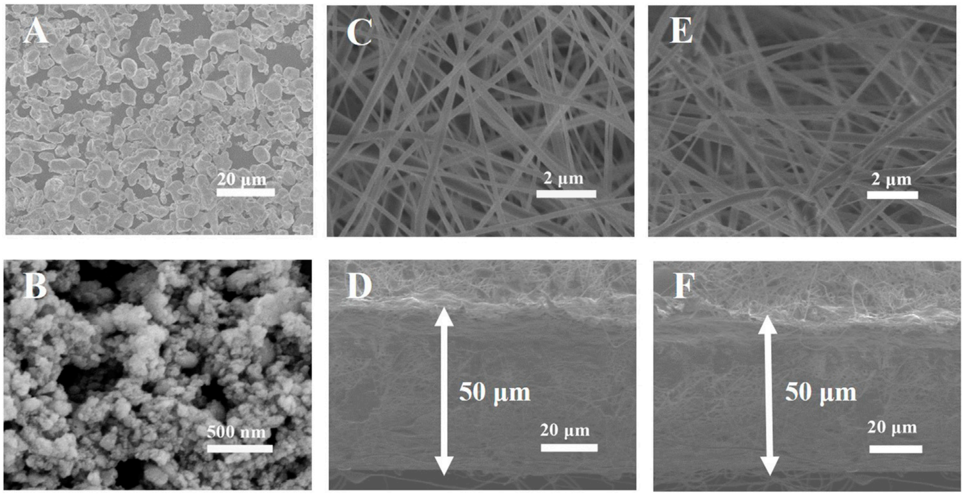

FIGURE 2 | SEM images of **(A)** LLZTO before and **(B)** after ball-milling, **(C)** PVDF-HFP and **(E)** PVDF-HFP-LLZTO, cross-sectional SEM image of **(D)** PVDF-HFP **(F)** PVDF-HFP-LLZTO.

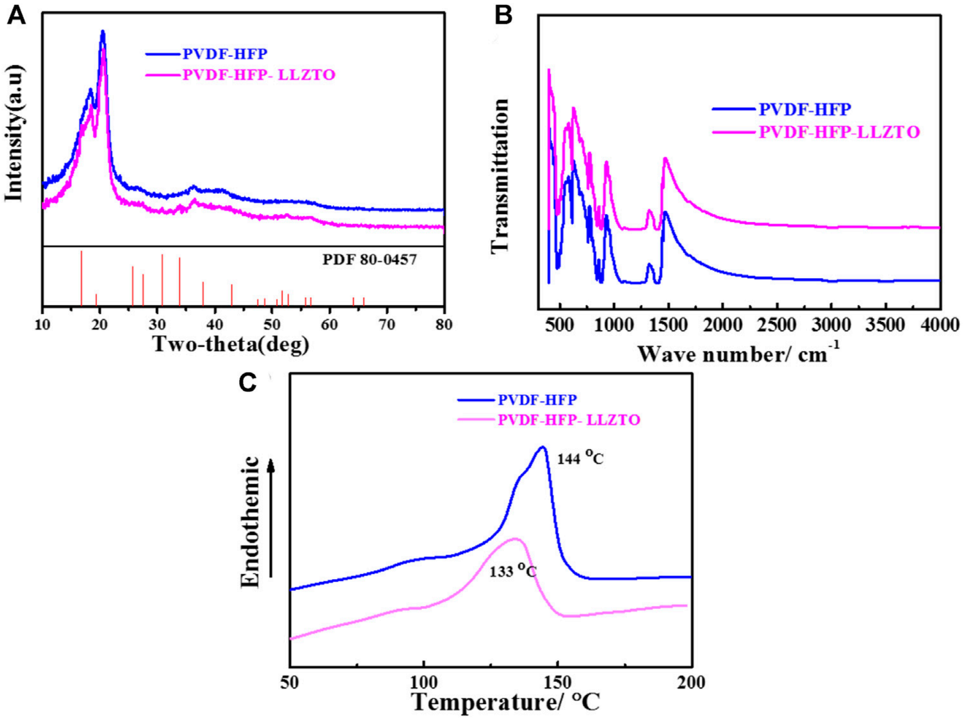

FIGURE 3 | (A) XRD patterns, **(B)** FTIR spectra, **(C)** DSC patterns of PVDF-HFP and PVDF-HFP-LLZTO.

2017). **Figure 3B** is the FTIR spectra of PVDF-HFP and PVDF-HFP-LLZTO membranes. After doping the LLZTO nanoparticles, the PVDF-HFP-LLZTO membrane shows similar peaks with the PVDF-HFP membrane, indicating that the combination of LLZTO nanoparticles and PVDF-HFP is a simple physical mixture without any chemical reaction, and the original foundation of PVDF-HFP matrix remained. DSC measurements are conducted to identify the thermal behavior of PVDF-HFP and PVDF-HFP-LLZTO membranes (**Figure 3C**). A sharp endothermic peak in both samples was observed, which indicated the melting temperatures (T_m) of the polymer. The PVDF-HFP-LLZTO membrane displays T_m at 133°C, which is much lower than that of PVDF-HFP (144°C). It can be attributed to the LLZTO nanoparticle doping that decreases the degree of

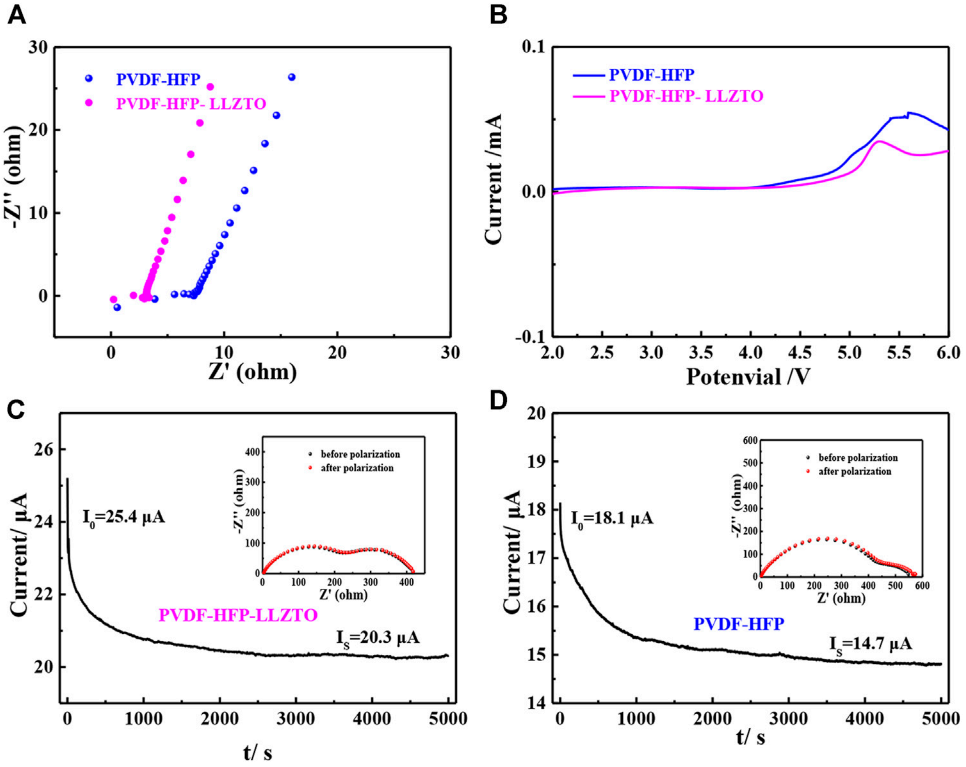

FIGURE 4 | (A) EIS of SS/PH/SS and SS/PHL/SS cells, **(B)** LSV of Li/PH/SS and Li/PHL/SS cells, current–time curve of **(C)** Li/PH/Li and **(D)** Li/PH/Li cells at a DC polarization of 0.01 V, inset: the EIS of the cell before and after polarization.

crystallinity of PVDF-HFP and enlarges the amorphous region in the PVDF-HFP matrix, as well as accelerate dynamic processes with plasticizing effect (Xia et al., 2017; Liang et al., 2018).

Broadening the working voltage is an effective way to improve the energy density of batteries (Chen et al., 2016). To evaluate the electrochemical properties of PVDF-HFP and PVDF-HFP-LLZTO membranes, linear sweep voltammetry (LSV) is carried out by using Li//electrolyte//stainless steel cells. As shown in **Figure 4B**, the LSV curve of the PVDF-HFP-LLZTO membrane is smooth without a noticeable oxidation current before 4.6 V (vs Li/Li$^+$), indicating an electrochemical stability window up to 4.6 V, which is higher than that of the PVDF-HFP membrane. The improved electrochemical stability of the PVDF-HFP-LLZTO membrane meets the requirement for the application of batteries with high voltage. **Figure 4A** shows the electrochemical impedance spectroscopy (EIS) of stainless steel//electrolyte//stainless steel, in which the semicircle at high frequency represents the impedance belonging to the electrolyte bulk. The ionic conductivity of the PVDF-HFP-LLZTO membrane at room temperature can be calculated as $9.44 \times 10^{-4}\,\mathrm{S\,cm^{-1}}$, which is higher than that of the PVDF-HFP membrane ($4.04 \times 10^{-4}\,\mathrm{S\,cm^{-1}}$). However, the ionic conductivity of the PVDF-HFP membrane is still higher than that of the PVDF-HFP membrane synthesized by the casting method, as it builds a porous 3D network that has strong electrolyte absorption (Lim et al., 2015; Xia et al., 2017). The Li-ion transference number (t_{Li+}) is an important parameter to reflect on the effective transportation of Li$^+$ in solid electrolyte, which can be measured by a dc polarization combined with EIS of symmetrical Li//electrolyte//Li cells. As shown in **Figure 4C**, polarization increases the interfacial resistance from 220 to 225 Ω. Meanwhile, current varies from an initial value of 25.2 μA before polarization to a steady value of 20.3 μA. Therefore, the Li-ion transference number could be calculated based on the Bruce-Vincent equation, and the t_{Li+} value of the PVDF-HFP-LLZTO membrane is 0.66, while the t_{Li+} value of the PVDF-HFP membrane is 0.53. The remarkable improvement of the Li-ion transference number can be ascribed to the LLZTO nanoparticle doping, which enhances the mobility of Li$^+$ and relax the local chain of polymer (Croce et al., 1998; Lin et al., 2005).

To evaluate the electrochemical properties of PH and PHL membranes, we assemble LFP//PH//Li and LFP//PHL//Li cells. **Figures 5A,B** compare the CV curve of LFP//PH//Li and LFP//PHL//Li cells in the potential range of 2.5–4.2 V (vs Li/Li$^+$) with a scanning rate of $0.1\,\mathrm{mV\,s^{-1}}$. There are two characteristic peaks of the LFP//PHL//Li cell appearing at around 3.53 and 3.34 V during anodic and cathodic scan. While the redox peaks of LFP//PH//Li cells are relatively broad, the anodic and cathodic peaks shift to 3.68 and 3.13 V, respectively. It demonstrates a decrease of cell polarization and an improved redox kinetics (Zhang et al., 2019).

To evaluate the rate capability of LFP//PH//Li and LFP//PHL//Li cells, the rate capability is tested at different current densities

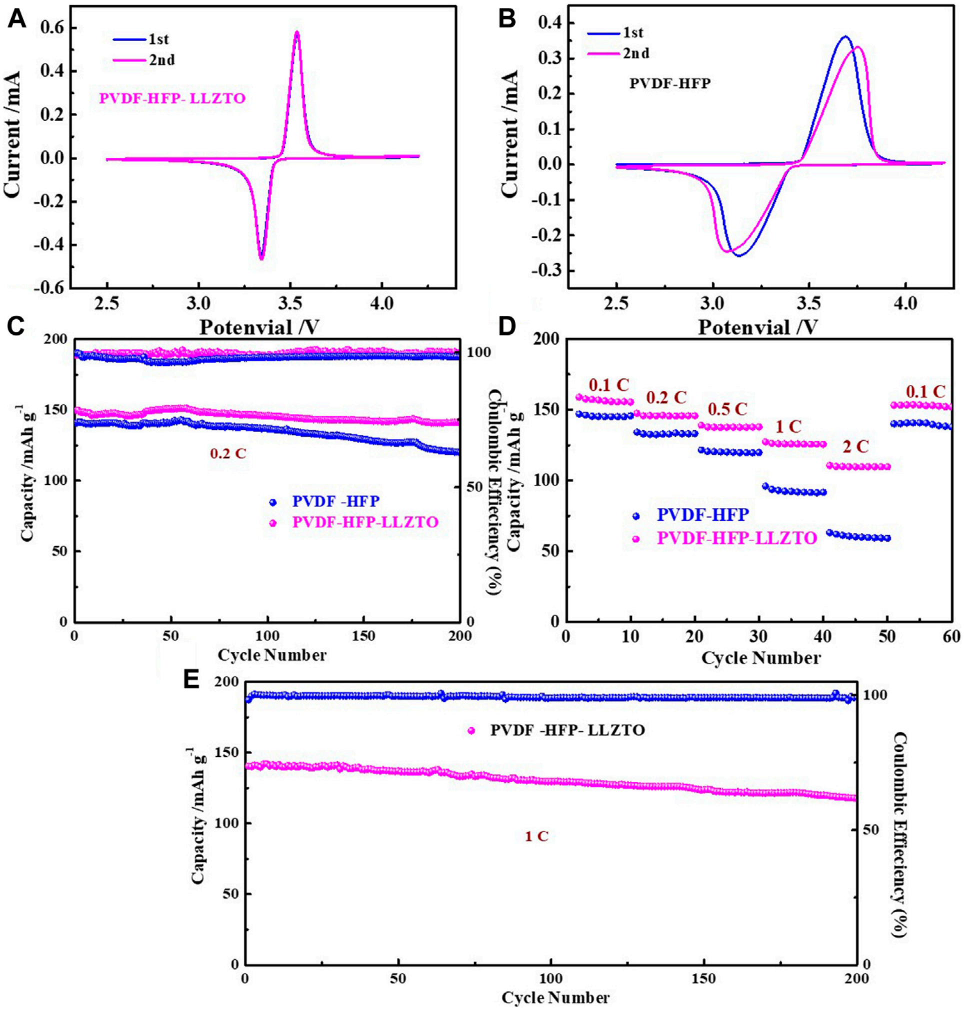

FIGURE 5 | The CV curve of **(A)** LFP/PHL/Li cell, **(B)** LFP/PH/Li cell, **(C)** cycling performance at 0.2 C, **(D)** rate performance, and **(E)** cycling performance at 1 of LFP/PHL/Li and LFP/PH/Li cells.

from 0.1 to 2 C. As shown in **Figure 5D**, the LFP//PHL//Li cell exhibits 158.9 mAh g^{-1}, 147.4 mAh g^{-1}, 139.1 mAh g^{-1}, 127.4 mAh g^{-1}, and 110.7 mAh g^{-1} at current densities of 0.1, 0.2, 0.5, 1, and 2 C, respectively. When the current density is converted from 2 to 0.1 C, the discharge capacity of the LFP//PHL//Li cell still can be recovered to 153.1 mAh g^{-1}, suggesting a good reversibility of the LFP//PHL//Li cell. In contrast, the LFP//PH//Li cell only delivers 147 mAh g^{-1}, 134.2 mAh g^{-1}, 121.6 mAh g^{-1}, 95.9 mAh g^{-1}, and 63.3 mAh g^{-1} at current densities of 0.1, 0.2, 0.5, 1, and 2 C, respectively.

We also test long cycle electrochemical performance of LFP//PH//Li and LFP//PHL//Li cells. The cycling performance of LFP//PH//Li and LFP//PHL//Li cells is measured at a current density of 0.2 C (**Figure 5C**), and the LFP//PHL//Li cell exhibits a higher initial capacity of 149.6 mAh g^{-1} than the LFP//PH//Li cell (140.6 mAh g^{-1}). It is worth noting that the capacity retention can be 94% even after 200 cycles and the Coulombic efficiency is almost 100% during the cycle. Additionally, high-rate long cycling life at 1 C of LFP//PHL//Li cells is shown in **Figure 5E**. The LFP//PHL//Li cell delivers the initial discharge capacities of 140.4 mAh g^{-1}, and the capacity remains 117.6 mAh g^{-1}, corresponding to a low capacity fading rate of only 0.089% per cycle. Therefore, the LFP//PHL//Li cell shows enhanced electrochemical performance which can be ascribed to the high ionic conductivity and transference number of the PVDF-HFP-LLZTO gel polymer electrolyte.

CONCLUSION

In summary, we prepare a three-dimensional highly porous polymer electrolyte based on PVDF-HFP with $Li_{6.4}La_3Zr_{1.4}Ta_{0.6}O_{12}$ (LLZTO) nanoparticle fillers using the electrospinning technique. This unique 3D hierarchical nanostructure with abundant porosity promotes the liquid electrolyte uptake and wetting, and favors the Li-ion transfer between the electrodes and electrolyte. And the LLZTO nanoparticle fillers decrease the crystallinity of PVDF-HFP; thus, the ionic conductivity and Li-ion transference number can reach 9.44×10^{-4} S cm^{-1} and 0.66. In addition, the LFP//PHL//Li cell exhibits enhanced electrochemical performance with improved cycling stability. This PVDF-HFP-LLZTO gel polymer electrolyte with high ionic conductivity and transference number demonstrates the potential application for solid-state batteries.

EXPERIMENTAL SECTION

Preparation of PVDF-HFP-LLZTO Gel Polymer Electrolyte

The PVDF-HFP-LLZTO gel polymer electrolyte (PHL) was prepared by electrospinning. First, the LLZTO powder was synthesized through a solid-state reaction according to the previous report. Then the microsize LLZTO powder was ball-milled into nanoparticles. 20 wt% PVDF-HFP was dissolved in *N*, *N*-dimethylformamide (DMF) with continuous stirring for 4 h. And a proper amount of LLZTO with 5 wt% was added into the solution with further stirring for 4 h to form a uniform solution. In the electrospinning process, the PVDF-HFP-LLZTO solution was electrospun onto the rotating aluminum collector with a flow rate of 1.5 ml h^{-1}, while the voltage applied to the needle tip was set at 15kV with the distance of 20 cm from the needle to the collector. The obtained electrospun membrane was removed from the collector and evaporated at 60°C for 12 h. And the dry membrane was cut into 19 mm in diameter and was activated by soaking the commercial liquid electrolyte (1 M $LiPF_6$ in EC/DEC 1: 1 by volume) for use. And the PVDF-HFP gel polymer electrolyte (PH) was prepared by the same method without LLZTO doping.

Material Characterization

The morphology and microstructure of the samples were characterized by scanning electron microscopy (SEM, Hitachi S-4800). The crystal structure was investigated using X-ray diffraction (XRD, Rigaku D/max 2550 PC, Cu Kα). Fourier transform infrared spectra (FTIR) were characterized between 4,000 and 400 cm^{-1} with the Bruker VERTEX 70 FTIR spectrometer. Differential scanning calorimetry (DSC) was carried out on DSC Q100 from room temperature to 200°C under N_2 flow at a heating rate of 5°C min^{-1}.

Electrochemical Measurements

To make the cathode, $LiFePO_4$ (LFP), carbon black, and PVDF with a weight ratio of 8:1:1 were then dispersed in N-methyl-2-pyrrolidone (NMP). After magnetic stirring for 4 h, the homogeneous slurry was then cast on the Al foil, and the LFP cathode was dried at 80°C in vacuum for 12 h. The 2032 type cell was assembled with LFP as cathode, metallic lithium foil as anode, and the gel polymer electrolyte as electrolyte and separator. Cyclic voltammetry (CV) tests were carried out on CHI660E electrochemical workstation between 2.5 and 4.2 V at a scan rate of 0.1 mV s^{-1}. The galvanostatic charge–discharge performance of the $LiFePO_4$/electrolyte/Li cell at different rates were conducted between 2.5 and 4.2 V (vs Li+/Li) at room temperature. The galvanostatic test were carried out on a Land CT 2001A battery testing system at room temperature. The ionic conductivity of different membranes was carried out with the symmetric cell, and its value can be calculated by **Eq. 2**.

$$\sigma = L/(R \times A), \tag{1}$$

where L is the thickness of the electrolyte membrane, A is the electrode area, and R represents bulk resistance of the symmetrical stainless blocking cells, which could be measured on the Princeton multichannel electrochemical workstation from 10^6 Hz to 10^{-2} Hz with an amplitude of 10 mV. The Li-ion transference number could be calculated by the Bruce–Vincent formula in **Eq. 2**.

$$t_{Li^+} = \frac{I_s(\Delta V - I_0 R_0)}{I_0(\Delta V - I_s R_s)}, \tag{2}$$

where I_0 and I_s represent the initial and stable current which could be obtained from the DC polarization of symmetrical Li/electrolyte/Li cell, respectively. And R_0 and R_s represent the impedance before and after polarization with a DC voltage (ΔV = 10 mV), respectively.

DATA AVAILABILITY STATEMENT

The original contributions presented in the study are included in the article/Supplementary Material; further inquiries can be directed to the corresponding author.

AUTHOR CONTRIBUTIONS

DW and DC: experimental design, conduct of experiment, collection of data, data analysis, and manuscript writing; YZ: experimental design, critical revision of this article, data analysis, and interpretation; ZJ: material properties analysis and discussion; SZ: electrochemical performance test and results discussion; XX and XW: review and editing; JT: critical revision of this article and final approval of article. All authors contributed to the article and approved the submitted version.

FUNDING

The authors acknowledge the support by the National Natural Science Foundation of China (Grant. No. 51971201), the Postdoctoral Science Foundation of Zhejiang Province (zj2019097), and the fellowship of China Postdoctoral Science Foundation (2020M680076).

REFERENCES

Bachman, J. C., Muy, S., Grimaud, A., Chang, H. H., Pour, N., Lux, S. F., et al. (2016). Inorganic Solid-State Electrolytes for Lithium Batteries: Mechanisms and Properties Governing Ion Conduction. *Chem. Rev.* 116 (1), 140–162. doi:10.1021/acs.chemrev.5b00563

Blake, A. J., Kohlmeyer, R. R., Hardin, J. O., Carmona, E. A., Maruyama, B., Berrigan, J. D., et al. (2017). 3D Printable Ceramic-Polymer Electrolytes for Flexible High-Performance Li-Ion Batteries with Enhanced thermal Stability. *Adv. Energ. Mater.*, 1602920. doi:10.1002/aenm.201602920

Cao, J., Wang, L., Shang, Y., Fang, M., Deng, L., Gao, J., et al. (2013). Dispersibility of Nano-TiO_2 on Performance of Composite Polymer Electrolytes for Li-Ion Batteries. *Electrochim. Acta* 111, 674–679. doi:10.1016/j.electacta.2013.08.048

Chen, R. J., Qu, W. J., Guo, X., Li, L., and Wu, F. (2016). The Pursuit of Solid-State Electrolytes for Lithium Batteries: from Comprehensive Insight to Emerging Horizons. *Mater. Horiz.* 3 (6), 487–516. doi:10.1039/c6mh00218h

Croce, F., Appetecchi, G. B., Persi, L., and Scrosati, B. (1998). Nanocomposite Polymer Electrolytes for Lithium Batteries. *Nature* 394 (6692), 456–458. doi:10.1038/28818

Cui, Y. Y., Liang, X. M., Chai, J. C., Cui, Z. L., Wang, Q. L., He, W. S., et al. (2017). High Performance Solid Polymer Electrolytes for Rechargeable Batteries: a Self-Catalyzed Strategy toward Facile Synthesis. *Adv. Sci.* doi:10.1002/advs.201700174

Deng, K., Qin, J., Wang, S., Ren, S., Han, D., Xiao, M., et al. (2018). Effective Suppression of Lithium Dendrite Growth Using a Flexible Single-Ion Conducting Polymer Electrolyte. *Small* 14 (31), 1801420. doi:10.1002/smll.201801420

Fan, L., Wei, S., Li, S., Li, Q., and Lu, Y. (2018). Recent Progress of the Solid-State Electrolytes for High-Energy Metal-Based Batteries. *Adv. Energ. Mater.* 8 (11), 1702657. doi:10.1002/aenm.201702657

Farooqui, U. R., Ahmad, A. L., and Hamid, N. A. (2017). Effect of Polyaniline (PANI) on Poly(vinylidene Fluoride-Co-Hexaflouro Propylene) (PVDF-Co-HFP) Polymer Electrolyte Membrane Prepared by Breath Figure Method. *Polym. Test.* 60, 124–131. doi:10.1016/j.polymertesting.2017.03.012

Fasciani, C., Panero, S., Hassoun, J., and Scrosati, B. (2015). Novel Configuration of Poly(vinylidenedifluoride)-Based Gel Polymer Electrolyte for Application in Lithium-Ion Batteries. *J. Power Sourc.* 294, 180–186. doi:10.1016/j.jpowsour.2015.06.068

Fergus, J. W. (2010). Ceramic and Polymeric Solid Electrolytes for Lithium-Ion Batteries. *J. Power Sourc.* 195 (15), 4554–4569. doi:10.1016/j.jpowsour.2010.01.076

Fu, X. T., Yu, D. N., Zhou, J. W., Li, S. W., Gao, X., Han, Y. Z., et al. (2016). Inorganic and Organic Hybrid Solid Electrolytes for Lithium-Ion Batteries. *CrystEngComm* 18 (23), 4236–4258. doi:10.1039/c6ce00171h

Gao, Z. H., Sun, H. B., Fu, L., Ye, F. L., Zhang, Y., Luo, W., et al. (2018). Promises, Challenges, and Recent Progress of Inorganic Solid-State Electrolytes for All-Solid-State Lithium Batteries. *Adv. Mater.* 30 (17), 1705702. doi:10.1002/adma.201705702

Guo, Q., Han, Y., Wang, H., Xiong, S., Li, Y., Liu, S., et al. (2017). New Class of LAGP-Based Solid Polymer Composite Electrolyte for Efficient and Safe Solid-State Lithium Batteries. *ACS Appl. Mater. Inter.* 9 (48), 41837–41844. doi:10.1021/acsami.7b12092

Hazama, T., Fujii, K., Sakai, T., Aoki, M., Mimura, H., Eguchi, H., et al. (2015). High-performance Gel Electrolytes with Tetra-Armed Polymer Network for Li Ion Batteries. *J. Power Sourc.* 286, 470–474. doi:10.1016/j.jpowsour.2015.04.011

Huang, X. Y., Zeng, S. S., Liu, J. J., He, T., Sun, L. Y., Xu, D. H., et al. (2015). High-performance Electrospun Poly(vinylidene Fluoride)/poly(propylene Carbonate) Gel Polymer Electrolyte for Lithium-Ion Batteries. *J. Phys. Chem. C* 119 (50), 27882–27891. doi:10.1021/acs.jpcc.5b09130

Jiang, T., He, P., Wang, G., Shen, Y., Nan, C. W., and Fan, L. Z. (2020). Solvent-free Synthesis of Thin, Flexible, Nonflammable Garnet-based Composite Solid Electrolyte for All-solid-state Lithium Batteries. *Adv. Energ. Mater.* 10 (12), 1903376. doi:10.1002/aenm.201903376

Jiang, Y., Yan, X., Ma, Z., Mei, P., Xiao, W., You, Q., et al. (2018). Development of the PEO Based Solid Polymer Electrolytes for All-Solid State Lithium Ion Batteries. *Polymers* 10 (11), 1237. doi:10.3390/polym10111237

Le, H. T., Ngo, D. T., Kalubarme, R. S., Cao, G., Park, C. N., and Park, C. J. (2016). Composite Gel Polymer Electrolyte Based on Poly(vinylidene Fluoride-Hexafluoropropylene) (PVDF-HFP) with Modified Aluminum-Doped Lithium Lanthanum Titanate (A-LLTO) for High-Performance Lithium Rechargeable Batteries. *ACS Appl. Mater. Inter.* 8 (32), 20710–20719. doi:10.1021/acsami.6b05301

Li, C., Qin, B., Zhang, Y., Varzi, A., Passerini, S., Wang, J., et al. (2019). Single-ion Conducting Electrolyte Based on Electrospun Nanofibers for High-Performance Lithium Batteries. *Adv. Energ. Mater.* 9 (10), 1803422. doi:10.1002/aenm.201803422

Li, S., Zhang, S. Q., Shen, L., Liu, Q., Ma, J. B., Lv, W., et al. (2020). Progress and Perspective of Ceramic/polymer Composite Solid Electrolytes for Lithium Batteries. *Adv. Sci.* 7 (5), 1903088. doi:10.1002/advs.201903088

Li, Y., Chen, X., Dolocan, A., Cui, Z., Xin, S., Xue, L., et al. (2018). Garnet Electrolyte with an Ultralow Interfacial Resistance for Li-Metal Batteries. *J. Am. Chem. Soc.* 140 (20), 6448–6455. doi:10.1021/jacs.8b03106

Liang, Y. F., Deng, S. J., Xia, Y., Wang, X. L., Xia, X. H., Wu, J. B., et al. (2018). A superior Composite Gel Polymer Electrolyte of $Li_7La_3Zr_2O_{12}$- Poly(vinylidene Fluoride-Hexafluoropropylene) (PVDF-HFP) for Rechargeable Solid-State Lithium Ion Batteries. *Mater. Res. Bull.* 102, 412–417. doi:10.1016/j.materresbull.2018.02.051

Lim, Y. J., Kim, H. W., Lee, S. S., Kim, H. J., Kim, J.-K., Jung, Y.-G., et al. (2015). Ceramic-Based Composite Solid Electrolyte for Lithium-Ion Batteries. *ChemPlusChem* 80 (7), 1100–1103. doi:10.1002/cplu.201500106

Lin, C. W., Hung, C. L., Venkateswarlu, M., and Hwang, B. J. (2005). Influence of TiO_2 Nano-Particles on the Transport Properties of Composite Polymer Electrolyte for Lithium-Ion Batteries. *J. Power Sourc.* 146 (1), 397–401. doi:10.1016/j.jpowsour.2005.03.028

Liu, M., Jiang, H. R., Ren, Y. X., Zhou, D., Kang, F. Y., and Zhao, T. S. (2016). *In-situ* Fabrication of a Freestanding Acrylate-Based Hierarchical Electrolyte for Lithium-Sulfur Batteries. *Electrochim. Acta* 213, 871–878. doi:10.1016/j.electacta.2016.08.015

Manthiram, A., Yu, X. W., and Wang, S. F. (2017). Lithium Battery Chemistries Enabled by Solid-State Electrolytes. *Nat. Rev. Mater.* 2 (4), 16103. doi:10.1038/natrevmats.2016.103

Mauger, A., Armand, M., Julien, C. M., and Zaghib, K. (2017). Challenges and Issues Facing Lithium Metal for Solid-State Rechargeable Batteries. *J. Power Sourc.* 353, 333–342. doi:10.1016/j.jpowsour.2017.04.018

Nair, J. R., Imholt, L., Brunklaus, G., and Winter, M. (2019). Lithium Metal Polymer Electrolyte Batteries: Opportunities and Challenges. *Electrochem. Soc. Interf.* 28 (2), 55–61. doi:10.1149/2.F05192if

Pandey, G. P., Klankowski, S. A., Li, Y., Sun, X. S., Wu, J., Rojeski, R. A., et al. (2015). Effective Infiltration of Gel Polymer Electrolyte into Silicon-Coated Vertically Aligned Carbon Nanofibers as Anodes for Solid-State Lithium-Ion Batteries. *ACS Appl. Mater. Inter.* 7 (37), 20909–20918. doi:10.1021/acsami.5b06444

Prasanth, R., Shubha, N., Hng, H. H., and Srinivasan, M. (2014). Effect of Poly(ethylene Oxide) on Ionic Conductivity and Electrochemical Properties of Poly(vinylidenefluoride) Based Polymer Gel Electrolytes Prepared by Electrospinning for Lithium Ion Batteries. *J. Power Sourc.* 245, 283–291. doi:10.1016/j.jpowsour.2013.05.178

Quartarone, E., and Mustarelli, P. (2011). Electrolytes for Solid-State Lithium Rechargeable Batteries: Recent Advances and Perspectives. *Chem. Soc. Rev.* 40 (5), 2525–2540. doi:10.1039/c0cs00081g

Ren, Y., Liu, T., Shen, Y., Lin, Y., and Nan, C.-W. (2016). Chemical Compatibility between Garnet-like Solid State Electrolyte $Li_{6.75}La_3Zr_{1.75}Ta_{0.25}O_{12}$ and Major Commercial Lithium Battery Cathode Materials. *J. Materiomics* 2 (3), 256–264. doi:10.1016/j.jmat.2016.04.003

Shen, S. S., Zhang, L. B., Zhang, Y. Y., Zhang, G. W., Yang, J. J., and Bai, R. B. (2019). Fabrication of Antifouling Membranes by Blending Poly(vinylidenefluoride) with Cationic Polyionic Liquid. *J. Appl. Polym. Sci.* 137, 48878. doi:10.1002/app.4887810.1002/APP.48878

Tan, D. H. S., Banerjee, A., Chen, Z., and Meng, Y. S. (2020). From Nanoscale Interface Characterization to Sustainable Energy Storage Using All-Solid-State Batteries. *Nat. Nanotechnol.* 15 (3), 170–180. doi:10.1038/s41565-020-0657-x

Thangadurai, V., Narayanan, S., and Pinzaru, D. (2014). Garnet-type Solid-State Fast Li Ion Conductors for Li Batteries: Critical Review. *Chem. Soc. Rev.* 43 (13), 4714–4727. doi:10.1039/c4cs00020j

Wang, C., Fu, K., Kammampata, S. P., McOwen, D. W., Samson, A. J., Zhang, L., et al. (2020). Garnet-type Solid-State Electrolytes: Materials, Interfaces, and Batteries. *Chem. Rev.* 120 (10), 4257–4300. doi:10.1021/acs.chemrev.9b00427

Wang, Y., Chen, C., Xie, H., Gao, T., Yao, Y., Pastel, G., et al. (2017). 3D-printed All-Fiber Li-Ion Battery toward Wearable Energy Storage. *Adv. Funct. Mater.*, 1703140. doi:10.1002/adfm.201703140

Wu, H., Cao, Y., Su, H., and Wang, C. (2018). Tough Gel Electrolyte Using Double Polymer Network Design for the Safe, Stable Cycling of Lithium Metal Anode. *Angew. Chem.* 57 (5), 1361–1365. doi:10.1002/anie.201709774

Xia, Y., Wang, X. L., Xia, X. H., Xu, R. C., Zhang, S. Z., Wu, J. B., et al. (2017). A Newly Designed Composite Gel Polymer Electrolyte Based on Poly(vinylidene Fluoride-Hexafluoropropylene) (PVDF-HFP) for Enhanced Solid-State Lithium-Sulfur Batteries. *Chem. Eur. J.* 23 (60), 15203–15209. doi:10.1002/chem.201703464

Yuan, X., Razzaq, A. A., Chen, Y., Lian, Y., Zhao, X., Peng, Y., et al. (2021). Polyacrylonitrile-based Gel Polymer Electrolyte Filled with Prussian Blue Forhigh-Performance Lithium Polymer Batteries. *Chin. Chem. Lett.* 32 (2), 890–894. doi:10.1016/j.cclet.2020.07.008

Zhang, D., Zhang, L., Yang, K., Wang, H., Yu, C., Xu, D., et al. (2017a). Superior Blends Solid Polymer Electrolyte with Integrated Hierarchical Architectures for All-Solid-State Lithium-Ion Batteries. *ACS Appl. Mater. Inter.* 9 (42), 36886–36896. doi:10.1021/acsami.7b12186

Zhang, S. Z., Xia, X. H., Xie, D., Xu, R. C., Xu, Y. J., Xia, Y., et al. (2019). Facile Interfacial Modification via *In-Situ* Ultraviolet Solidified Gel Polymer Electrolyte for High-Performance Solid-State Lithium Ion Batteries. *J. Power Sourc.* 409, 31–37. doi:10.1016/j.jpowsour.2018.10.088

Zhang, X., Liu, T., Zhang, S., Huang, X., Xu, B., Lin, Y., et al. (2017b). Synergistic Coupling between $Li_{6.75}La_3Zr_{1.75}Ta_{0.25}O_{12}$ and Poly(vinylidene Fluoride) Induces High Ionic Conductivity, Mechanical Strength, and thermal Stability of Solid Composite Electrolytes. *J. Am. Chem. Soc.* 139 (39), 13779–13785. doi:10.1021/jacs.7b06364

Zhao, B., Ma, L., Wu, K., Cao, M., Xu, M., Zhang, X., et al. (2021). Asymmetric Double-Layer Composite Electrolyte with Enhanced Ionic Conductivity and Interface Stability for All-Solid-State Lithium Metal Batteries. *Chin. Chem. Lett.* 32 (1), 125–131. doi:10.1016/j.cclet.2020.10.045

Zhao, Q., Stalin, S., Zhao, C. Z., and Archer, L. A. (2020). Designing Solid-State Electrolytes for Safe, Energy-Dense Batteries. *Nat. Rev. Mater.* 5 (3), 229–252. doi:10.1038/s41578-019-0165-5

Zhou, D., He, Y. B., Liu, R. L., Liu, M., Du, H. D., Li, B. H., et al. (2015). *In Situ* synthesis of a Hierarchical All-Solid-State Electrolyte Based on Nitrile Materials for High-Performance Lithium-Ion Batteries. *Adv. Energ. Mater.* 5 (15), 1500353. doi:10.1002/aenm.201500353

Zhou, X., Jiang, H., Zheng, H., Sun, Y., Liang, X., and Xiang, H. (2020). Nonflammable Hybrid Solid Electrolyte Membrane for a Solid-State Lithium Battery Compatible with Conventional Porous Electrodes. *J. Membr. Sci.* 603, 117820. doi:10.1016/j.memsci.2020.117820

Zhou, Y., Wang, X., Zhu, H., Yoshizawa-Fujita, M., Miyachi, Y., Armand, M., et al. (2017). Solid-state Lithium Conductors for Lithium Metal Batteries Based on Electrospun Nanofiber/plastic crystal Composites. *ChemSusChem* 10 (15), 3135–3145. doi:10.1002/cssc.201700691

Conflict of Interest: The authors declare that the research was conducted in the absence of any commercial or financial relationships that could be construed as a potential conflict of interest.

frontiers in Chemistry

ORIGINAL RESEARCH
published: 18 November 2021
doi: 10.3389/fchem.2021.769186

Nitrogen-Doped Carbon Encapsulated Partial Zinc Stannate Nanocomposite for High-Performance Energy Storage Materials

Jiage Yu*, Zhijie Liu, Xian Zhang, Yu Ding, Zhengbing Fu and Feng Wang*

School of Chemistry and Materials Science, Hubei Engineering University, Xiaogan, China

As a bimetal oxide, partial zinc stannate ($ZnSnO_3$) is one of the most promising next-generation lithium anode materials, which has the advantages of low operating voltage, large theoretical capacity (1,317 mA h g^{-1}), and low cost. However, the shortcomings of large volume expansion and poor electrical conductivity hinder its practical application. The core-shell $ZnSnO_3$@ nitrogen-doped carbon (ZSO@NC) nanocomposite was successfully obtained by coating $ZnSnO_3$ with polypyrrole (PPy) through *in situ* polymerization under ice-bath conditions. Benefiting from this unique compact structure, the shell formed by PPy cannot only effectively alleviate the volume expansion effect of $ZnSnO_3$ but also enhance the electrical conductivity, thus, greatly improving the lithium storage performance. ZSO@NC can deliver a reversible capacity of 967 mA h g^{-1} at 0.1 A g^{-1} after 300 cycles and 365 mA h g^{-1} at 2 A g^{-1} after 1,000 cycles. This work may provide a new avenue for the synthesis of bimetal oxide with a core–shell structure for high-performance energy storage materials.

Keywords: partial zinc stannate, nitrogen-doped carbon, core–shell structure, high-performance energy storage materials, battery

Edited by:
Yu Ding,
University of Maryland, United States

Reviewed by:
Chang Liu,
University of Virginia, United States
Hao Wang,
Institute of Process Engineering (CAS), China

***Correspondence:**
Feng Wang
hbeukj@126.com
Jiage Yu
hbeuyjg@126.com

Specialty section:
This article was submitted to Electrochemistry, a section of the journal Frontiers in Chemistry

Received: *01 September 2021*
Accepted: *08 October 2021*
Published: *18 November 2021*

Citation:
Yu J, Liu Z, Zhang X, Ding Y, Fu Z and Wang F (2021) Nitrogen-Doped Carbon Encapsulated Partial Zinc Stannate Nanocomposite for High-Performance Energy Storage Materials. Front. Chem. 9:769186. doi: 10.3389/fchem.2021.769186

INTRODUCTION

The 14th Five-Year Plan points out that the key core technologies of new energy vehicles should be broken through to make pure electric vehicles become the mainstream. First of all, the development of power Li-ion battery is one of the key core technologies to be addressed (Zhang et al., 2020a; Peng et al., 2021; Yu et al., 2021). At present, the capacity of commercial graphite anode materials has been developed to the ceiling (the theoretical lithium storage capacity is 372 mA h g^{-1}), and it is urgent to develop a new generation of power anode materials, such as ZnO, SnO, Co_3O_4, and so on (Wang et al., 2019; Zhou et al., 2019; Xie et al., 2020). For the special bimetal oxide structure, Zinc stannate ($ZnSnO_3$) has more advantages than single metal oxides. For instance, $ZnSnO_3$ possesses higher theoretical capacity (1,317 mA h g^{-1}) and lower working potential than that of SnO_2 (Zhou et al., 2017; Ma et al., 2018; Tan et al., 2018; Wen et al., 2019). However, the shortcomings of large volume expansion and poor electrical conductivity hinder its commercial application.

Recently, various reports (Liu et al., 2018; Wang et al., 2020a; Kong et al., 2021) revealed that it is an effective strategy to address these problems by constructing the core–shell structure, with the active material as the core and the conductive carbon layer as the shell. For example, Tao Liu et al. (2018) presented a facile and efficient template method for the synthesis of core–shell Co_3O_4/ nitrogen-doped carbon hollow spheres, which deliver an excellent electrochemical performance.

Kuaibing Wang et al. (2020a) reported a successful and effective strategy to prepare core-shell nickel/nitrogen codoped carbon (Ni@NC) materials. The as-prepared material serving as both the positive and negative electrodes, deliver excellent electrochemical performance. Fanjun Kong et al. (2021) obtained the core–shell SnSe@C with high performance by electrospinning, which display superior cycling and rate performance owing to this compact core–shell structure. All these examples show that the core-shell structure with carbon material as the shell can effectively reduce the volume expansion effect and greatly improve the electrochemical performance. Among them, the choice of shell material is crucial. For the low cost, stable voltage window, excellent mechanical resilience and high electronic conductivity (10–50 $S\,cm^{-1}$), polypyrrole (PPy) is one of the star conductive coating layer materials (Ma et al., 2019; Wang et al., 2020b; Zhang et al., 2020b; Chu et al., 2020). Jun-Hong Zhang et al. (2020b) constructed a core–shell NiO-$NiMoO_4$/PPy composite. The flexible PPy cannot only construct a pathway and promote electrons transferring on the active materials but also can serve as the mechanical protection film to refrain from the pulverization of the active materials. What is more, it confirmed that the PPy modification was a direct and effective strategy to improve the reversible capacity and cycling performance of active materials.

Herein, inspired by the above work and our previous study, the PPy modification strategy is adopted to prepare the ZSO@NC nanocomposite. The core–shell ZSO@NC nanocomposite was successfully obtained by coating $ZnSnO_3$ with PPy through *in situ* polymerization under ice-bath conditions. The as-prepared $ZnSnO_3$@NC nanocomposites display superior cycling and rate performances, owing to this unique compact core–shell structure.

EXPERIMENTAL SECTION

Synthesis of $ZnSn(OH)_6$ Precursors and Pure Zinc Stannate

The 6-mmol $SnCl_4{\bullet}5H_2O$ and 24-mmol NaOH were dissolved in 60 ml of ultra-pure water and stirred in an ice bath for 60 min. Then, 30 ml of 0.2 mmol/L $ZnSO_4{\bullet}7H_2O$ solution was slowly added into the reaction container under continuous agitation. At this time, white suspended matter would gradually appear, indicating the formation of $ZnSn(OH)_6$. After centrifugation and washing operation, the product was placed in a vacuum drying oven and dried for 10 h to get the $ZnSn(OH)_6$ powder. The precursor powder was calcined at 500°C for 2 h at a heating rate of 5°C/min under a protective atmosphere. Finally, the pure $ZnSnO_3$ powders were obtained.

Synthesis of ZSO@NC

The 0.4 g of $ZnSn(OH)_6$ was dispersed in 200 ml of deionized water by ultrasonic manipulation. Then, 0.5 ml of pyrrole monomer was quickly added to the beaker under the ice-bath environment, followed by 200 ml of 0.02 M ammonium persulfate solution slowly added, and continuous stirring for 12 h. The above samples were successively washed by water and ethanol three times, and then filtered and dried in a vacuum drying oven at 80°C. Finally, under inert gas protection, the samples were heated to 500°C at 2°C/min for 2 h in a tubular furnace to obtain NC@ZSO-2. As the control group, different volumes of pyrrole monomers were coated in this experiment. In the experiment, 0.25 ml of pyrrole was added to get NC@ZSO-1, and 1 ml of pyrrole was added to get NC@ZSO-3. The corresponding original contributions presented in the study are included in **Supplementary Material**.

Synthesis of ZnO-SnO_2@NC and Nitrogen-Doped Carbon

Except for the different calcination conditions, the preparation process of ZnO-SnO_2@NC is identical with that of ZSO@NC-2. ZnO-SnO_2@NC is obtained at 800°C for 2 h at a heating rate of 5°C/min under a protective atmosphere. Similarly, nitrogen-doped carbon (NC) is prepared by imitating the production process of ZSO@NC-2 without adding zinc source and tin source.

RESULTS AND DISCUSSION

Figure 1 illustrates the synthesis procedure of ZSO@NC nanocomposites with the core–shell structure. First, $ZnSn(OH)_6$ precursors were obtained by co-precipitation method under ice-bath conditions. Then, PPy was coated on the surface of $ZnSnO_3$ nanoparticles by *in situ* polymerization under ice-bath conditions. Finally, the ZSO@NC composites were obtained by calcination in an inert atmosphere. Through optimizing the synthesis conditions, the composites with special core–shell structure were obtained. The XRD patterns of $ZnSn(OH)_6$ are shown in **Supplementary Figure S1**, with all the diffraction peaks corresponding to the standard peaks of $ZnSn(OH)_6$ (JCPDS-No. 20-1455). **Figure 2A** displays the XRD patterns of ZSO@NC-(1,2,3) and pure $ZnSnO_3$. These diffraction peaks can basically be indexed to the standard cards $ZnSnO_3$ phase (JCPDS-No. 28-1486), indicating partial $ZnSn(OH)_6$ had transformed to the $ZnSnO_3$ phase under calcination conditions (Ma et al., 2018). In addition, with the increase in pyrrole content in the above four samples, the carbon peak at 26.5° was significantly enhanced, indicating the presence of amorphous carbon (Liu et al., 2020; He et al., 2017). **Figure 2B** shows the thermogravimetric analysis (TGA) of ZSO@NC-(1,2,3) and pure $ZnSnO_3$. It revealed that the amount of NC in the ZSO@NC-(1,2,3) composites is about 16.9, 29.5, and 47.5 wt%, respectively, and there is little mass loss in the pure $ZnSnO_3$. **Supplementary Figure S2** shows the Raman spectra of all the composites. The difference between ZSO@NC-(1,2,3) and pure $ZnSnO_3$ is that there are two main peaks located at ~1,350 and ~1,557 cm^{-1}, which can be attributed to the D peak of amorphous carbon and the G peak of graphitized carbon. For NC@ZSO-2, the intensity ratio of D peak to G peak is 1.02. This indicates that there are lots of vacancies and graphitized carbon between the layers of carbon in this material (Yu et al., 2018). The surface elemental compositions and electronic states of ZSO@NC-2 were characterized by XPS measurement. The deconvolutions of the

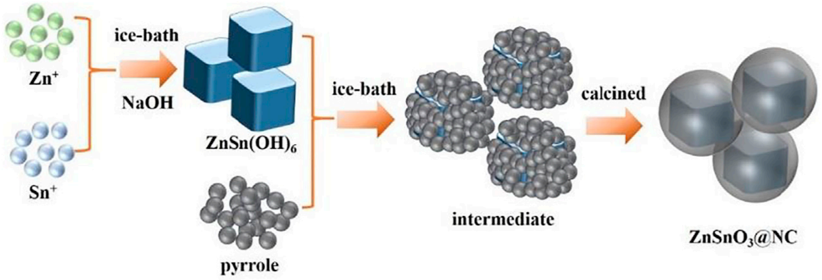

FIGURE 1 | Schematic illustration of the synthesis process of ZSO@NC.

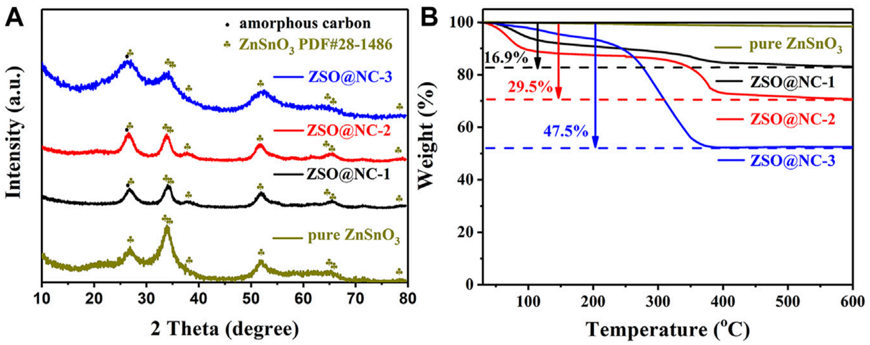

FIGURE 2 | XRD patterns **(A)** and TGA curves **(B)** of the ZSO@NC-(1,2,3) and pure zinc stannate ($ZnSnO_3$).

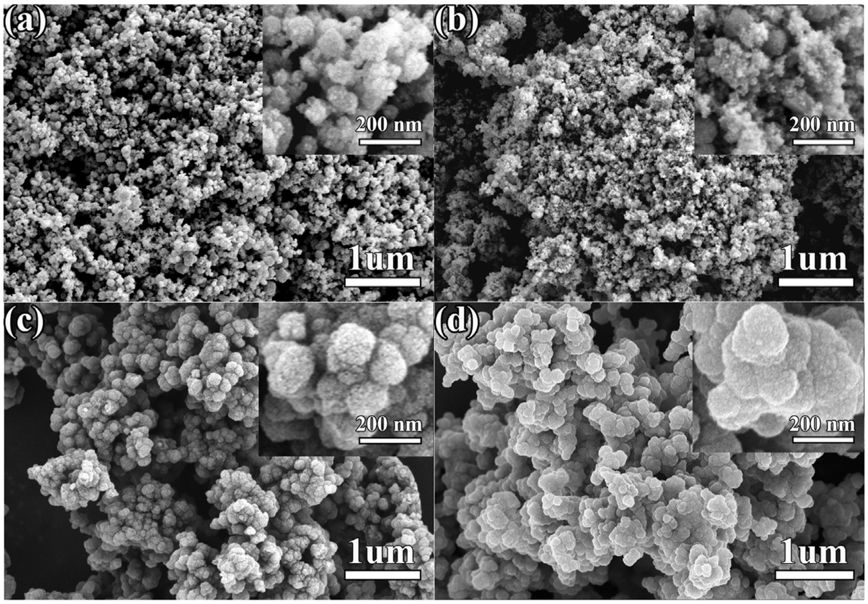

FIGURE 3 | FE-SEM image of pure $ZnSnO_3$ **(A)**, ZSO@NC-1 **(B)**, ZSO@NC-2 **(C)**, and ZSO@NC-3 **(D)**.

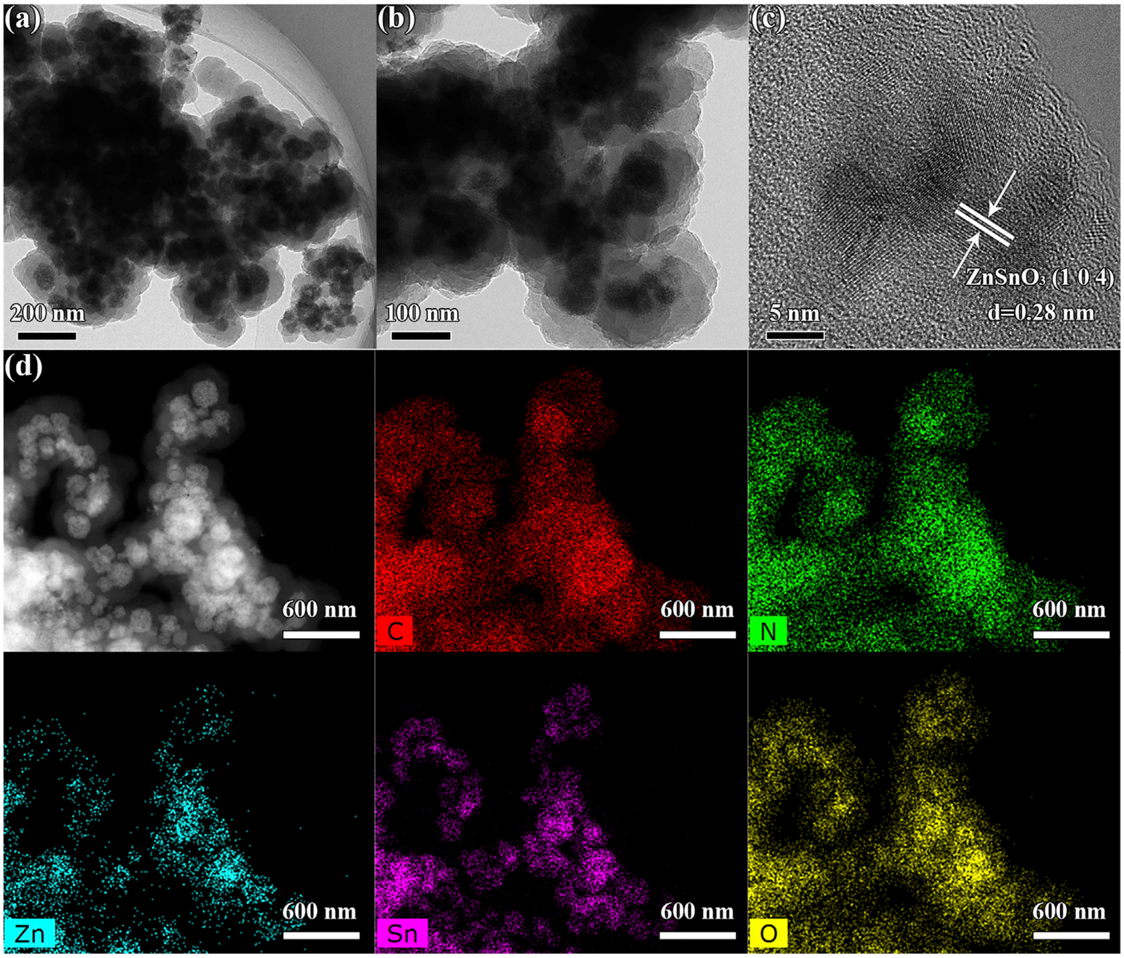

FIGURE 4 | TEM **(A, B)** and HRTEM **(C)** and EDS mapping **(D)** images of NC@ZSO-2.

C1s spectra are exhibited in **Supplementary Figure S3A**. The peaks at 284.3, 285.4, and 287.6 are associated with C-C, C=C, and C-N functional groups, respectively. In **Supplementary Figure S3B**, the N1s spectra can be deconvoluted into two individual peaks that are assigned to pyridinic N (398.0 eV) and pyrrolic N (399.8 eV) (Hu et al., 2013). **Supplementary Figure S3C** shows the high-resolution XPS spectrum of the Zn 2p. The two photoelectron peaks at binding energies of 1,021.8 and 1,044.9 eV correspond to Zn 2p3/2 and Zn 2p1/2, respectively. For the spectrum of Sn 3d, the two peaks observed at 486.9 and 495.4 are related to Sn 3d5/2 and Sn 3d3/2, respectively, as observed in **Supplementary Figure S3D**. It manifests the existence of Zn^{2+} and Sn^{4+} in the ZSO@NC-2 particles (Liang et al., 2018). The XPS results further verify the coexistence of $ZnSnO_3$ and NC in the composite, which agrees well with the XRD results.

Special FE-SEM images provide insight into the morphologies and structures of the as-synthesized ZSO@NC-(1,2,3) and pure $ZnSnO_3$. As shown in **Figure 3A**, pure $ZnSnO_3$ are numerous homogeneous nanoparticles, and the average size of nanoparticles is estimated from a statistic of 200 samples to be about 80.5 nm (**Supplementary Figure S4A**). The FE-SEM images of ZSO@NC-2 is observed in **Figure 3B**, it revealed that the surface of the $ZnSnO_3$ nanoparticle is covered with many smaller particles. By comparing **Figures 3A, B**, it can be inferred that the smaller nanoparticle is carbon. As displayed in **Figure 3C**, the ZSO@NC-2 is composed of large particles, which are agglomerated one by one. After NC coating, the average size of nanoparticles is significantly increased to 181.4 nm estimated from a statistic of 200 samples (**Supplementary Figure S4B**). Compared with **Figure 3C**, the particles in **Figure 3D** are larger, and the agglomeration phenomenon is more serious, which may be caused by the thicker carbon layer formed by a higher carbon content in ZSO@NC-3. The structural and morphological characteristics of ZSO@NC-2 are further revealed by TEM, HRTEM, and EDS mapping in **Figure 4**. As shown in **Figures 4A, B**, ZSO@NC-2 has a unique core–shell structure, consisting of a carbon layer completely encapsulated with $ZnSnO_3$ particles. **Figure 4C** displays the corresponding HRTEM image, and these nanoparticles are crystalline with the fringe spacing of 0.28 nm, corresponding to the (104) plane of $ZnSnO_3$ (Zhou et al., 2017). **Figure 4D** is the EDS-Mapping

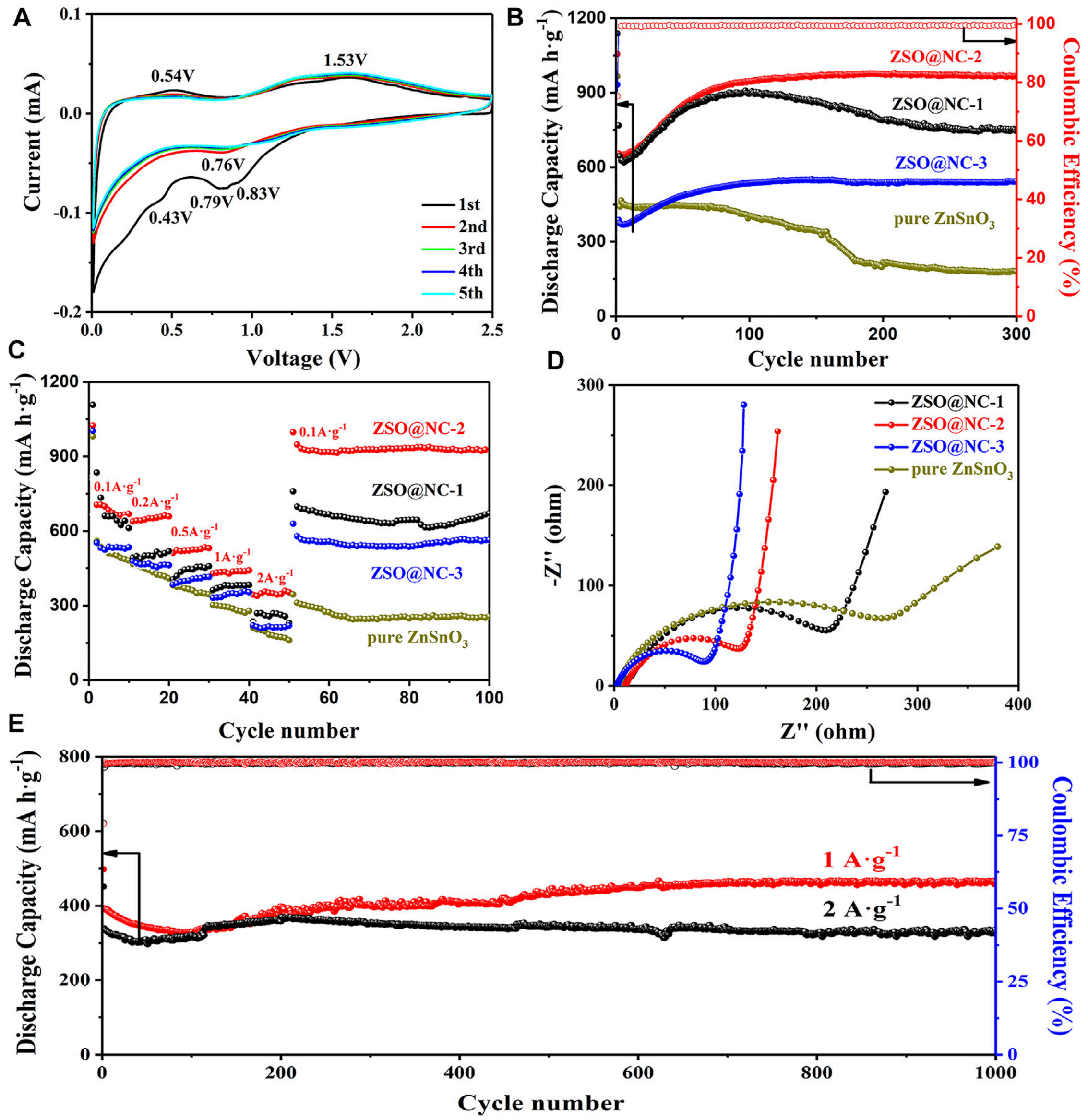

FIGURE 5 | (A) Typical CV curves of ZSO@NC-2, **(B)** Cyclic performance curves of ZSO@NC-(1,2,3) and pure $ZnSnO_3$ at 0.1 A g^{-1}. **(C)** Specific capacity versus current densities. **(D)** EIS curves of ZSO@NC-(1,2,3) and pure $ZnSnO_3$. **(E)** Cyclic performance curves of ZSO@NC-2 at 1 and 2 A g^{-1}.

image of ZSO@NC-2. It can be found that the distribution of C and N elements is exactly the same, indicating that this carbon layer is composed of nitrogen-doped carbon (NC). The elemental distribution of Zn, Sn, and O is basically the same. Meanwhile, the elemental distribution range of C and N completely covers that of Sn, Zn, O element, which further confirms that ZSO@NC-2 is a core–shell structure composed of NC completely coated $ZnSnO_3$ particles.

The electrochemical mechanism of NC@ZSO-2 was explored by cyclic voltammetry test in **Figure 5A**. In the first cycle, two wide inconspicuous cathodic peaks centered at 0.43 and 0.79 V, which could be attributed to the formation of SEI film and the decomposition of $ZnSnO_3$ (Ma et al., 2018). Another two obvious oxidation peaks at 0.54 and 1.53 V were observed, which could be interpreted as the reaction of Li^+ detachment from the metal alloy Li–Sn and Li–Zn. In the second and subsequent cycles, the peak of 0.79 V shifted to 0.83 V. The two redox couples, indexed as 0.05/0.53 and 0.83/1.53 V, appeared due to the alloying/dealloying process and the formation/decomposition of Li_2O. After the first cycle, the subsequent CV curves are well overlapped, confirming the stable storage and release of Li^+ in the ZSO@NC-2 material. **Figure 5B** shows a comparison of the cycling performance of the ZSO@NC-(1,2,3) and pure $ZnSnO_3$ at 0.1 A g^{-1}. The discharge capacity of ZSO@NC-2 decreased in the initial several cycles, then increased gradually with continuous cycling. Finally, a relatively stable discharge capacity of

967 mA h g^{-1} was achieved after 300 cycles with the CE approaching 100%. The gradual increase in the capacity may have mainly resulted from the formation of a gel-like polymeric layer and possibly interfacial lithium storage as well as electrochemical activation process of the composite during the repeated Li insertion/extraction (Yu et al., 2018; Hu et al., 2013; Liang et al., 2018). To highlight the advantage of bimetallic oxide, ZnO-SnO_2@NC is obtained at 800°C for 2 h at a heating rate of 5°C/min under a protective atmosphere. Except for the different calcination conditions, the preparation process of ZnO-SnO_2@NC is identical with that of ZSO@NC-2. Similarly, nitrogen-doped carbon (NC) is prepared by imitating the production process of ZSO@NC-2 without adding zinc source and tin source. As shown in **Supplementary Figure S5A**, ZnO-SnO_2@NC is mainly composed of SnO_2 (PDF#24–1,470), Zn_2SnO_4 (PDF#41–1,445), and amorphous carbon. The cyclic performance of the above materials is tested at 0.1 A·g^{-1} by assembling into the Li^+ half-battery (**Supplementary Figure S5B**). Compared with $ZnSnO_3$, the cycle stability of ZnO-SnO2@NC electrode is extremely poor with only 134 mA h g^{-1} after 200 cycles, which indicates that the unique bimetal structure of $ZnSnO_3$ has performance advantages. The cycling performance curve of ZSO@NC-3 is similar to that of ZSO@NC-2. Due to the high NC content of the former, the specific capacity of the former is lower than that of the latter after stabilization. The reversible capacity of ZSO@NC-3 is 544 mA h g^{-1} after 300 cycles. Compared with the above two samples, ZSO@NC-1 has a lower cyclic stability, attributing to the lower NC content. The reversible capacity of ZSO@NC-1 is 745 mA h g^{-1} after 300 cycles. Compared with the previous three samples, pure $ZnSnO_3$ exhibit extremely worst cycle stability (187 mA h g^{-1} after 300 cycles), which can be attributed to the violent volumetric expansion effect during the repeated Li insertion/extraction process. Nitrogen-doped carbon (NC) is successfully prepared by imitating the production process of ZSO@NC-2 without adding zinc source and tin source. As shown in **Supplementary Figure S6A**, NC is mainly composed of amorphous carbon. The NC electrode shows excellent cycling stability (**Supplementary Figure S6B**). However, its specific capacity is only about 250 mA h g^{-1}, which is too low to compare with that of ZSO@NC-2, and NC (in **Supplementary Figure S6D**) also shows a good rate capability. The corresponding reversible capacities were 301, 252, 205, 177, and 152 mA h g^{-1} at 0.1, 0.2, 0.5, 1, and 2 A g^{-1} after 10 cycles, respectively. As shown in **Figure 5C**, ZSO@NC-2 showed the best rate capability among the as-synthesized samples. The corresponding reversible capacities were 698, 641, 521, 436, and 362 mA h g^{-1} at 0.1, 0.2, 0.5, 1, and 2 A g^{-1} after 10 cycles, respectively. In contrast, pure $ZnSnO_3$ only delivered 480, 409, 344, 278, and 169 mA h g^{-1} at the same current densities, respectively. When the current density recovered from 2 to 0.1 A g^{-1}, ZSO@NC-2 delivered an even higher capacity than the primary capacity at various current densities, indicating good reproducibility. The excellent cyclic performance of ZSO@NC-2 can be attributed to its unique compact core–shell structure. The shell formed by nitrogen doping carbon cannot only effectively alleviate the volume expansion effect of $ZnSnO_3$ but also enhance the conductive property of the material, thus, greatly improving the lithium storage performance of the material. **Figure 5D** reveals the Nyquist plots of ZSO@NC-(1,2,3) and pure $ZnSnO_3$. In general, the electrolyte resistance (R_s) corresponds to the first intercept of semicircle on the Z' axis, the charge transfer resistance (R_{ct}) is determined by the diameter of the semicircle, and the resistance of Li ion diffusion (Z_w) is related to the linear slope (Yu et al., 2018). The R_s and R_{ct} values of ZSO@NC-2 are 11.1 and 143.4 Ω, respectively. Oi contrast, that of pure $ZnSnO_3$ is larger (11.7 and 302.1 Ω) (**Supplementary Table S1**). **Supplementary Figure S6C** reveals the Nyquist plot of NC. The R_s and R_{ct} values of NC are 3.5 and 13.9 Ω, respectively, indicating that the material has excellent electrical conductivity. The shell formed by nitrogen doping carbon cannot only effectively alleviate the volume expansion effect of ZnSnO3 but also enhance the conductive property of the material, thus, greatly improving the lithium storage performance of the material. The low Rct value enables faster charge transfer, achieving better rate capability of the ZSO@NC-2 electrode. To examine the longer cycling stability of ZSO@NC-2, it was further cycled to 1,000 cycles at a higher current density of 1 and 2 A g^{-1}. As shown in **Figure 5E**, when cycled at 1 and 2 A g^{-1}, the reversible capacity remained stabilized at 458 and 365 mA h g^{-1} after 1,000 cycles. The cyclic failure mechanism of materials with high specific capacity can be attributed to the severe volume expansion effect generated during the cyclic process, which will continuously destroy SEI, consume electrolytes to form new SEI, and eventually lead to extremely poor cyclic stability. As shown in **Supplementary Figure S6**, the NC electrode shows good conductivity and excellent cycle stability, which indicates that the NC electrode can easily form a stable SEI layer. A large number of studies have shown that the core–shell structure can effectively improve the cyclic stability, with NC as the shell and high specific capacity active substance as the core. On the one hand, the NC shell can alleviate the volume expansion effect. On the other hand, the NC layer can effectively separate the active substance from the electrolyte and contribute to the formation of the stable SEI layer. What is more, the excellent electrical conductivity of the NC shell also contributes to the formation of the stable SEI layer, which greatly improves cycle stability.

CONCLUSION

In this paper, a core–shell ZSO@NC nanocomposite was successfully obtained by coating $ZnSnO_3$ with polypyrrole (PPy) through *in situ* polymerization under ice-bath conditions. Through a series of physical characterization, it revealed that the composite has a unique core–shell structure. The shell is composed of nitrogen-doped carbon spheres, and the core is composed of cubic $ZnSnO_{3.}$ Benefiting from this unique compact structure, ZSO@NC-2 delivers an excellent lithium storage performance. When the current density is 0.1 A g^{-1}, the ZSO@NC can deliver a reversible capacity of 967 mA h g^{-1} after 300 cycles, which is nearly five times that of pure $ZnSnO_3$. When the current density increases to 1 and 2 A g^{-1}, the reversible capacity of ZSO@NC-2 can reach 458 and 365 mA h g^{-1} after 1,000 cycles, respectively.

DATA AVAILABILITY STATEMENT

The original contributions presented in the study are included in the article/**Supplementary Material**. Further inquiries can be directed to the corresponding authors.

AUTHOR CONTRIBUTIONS

YJ performed the material characterization, data analysis, and manuscript writing. LZ handled the material preparation, electrochemical performance test, and result discussion. ZX was in charge of the manufacture and result analysis of the battery. DY took part in the material property analysis and discussion. WF contributed to the experimental design and manuscript revision. All authors contributed to the article and approved the submitted version.

FUNDING

The authors are thankful for the financial support from the National Nature Science Foundation of China (51402096, 52001118), the Nature Science Foundation of Hubei Province of China (T201517, 2019CFB237), the Nature Science Program of Xiaogan City of China (XGKJ2021010011), and the Educational Commission of Hubei Province of China (Q20212705).

SUPPLEMENTARY MATERIAL

The Supplementary Material for this article can be found online at: https://www.frontiersin.org/articles/10.3389/fchem.2021.769186/full#supplementary-material

REFERENCES

Chu, R., Tan, D., Zhang, J., Chen, Y., Jiang, H., Lin, J., et al. (2020). Long-term Cycling of Core-Shell Fe3O4-Polypyrrole Composite Electrodes via Diffusive and Capacitive Lithiation. *J. Alloys Compounds* 835, 155192. doi:10.1016/j.jallcom.2020.155192

He, W., Wang, C., Zhuge, F., Deng, X., Xu, X., and Zhai, T. (2017). Flexible and High Energy Density Asymmetrical Supercapacitors Based on Core/shell Conducting Polymer Nanowires/manganese Dioxide Nanoflakes. *Nano Energy* 35, 242–250. doi:10.1016/j.nanoen.2017.03.045

Hu, Y.-Y., Liu, Z., Nam, K.-W., Borkiewicz, O. J., Cheng, J., Hua, X., et al. (2013). Origin of Additional Capacities in Metal Oxide Lithium-Ion Battery Electrodes. *Nat. Mater* 12 (12), 1130–1136. doi:10.1038/nmat3784

Kong, F., Han, Z., Tao, S., and Qian, B. (2021). Core-shell Structured SnSe@C Microrod for Na-Ion Battery Anode. *J. Energ. Chem.* 55, 256–264. doi:10.1016/j.jechem.2020.07.016

Liang, C., Liang, S., Xia, Y., Gan, Y., Fang, L., Jiang, Y., et al. (2018). Synthesis of Hierarchical Porous Carbon from Metal Carbonates towards High-Performance Lithium Storage. *Green. Chem.* 20, 1484–1490. doi:10.1039.C1037GC02841E10.1039/c7gc02841e

Liu, T., Zhang, L., You, W., and Yu, J. (2018). Core-Shell Nitrogen-Doped Carbon Hollow Spheres/Co3 O4 Nanosheets as Advanced Electrode for High-Performance Supercapacitor. *Small* 14 (12), 1702407. doi:10.1002/smll.201702407

Liu, X., Li, Q., Qin, Y., and Jiang, Y. (2020). Constructing High-Performance Electrode Materials Using Core-Shell ZnCo2O4@PPy Nanowires for Hybrid Batteries and Water Splitting. *RSC Adv.* 10 (47), 28324–28331. doi:10.1039/d0ra05177b

Ma, J., Zhang, Z., Mentbayeva, A., Yuan, G., Wang, B., Wang, H., et al. (2019). Enhanced Electrochemical Performance of Hollow Heterostructured Carbon Encapsulated Znic Metastanate Microcube Composite for Lithium-Ion and Sodium-Ion Batteries. *Electrochimica Acta* 312, 31–44. doi:10.1016/j.electacta.2019.04.167

Ma, Y., Jiang, R., Li, D., Dong, Y., Liu, Y., and Zhang, J. (2018). Embedding Ultrafine ZnSnO3 Nanoparticles into Reduced Graphene Oxide Composites as High-Performance Electrodes for Lithium Ion Batteries. *Nanotechnology* 29 (19), 195401. doi:10.1088/1361-6528/aab07e

Peng, J., Tao, J., Liu, Z., Yang, Y., Yu, L., Zhang, M., et al. (2021). Ultra-stable and High Capacity Flexible Lithium-Ion Batteries Based on Bimetallic MOFs Derivatives Aiming for Wearable Electronic Devices. *Chem. Eng. J.* 417, 129200. doi:10.1016/j.cej.2021.129200

Tan, H., Cho, H.-W., and Wu, J.-J. (2018). Binder-free ZnO@ZnSnO3 Quantum Dots Core-Shell Nanorod Array Anodes for Lithium-Ion Batteries. *J. Power Sourc.* 388, 11–18. doi:10.1016/j.jpowsour.2018.03.066

Wang, J., Wang, C., and Zhen, M. (2019). Template-free Synthesis of Multifunctional Co3O4 Nanotubes as Excellent Performance Electrode Materials for superior Energy Storage. *Chem. Eng. J.* 356, 1–10. doi:10.1016/j.cej.2018.09.014

Wang, K., Wang, Z., Liu, J., Li, C., Mao, F., Wu, H., et al. (2020). Enhancing the Performance of a Battery-Supercapacitor Hybrid Energy Device through Narrowing the Capacitance Difference between Two Electrodes via the Utilization of 2D MOF-Nanosheet-Derived Ni@ Nitrogen-Doped-Carbon Core-Shell Rings as Both Negative and Positive Electrodes. *ACS Appl. Mater. Inter.* 12 (42), 47482–47489. doi:10.1021/acsami.0c12830

Wang, Y., Cao, L., Li, J., Kou, L., Huang, J., Feng, Y., et al. (2020). Cu/Cu2O@Ppy Nanowires as a Long-Life and High-Capacity Anode for Lithium Ion Battery. *Chem. Eng. J.* 391, 123597. doi:10.1016/j.cej.2019.123597

Wen, S., Zhao, J., Wang, H., and Xu, J. (2019). Facile Synthesis of MSnO3 (M=Mn, Co, Zn)/reduced Graphene Oxide Nanocomposites as Anode Materials for Sodium-Ion Batteries. *J. Alloys Compounds* 784, 88–95. doi:10.1016/j.jallcom.2018.12.378

Xie, X., Liang, S., Gao, J., Guo, S., Guo, J., Wang, C., et al. (2020). Manipulating the Ion-Transfer Kinetics and Interface Stability for High-Performance Zinc Metal Anodes. *Energy Environ. Sci.* 13 (2), 503–510. doi:10.1039/c9ee03545a

Yu, J., Hui, H., Gan, Y., Yang, X., and Zhang, W. (2018). A New Strategy to Construct 3D TiO_2 Nanowires/reduced Graphene Oxide for High-Performance Lithium/sodium Batteries. *J. Mater. Chem. A.* 6 (47). 24256-24266. doi:10.1039/c8ta08214f

Yu, J., Wang, K., Song, W., Huang, H., Liang, C., Xia, Y., et al. (2021). A Low Temperature MgH2-AlCl3-SiO2 System to Synthesize Nano-Silicon for High-Performance Li-Ion Batteries. *Chem. Eng. J.* 406, 126805. doi:10.1016/j.cej.2020.126805

Zhang, J.-H., Yue, H., Ma, Y., Han, X., Mei, J., Zhao, J., et al. (2020). Fabrication of NiO-NiMoO4/PPy Microspheres as High-Performance Anode Material for Lithium-Ion Battery. *Ionics* 26 (8), 3823–3830. doi:10.1007/s11581-020-03534-4

Zhang, J., Li, L., Zheng, C., Xia, Y., Gan, Y., Huang, H., et al. (2020). Silicon-Doped Argyrodite Solid Electrolyte Li6PS5I with Improved Ionic Conductivity and Interfacial Compatibility for High-Performance All-Solid-State Lithium Batteries. *ACS Appl. Mater. Inter.* 12 (37), 41538–41545. doi:10.1021/acsami.0c11683

Zhou, L., Zhang, J., Wu, Y., Wang, W., Ming, H., Sun, Q., et al. (2019). Understanding Ostwald Ripening and Surface Charging Effects in Solvothermally-Prepared Metal Oxide-Carbon Anodes for High Performance Rechargeable Batteries. *Adv. Energ. Mater.* 9 (43), 1902194. doi:10.1002/aenm.201902194

Zhou, T., Zhang, T., Zhang, R., Lou, Z., Deng, J., and Wang, L. (2017). Hollow ZnSnO3 Cubes with Controllable Shells Enabling Highly Efficient Chemical Sensing Detection of Formaldehyde Vapors. *ACS Appl. Mater. Inter.* 9 (16), 14525–14533. doi:10.1021/acsami.7b03112

Conflict of Interest: The authors declare that the research was conducted in the absence of any commercial or financial relationships that could be construed as a potential conflict of interest.

frontiers in Chemistry

ORIGINAL RESEARCH
published: 22 November 2021
doi: 10.3389/fchem.2021.790659

The Synergetic Effect Induced High Electrochemical Performance of CuO/Cu_2O/Cu Nanocomposites as Lithium-Ion Battery Anodes

Lin-Hui Wang[1], Shang Gao[2], Long-Long Ren[3], En-Long Zhou[4] and Yu-Feng Qin[1]*

[1]College of Information Science and Engineering, Shandong Agricultural University, Taian, China, [2]School of Science, Shandong Jiaotong University, Jinan, China, [3]College of Mechanical and Electronic Engineering, Shandong Agricultural University, Taian, China, [4]College of Chemistry and Material Science, Shandong Agricultural University, Taian, China

Due to the high theoretical capability, copper-based oxides were widely investigated. A facile water bath method was used to synthesis CuO nanowires and CuO/Cu_2O/Cu nanocomposites. Owing to the synergetic effect, the CuO/Cu_2O/Cu nanocomposites exhibit superior electrochemical performance compared to the CuO nanowires. The initial discharge and charge capacities are 2,660.4 mAh/g and 2,107.8 mAh/g, and the reversible capacity is 1,265.7 mAh/g after 200 cycles at 200 mA/g. Moreover, the reversible capacity is 1,180 mAh/g at 800 mA/g and 1,750 mAh/g when back to 100 mA/g, indicating the excellent rate capability. The CuO/Cu_2O/Cu nanocomposites also exhibit relatively high electric conductivity and lithium-ion diffusion coefficient, especially after cycling. For the energy storage mechanism, the capacitive controlled mechanism is predominance at the high scan rates, which is consistent with the excellent rate capability. The outstanding electrochemical performance of the CuO/Cu_2O/Cu nanocomposites indicates the potential application of copper-based oxides nanomaterials in future lithium-ion batteries.

Keywords: CuO/Cu_2O/Cu nanocomposites, CuO nanowires, lithium-ion batteries, anodes, water bath method, electrochemical performance

Edited by:
Hongsen Li,
Qingdao University, China

Reviewed by:
Yuxiang Hu,
The University of Queensland, Australia
Huanlei Wang,
Ocean University of China, China

Correspondence:
Yu-Feng Qin
qinyufeng@sdau.edu.cn

Specialty section:
This article was submitted to Electrochemistry, a section of the journal Frontiers in Chemistry

Received: *07 October 2021*
Accepted: *04 November 2021*
Published: *22 November 2021*

Citation:
Wang L-H, Gao S, Ren L-L, Zhou E-L and Qin Y-F (2021) The Synergetic Effect Induced High Electrochemical Performance of CuO/Cu_2O/Cu Nanocomposites as Lithium-Ion Battery Anodes. Front. Chem. 9:790659. doi: 10.3389/fchem.2021.790659

INTRODUCTION

Rechargeable Lithium-ion batteries (LIBs) have been widely used in many fields, such as electric vehicles, cameras, and other portable electronic devices, because of their high working potential, lack of memory effect, and high energy density (Wang et al., 2020; Hu et al., 2020; Teng et al., 2020; Zhang et al., 2020; Zuo and Gong, 2020; Li et al., 2021; Wang et al., 2021; Li et al., 2021; Li et al., 2021d; Wu et al., 2021; Liang et al., 2022). However, the traditional graphite anodes cannot meet further demands of high-power hybrid electric vehicles in the future because of the relatively inferior rate performance and the low theoretical capacity (372 mAh/g) (Shen et al., 2013; Zhang et al., 2013; Zhou et al., 2014; Wang et al., 2020; Pan et al., 2020; Wang et al., 2021). The transition metal oxides have been widely researched for their low cost, widespread availability, and high theoretical capacities (500–1,000 mAh/g) (Shen et al., 2013; Zhang et al., 2013; Zhou et al., 2014; Ananya et al., 2016; Pan et al., 2020). Especially, copper-based oxides were paid much more attention owing to their abundance, environment-friendly, superior rate performance, and high theoretical capacities (674 mAh/g for CuO and 375 mAh/g for Cu_2O) (Shen et al., 2013; Zhang et al., 2013; Wang et al., 2014; Zhou et al., 2014; Ananya et al., 2016; Kim et al., 2019; Pan et al., 2020; Zhang et al., 2021). However, there are also some intrinsic disadvantages, such as volume expansion and low electric conductivity during the charge-discharge process, which should be resolved (Shen et al., 2013; Zhang et al., 2013; Zhou et al., 2014; Ananya et al., 2016; Pan et al., 2020). To solve these problems, many different kinds of nanostructures and morphologies were designed and prepared by many kinds of methods (Wang et al., 2014; Wang et al., 2014; Xu et al., 2016; Kim et al., 2019; Yuan et al., 2019; Zhang et al., 2021). Zhang et al. (2013) synthesized porous CuO nanosphere film which was used as anodes, exhibiting a high reversible discharge capacity of 799.7 mAh/g. Park et al. prepared structure-controlled octahedral Cu_2O nanostructures using polymers as additives during the synthesis, which exhibited superior electrochemical performance (Kim et al., 2019). The CuO nanoparticles with different diameters were also prepared to clarify the effects of the particle's size, delivering a reversible capacity of 540 mAh/g (Wang et al., 2014). Moreover, carbon-based materials were added to enhance the electric conductivity and to relieve the pulverization of the copper-based oxides (Huang et al., 2011; Mai et al., 2011; Shen et al., 2013; Zhou et al., 2014; Chen et al., 2015; Xu et al., 2015; Ananya et al., 2016; Kim et al., 2019; Pan et al., 2020; Trukawka et al., 2021; Zhang et al., 2021). Mu et al. reported that the Cu_2O nanoparticles distributed in the porous carbon channels exhibited a high capacity of 884.4 mAh/g (Zhou et al., 2014). Tu et al. synthesized CuO/graphene composite, whose electrochemical performance was improved with a discharge capacity of 583.5 mAh/g (Mai et al., 2011). Cu_2O@GO composite with a core-shell structure was also synthesized, exhibiting a discharge capacity of 458 mAh/g (Xu et al., 2015).

Recently, due to the synergetic effect, many ternary and quaternary materials were investigated and exhibited excellent electrochemical performance (Shi et al., 2016; Yuan et al., 2017; Wu et al., 2018; Xu et al., 2019; Wang et al., 2020; Gao et al., 2020; Murphin Kumar et al., 2020; Wang et al., 2021b; Li et al., 2021c; Trukawka et al., 2021). Wang et al. prepared Co_3O_4/CuO composite, which exhibited a high charge-discharge capacity of 1,056 mAh/g (Shi et al., 2016). Krishnan et al. fabricated porous Cu_2O: Mo microspheres, which showed a reversible capacity of 1,082 mAh/g (Murphin Kumar et al., 2020). Gao et al. synthesized polypyrrole coated Cu/Cu_2O nanowire, which exhibited an increased capacity of 787 mAh/g (Wang et al., 2020b). Tang et al. prepared C@SnO_2/Cu_2O nanosheet clusters, which exhibited an initial discharge capacity of 1726 mAh/g at 0.5C (Wang et al., 2021b). The synergetic effect of more than three components is crucial to develop the electrochemical performance of copper-based oxides. However, the specific capacity and rate performance should be further improved to satisfy the demands of future applications.

In this work, CuO nanowires and CuO/Cu_2O/Cu nanocomposites were prepared by a facile water bath method that has not been used to prepare copper-based oxides anodes before. The initial discharge capability and charge capacity of CuO nanowires are 1,061.8 mAh/g and 922.1 mAh/g at 200 mA/g. While for the CuO/Cu_2O/Cu nanocomposites, they are 2,660.4 mAh/g and 2,107.8 mAh/g with a high initial Coulombic efficiency of 79.23%. The Coulombic efficiency increases to 98% in the second cycle and is maintained near 100% in the following cycles. The reversible capacity of 1,265.7 mAh/g was obtained after 200 cycles. Moreover, the reversible capacity is 1,180 mAh/g at 800 mA/g and increases to 1,750 mA/g when back to 100 mA/g, which indicates the excellent rate performance. As far as we know, the CuO/Cu_2O/Cu nanocomposites exhibit superior electrochemical performance to the reported results of copper-based oxides, which could be due to the synergetic effect and the facile water bath method. Our results indicate that the copper-based oxides anodes with a synergetic effect will satisfy the demands of the next-generation LIBs.

EXPERIMENTAL SECTION

Materials and Methods

The schematic illustration of preparing CuO nanowires and CuO/Cu_2O/Cu nanocomposites was shown in **Figure 1**. The mixed solution of 49 ml dimethylformamide (DMF) and 21 ml pure water was magnetically stirred for 2 min in a beaker, and then 2 mmol copper acetate monohydrate $Cu(CO_2CH_3)_2{\cdot}H_2O$ was added. After ultrasonic stirring for 30 min to thoroughly dissolve, 8 mmol hexadecyl trimethyl ammonium bromide (CTAB) was added successively. After another 30 min of ultrasonic stirring, 10 mmol NaOH was added. Then the above solution was put into a 60°C water bath and magnetically stirred for 8 min. When naturally cooled to room temperature, the solution was centrifuged by pure water and ethanol, in turn, many times. The obtained black precipitates were dried at 60°C for 12 h in a vacuum oven, and finally, the CuO nanowires were obtained. The preparing route of the CuO/Cu_2O/Cu nanocomposites was the same as the above process, except that 1 mmol of reductive agent $NaBH_4$ was added and stirred for 6 min before adding 10 mmol NaOH.

Structure and Morphology

The structure and morphology of the CuO nanowires and CuO/Cu_2O/Cu nanocomposites were characterized by X-ray diffraction (XRD, Smart Lab, Rigku Japan) and scanning electron microscope (SEM, GeminiSEM300, Zeiss, Germany). The XRD measurements were performed in the range of 20°–80° at a scan rate of 3°/min using a Cu Kα radiation.

Electrochemical Performance Characterization

The testing anodes were mixed with as-prepared active materials (CuO nanowires or CuO/Cu_2O/Cu nanocomposites, 70wt%), carbon black (20wt%), and carboxymethyl cellulose (CMC, 10wt%) dissolved in pure water. The black slurry was uniformly coated on a copper foil and dried at 60°C for 12 h in a vacuum oven. Finally, the obtained coated foil was punched into disks with a diameter of 12 mm. The half-cells (CR-2032) were assembled in a glove box. Lithium metal disk and the Celgard 2,250 film were used as the counter electrode and the

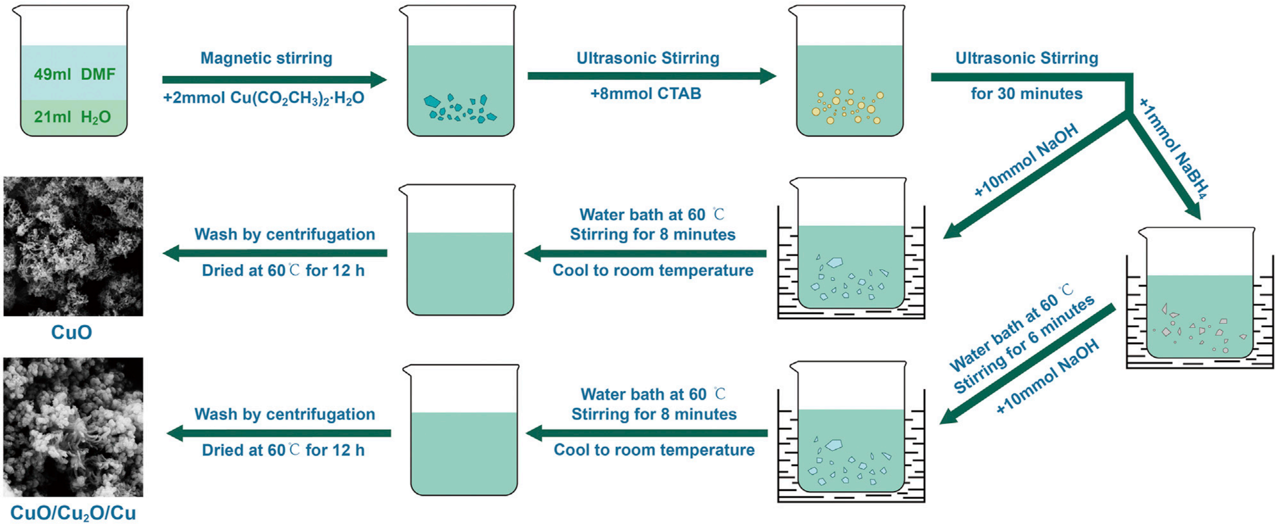

FIGURE 1 | The schematic illustration of preparing CuO nanowires and CuO/Cu_2O/Cu nanocomposites.

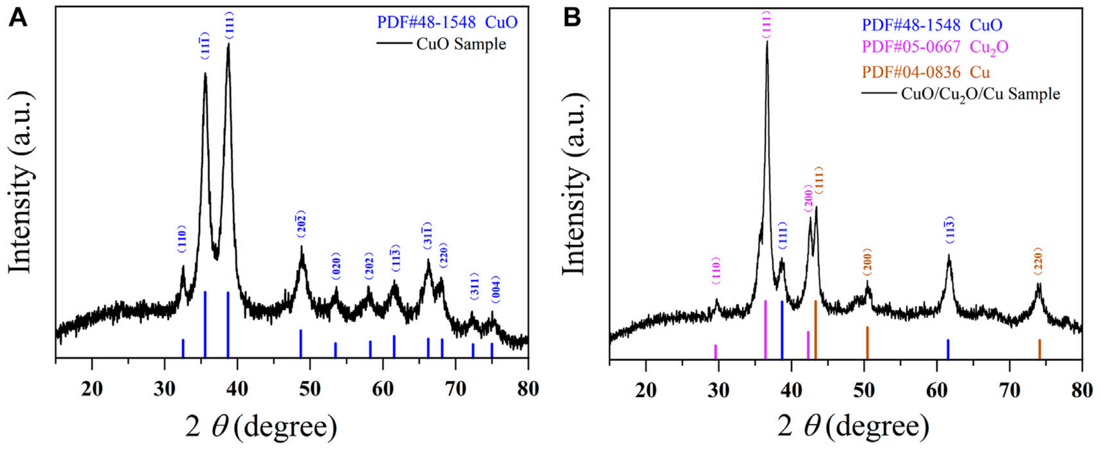

FIGURE 2 | The XRD patterns of CuO nanowires **(A)** and CuO/Cu_2O/Cu nanocomposites **(B)**.

diaphragm, respectively. The electrolyte was 1M LiPF6 dissolved in a mixture of ethyl carbonate (EC, 50 v/v%) and dimethyl ethyl carbonate (DEC, 50 v/v%). The electrochemical performance was measured by battery measuring systems (Land-ct2001A, China) and electrochemical workstation (CHI660E, China) with potential from 0.01 to 3.0 V at room temperature. To make sure the thorough penetration of the electrolyte, all cells were left to stand for 12 h before being measured.

RESULTS AND DISCUSSION

Structure and Morphology

As is shown in **Figure 2A**, the XRD patterns of CuO nanowires consist with the standard card of PDF No. 48–1548 (CuO) with no other diffraction peak, which indicates the purity of CuO nanowires. The characteristic peaks at 32.5°, 35.5°, 38.7°, 48.7°, 53.5°, 58.3°, 61.5°, 66.2°, 68.1°, 72.4°, and 75.0° stand for (110), (11$\bar{1}$), (111), (20$\bar{2}$), (020), (202), (11$\bar{3}$), (31$\bar{1}$), (220), (311), and (004) crystal plane of monolithic CuO phase respectively, which indicates the good crystallinity of CuO (Huang et al., 2011; Chen et al., 2015; Shi et al., 2016; Yuan et al., 2017; Wu et al., 2018; Xu et al., 2019; Murphin Kumar et al., 2020; Li et al., 2021c; Trukawka et al., 2021). From the XRD patterns of CuO/Cu_2O/Cu nanocomposites shown in **Figure 2B**, we can see that the as-prepared sample comprises CuO, Cu_2O, and Cu phases. The characteristic peaks at 38.7° and 61.5° signify (111) and (11$\bar{3}$) crystal plane of monolithic CuO phase (PDF No. 48–1548) (Huang et al., 2011; Chen et al., 2015; Shi et al., 2016; Yuan et al., 2017; Wu et al., 2018; Xu et al., 2019; Trukawka et al., 2021), and the peaks at 29.6°, 36.4°, and 42.3° index to (110), (111), and (200) crystal plane of cubic Cu_2O phase (PDF No. 05–0667) (Wu

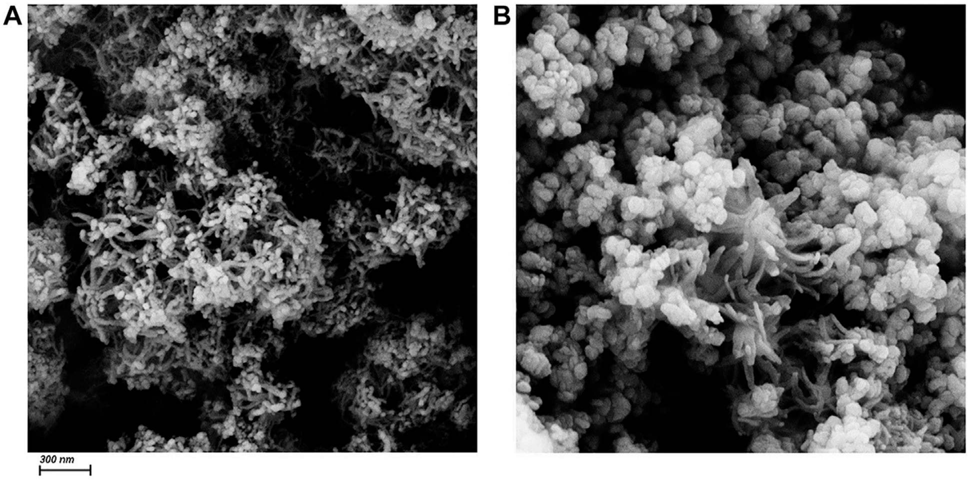

FIGURE 3 | The SEM images of CuO nanowires **(A)** and CuO/Cu_2O/Cu nanocomposites **(B)**. The scale bar is 300 nm.

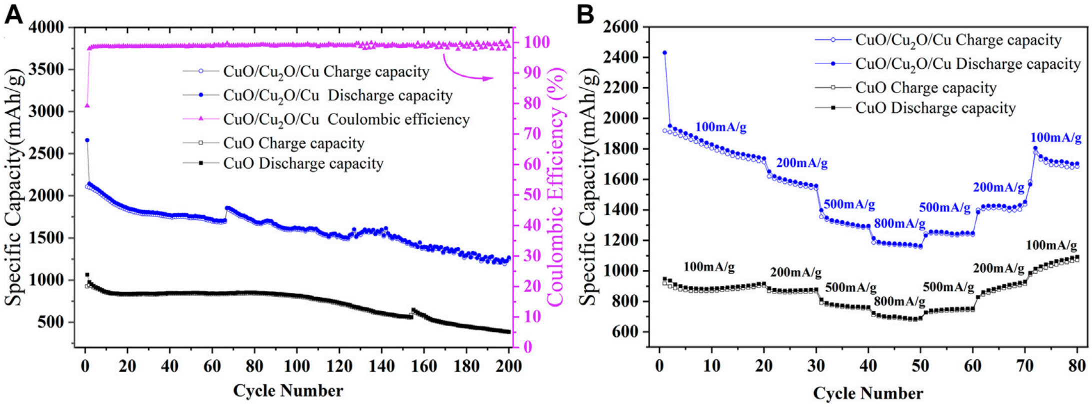

FIGURE 4 | The cycle stability **(A)** at a current density of 200 mA/g and rate capability **(B)** at different current densities of CuO nanowires and CuO/Cu_2O/Cu nanocomposites.

et al., 2018; Xu et al., 2019; Wang et al., 2020b; Gao et al., 2020; Murphin Kumar et al., 2020; Wang et al., 2021b; Li et al., 2021c), and the peaks of 43.3°, 50.4°, and 74.1° assign to (111), (200), and (220) crystal plane of cubic Cu phase (PDF No. 04–0836) (Wang et al., 2020b; Wang et al., 2021b; Li et al., 2021c). The appearance of Cu_2O and Cu phases was caused by the reductive reaction induced by the common mild reductive agent of $NaBH_4$. The weight ratios of CuO, Cu_2O, and Cu phases are 17.8, 60.5, and 21.7%, respectively, which was calculated by the intensity ratio of the 111) crystal plane peaks ($I_{\mathrm{CuO}} : I_{\mathrm{Cu_2O}} : I_{\mathrm{Cu}}$) (Yu et al., 2007; Hu et al., 2013; Zhou et al., 2014; Meng et al., 2015; Kim et al., 2016; Xu et al., 2019; Li et al., 2021c).

As is shown in **Figure 3**, the morphology of CuO nanowires and CuO/Cu_2O/Cu nanocomposites can be identified by the SEM images with a scale bar of 300 nm. From **Figure 3A**, we can see a lot of tangled nanowires with an average diameter of about 25 nm. But we can't obtain the length of these nanowires because of the tangled morphology. CuO/Cu_2O/Cu nanocomposites consist of a part of nanowires and much more nanoparticles with an average diameter of 95 nm, as is shown in **Figure 3B**. The appearance of the nanoparticles in the SEM image consists with the appearance of Cu_2O and Cu phases in the XRD pattern due to the reductive reaction. Therefore, it is reasonable to conclude that the nanowires are the CuO phase not reduced, and the nanoparticles should be the Cu_2O or Cu phases. The small number of nanowires in the SEM image is also consistent with the small amount of CuO (17.8%) estimated by the XRD patterns.

Electrochemical Performance

The cycle stability at 200 mA/g and the rate capability of CuO nanowires and CuO/Cu_2O/Cu nanocomposites are shown in **Figure 4**. From the cycle curves shown in **Figure 4A**, the initial discharge capacity and charge capacity of CuO nanowires are 1,061.8 mAh/g and 922.1 mAh/g, respectively. which is better than many previous reports of copper-based

TABLE 1 | The list of electrochemical results in this work and some reported results of copper-based oxides.

Materials	Initial discharge capacity (mAh/g)	Initial coulombic efficiency	Reversible capacity (mAh/g)	Current density (mA/g)	References
CuO/Cu_2O/Cu	2,660.4	79.23%	1,265.7 (200 cycles)	200	This work
CuO	1,061.8	86.84%	385 (200 cycles)	200	This work
CuO-Cu_2O	1,083	65.1%	487 (60 cycles)	200	Zhou et al. (2014)
CuO	803.7	70.4%	799.7 (100 cycles)	0.1C	Zhang et al. (2013)
Cu_2O	1,383.9	64%	884.4 (100 cycles)	100	Shen et al. (2013)
Cu_2O-Mn_3O_4	1,257	72.3%	792 (350 cycles)	1,500	Pan et al. (2020)
Cu_2O/HEG	2050 (0.05C)	50%	430 (25 cycles)	0.1C	Ananya et al. (2016)
Cu_2O	1,100	36.4%	666 (200 cycles)	200	Kim et al. (2019)
CuO/Cu_2O/Coal	1,200	65%	767 (200 cycles)	100	Zhang et al. (2021)
CuO	1,000	56.2%	677.1 (50 cycles)	0.1C	Wang et al. (2014a)
Cu@CuO	672.7	67.7%	354.1 (200 cycles)	100	Yuan et al. (2019)
CuO	1,196	56.2%	540 (100 cycles)	0.5C	Wang et al. (2014b)
CuO/graphene	817	68.7%	583.5 (50 cycles)	0.1C	Mai et al. (2011)
Cu_2O	1,097	65.8%	458 (50 cycles)	100	Xu et al. (2015)
CuO/C	1,150	50%	470 (50 cycles)	100	Huang et al. (2011)
Co_3O_4/CuO	1,229	75.8%	1,056 (500 cycles)	200	Shi et al. (2016)
Cu_2O/CuO/rGO	600	-	550 (100 cycles)	0.5C	Wu et al. (2018)
CuO/Cu_2O/C	887 (20 mA/g)	44%	260 (600 cycles)	200	Xu et al. (2019)
Cu_2O:Mo	1,128	-	1,082 (100 cycles)	100	Murphin Kumar et al. (2020)
Cu_2O/CuO/Cu	508.9	55.8%	479.9 (150 cycles)	50	Li et al. (2021c)
Cu/Cu_2O@Ppy	699.2	64.6%	787 (250 cycles)	100	Wang et al. (2020b)
C@SnO_2/Cu_2O	1726	46.3%	814 (300 cycles)	0.5C	Wang et al. (2021b)
CuO/Cu_2O	727	70.6%	740 (250 cycles)	100	Hu et al. (2013)
CuO	1,095 (100 mA/g)	59.5%	613.9 (100 cycles)	500	Li et al. (2018)
Cu_2O	555	48%	559 (50 cycles)	2000	Liu et al. (2021)

oxides (Shen et al., 2013; Zhang et al., 2013; Wang et al., 2014a; Wang et al., 2014b; Zhou et al., 2014; Ananya et al., 2016; Xu et al., 2016; Kim et al., 2019; Yuan et al., 2019; Pan et al., 2020; Zhang et al., 2021). However, the reversible capability decreases to 385 mAh/g after 200 cycles. While for the CuO/Cu_2O/Cu nanocomposites, the initial discharge capacity and charge capacity were 2,660.4 mAh/g and 2,107.8 mAh/g with an initial Coulombic efficiency of 79.23%. The Coulombic efficiency increased to 98% in the second cycle and was maintained near 100% in the following cycles. Furthermore, the reversible capacity of 1,265.7 mAh/g after 200 cycles was obtained, which is the highest of all reported results as far as we know (Huang et al., 2011; Mai et al., 2011; Shen et al., 2013; Zhang et al., 2013; Wang et al., 2014a; Wang et al., 2014b; Zhou et al., 2014; Chen et al., 2015; Xu et al., 2015; Ananya et al., 2016; Shi et al., 2016; Xu et al., 2016; Yuan et al., 2017; Wu et al., 2018; Kim et al., 2019; Xu et al., 2019; Yuan et al., 2019; Pan et al., 2020; Trukawka et al., 2021; Zhang et al., 2021). The jumps in the cycle curves at the 155th and 65th cycles for CuO nanowires and CuO/Cu_2O/Cu nanocomposites were caused by the interruption of electrical power.

To test the rate performance, the charge-discharge cycles of our samples at different current densities were carried out, as is shown in **Figure 4B**. The reversible capabilities of CuO nanowires are 885, 870, 772, and 704 mAh/g at 100, 200, 500, and 800 mA/g, and the capabilities increase to 747, 890, and 1,052 mAh/g when back to 500, 200, and 100 mA/g, which indicates the excellent rate performance because of the unique tangled nanowires structure and the water bath method. The reversible capabilities of CuO/Cu_2O/Cu nanocomposites are 1,840, 1,590, 1,319, and 1,180 mAh/g at 100, 200, 500, and 800 mA/g, and the capabilities increase to 1,252, 1,428, and 1750 mAh/g when back to 500, 200, and 100 mA/g, which is much better than that of CuO nanowires. The electrochemical results of CuO nanowires and CuO/Cu_2O/Cu nanocomposites in this work and some previously reported results of copper-based oxides were listed in **Table 1**. To our knowledge, the electrochemical performance of the CuO/Cu_2O/Cu nanocomposites was superior to all the reported results of copper-based oxides, which could be due to the synergetic effect and the water bath method. In our case, the Cu composite may provide the conductive network and the accommodation of the volume explanation during the cycles to improve the cycling stability, and the CuO and Cu_2O composites may provide more active sites to enhance the reversible capacity.

The first five cyclic voltammetry (CV) curves of CuO/Cu_2O/Cu nanocomposites at a scan rate of 0.1 mV/s were shown in **Figure 5A** to clarify the electrochemical reaction mechanism. In the first cycle, there are three reduction peaks at 2.14, 1.17, and 0.8 V, which correspond to the reductive process of CuO to a $Cu^{II}_{1-x}Cu^{I}_{x}O_{1-x/2}$ $(0 \leq x \leq 0.4)$ solid-solution mixed-phase (Huang et al., 2011; Yuan et al., 2019; Zhang et al., 2021), formation of Cu_2O phase (Zhang et al., 2013; Wu et al., 2018; Zhang et al., 2021), and the following transformation into Cu phase as well as the formation of solid electrolyte interface (SEI) (Shi et al., 2016; Yuan et al., 2017; Li et al., 2021c). The three reduction peaks increase to 2.34, 1.32, and 0.83 V and overlap in the following cycles (Xu et al., 2019), which indicates the excellent reversible cycle stability (Huang et al., 2011; Chen et al., 2015; Shi et al., 2016; Yuan et al., 2017; Trukawka et al., 2021). There are

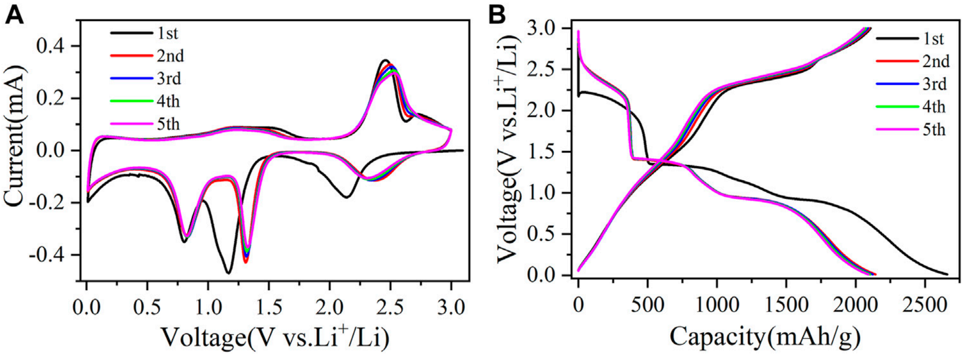

FIGURE 5 | The first five cyclic voltammetry curves **(A)** at a scan rate of 0.1 mV/s and the first five charge-discharge curves **(B)** at a current density of 200 mA/g for CuO/Cu_2O/Cu nanocomposites.

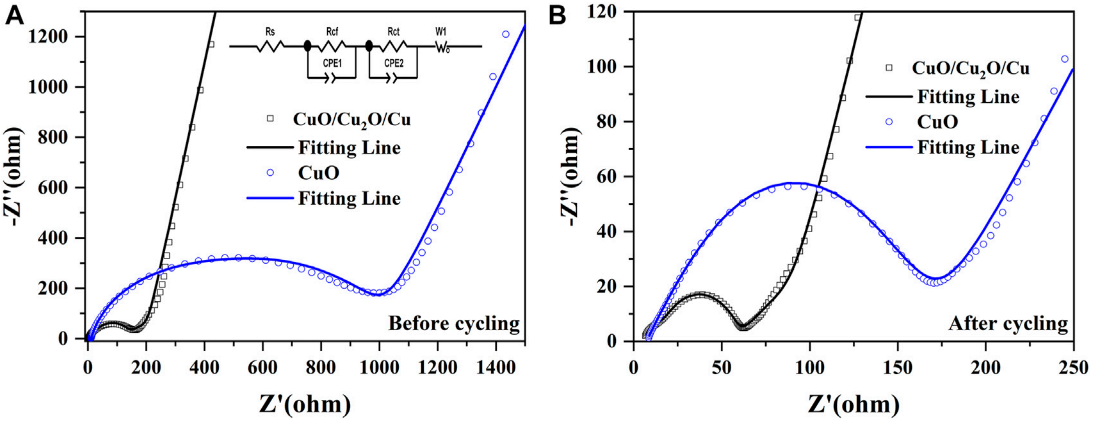

FIGURE 6 | The electrochemical impedance spectroscopy of CuO/Cu_2O/Cu nanocomposites and CuO nanowires before **(A)** and after **(B)** cycling between 10^{-2} Hz and 10^5 Hz. The inset of **(A)** is the equivalent circuit.

also three oxidation peaks located at 1.57, 2.46, and 2.72 V in the first cycle, which were induced by the decomposition of the SEI layer (Shen et al., 2013; Wang et al., 2020b), the oxidation of Cu to Cu_2O (Huang et al., 2011; Wang et al., 2014a; Yuan et al., 2019), and the further oxidation reaction to CuO (Huang et al., 2011; Yuan et al., 2019). In the second cycle, the oxidation peak at 1.57 V disappears due to the stability of the SEI layer. The peak at 2.72 V decreases to 2.70 V in the second cycle and then vanishes in the following cycles because of the polarization during electrode reaction (Wang et al., 2020b; Zhang et al., 2021). The position of oxidation peak at 2.46 V increases a little in the following four cycles due to the tiny structure change of copper-based oxides (Wang et al., 2014a; Xu et al., 2019).

The first five charge-discharge curves of CuO/Cu_2O/Cu nanocomposites at 200 mA/g were also shown in **Figure 5B** to verify the results of CV curves. There are three discharge plateaus around 2.20–1.85, 1.35–1.10 V, and 0.95–0.75 V in the first discharge process, which consist with the reduction peaks in the initial CV cathodic sweep. In the first charge curve, the three charge platforms around 1.10–1.75, 2.20–2.52, and 2.60–2.84 V correspond to the oxidation peaks in the initial CV anodic sweep. The plateaus in the following discharge-charge cycles are consistent with the redox reactions peaks in the CV curves. Furthermore, the discharge-charge curves also almost overlap, indicating the reversible electrochemical reactions and the high reversible cycle capability (Yuan et al., 2017; Yuan et al., 2019; Murphin Kumar et al., 2020).

As is shown in **Figure 6**, The electrochemical impedance spectroscopy (EIS) of CuO/Cu_2O/Cu nanocomposites and CuO nanowires were measured between 10^{-2} Hz and 10^5 Hz before and after cycling to further understand the reaction kinetics and the enhanced electrochemical performance (Yuan et al., 2017; Yuan et al., 2019; Wang et al., 2021b). Two semicircles and a straight line were found in the Nyquist plots (scatters) (Murphin Kumar et al., 2020; Wang et al., 2020b; Li et al., 2021c; Wang et al., 2021b), which are well fitted by the equivalent circuit (fitting lines). The equivalent circuit is shown in **Figure 6A** inset, and the parameters of R_s represents the ohmic resistance, R_{cf} signifies the impedance of the SEI layer, R_{ct} denotes the charge transfer resistance, W_1 designates the Warburg impedance (Wang t al., 2020b; Murphin Kumar et al., 2020; Wang et al., 2021b; Li et al., 2021c). Moreover, the Li-ions diffusion coefficient

TABLE 2 | The fitted resistance parameters of electrochemical impedance spectroscopy and the Li-ions diffusion coefficients before and after cycling.

Materials	R_s (Ω)	R_{cf} (Ω)	R_{ct} (Ω)	R_{total} (Ω)	D_{Li^+} (cm^2/s)
CuO/Cu_2O/Cu Before cycling	2.41	16.75	101	120.16	1.20×10^{-15}
CuO/Cu_2O/Cu After cycling	6.03	9.21	41.78	57.02	4.34×10^{-12}
CuO nanowires Before cycling	10.49	389.3	94.87	494.66	4.82×10^{-15}
CuO nanowires Before cycling	7.27	111.7	52.56	171.53	2.17×10^{-13}

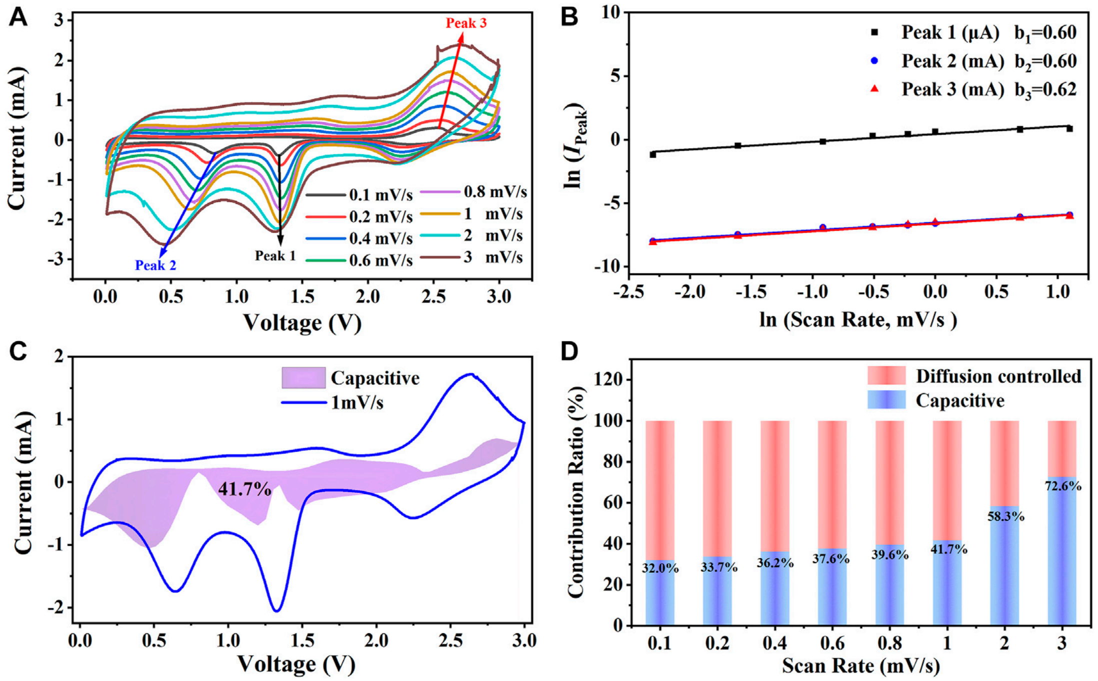

FIGURE 7 | (A) The cyclic voltammetry curves of CuO/Cu_2O/Cu nanocomposites with different scan rates. **(B)** The linear fitting results of log (I_{Peak}) vs. log(ν). **(C)** Capacitive contribution at 1 mV/s. **(D)** Capacitive contributions to the lithium-ion storage at different scan rates.

(D_{Li^+}) can be calculated by the equations below according to the EIS data in the low-frequency region (Shen et al., 2013; Zhou et al., 2014; Wang et al., 2020a; Gao et al., 2020).

$$D_{Li^+} = \frac{R^2T^2}{2A^2n^4F^4C^2\sigma^2} \qquad (1)$$

$$Z_{real} = R_{total} + \sigma\omega^{-1/2} \qquad (2)$$

The physical quantities of R, T, A, n, F, C, and σ denote the gas constant, the measuring temperature, the surface area of the electrode, the number of transferred electrons, the Faraday constant, the concentration of lithium ions, and the Warburg coefficient, respectively (Shen et al., 2013; Zhou et al., 2014; Wang et al., 2020a). The value of σ could be fitted by **Eq. 2**, in which the parameter of ω is the angular frequency (Gao et al., 2020). The fitted resistance parameters of EIS and the Li-ions diffusion coefficients before and after cycling are listed in **Table 2**.

The R_{cf}, R_{ct}, and the total resistance of R_{total} for both CuO/Cu_2O/Cu nanocomposites and CuO nanowires are much smaller after cycling, which indicates the increased electric conductivity due to the structure change and the formation of Cu component during the cycling process (Li et al., 2018; Hong et al., 2020; Wang et al., 2020b; Liu et al., 2021). The relatively high R_{total} (117.53 Ω) and the low Li-ions diffusion coefficient (2.17×10^{-13} cm^2/s)of the CuO nanowires after cycling imply the low reversible capability of 385 mAh/g after 200 cycles shown in **Figure 4**. However, the CuO/Cu_2O/Cu nanocomposites after cycling exhibit the lowest R_{cf} (9.21 Ω), R_{ct} (41.78 Ω), and R_{total} (57.02 Ω), as well as the highest Li-ions diffusion coefficient (4.34×10^{-12} cm^2/s), indicating the higher electrochemical kinetics compared to the CuO nanowires, which are consistent with the outstanding electrochemical performance shown in **Figures 4**, **5** (Li et al., 2018; Hong et al., 2020; Liu et al., 2021). The outstanding electrochemical performance of the CuO/Cu_2O/Cu nanocomposites could result from the unique nanocomposites structure and the synergetic effect of the components (Hu et al., 2013; Kim et al., 2016; Wang et al., 2020b; Murphin Kumar et al., 2020; Wang et al., 2021b; Li et al., 2021c).

On account of the outstanding electrochemical performance of the CuO/Cu_2O/Cu nanocomposites, as is shown in **Figure 7A**, the CV curves with scan rates in the range of 0.1 mV/s—3 mV/s were further measured to clarify the energy storage mechanism. The shapes of the CV curves are much similar, and the redox peaks are obvious even at 3 mV/s, indicating the outstanding lithium-ion intercalation dynamics (Wang et al., 2020b). The positions and the values of the three redox peaks marked by the arrows in **Figure 7A** change regularly with the scan rates due to different reaction processes according to scan rates (Wang et al., 2020b; Liu et al., 2021; Zhang et al., 2021). The peak current (I_{Peak}) can be expressed by the equations with scan rates (ν).

$$I_{\text{Peak}} = a\,\nu^{b} \tag{3}$$

$$\ln(I_{\text{Peak}}) = b\ln(\nu) + \ln a \tag{4}$$

The lithium-ion storage mechanism can be identified by the value of b, which is between 0.5 and 1 depending on the contribution ratios of diffusion-controlled (b = 0.5) and capacitance controlled (b = 1) (Li et al., 2018; Hong et al., 2020; Liu et al., 2021). According to **Figure 7B**, the values of b for the two reduction peaks and the oxidation peak are 0.6 and 0.62, respectively, indicating the diffusion-controlled mechanism is dominant (Li et al., 2018; Hong et al., 2020; Liu et al., 2021). The quantitative contribution ratios can be calculated by the equations below.

$$I = k_1\nu + k_2\nu^{0.5} \tag{5}$$

$$I/\nu^{0.5} = k_1\nu^{0.5} + k_2 \tag{6}$$

The parameters of $k_1\nu$ and $k_2\nu^{0.5}$ represent the contribution of capacitance controlled and diffusion-controlled, respectively. k_1 can be obtained by linear fitting of $I/\nu^{0.5}$ vs. $\nu^{0.5}$ in **Eq. 6** at a certain voltage with different currents and scan rates. As is shown in **Figure 7C**, after obtaining enough numbers of k_1, the capacitance contribution ratio was calculated by the area ratio of the shadow and the CV curves, and the ratio is 41.7% at 1 mV/s. As is shown in **Figure 7D**, at the low scan rates, the diffusion-controlled mechanism is dominant, while at the high scan rates, the capacitive controlled mechanism is predominance. The capacitance contribution ratio to the lithium-ion storage is up to 72.6% at the scan rate of 3 mV/s, which is consistent with the excellent rate capability shown in **Figure 4B**.

CONCLUSION

In this work, CuO/Cu_2O/Cu nanocomposites and CuO nanowires were prepared by a facile water bath method. The CuO nanowires exhibit a high initial discharge capacity and charge capacity of 1,061.8 mAh/g and 922.1 mAh/g at 200 mA/g, but a low reversible capability of 385 mAh/g after 200 cycles. While for the CuO/Cu_2O/Cu nanocomposites, the initial capacities are 2,660.4 mAh/g and 2,107.8 mAh/g, respectively, and the reversible capacity is 1,265.7 mAh/g. The rate performance of the CuO/Cu_2O/Cu nanocomposites was also excellent with a reversible capacity of 1,180 mAh/g at 800 mA/g and 1750 mA/g when back to 100 mA/g. The outstanding electrochemical performance of the CuO/Cu_2O/Cu nanocomposites could result from the synergetic effect of multivalent states metal and the facile water bath method. Copper-based oxides nanomaterials with the synergetic effect could be used as anodes for lithium-ion batteries.

DATA AVAILABILITY STATEMENT

The original contributions presented in the study are included in the article/Supplementary Material, further inquiries can be directed to the corresponding author.

AUTHOR CONTRIBUTIONS

All authors listed have made a substantial, direct, and intellectual contribution to the work and approved it for publication.

FUNDING

This work was supported by a Project of Shandong Province Higher Educational Science and Technology Program No. J17KA184, and the Youth Science and technology innovation fund of Shandong Agricultural University number 140/24047.

REFERENCES

Ananya, G., Pranati, N., and Ramaprabhu, S. (2016). Investigation of the Role of Cu_2O Beads over the Wrinkled Graphene as an Anode Material for Lithium Ion Battery. *Int. J. Hydrogen Energ.* 41, 3974–3980. doi:10.1016/j.ijhydene.2016.01.015

Chen, X., Huang, Y., Zhang, X., Li, C., Chen, J., and Wang, K. (2015). Graphene Supported ZnO/CuO Flowers Composites as Anode Materials for Lithium Ion Batteries. *Mater. Lett.* 152, 181–184. doi:10.1016/j.matlet.2015.03.136

Gao, L., Wang, Z., Hu, H., Cheng, H., Zhang, L., and Yang, X. (2020). Nitrogen-doped Carbon Microfiber Networks Decorated with CuO/Cu Clusters as Self-Supported Anode Materials for Potassium Ion Batteries. *J. Electroanalytical Chem.* 876, 114483. doi:10.1016/j.jelechem.2020.114483

Hong, J. H., Park, G. D., Jung, D. S., and Kang, Y. C. (2020). Lithium Ion Storage Mechanism Exploration of Copper Selenite as Anode Materials for Lithium-Ion Batteries. *J. Alloys Comp.* 827, 154309. doi:10.1016/j.jallcom.2020.154309

Hu, H., Li, Q., Li, L., Teng, X., Feng, Z., Zhang, Y., et al. (2020). Laser Irradiation of Electrode Materials for Energy Storage and Conversion. *Matter* 3, 95–126. doi:10.1016/j.matt.2020.05.001

Hu, L., Huang, Y., Zhang, F., and Chen, Q. (2013). CuO/Cu_2O Composite Hollow Polyhedrons Fabricated from Metal-Organic Framework Templates for Lithium-Ion Battery Anodes with a Long Cycling Life. *Nanoscale* 5, 4186–4190. doi:10.1039/c3nr00623a

Huang, X. H., Wang, C. B., Zhang, S. Y., and Zhou, F. (2011). CuO/C Microspheres as Anode Materials for Lithium Ion Batteries. *Electrochimica Acta* 56, 6752–6756. doi:10.1016/j.electacta.2011.05.072

Kim, A.-Y., Kim, M. K., Cho, K., Woo, J.-Y., Lee, Y., Han, S.-H., et al. (2016). One-Step Catalytic Synthesis of CuO/Cu_2O in a Graphitized Porous C Matrix Derived from the Cu-Based Metal-Organic Framework for Li- and Na-Ion Batteries. *ACS Appl. Mater. Inter.* 8, 19514–19523. doi:10.1021/acsami.6b05973

Kim, E.-S., Kim, M.-C., Moon, S.-H., Shin, Y.-K., Lee, J.-E., Choi, S., et al. (2019). Surface Modified and Size-Controlled Octahedral Cu_2O Nanostructured Electrodes for Lithium-Ion Batteries. *J. Alloys Comp.* 794, 84–93. doi:10.1016/j.jallcom.2019.04.225

Li, H., Hu, Z., Xia, Q., Zhang, H., Li, Z., Wang, H., et al. (2021a). Operando Magnetometry Probing the Charge Storage Mechanism of CoO Lithium-Ion Batteries. *Adv. Mater.* 33, 2006629. doi:10.1002/adma.202006629

Li, Q., Li, H., Xia, Q., Hu, Z., Zhu, Y., Yan, S., et al. (2021b). Extra Storage Capacity in Transition Metal Oxide Lithium-Ion Batteries Revealed by *In*

Situ Magnetometry. *Nat. Mater.* 20, 76–83. doi:10.1038/s41563-020-0756-y

Li, Z., Li, G., Xu, W., Zhou, M., Xu, C., Shi, M., et al. (2018). Self-Integrated Porous Leaf-like CuO Nanoplate Array-Based Anodes for High-Performance Lithium-Ion Batteries. *ChemElectroChem* 5, 2774–2780. doi:10.1002/celc.201800858

Li, Z., Xie, G., Wang, C., Liu, Z., Chen, J., and Zhong, S. (2021c). Binder Free Cu_2O/CuO/Cu/Carbon-Polymer Composite Fibers Derived from Metal/organic Hybrid Materials through Electrodeposition Method as High Performance Anode Materials for Lithium-Ion Batteries. *J. Alloys Comp.* 864, 158585. doi:10.1016/j.jallcom.2020.158585

Li, Z., Zhang, Y., Li, X., Gu, F., Zhang, L., Liu, H., et al. (2021d). Reacquainting the Electrochemical Conversion Mechanism of FeS_2 Sodium-Ion Batteries by Operando Magnetometry. *J. Am. Chem. Soc.* 143, 12800–12808. doi:10.1021/jacs.1c06115

Liang, H., Zhang, H., Zhao, L., Chen, Z., Huang, C., Zhang, C., et al. (2022). Layered $Fe_2(MoO_4)_3$ Assemblies with Pseudocapacitive Properties as Advanced Materials for High-Performance Sodium-Ion Capacitors. *Chem. Eng. J.* 427, 131481. doi:10.1016/j.cej.2021.131481

Liu, W., Xiang, P., Dong, X., Yin, H., Yu, H., Cheng, P., et al. (2021). Two Advantages by a Single Move: Core-Bishell Electrode Design for Ultrahigh-Rate Capacity and Ultralong-Life Cyclability of Lithium Ion Batteries. *Composites B: Eng.* 216, 108883. doi:10.1016/j.compositesb.2021.108883

Mai, Y. J., Wang, X. L., Xiang, J. Y., Qiao, Y. Q., Zhang, D., Gu, C. D., et al. (2011). CuO/graphene Composite as Anode Materials for Lithium-Ion Batteries. *Electrochimica Acta* 56, 2306–2311. doi:10.1016/j.electacta.2010.11.036

Meng, H., Yang, W., Ding, K., Feng, L., and Guan, Y. (2015). Cu_2O Nanorods Modified by Reduced Graphene Oxide for NH_3 Sensing at Room Temperature. *J. Mater. Chem. A.* 3, 1174–1181. doi:10.1039/c4ta06024e

Murphin Kumar, P. S., Al-Muhtaseb, A. a. H., Kumar, G., Vinu, A., Cha, W., Villanueva Cab, J., et al. (2020). Piper Longum Extract-Mediated Green Synthesis of Porous Cu_2O:Mo Microspheres and Their Superior Performance as Active Anode Material in Lithium-Ion Batteries. *ACS Sust. Chem. Eng.* 8, 14557–14567. doi:10.1021/acssuschemeng.0c05067

Pan, Y., Xu, M., Yang, L., Yu, M., Liu, H., and Zeng, F. (2020). Porous Architectures Assembled with Ultrathin Cu_2O-Mn_3O_4 Hetero-Nanosheets Vertically Anchoring on Graphene for High-Rate Lithium-Ion Batteries. *J. Alloys Comp.* 819, 152969. doi:10.1016/j.jallcom.2019.152969

Shen, X., Chen, S., Mu, D., Wu, B., and Wu, F. (2013). Novel Synthesis and Electrochemical Performance of Nano-Structured Composite with Cu_2O Embedment in Porous Carbon as Anode Material for Lithium Ion Batteries. *J. Power Sourc.* 238, 173–179. doi:10.1016/j.jpowsour.2013.03.085

Shi, L., Fan, C., Fu, X., Yu, S., Qian, G., and Wang, Z. (2016). Carbonate-assisted Hydrothermal Synthesis of Porous Hierarchical Co_3O_4/CuO Composites as High Capacity Anodes for Lithium-Ion Batteries. *Electrochimica Acta* 197, 23–31. doi:10.1016/j.electacta.2016.03.001

Teng, X., Zhang, F., Li, Q., Wang, X., Ye, W., Li, H., et al. (2020). Interfacial Engineering of Self-Supported SnO_2 Nanorod Arrays as Anode for Flexible Lithium-Ion Batteries. *J. Electrochem. Soc.* 167, 120515–120524. doi:10.1149/1945-7111/abac86

Trukawka, M., Wenelska, K., Singer, L., Klingeler, R., Chen, X., and Mijowska, E. (2021). Hollow Carbon Spheres Loaded with Uniform Dispersion of Copper Oxide Nanoparticles for Anode in Lithium- Ion Batteries. *J. Alloys Comp.* 853, 156700. doi:10.1016/j.jallcom.2020.156700

Wang, C., Li, Q., Wang, F., Xia, G., Liu, R., Li, D., et al. (2014a). Morphology-dependent Performance of CuO Anodes via Facile and Controllable Synthesis for Lithium-Ion Batteries. *ACS Appl. Mater. Inter.* 6, 1243–1250. doi:10.1021/am405061c

Wang, L.-H., Dai, Y.-K., Qin, Y.-F., Chen, J., Zhou, E.-L., Li, Q., et al. (2020a). One-Pot Synthesis and High Electrochemical Performance of CuS/Cu1.8S Nanocomposites as Anodes for Lithium-Ion Batteries. *Materials* 13, 3797. doi:10.3390/ma13173797

Wang, L.-H., Teng, X.-L., Qin, Y.-F., and Li, Q. (2021a). High Electrochemical Performance and Structural Stability of CoO nanosheets/CoO Film as Self-Supported Anodes for Lithium-Ion Batteries. *Ceramics Int.* 47, 5739–5746. doi:10.1016/j.ceramint.2020.10.160

Wang, L., Tang, K., Zhang, M., Zhang, X., and Xu, J. (2014b). Facile Synthesis of CuO Nanoparticles as Anode for Lithium Ion Batteries with Enhanced Performance. *Funct. Mater. Lett.* 07, 1440008. doi:10.1142/s1793604714400086

Wang, M., Zhang, X., He, X., Zhu, B., Tang, H., and Wang, C. (2021b). *In-situ* Grown Flower-like C@SnO_2/Cu_2O Nanosheet Clusters on Cu Foam as High Performance Anode for Lithium-Ion Batteries. *J. Alloys Comp.* 856, 158202. doi:10.1016/j.jallcom.2020.158202

Wang, Y., Cao, L., Li, J., Kou, L., Huang, J., Feng, Y., et al. (2020b). Cu/Cu_2O@Ppy Nanowires as a Long-Life and High-Capacity Anode for Lithium Ion Battery. *Chem. Eng. J.* 391, 123597. doi:10.1016/j.cej.2019.123597

Wu, C.-P., Xie, K.-X., He, J.-P., Wang, Q.-P., Ma, J.-M., Yang, S., et al. (2021). SnO_2 Quantum Dots Modified N-Doped Carbon as High-Performance Anode for Lithium Ion Batteries by Enhanced Pseudocapacitance. *Rare Met.* 40, 48–56. doi:10.1007/s12598-020-01623-x

Wu, S., Fu, G., Lv, W., Wei, J., Chen, W., Yi, H., et al. (2018). A Single-step Hydrothermal Route to 3D Hierarchical Cu_2O/CuO/rGO Nanosheets as High-Performance Anode of Lithium-Ion Batteries. *Small* 14, 1702667. doi:10.1002/smll.201702667

Xu, C., Manukyan, K. V., Adams, R. A., Pol, V. G., Chen, P., and Varma, A. (2019). One-step Solution Combustion Synthesis of CuO/Cu_2O/C Anode for Long Cycle Life Li-Ion Batteries. *Carbon* 142, 51–59. doi:10.1016/j.carbon.2018.10.016

Xu, S., Lu, L., Zhang, Q., Jiang, Q., Luo, Z., Wang, S., et al. (2016). A Facile Synthesis of Flower-like CuO as Anode Materials for Lithium (Sodium) Ion Battery Applications. *j nanosci nanotechnol* 16, 7655–7661. doi:10.1166/jnn.2016.11593

Xu, Y.-T., Guo, Y., Li, C., Zhou, X.-Y., Tucker, M. C., Fu, X.-Z., et al. (2015). Graphene Oxide Nano-Sheets Wrapped Cu_2O Microspheres as Improved Performance Anode Materials for Lithium Ion Batteries. *Nano Energy* 11, 38–47. doi:10.1016/j.nanoen.2014.10.011

Yu, H., Yu, J., Liu, S., and Mann, S. (2007). Template-free Hydrothermal Synthesis of CuO/Cu_2O Composite Hollow Microspheres. *Chem. Mater.* 19, 4327–4334. doi:10.1021/cm070386d

Yuan, W., Luo, J., Pan, B., Qiu, Z., Huang, S., and Tang, Y. (2017). Hierarchical Shell/core CuO Nanowire/carbon Fiber Composites as Binder-free Anodes for Lithium-Ion Batteries. *Electrochimica Acta* 241, 261–271. doi:10.1016/j.electacta.2017.04.159

Yuan, W., Qiu, Z., Huang, Y., Wang, C., Huang, H., Yang, Y., et al. (2019). Honeycomb-Inspired Surface-Patterned Cu@CuO Composite Current Collector for Lithium-Ion Batteries. *Energy Technol.* 7, 1900445. doi:10.1002/ente.201900445

Zhang, F., Teng, X., Shi, W., Song, Y., Zhang, J., Wang, X., et al. (2020). SnO_2 Nanoflower Arrays on an Amorphous Buffer Layer as Binder-free Electrodes for Flexible Lithium-Ion Batteries. *Appl. Surf. Sci.* 527, 146910–146920. doi:10.1016/j.apsusc.2020.146910

Zhang, W., Wang, H., Zhang, Y., Yang, Z., Wang, Q., Xia, J., et al. (2013). Facile Microemulsion Synthesis of Porous CuO Nanosphere Film and its Application in Lithium Ion Batteries. *Electrochimica Acta* 113, 63–68. doi:10.1016/j.electacta.2013.09.043

Zhang, Y., Liu, W., Zhu, Y., Zhang, Y., Zhang, R., Li, K., et al. (2021). Facile Self-Assembly Solvothermal Preparation of CuO/Cu_2O/Coal-Based Reduced Graphene Oxide Nanosheet Composites as an Anode for High-Performance Lithium-Ion Batteries. *Energy Fuels* 35, 8961–8969. doi:10.1021/acs.energyfuels.1c00473

Zhou, X., Shi, J., Liu, Y., Su, Q., Zhang, J., and Du, G. (2014). Microwave-assisted Synthesis of Hollow CuO-Cu_2O Nanosphere/graphene Composite as Anode for Lithium-Ion Battery. *J. Alloys Comp.* 615, 390–394. doi:10.1016/j.jallcom.2014.07.013

Zuo, J.-H., and Gong, Y.-J. (2020). Applications of Transition-Metal Sulfides in the Cathodes of Lithium-Sulfur Batteries. *Tungsten* 2, 134–146. doi:10.1007/s42864-020-00046-6

Conflict of Interest: The authors declare that the research was conducted in the absence of any commercial or financial relationships that could be construed as a potential conflict of interest.

frontiers in Chemistry

ORIGINAL RESEARCH
published: 05 January 2022
doi: 10.3389/fchem.2021.818255

One-Pot Synthesized Amorphous Cobalt Sulfide With Enhanced Electrochemical Performance as Anodes for Lithium-Ion Batteries

Long-Long Ren[1†], *Lin-Hui Wang*[2†], *Yu-Feng Qin*[2*] *and Qiang Li*[3]

[1]College of Mechanical and Electronic Engineering, Shandong Agricultural University, Taian, China, [2]College of Information Science and Engineering, Shandong Agricultural University, Taian, China, [3]College of Physics, University-Industry Joint Center for Ocean Observation and Broadband Communication, Qingdao University, Qingdao, China

In order to solve the poor cycle stability and the pulverization of cobalt sulfides electrodes, a series of amorphous and crystalline cobalt sulfides were prepared by one-pot solvothermal synthesis through controlling the reaction temperatures. Compared to the crystalline cobalt sulfide electrodes, the amorphous cobalt sulfide electrodes exhibited superior electrochemical performance. The high initial discharge and charge capacities of 2,132 mAh/g and 1,443 mAh/g at 200 mA/g were obtained. The reversible capacity was 1,245 mAh/g after 200 cycles, which is much higher than the theoretical capacity. The specific capability was 815 mAh/g at 800 mA/g and increased to 1,047 mAh/g when back to 100 mA/g, indicating the excellent rate capability. The outstanding electrochemical performance of the amorphous cobalt sulfide electrodes could result from the unique characteristics of more defects, isotropic nature, and the absence of grain boundaries for amorphous nanostructures, indicating the potential application of amorphous cobalt sulfide as anodes for lithium-ion batteries.

Keywords: amorphous, cobalt sulfide, one-pot synthesis, anodes, lithium-ion batteries, high electrochemical performance

Edited by:
Pan Xiong,
Nanjing University of Science and Technology, China

Reviewed by:
Lishuang Fan,
Harbin Institute of Technology, China
Bing Sun,
University of Technology Sydney, Australia
Liubing Dong,
Jinan University, China

Correspondence:
Yu-Feng Qin
qinyufeng@sdau.edu.cn

†These authors have contributed equally to this work

Specialty section:
This article was submitted to Electrochemistry, a section of the journal Frontiers in Chemistry

Received: *19 November 2021*
Accepted: *13 December 2021*
Published: *05 January 2022*

Citation:
Ren L-L, Wang L-H, Qin Y-F and Li Q (2022) One-Pot Synthesized Amorphous Cobalt Sulfide With Enhanced Electrochemical Performance as Anodes for Lithium-Ion Batteries. Front. Chem. 9:818255. doi: 10.3389/fchem.2021.818255

INTRODUCTION

Lithium-ion batteries (LIBs) have been wildly used in small consumer electronics, electric vehicles, and medical apparatus as energy storage devices due to their advantages of high energy density, long cycle life, high working voltage, no memory effect, small self-discharge, and wide operating temperature range (Sun et al., 2010; Wang et al., 2020c; Gu et al., 2021; Li et al., 2021a; Li et al., 2021b; Li et al., 2021c; Li et al., 2021d; Zhao et al., 2021; Liang et al., 2022). However, to apply in large-scale energy storage projects and other high-power systems, the electrochemical properties of power density, rate capacity, cycle stability, and safety issue should be further improved (Sun et al., 2011; Zhang et al., 2019b; Wang et al., 2020b; Zhang et al., 2020a; Wang et al., 2021b). Current commercial graphite anode materials exhibit the advantages of high energy density, high conductivity, and security. Still, their low theoretical capacity of 372mAh/g and poor rate capability have confined the further development of LIBs(Zhang et al., 2019a; Hou et al., 2020; Li et al., 2020b; Gao et al., 2021; Wang et al., 2021a). Therefore, it is urgent to develop high-performance anode materials to meet the high power energy needs in the future (Zhao et al., 2019; Zhao et al., 2020; Liu et al., 2021a). It has long been discovered that cobalt sulfides (CoS, CoS_2, Co_3S_4, Co_9S_8) have lithium storage ability and high reversible capacities (Yan et al., 2005; Shi et al., 2012; Gu et al., 2013). In order to achieve the practical application of cobalt sulfides as anode materials, the intrinsic drawbacks of low conductivity and significant volume expansion during cycles must be solved (Gu et al., 2013; Jiang et al., 2020). Many different crystalline nanostructures and morphologies have been designed and prepared to relieve the decomposition caused by the volume expansion. Carbon-based materials have also been introduced to increase the conductivity (Yan et al., 2005; Shi et al., 2012; Gu et al., 2013; Jiang et al., 2020). Yang *et al.* reported that the cubic phase of CoS_2 was prepared by calcination at high temperature and exhibited the initial discharge capacity of 1,280 mA h/g and the reversible capacity of 350 mA h/g after ten cycles at 50 mA/g (Yan et al., 2005). Yan *et al.* prepared carbon-coated Co_9S_8 nano-dandelions by a facile solvothermal method, and the high reversible capacity of 520 mA h/g at the current density of 1 A/g (1.8 C) after the 50th cycle was obtained (Shi et al., 2012). Wang *et al.* prepared standard hexagonal CoS nanocomposites wrapped by graphene by a solvothermal method. The CoS nanocomposites exhibited a high reversible capacity of 749 mA h/g after 40 cycles at 62.5 mA/g (Gu et al., 2013). Wei *et al.* prepared the polycrystalline Co_9S_8/C composites by an electrospinning method, and the electrodes exhibited an initial discharge capacity of 823 mA h/g and a reversible capacity of 1,063 mA h/g after 200 cycles at 300 mA/g (Jiang et al., 2020). Even though good electrochemical performance has been observed in these crystalline cobalt sulfides, the poor cycle stability and the pulverization of the materials caused by the volume expansion still exist. Therefore, it is necessary to find a new way to solve these problems. Amorphous nanostructures always have more defects, which will provide more active sites. Furthermore, the isotropic nature and the absence of grain boundaries for amorphous nanostructures could improve the capacity to sustain high strain and the insertion of lithium ions, which is helpful to inhibit the volume expansion (Liu et al., 2013; Lu et al., 2018; Wu et al., 2019; Duan et al., 2021; Wu et al., 2021). Zhao *et al.* reported that the amorphous $VO(PO_3)_2$ exhibited a high initial discharge capacity of 1,297 mA h/g and a reversible capacity of 676 mA h/g after 150 cycles at the current of 100 mA/g, which is much higher than those of crystalline $VO(PO_3)_2$ due to the isotropic ions diffusion paths (Wu et al., 2021). Wu *et al.* reported that amorphous V_2O_3/C composite exhibited higher reversible capacity and superior cycling stability than crystalline V_2O_3/C composite, which accounted for the oxygen vacancies and amorphous phase (Wu et al., 2019). Yang *et al.* reported that compared to the crystalline Sn@C anodes, better rate capability, longer cycle life, and higher capacity had been observed for amorphous Sn@C anodes because of the defect sites and the improved strain regulation (Duan et al., 2021). However, as far as we know, the amorphous anode materials have not been systematically investigated, and the amorphous cobalt sulfides anode materials for LIBs have not been reported.

In this work, a series of amorphous and crystalline cobalt sulfide nanomaterials were prepared by a facile solvothermal method at different reaction temperatures. Due to the unique characteristics of more defects, isotropic nature, and the absence of grain boundaries for amorphous nanostructures, the amorphous cobalt sulfide exhibited superior electrochemical performance compared to the crystalline cobalt sulfide. The initial discharge and charge capacities of the amorphous samples are 2,132 mAh/g and 1,443 mAh/g, respectively, at 200 mA/g. The Coulombic efficiency sharply increased to 97.44% in the second cycle and maintained near 100% to the 200th cycle. The high reversible capacity of 1,245 mAh/g after 200 cycles was observed. The specific capability was 815 mAh/g at 800 mA/g and increased to 1,047mAh/g when back to 100 mA/g, indicating the excellent rate capability. The amorphous cobalt sulfide nanomaterials with outstanding electrochemical performance have the potential application as anodes for LIBs.

EXPERIMENTAL SECTION

Materials and Batteries

The schematic illustration of preparing CoS (amorphous and crystalline) materials and the assembling of the half cells (CR-2032) is shown in **Figure 1**. The cobalt sulfide nanomaterials were prepared as follows. 713.79 mg (3 mmol) of $CoCl_2 \cdot 6H_2O$ were added into 70 ml of ethylene glycol and magnetically stirred for 2~3 h. 89.7 mg (4 mmol) of L-cysteine were added consequently and magnetically stirred for another 2~3 h to dissolve completely. The mixed solution was divided into two Teflon-lined autoclaves (50 ml) and put in an air blast drying cabinet for 24 h at different reaction temperatures of 140°C, 160°C, 180°C, and 200°C, respectively. After the precipitates were alternately washed with deionized water and absolute alcohol several times, the precipitates were dried in a vacuum drying oven at 60°C for 12 h. Finally, the amorphous and crystalline cobalt sulfide nanomaterials were obtained. According to the reaction temperatures, the as-prepared cobalt sulfide nanomaterials were denoted by CoS-140, CoS-160, CoS-180, and CoS-200, respectively.

The cobalt sulfide nanomaterials, carbon black, and binder were mixed at a weight of 7: 2: 1 and roundly ground. The binder is carboxymethyl cellulose (CMC) dissolved in deionized water with a weight ratio of 10%. The black slurry was smeared evenly on the copper foil and then dried in a vacuum drying oven at 60°C for 12 h. The copper foil was punched into many disks with an area of 113 mm^2. The average loading mass of the active materials is 0.82 mg/cm^2. Finally, the half cells were assembled with the copper disks and the lithium metal foil in an argon-filled glove box. The diaphragm and electrolyte are the Celgard 2,250 film and 1M LiPF6 dissolved in a mixed solution of ethyl carbonate and dimethyl ethyl carbonate with a volume ratio of 1:1.

Structure and Morphology

The structure was characterized by X-ray diffraction (XRD, Smart Lab, Rigku Japan) in the range of 20°–80° using a Cu Kα radiation. The morphology was further identified by a scanning electron microscope (SEM, GeminiSEM300, Zeiss, Germany).

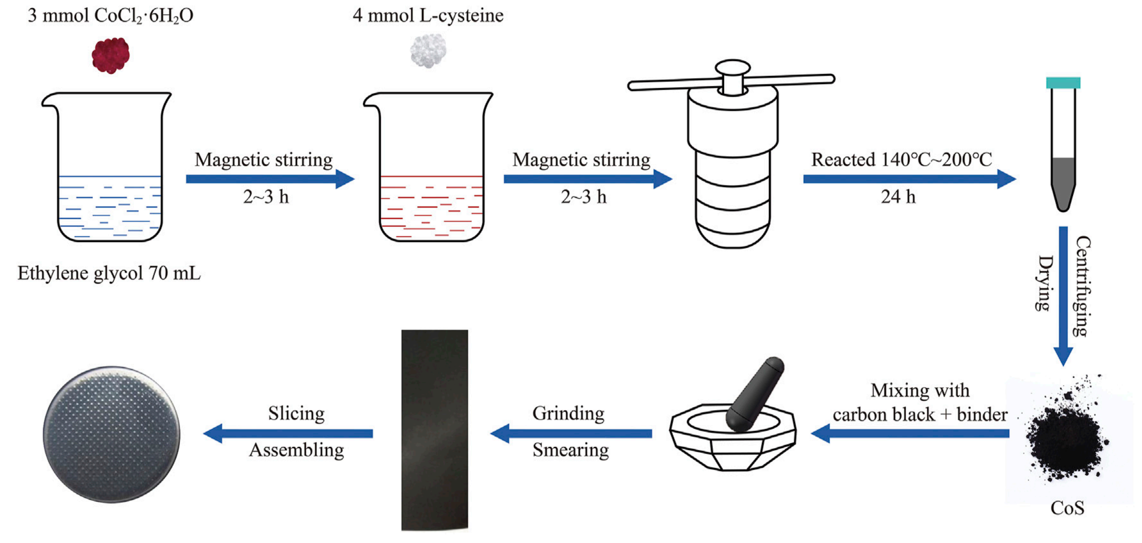

FIGURE 1 | The schematic illustration of preparing the CoS materials and assembling half cells.

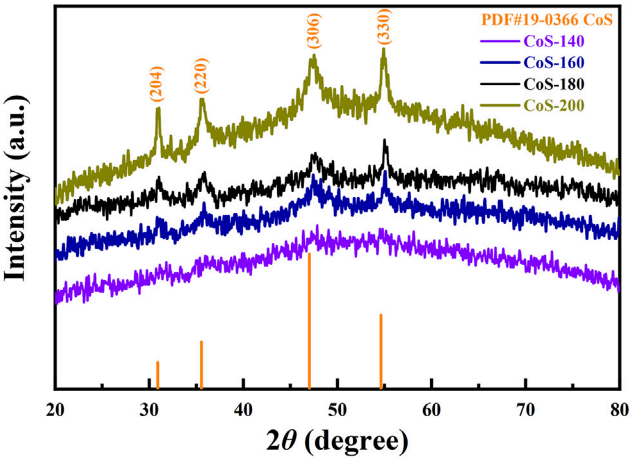

FIGURE 2 | The XRD patterns of the CoS samples prepared at different temperatures.

Electrochemical Performance Characterization

The electrochemical performance and impedance characteristics were measured by battery measuring systems (Land-ct2001A, China) and electrochemical workstation (CHI660E, China) in the potential range of 0.01–3.0 V at room temperature.

RESULTS AND DISCUSSION

Structure and Morphology

The XRD patterns of the as-prepared materials reacted at different temperatures are shown in **Figure 2**. With the increase of the reaction temperatures, the diffraction peaks gradually become apparent. No diffraction peak is observed for the CoS-140 sample, indicating the amorphous or nanocrystalline structure due to low reaction temperature. The diffraction peaks gradually appear, and the intensities increase gradually for the CoS-160 and CoS-180 samples, which indicates a progressively crystallized process with the increase of the reaction temperatures. For the CoS-200 sample, the diffraction peaks are very remarkable, which means good crystallization. The diffraction peaks at 31.05°, 35.68°, 47.13°, and 54.91° are consistent with the standard card of PDF No. 19–0366 ($CoS_{1.097}$), and these peaks correspond to the (204), (220), (306) and (330) crystal planes of hexagonal $CoS_{1.097}$, respectively. In addition, no other diffraction peaks are observed, indicating the pure cobalt sulfide nanomaterials of our samples. The degree of crystallization increases with the reaction temperatures. A series of amorphous and crystalline cobalt sulfide nanomaterials were prepared by controlling the reaction temperatures.

The morphologies of the amorphous and crystalline cobalt sulfide nanomaterials can be determined by the SEM images shown in **Figure 3**. From **Figure 3A**, the morphology of the amorphous CoS-140 sample is rough and irregular with many pits on the surface, and there are no noticeable regular crystalline grains observed, which is consistent with the absence of pronounced diffraction peaks shown in **Figure 2**. For the CoS-160 sample, some regular nanospheres are observed on the rough surface. And the regular nanospheres with different diameters should be crystalline structures. While for the CoS-180 sample, in addition to the regular nanospheres, some cracks are observed on the surface, which could result from the growth of the crystalline grains. A lot of small regular nanoparticles are observed for the CoS-200 sample, indicating crystalline growth of the sample, which strongly consists with the obvious diffraction peaks shown in **Figure 2**. Controlling reaction temperatures is crucial to synthesizing the cobalt sulfide nanomaterials with different amorphous or crystalline structures.

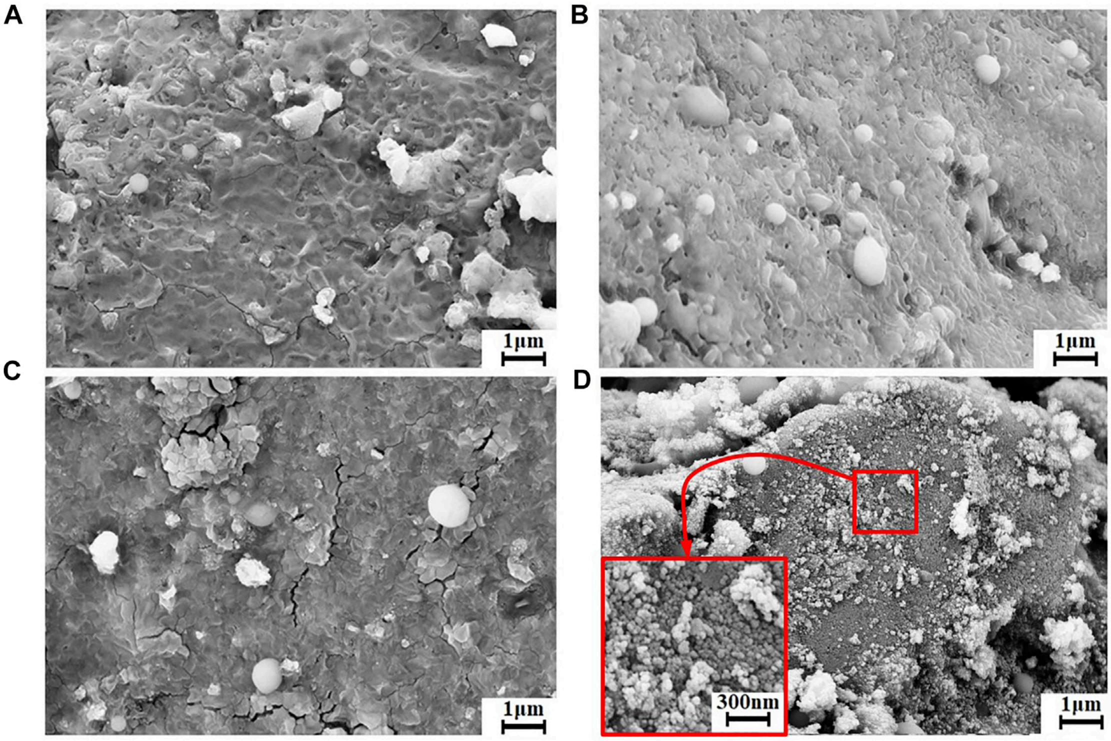

FIGURE 3 | The SEM images of CoS-140 **(A)**, CoS-160 **(B)**, CoS-180 **(C)**, and CoS-200 **(D)**.

Electrochemical Performance

In order to compare the electrochemical performance of the series of amorphous and crystalline cobalt sulfide nanomaterials, the cycle performance at 200 mA/g and the rate capability at different current densities were measured and shown in **Figure 4**. From **Figure 4A**, the samples of the CoS-140 and CoS-160 exhibit the relative constant reversible capacities, which indicates better cycle stability than that of the crystalline cobalt sulfide samples (CoS-160 and CoS-200). For the CoS-180 and CoS-200 samples, the specific capacities decrease first and then increase with the cycles, which is very common for the crystalline transition metal sulfides electrodes (Zhou et al., 2015). The first decrease could be due to the evolution of the SEI layers and the insufficient reaction of some active sites, and the subsequent increase could result from the polymeric gel-like layer and the decomposition of the crystal structure of CoS nanoparticles during the discharge-charge cycles (Zhou et al., 2020). However, the specific capacity of the CoS-200 sample decreases more sharply and obviously in the first cycles, which could result from the rapid decomposition of the crystalline structure during the cycles (Zhou et al., 2015; Wang et al., 2020b; Jiang et al., 2020). The CoS-140 sample exhibits the best cycling stability with the initial discharge and charge capacities of 2,132 mAh/g and 1,443 mAh/g, respectively. The Coulombic efficiency in the first cycle is 67.67% and radically increases to 97.44% in the second cycle, and maintains near 100% to the 200th cycle. Significantly, the reversible capacity of 1,245 mAh/g after 200 cycles was obtained, which is much higher than the theoretical capacity of 589 mAh/g (Yan et al., 2005). The initial discharge capacity and the reversible capacity in this work and those of other reported cobalt sulfide-based electrodes are listed in **Table 1**, which indicates the outstanding electrochemical performance of the amorphous sample of CoS-140.

From **Figure 4B**, the samples of the CoS-140 and CoS-160 also exhibit better rate capability than that of the crystalline cobalt sulfide, which is consistent with the results of the cycle performance shown in **Figure 4A**. Even though the reversible capacity returns to 658 mA h/g when the current density goes back to 100 mA/g, the crystalline sample of CoS-200 exhibits the worst rate capability than other samples. The details of the average reversible capacities for the series of cobalt sulfide nanomaterials at different current densities are listed in **Table 2**, which also indicates the best rate capability of the amorphous sample of CoS-140 at each current density. The reversible capabilities of the amorphous CoS-140 sample are 1,450 mAh/g, 1,170 mAh/g, 958 mAh/g, and 815 mAh/g at 100 mA/g, 200 mA/g, 500 mA/g, and 800 mA/g, and the capabilities increase to 889 mAh/g, 1,015 mAh/g, and 1,047 mAh/g when back to 500 mA/g, 200 mA/g, and 100 mA/g, indicating the excellent rate capability. The outstanding electrochemical performance of the amorphous sample could result from the more active sites due to the more defects and the improved ability of the volume accommodation because of the isotropic nature and the absence of grain boundaries for the amorphous structure (Li et al., 2012; Liu et al., 2013; Wu et al., 2019; Wang et al., 2020b; Duan et al., 2021; Wu et al., 2021).

Due to the best electrochemical performances, further investigation was focused on the amorphous CoS-140 sample. In order to comprehend the electrochemical reaction mechanism, the

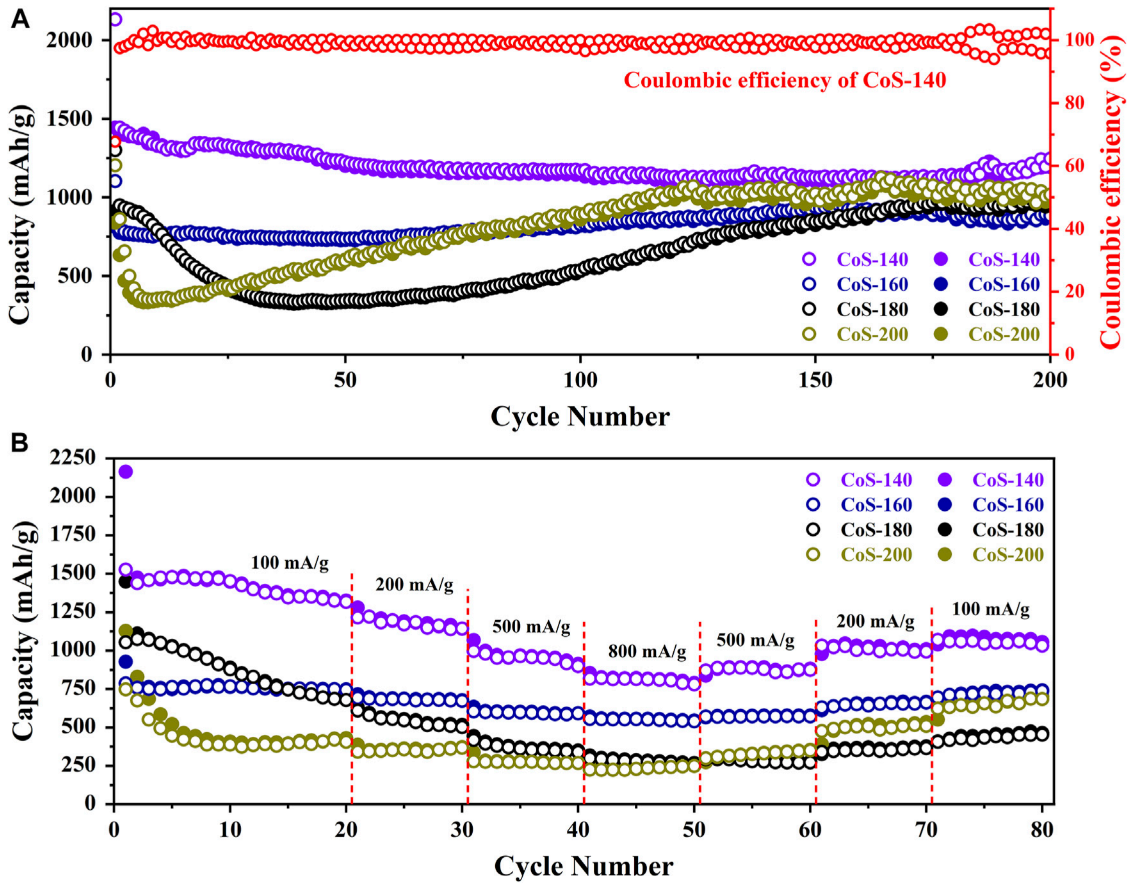

FIGURE 4 | The cycle stabilities at 200 mA/g **(A)** and rate capabilities **(B)** of the CoS samples prepared at different temperatures. The solid and hollow circles represent the discharge and charge capacities, respectively.

TABLE 1 | The comparison of the electrochemical performance between this work and other reported cobalt sulfide-based electrodes.

Materials	Initial discharge capacity (mAh/g)	Reversible capacity (mAh/g)	Current density (mA/g)	References
Amorphous CoS	2,132	1,443 (200 cycles)	200	This work
Crystalline CoS	1,205	1,017 (200 cycles)		
C@Co$_9$S$_8$	848	520 (50 cycles)	1.8 C	Shi et al. (2012)
CoS$_2$	1,280	350 (50 cycles)	50	Yan et al. (2005)
CoS/graphene	1,669	749 (40 cycles)	0.1 C	Gu et al. (2013)
Co$_9$S$_8$/C	2026	1,063 (200 cycles)	300	Jiang et al. (2020)
Co$_9$S$_8$-650@C	1,584	1,414 (100 cycles)	100	Zhou et al. (2015)
CoS$_2$NP@G-CoS$_2$	1,504	1,022 (50 cycles)	100	He et al. (2015)
CoS-NP/ACFs	1,137.3	576.7 (200cycles)	100	Yuan et al. (2020b)
CoS$_2$-C/CNT	1,339	1,030 (120 cycles)	100	Ma et al. (2018)
Co$_3$S$_4$/CNF	991	742 (200 cycles)	1,000	Luo et al. (2019)
Si@C-Co$_9$S$_8$/C	1,441	1,399 (200 cycles)	100	Yuan et al. (2020a)
CMF@Co$_9$S$_8$-C	1,315	615 (450 cycles)	500	Zhang et al. (2020)
Co$_4$S$_3$/CNA@CC	1,200	720 (200 cycles)	1,000	Shi et al. (2020)
Co$_9$S$_8$	1,100	910 (100 cycles)	500	Lu et al. (2017)
CNTs@NC	1,366	914 (100 cycles)	100	Wang et al. (2020a)
Co$_9$S$_8$/Ni	1,580	720 (100 cycles)	100	Jin et al. (2016)
CoS$_2$	1,542	737 (200 cycles)	1,000	Yu et al. (2016)
CoS$_2$ NG	1,120	1,018 (50 cycles)	100	Qiu et al. (2015)
CoS$_2$	1,416	883 (100 cycles)	100	Jin et al. (2015)

TABLE 2 | The reversible capacities of the CoS samples at different current densities.

Samples	100 mA/g	200 mA/g	500 mA/g	800 mA/g	500 mA/g	200 mA/g	100 mA/g
CoS-140	1,451	1,170	958	815	889	1,015	1,047
CoS-160	766	684	595	551	572	643	723
CoS-180	879	546	361	279	280	347	434
CoS-200	389	357	276	230	326	485	658

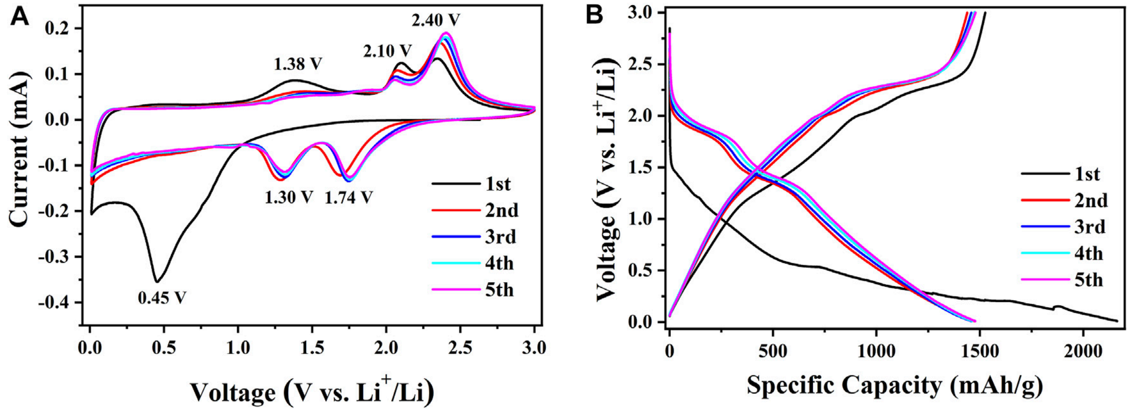

FIGURE 5 | The first five CV curves at 0.1 m V/s **(A)** and the first five discharge-charge curves at 100 mA/g **(B)** for the amorphous CoS-140 sample.

first five voltammetry (CV) curves of the amorphous CoS-140 sample were measured at a scan rate of 0.1 mV/s, as is shown in **Figure 5A**. In the first discharge process, there is a broad reduction peak at 0.45 V, which relates to the formation of the solid electrolyte interface (SEI) and the process of cobalt sulfide reduced to cobalt metal and Li_2S (He et al., 2015; Zhou et al., 2015; Yuan et al., 2020b). In the following cathodic sweeps, the broad peak divides into two sharp peaks located at 1.74 and 1.30 V, which correspond to the formation of Li_xCoS and the further convention reaction of Li_xCoS to Co. metal (Ma et al., 2018; Yuan et al., 2020b). There is a broad peak at 1.38 V in the first charge process, which consists with the decomposition of the SEI layer (Zhou et al., 2015; Ma et al., 2018). This broad peak almost disappears in the following cycles due to the stability of the SEI layer, which is beneficial for the cycle stability (Zhou et al., 2015; Ma et al., 2018). There are also two oxidation peaks around 2.10 and 2.40 V in the five cathodic sweeps, which are consistent with the above reversible reactions of extraction of lithium ions to form CoS and the reduction process of Li_2S to S (Zhou et al., 2015; Ma et al., 2018; Luo et al., 2019; Yuan et al., 2020b). The tiny changes of the positions for the two reduction peaks (1.74 and 1.30 V) and the two oxidation peaks (2.10 and 2.40 V) could result from a slight transformation of the structure (Zhou et al., 2015; Luo et al., 2019). The oxidation and reduction peaks almost coincide after the first cycle, indicating the stable electrochemical reaction process. The approximate overlap of the CV curves after the first cycle also shows excellent cycle stability and reversibility (Ma et al., 2018; Luo et al., 2019; Yuan et al., 2020b).

The first five discharge-charge curves at 100 mA/g are also shown in **Figure 5B** to compare the results of the CV curves. An extended voltage plateau from 0.63 to 0.15 V can be observed in the first discharge curves, which corresponds to the broad reduction peak at 0.45 V in the first CV cathodic sweep. There are two discharge plateaus around 2.10–1.70 V and 1.45–1.25 V in the following discharge curve, which consist with the division of the peak of 0.45 V into two peaks of 1.74 and 1.30V. For the first charge curve, there are three plateaus around 1.20 V-2.00 V, 2.00 V-2.20 V, and 2.20–2.46 V, corresponding to the three peaks of 1.36, 2.10, and 2.40 V in the first anodic sweep. The voltage plateau of 1.20–2.00 V disappears in the following cycles, indicating the stability of the SEI layer, which is in agreement with the disappearance of the oxidation peak at 1.38 V. After the initial cycle, the discharge-charge curves nearly overlap, which indicates the high reversible cycle stability and the reversible redox reactions of the amorphous sample.

In order to deeply comprehend the enhanced electrochemical performance and the reaction kinetics of the amorphous CoS-140 sample, the electrochemical impedance spectroscopies (EIS) were measured from 10^{-2} Hz–10^5 Hz before and after cycling, as is shown in **Figure 6**. Both the two Nyquist plots (black scatters) are composed of one depressed semicircle in high-frequency regions and one straight line in low-frequency regions, which can be well fitted by the equivalent circuit (red fitting lines) that is shown in the inset of **Figure 6A**. In the equivalent circuit, the parameter of R_s denotes the ohmic resistance of the electrode and electrolyte, and the parameter of R_{ct} signifies the charge transfer resistance (Wu et al., 2019; Duan et al., 2021; Wu et al., 2021). The fitted R_{ct} after cycling (229.5 Ω) is much lower than that of before cycling (7645 Ω), indicating the higher reaction kinetics activity during the cycles, which is in agreement with the excellent cycle stability and the rate capability shown in **Figure 4**. Moreover, the Li-ions diffusion coefficient (D_{Li^+}) can be obtained by the following equations (Wang et al., 2020b; Duan et al., 2021).

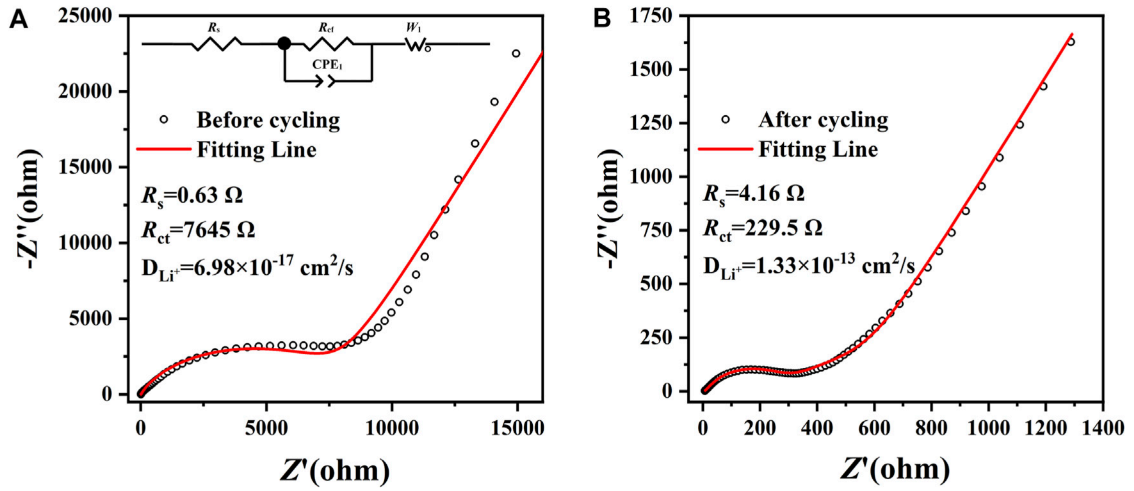

FIGURE 6 | The EIS of the amorphous CoS-140 sample before **(A)** and after **(B)** cycling from 10^{-2} Hz–10^{5} Hz. The equivalent circuit is shown in the inset of **(A)**.

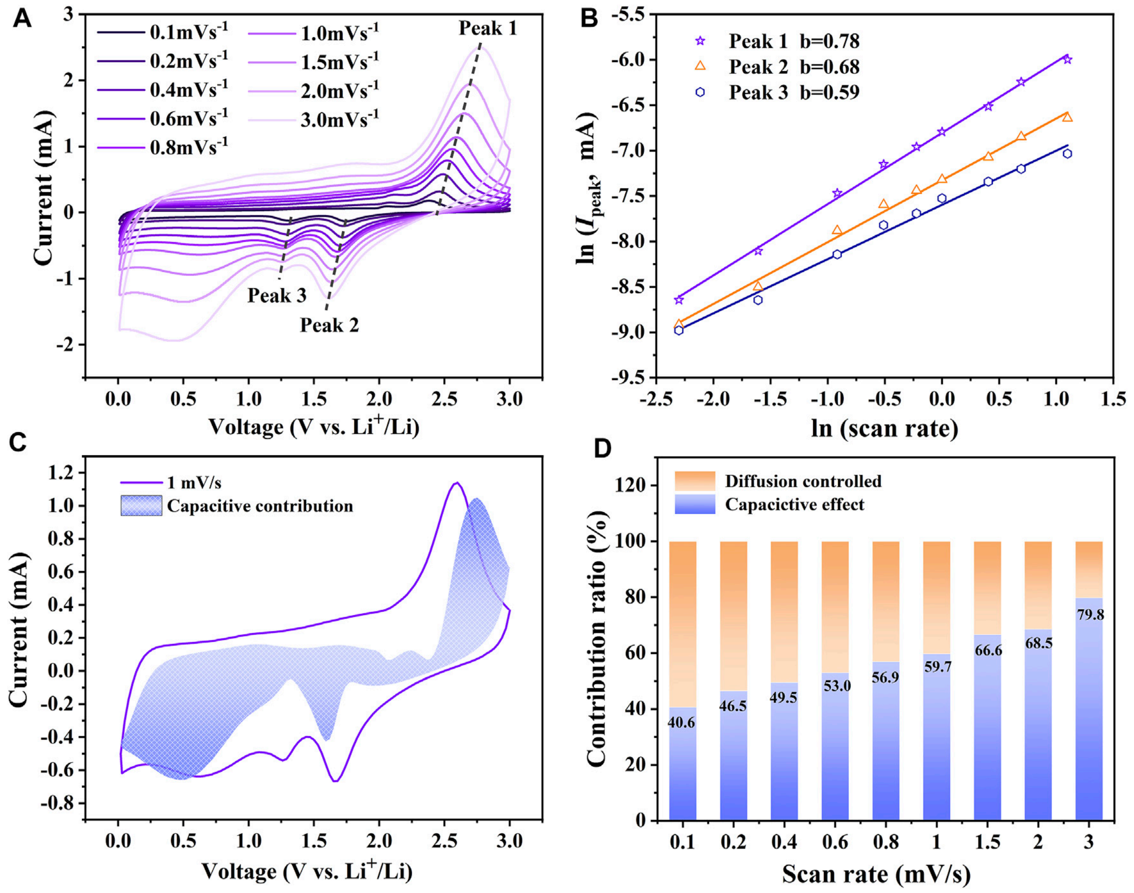

FIGURE 7 | (A) The CV curves of the amorphous CoS-140 sample with different scan rates **(B)** The linear fitting of ln (I_{Peak}) vs ln(ν). **(C)** Capacitive contribution at 1 mV/s. **(D)** Capacitive contributions at different scan rates.

$$D_{\mathrm{Li}^+} = \frac{R^2T^2}{2A^2n^4F^4C^2\sigma^2} \quad (1)$$

$$Z_{\mathrm{real}} = R_{\mathrm{s}} + R_{\mathrm{ct}} + \sigma\omega^{-1/2} \quad (2)$$

The parameters of R, T, A, n, F, C, σ, and ω are the general physical parameters gas constant, the measuring temperature, the surface area of the electrode, the number of transferred electrons, the Faraday constant, the concentration of lithium ions, the Warburg coefficient, and the angular frequency, respectively (Wang et al., 2020b; Yuan et al., 2020b). The value of σ could be fitted by **Eq. 2** according to the EIS data in the low-frequency regions, and then the Li-ions diffusion coefficient can be calculated by **Eq. 1**. The Li-ions diffusion coefficient after cycling (1.33×10^{-13} cm^2/s) is much higher than before cycling (6.98×10^{-17} cm^2/s), which also indicates the better electrochemical kinetic activity during cycles. The three-dimensional isotropy structure of the amorphous CoS-140 could promote the penetration of the electrolyte and accelerate the diffusion velocity of the lithium ions into the active materials during the lithium storage process (Etacheri et al., 2015; Wu et al., 2018; Wu et al., 2020).

It is necessary to further understand the reason for the fast reaction kinetic and the energy storage mechanism of the amorphous CoS-140 sample. The CV curves with different scan rates (0.1–3 mV/s) were measured and shown in **Figure 7A**. The CV curves maintain analogous shapes, while the areas enclosed by the CV curves and the identities of the redox reaction peaks gradually increase with the scan rates, which are always reported by other works of literature (Wu et al., 2019; Duan et al., 2021; Wu et al., 2021). The redox peaks are even evident at the high scan rate of 3 mV/s, indicating the high reaction dynamics (Wang et al., 2020d). The total energy storage of the electrode is generally contributed by two reaction processes of surface capacitive mechanism and diffusion mechanism (Duan et al., 2021), which can be roughly estimated by the following equations (Wang et al., 2020b; Yuan et al., 2020b).

$$I_{\mathrm{Peak}} = av^b \quad (3)$$

$$1\mathrm{n}\left(I_{\mathrm{Peak}}\right) = b1\mathrm{n}(v) + 1\mathrm{n}a \quad (4)$$

I_{Peak} represents the currents of the redox peaks at different scan rates marked by the arrows in **Figure 7A**, and v denotes the corresponding scan rates. a and b are the variable parameters, and generally, the value of b is between 0.5 and one according to the different contribution ratios of the two parts. When $b = 0.5$, the electrochemical system is controlled by charge diffusion, while $b = 1$, the capacitive behavior is dominant (Wu et al., 2019; Wang et al., 2020b; Jiang et al., 2020; Duan et al., 2021; Wu et al., 2021). According to the linear fitting of ln (I_{Peak}) vs ln(v) shown in **Figure 7B** the values of b for the three redox reaction peaks are 0.68, 0.59, and 0.78, respectively, which indicates the mixed contribution of surface capacitive effect and diffusion-controlled process. The quantitative contribution of surface capacitive effect for the electrochemical system can be further analyzed by the following equations (Wu et al., 2019; Duan et al., 2021; Wu et al., 2021).

$$I = k_1v + k_2v^{0.5} \quad (5)$$

$$\frac{I}{v^{0.5}} = k_1v^{0.5} + k_2 \quad (6)$$

k_1v and $k_2v^{1/2}$ represent the surface capacitive contribution and the charge diffusion contribution, respectively (Wu et al., 2019; Duan et al., 2021). A series of k_1 and k_2 can be obtained by the slope and intercept of $I/v^{0.5}$ vs $v^{0.5}$ plots at different voltages. As shown in **Figure 7C**, the capacity contribution of the surface capacitive effect is 59.7% for the CV curves at the scan rate of 1 mV/s. The surface capacitive contributions for the capacities at different scan rates are shown in **Figure 7D**. The capacitive behavior contribution ratio gradually increases with the increase of the scan rates. The maximum contribution ratio of 79.8% is achieved at the scan rate of 3.0 mV/s, indicating the dominance of the capacitive behavior at a high scan rate, which is in agreement with the outstanding rate capability. The large contribution ratio of the capacitive behavior could result from the more surface defects and the inside void space of the amorphous structure for the CoS-140 sample, which is beneficial for the enhanced electrochemical performance (Lian et al., 2017; Li et al., 2020a; Liu et al., 2021b).

CONCLUSION

In summary, through controlling the reaction temperatures, a series of amorphous and crystalline cobalt sulfide nanomaterials were prepared by a facile solvothermal method. Compared to the crystalline cobalt sulfide, the amorphous cobalt sulfide exhibited superior electrochemical performance with the initial discharge and charge capacities of 2,132 mAh/g and 1,443 mAh/g at 200 mA/g. The reversible capacity of 1,245 mAh/g after 200 cycles was obtained. After discharge-charge cycles at different current densities, the specific capability increased to 1,047 mAh/g when back to 100 mA/g. The outstanding electrochemical performance of the amorphous cobalt sulfide nanomaterials could result from the special structural characteristics of amorphous materials. The amorphous cobalt sulfide nanomaterials could be used as anodes for LIBs in the future.

DATA AVAILABILITY STATEMENT

The raw data supporting the conclusion of this article will be made available by the authors, without undue reservation.

AUTHOR CONTRIBUTIONS

All authors listed have made a substantial, direct, and intellectual contribution to the work and approved it for publication.

FUNDING

This work was funded by the National Natural Science Foundation of China No. 22179066 and the Project of Shandong Province Higher Educational Science and Technology Program No. J17KA184.

REFERENCES

Duan, Y., Du, S., Tao, H., and Yang, X. (2021). Sn@C Composite for Lithium Ion Batteries: Amorphous vs. Crystalline Structures. *Ionics* 27, 1403–1412. doi:10.1007/s11581-021-03906-4

Etacheri, V., Hong, C. N., and Pol, V. G. (2015). Upcycling of Packing-Peanuts into Carbon Microsheet Anodes for Lithium-Ion Batteries. *Environ. Sci. Technol.* 49, 11191–11198. doi:10.1021/acs.est.5b01896

Gao, M., Zhou, W.-Y., Mo, Y.-X., Sheng, T., Deng, Y., Chen, L., et al. (2021). Outstanding Long-Cycling Lithium−sulfur Batteries by Core-Shell Structure of S@Pt Composite with Ultrahigh Sulfur Content. *Adv. Powder Mater.* doi:10.1016/j.apmate.2021.09.006

Gu, Y., Xu, Y., and Wang, Y. (2013). Graphene-wrapped CoS Nanoparticles for High-Capacity Lithium-Ion Storage. *ACS Appl. Mater. Inter.* 5, 801–806. doi:10.1021/am3023652

Gu, Z. Y., Guo, J. Z., Zhao, X. X., Wang, X. T., Xie, D., Sun, Z. H., et al. (2021). High-ionicity Fluorophosphate Lattice via Aliovalent Substitution as Advanced Cathode Materials in Sodium-ion Batteries. *InfoMat* 3, 694–704. doi:10.1002/inf2.12184

He, J., Chen, Y., Li, P., Fu, F., Wang, Z., and Zhang, W. (2015). Self-assembled CoS_2 Nanoparticles Wrapped by CoS_2-Quantum-Dots-Anchored Graphene Nanosheets as superior-capability Anode for Lithium-Ion Batteries. *Electrochimica Acta* 182, 424–429. doi:10.1016/j.electacta.2015.09.131

Hou, X., Li, W., Wang, Y., Li, S., Meng, Y., Yu, H., et al. (2020). Sodium-based Dual-Ion Batteries via Coupling High-Capacity Selenium/graphene Anode with High-Voltage Graphite Cathode. *Chin. Chem. Lett.* 31, 2314–2318. doi:10.1016/j.cclet.2020.04.021

Jiang, W., Liu, Q., Peng, J., Jiang, Y., Ding, Y., and Wei, Q. (2020). Co_9S_8 Nanoparticles Embedded into Amorphous Carbon as Anode Materials for Lithium-Ion Batteries. *Nanotechnology* 31, 235713. doi:10.1088/1361-6528/ab7887

Jin, R., Yang, L., Li, G., and Chen, G. (2015). Hierarchical Worm-like CoS_2 Composed of Ultrathin Nanosheets as an Anode Material for Lithium-Ion Batteries. *J. Mater. Chem. A.* 3, 10677–10680. doi:10.1039/C5TA02646F

Jin, R., Zhou, J., Li, G., and Yang, L. (2016). Co 9 S 8 Nanosheet Arrays Supported on Nickel Foam for Enhanced Performance as Anode Material for Li-Ion Batteries. *Mater. Lett.* 163, 183–186. doi:10.1016/j.matlet.2015.10.093

Li, H., Hu, Z., Xia, Q., Zhang, H., Li, Z., Wang, H., et al. (2021a). Operando Magnetometry Probing the Charge Storage Mechanism of CoO Lithium-Ion Batteries. *Adv. Mater.* 33, 2006629. doi:10.1002/adma.202006629

Li, L.-W., Wang, L.-P., Zhang, M.-Y., Huang, Q.-Z., He, K.-J., and Wu, F.-X. (2020a). Enhancement of Lithium Storage Capacity and Rate Performance of Se-Modified MnO/Mn_3O_4 Hybrid Anode Material via Pseudocapacitive Behavior. *Trans. Nonferrous Met. Soc. China* 30, 1904–1915. doi:10.1016/S1003-6326(20)65349-3

Li, Q., Li, H., Xia, Q., Hu, Z., Zhu, Y., Yan, S., et al. (2021b). Extra Storage Capacity in Transition Metal Oxide Lithium-Ion Batteries Revealed by *In Situ* Magnetometry. *Nat. Mater.* 20, 76–83. doi:10.1038/s41563-020-0756-y

Li, S.-F., Gu, Z.-Y., Guo, J.-Z., Hou, X.-K., Yang, X., Zhao, B., et al. (2021c). Enhanced Electrode Kinetics and Electrochemical Properties of Low-Cost $NaFe_2PO_4(SO_4)_2$ via Ca_{2+} Doping as Cathode Material for Sodium-Ion Batteries. *J. Mater. Sci. Technol.* 78, 176–182. doi:10.1016/j.jmst.2020.10.047

Li, W.-H., Liang, H.-J., Hou, X.-K., Gu, Z.-Y., Zhao, X.-X., Guo, J.-Z., et al. (2020b). Feasible Engineering of Cathode Electrolyte Interphase Enables the Profoundly Improved Electrochemical Properties in Dual-Ion Battery. *J. Energ. Chem.* 50, 416–423. doi:10.1016/j.jechem.2020.03.043

Li, X., Meng, X., Liu, J., Geng, D., Zhang, Y., Banis, M. N., et al. (2012). Tin Oxide with Controlled Morphology and Crystallinity by Atomic Layer Deposition onto Graphene Nanosheets for Enhanced Lithium Storage. *Adv. Funct. Mater.* 22, 1647–1654. doi:10.1002/adfm.201101068

Li, Z., Zhang, Y., Li, X., Gu, F., Zhang, L., Liu, H., et al. (2021d). Reacquainting the Electrochemical Conversion Mechanism of FeS_2 Sodium-Ion Batteries by Operando Magnetometry. *J. Am. Chem. Soc.* 143, 12800–12808. doi:10.1021/jacs.1c06115

Lian, Q., Zhou, G., Liu, J., Wu, C., Wei, W., Chen, L., et al. (2017). Extrinsic Pseudocapacitve Li-Ion Storage of SnS Anode via Lithiation-Induced Structural Optimization on Cycling. *J. Power Sourc.* 366, 1–8. doi:10.1016/j.jpowsour.2017.09.009

Liang, H., Zhang, H., Zhao, L., Chen, Z., Huang, C., Zhang, C., et al. (2022). Layered $Fe_2(MoO_4)_3$ Assemblies with Pseudocapacitive Properties as Advanced Materials for High-Performance Sodium-Ion Capacitors. *Chem. Eng. J.* 427, 131481. doi:10.1016/j.cej.2021.131481

Liu, C., Li, Q., and Wang, K. (2021a). State-of-charge Estimation and Remaining Useful Life Prediction of Supercapacitors. *Renew. Sustain. Energ. Rev.* 150, 111408. doi:10.1016/j.rser.2021.111408

Liu, H., Hu, R., Sun, W., Zeng, M., Liu, J., Yang, L., et al. (2013). Sn@SnOx/C Nanocomposites Prepared by Oxygen Plasma-Assisted Milling as Cyclic Durable Anodes for Lithium Ion Batteries. *J. Power Sourc.* 242, 114–121. doi:10.1016/j.jpowsour.2013.05.087

Liu, W., Xiang, P., Dong, X., Yin, H., Yu, H., Cheng, P., et al. (2021b). Two Advantages by a Single Move: Core-Bishell Electrode Design for Ultrahigh-Rate Capacity and Ultralong-Life Cyclability of Lithium Ion Batteries. *Composites B: Eng.* 216, 108883. doi:10.1016/j.compositesb.2021.108883

Lu, M., Liao, C., Jiang, C., Du, Y., Zhang, Z., and Wu, S. (2017). Remarkable High-Temperature Performance of Hollow Co_9 S_8 Nanoparticles Integrated with Carbon Materials for Lithium-Ion Batteries. *Electrochimica Acta* 250, 196–202. doi:10.1016/j.electacta.2017.08.019

Lu, Y., Huang, G., Wang, Y., Li, H., Qin, Z., and Lu, X. (2018). Crack-free Fe-Based Amorphous Coating Synthesized by Laser Cladding. *Mater. Lett.* 210, 46–50. doi:10.1016/j.matlet.2017.08.125

Luo, F., Ma, D., Li, Y., Mi, H., Zhang, P., and Luo, S. (2019). Hollow Co_3S_4/C Anchored on Nitrogen-Doped Carbon Nanofibers as a Free-Standing Anode for High-Performance Li-Ion Batteries. *Electrochimica Acta* 299, 173–181. doi:10.1016/j.electacta.2018.12.175

Ma, Y., Ma, Y., Bresser, D., Ji, Y., Geiger, D., Kaiser, U., et al. (2018). Cobalt Disulfide Nanoparticles Embedded in Porous Carbonaceous Micro-polyhedrons Interlinked by Carbon Nanotubes for Superior Lithium and Sodium Storage. *ACS Nano* 12, 7220–7231. doi:10.1021/acsnano.8b03188

Qiu, W., Jiao, J., Xia, J., Zhong, H., and Chen, L. (2015). A Self-Standing and Flexible Electrode of Yolk-Shell CoS2Spheres Encapsulated with Nitrogen-Doped Graphene for High-Performance Lithium-Ion Batteries. *Chem. Eur. J.* 21, 4359–4367. doi:10.1002/chem.201405821

Shi, M., Wang, Q., Hao, J., Min, H., You, H., Liu, X., et al. (2020). MOF-derived Hollow Co_4S_3/C Nanosheet Arrays Grown on Carbon Cloth as the Anode for High-Performance Li-Ion Batteries. *Dalton Trans.* 49, 14115–14122. doi:10.1039/d0dt03070h

Shi, W., Zhu, J., Rui, X., Cao, X., Chen, C., Zhang, H., et al. (2012). Controlled Synthesis of Carbon-Coated Cobalt Sulfide Nanostructures in Oil Phase with Enhanced Li Storage Performances. *ACS Appl. Mater. Inter.* 4, 2999–3006. doi:10.1021/am3003654

Sun, B., Chen, Z., Kim, H.-S., Ahn, H., and Wang, G. (2011). MnO/C Core-Shell Nanorods as High Capacity Anode Materials for Lithium-Ion Batteries. *J. Power Sourc.* 196, 3346–3349. doi:10.1016/j.jpowsour.2010.11.090

Sun, B., Horvat, J., Kim, H. S., Kim, W.-S., Ahn, J., and Wang, G. (2010). Synthesis of Mesoporous α-Fe_2O_3 Nanostructures for Highly Sensitive Gas Sensors and High Capacity Anode Materials in Lithium Ion Batteries. *J. Phys. Chem. C* 114, 18753–18761. doi:10.1021/jp102286e

Wang, G., Yue, H., Jin, R., Wang, Q., and Gao, S. (2020a). Co_3S_4 Ultrathin Nanosheets Entangled on N-Doped Amorphous Carbon Coated Carbon Nanotubes with C S Bonding for High Performance Li-Ion Batteries. *J. Electroanalytical Chem.* 858, 113794. doi:10.1016/j.jelechem.2019.113794

Wang, L.-H., Dai, Y.-K., Qin, Y.-F., Chen, J., Zhou, E.-L., Li, Q., et al. (2020b). One-Pot Synthesis and High Electrochemical Performance of $CuS/Cu_{1.8}S$ Nanocomposites as Anodes for Lithium-Ion Batteries. *Materials* 13, 3797. doi:10.3390/ma13173797

Wang, L.-H., Gao, S., Ren, L.-L., Zhou, E.-L., and Qin, Y.-F. (2021a). The Synergetic Effect Induced High Electrochemical Performance of $CuO/Cu_2O/Cu$ Nanocomposites as Lithium-Ion Battery Anodes. *Front. Chem.* 9. doi:10.3389/fchem.2021.790659

Wang, L.-H., Teng, X.-L., Qin, Y.-F., and Li, Q. (2021b). High Electrochemical Performance and Structural Stability of CoO nanosheets/CoO Film as Self-Supported Anodes for Lithium-Ion Batteries. *Ceramics Int.* 47, 5739–5746. doi:10.1016/j.ceramint.2020.10.160

Wang, M., Fan, L., Sun, X., Guan, B., Jiang, B., Wu, X., et al. (2020c). Nitrogen-Doped $CoSe_2$ as a Bifunctional Catalyst for High Areal Capacity and Lean Electrolyte of Li-S Battery. *ACS Energ. Lett.* 5, 3041–3050. doi:10.1021/acsenergylett.0c01564

Wang, Y., Cao, L., Li, J., Kou, L., Huang, J., Feng, Y., et al. (2020d). Cu/Cu_2O@Ppy Nanowires as a Long-Life and High-Capacity Anode for Lithium Ion Battery. *Chem. Eng. J.* 391, 123597. doi:10.1016/j.cej.2019.123597

Wu, C., Zhao, Y., Fan, Q., Kuang, Q., and Dong, Y. (2021). Facile Synthesis and Electrochemical Properties of Amorphous/crystalline $VO(PO_3)_2$@C as the Anodes for Lithium-Ion Battery. *J. Electroanalytical Chem.* 895, 115541. doi:10.1016/j.jelechem.2021.115541

Wu, H., Qin, M., Wang, W., Cao, Z., Liu, Z., Yu, Q., et al. (2018). Ultrafast Synthesis of Amorphous VOxembedded into 3D Strutted Amorphous Carbon Frameworks-Short-Range Order in Dual-Amorphous Composites Boosts Lithium Storage. *J. Mater. Chem. A.* 6, 7053–7061. doi:10.1039/C8TA00654G

Wu, H., Zhang, Z., Qin, M., Wang, Q., Cao, Z., Yu, Y., et al. (2019). Solution Combustion Synthesis of Crystalline $V_2 O_3$ and Amorphous $V_2 O_3$/C as Anode for Lithium-ion Battery. *J. Am. Ceram. Soc.* 103, 2643–2652. doi:10.1111/jace.16962

Wu, H., Zhou, S., Tseng, C., Qin, M., Shiue, A., Chu, A., et al. (2020). One-pot Solution Combustion Synthesis of Crystalline and Amorphous Molybdenum Trioxide as Anode for Lithium-ion Battery. *J. Am. Ceram. Soc.* 104, 1102–1109. doi:10.1111/jace.17499

Yan, J. M., Huang, H. Z., Zhang, J., Liu, Z. J., and Yang, Y. (2005). A Study of Novel Anode Material CoS_2 for Lithium Ion Battery. *J. Power Sourc.* 146, 264–269. doi:10.1016/j.jpowsour.2005.03.144

Yu, L., Yang, J. F., and Lou, X. W. D. (2016). Formation of CoS_2 Nanobubble Hollow Prisms for Highly Reversible Lithium Storage. *Angew. Chem. Int. Ed.* 55, 13422–13426. doi:10.1002/anie.201606776

Yuan, C., Lu, D., An, Y., and Bian, X. (2020a). A Nanocomposite of Si@C Nanosphere and Hollow Porous $Co_9 S_8$/C Polyhedron as High-Performance Anode for Lithium-Ion Battery. *ChemElectroChem* 7, 4423–4430. doi:10.1002/celc.202001052

Yuan, H., Wang, F., Li, S., Lin, Z., and Huang, J. (2020b). A Cellulose Substance Derived Nanofibrous CoS-Nanoparticle/carbon Composite as a High-Performance Anodic Material for Lithium-Ion Batteries. *New J. Chem.* 44, 1846–1857. doi:10.1039/c9nj05587h

Zhang, F., Teng, X., Shi, W., Song, Y., Zhang, J., Wang, X., et al. (2020a). SnO_2 Nanoflower Arrays on an Amorphous Buffer Layer as Binder-free Electrodes for Flexible Lithium-Ion Batteries. *Appl. Surf. Sci.* 527, 146910–146920. doi:10.1016/j.apsusc.2020.146910

Zhang, P., Tian, R., Cao, M., Feng, Y., and Yao, J. (2020). Embedding Co_9S_8 Nanoparticles into Porous Carbon Foam with High Flexibility and Enhanced Lithium Ion Storage. *J. Electroanalytical Chem.* 863, 114062. doi:10.1016/j.jelechem.2020.114062

Zhang, Y., Wang, P., Yin, Y., Liu, N., Song, N., Fan, L., et al. (2019a). Carbon Coated Amorphous Bimetallic Sulfide Hollow Nanocubes towards Advanced Sodium Ion Battery Anode. *Carbon* 150, 378–387. doi:10.1016/j.carbon.2019.05.048

Zhang, Y., Wang, P., Yin, Y., Zhang, X., Fan, L., Zhang, N., et al. (2019b). Heterostructured SnS-ZnS@C Hollow Nanoboxes Embedded in Graphene for High Performance Lithium and Sodium Ion Batteries. *Chem. Eng. J.* 356, 1042–1051. doi:10.1016/j.cej.2018.09.131

Zhao, S., Yan, K., Zhang, J., Sun, B., and Wang, G. (2021). Reaction Mechanisms of Layered Lithium-Rich Cathode Materials for High-Energy Lithium-Ion Batteries. *Angew. Chem. Int. Ed.* 60, 2208–2220. doi:10.1002/anie.202000262

Zhao, Z., Hu, Z., Jiao, R., Tang, Z., Dong, P., Li, Y., et al. (2019). Tailoring Multi-Layer Architectured FeS_2@C Hybrids for superior Sodium-, Potassium- and Aluminum-Ion Storage. *Energ. Storage Mater.* 22, 228–234. doi:10.1016/j.ensm.2019.01.022

Zhao, Z., Hu, Z., Li, Q., Li, H., Zhang, X., Zhuang, Y., et al. (2020). Designing Two-Dimensional WS_2 Layered Cathode for High-Performance Aluminum-Ion Batteries: From Micro-assemblies to Insertion Mechanism. *Nano Today* 32, 100870. doi:10.1016/j.nantod.2020.100870

Zhou, Y., Wang, Y., Wang, K., Kang, L., Peng, F., Wang, L., et al. (2020). Hybrid Genetic Algorithm Method for Efficient and Robust Evaluation of Remaining Useful Life of Supercapacitors. *Appl. Energ.* 260, 114169–114184. doi:10.1016/j.apenergy.2019.114169

Zhou, Y., Yan, D., Xu, H., Feng, J., Jiang, X., Yue, J., et al. (2015). Hollow Nanospheres of Mesoporous $Co_9 S_8$ as a High-Capacity and Long-Life Anode for Advanced Lithium Ion Batteries. *Nano Energy* 12, 528–537. doi:10.1016/j.nanoen.2015.01.019

Conflict of Interest: The authors declare that the research was conducted in the absence of any commercial or financial relationships that could be construed as a potential conflict of interest.

frontiers
in Chemistry

MINI REVIEW
published: 01 February 2022
doi: 10.3389/fchem.2022.837978

Regulation of the Interfaces Between Argyrodite Solid Electrolytes and Lithium Metal Anode

Bo Pang, Yongping Gan*, Yang Xia, Hui Huang, Xinping He and Wenkui Zhang*

College of Materials Science and Engineering, Zhejiang University of Technology, Hangzhou, China

Lithium-ion batteries (LIBs) are widely used in portable electronic devices, electric vehicles and large scale energy storage, due to their considerable energy density, low cost and long cycle life. However, traditional liquid batteries suffer from safety problems such as leakage, thermal runaway and even explosion. Part of the issues are caused by lithium dendrites puncturing the liquid electrolyte during cycling. In order to achieve the objective of higher safety and energy density, a rigid solid-state electrolyte (SSE) is proposed instead of liquid electrolyte (LE). Thereinto, sulfide SSEs have received of the most attention due to their high ionic conductivity. Among all the sulfide SSEs, argyrodite SSEs are considered to be one of the most promising solid-state electrolytes due to their high ionic conductivity, high thermal stability and good processablity. On the other hand, lithium metal is an ideal material for anode because of its high specific energy, low potential and large storage capacity. However, interfacial problems between argyrodite SSEs and the anode (interfacial reactions, lithium dendrites, etc.) are considered to be important factors affecting their availability. In this mini review, we summarize the behavior, properties and problems arising at the interface between argyrodite SSEs and anode. Strategies to solve interface problems and stabilize interfaces in recent years are also discussed. Finally, a brief outlook about argyrodite SSEs is presented.

Keywords: argyrodite solid electrolyte, lithium metal anode, lithium dendrites, interface reaction, all-solid-state lithium batteries

Edited by:
Hongsen Li,
Qingdao University, China

Reviewed by:
Yongfu Tang,
Yanshan University, China
Guiyin Xu,
Massachusetts Institute of Technology, United States

****Correspondence:***
Yongping Gan
ganyp@zjut.edu.cn
Wenkui Zhang
msechem@zjut.edu.cn

Specialty section:
This article was submitted to Electrochemistry, a section of the journal Frontiers in Chemistry

Received: *17 December 2021*
Accepted: *03 January 2022*
Published: *01 February 2022*

Citation:
Pang B, Gan Y, Xia Y, Huang H, He X and Zhang W (2022) Regulation of the Interfaces Between Argyrodite Solid Electrolytes and Lithium Metal Anode. Front. Chem. 10:837978. doi: 10.3389/fchem.2022.837978

INTRODUCTION

With the large-scale use of electrification and the development of energy storage science and technology, there is an urgent demand for a new generation of energy storage materials with high energy density, high safety and long cycle life. Lithium metal has the advantages of high theoretical capacity, low potential and large reserves, has been attracting much attention. The advent of the liquid lithium-ion battery (LIB) has increased the utilization and storage of electrical energy as a result of its high energy density and long cycle life. However, traditional LIBs have safety issues such as leakage and thermal runaway caused by lithium dendrites piercing the liquid electrolyte. In order to solve the safety problem and improve the energy density of the battery, solid-state electrolyte (SSE) is proposed and researched intensively. Inorganic solid electrolytes can be divided into sulfide solid electrolytes, oxide solid electrolytes, halide solid electrolytes, and ect (Tang et al., 2018).

The sulfide solid electrolyte structure is derived from oxide by replacing the oxygen element by sulfur, which expands its original ion radius and thus making the lithium ion transport channel larger (Minami et al., 2000). Since the discovery of binary sulfide solid electrolyte systems Li_2S-GeS_5,

TABLE 1 | Summary of the performance of sulphide solid electrolytes.

Sulfide solid electrolytes	Material type	Conductivity (S cm^{-1})	Reference
$Li_7P_3S_{11}$	Glass–ceramic	5.2×10^{-3}	Minami et al. (2011)
$Li_7P_{2.9}S_{10.85}Mo_{0.01}$	Crystal	4.8×10^{-3}	Xu et al. (2017)
$Li_{10}GeP_2S_{12}$	Crystal	1.2×10^{-2}	Kamaya et al. (2011)
$Li_{10}SnP_2S_{12}$	Crystal	4×10^{-3}	Bron et al. (2013)
Li_6PS_5Cl	Crystal	1.33×10^{-3}	Boulineau et al. (2012)
Li_6PS_5Br	Crystal	2.58×10^{-3}	Yu et al. (2019)
$Li_6PS_5Cl_{0.25}Br_{0.75}$	Crystal	3.4×10^{-3}	Zhou et al. (2019b)
Li_6PS_5I (with excess Li_2S)	Crystal	1.5×10^{-5}	Ge et al. (2018)

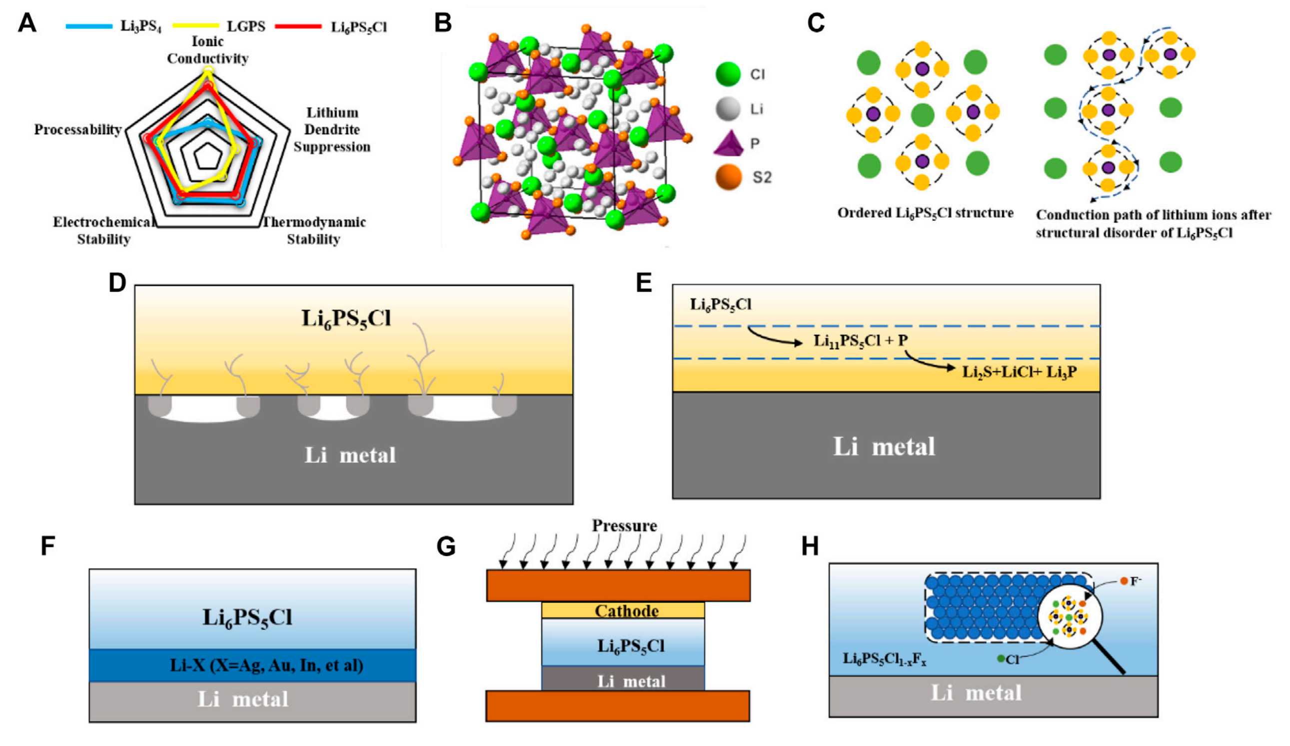

FIGURE 1 | **(A)** Crystal structures of argyrodite sulfide SSEs. **(B)** Conduction paths of lithium ions in argyrodite SSEs with different degrees of disorder. **(C)** Comparison of performance of three typical sulfide SSEs. **(D)** Schematic of lithium dendrite growth. **(E)** Schematic of interface reaction. **(F)** Schematic of alloy negative electrode. **(G)** Pressurization during battery cycling. **(H)** Schematic of doping using F instead of Cl element.

Li_2S-P_2S_5, Li_2S-B_2S_3 has been reported, the most studied glassy sulfide solid electrolyte is the Li_2S-P_2S_5 system (Mercier et al., 1981; Zhang and Kennedy, 1990; Kanno and Murayama, 2001; Zhang et al., 2019a; Zhang et al., 2020a). Glassy sulfide SSEs exhibits higher ionic conductivity than other sulfide SSEs because of the characteristics of intimate particle contact during the extrusion molding process and the eliminated grain boundary resistances (Janek and Zeier, 2016). In the xLi_2S-(100-x)P_2S_5 system, Li_3PS_4 (75Li_2S-25P_2S_5) (Tatsumisago et al., 2002), Li_7PS_6 (88 Li_2S-P_2S_5) (Kong et al., 2010), $Li_7P_3S_{11}$ (70Li_2S-30P_2S_5) (Yamane et al., 2007), and $Li_4P_2S_6$ (67Li_2S-33P_2S_5) (Mercier et al., 1982), exhibit relatively high ionic conductivity. In 1976, Goodenough's team (Goodenough et al., 1976) synthesized NASICON-type oxide solid-state electrolytes by high-temperature solid-phase development. On this basis, the researchers used lithium ions to replace sodium ions and introduced sulfur to synthesize Thio-lithium superionic conductor (Thio-LISICON). Among Thio-LISICONs, Kanno's team (Kamaya et al., 2011) reported $Li_{10}GeP_2S_{12}$ (LGPS) with the highest room temperature conductivity (12 mS cm^{-1}). The high conductivity of $Li_{10}GeP_2S_{12}$ can be attributed to the fact that the electrolyte has a two-dimensional lithium-ion transport channel in the ab plane of the cell and a one-dimensional fast lithium-ion transport channel in the c axis. Besides, a series of Thio-LISICON of $Li_{10\pm1}MP_2S_{12}$ (M = Si, Ge, Sn, Ga, Sb or P) was also developed. $Li_{10}SnP_2S_{12}$, as an isomer of LGPS, has gained widespread attention because of the high reserves of Sn elements and low cost (Bron et al., 2013), while ensuring its room temperature conductivity of 4×10^{-3} S cm^{-1}. In **Table 1** we have listed several sulfide solid electrolytes and described their properties.

Although LGPS has an ionic conductivity that compares favorably with that of liquid, but is limited in practical applications by side reactions with the lithium metal anode and narrow electrochemical window. While the LPS system is compatible with mainstream cathode and anode, its low ionic conductivity limits its development prospects. In recent years, argyrodite SSEs have received a lot of attention from researchers due to their high ionic conductivity and relatively stable crystal structure (Zhang et al., 2018). Compared with LGPS and LPS electrolytes, argyrodite SSEs has both high ionic conductivity and good interfacial compatibility (**Figure 1A**). However, argyrodite SSEs still has many aspects that need to been improved. Problems such as interfacial reactions and disordered growth of lithium dendrites can still occur in argyrodite SSEs and Li-metal anode. To implement argyrodite SSEs for practical applications, the problem at the interface must be solved. In this review, various problems at the interface between argyrodite SSEs and Li anode are comprehensively described, and the research strategies proposed to improve the interface in recent years are summarized. Finally, strategies for these interfacial problems and outlooks are prospected.

Inspired by the structure of argyrodite Ag_8GeS_6, Deiseroth's team (Deiseroth et al., 2008) has developed a Li_6PS_5X (X = Cl, Br or I) sulfide solid-state electrolyte. Structural studies have shown that Li_6PS_5X represents a series of argyrodites whose chemical formulae are based on the known substitution of a halogen atom for an Ag or Cu atom. The structure of Li_6PS_5X is a cubic crystal structure in which the S^{2-} anion is located in the tetrahedral gap at 16e, P at 4b, and the halogen group elements are located at the apex and face center of the cubic crystal structure. Besides, the structure has four individual S atoms at the 4C position surrounded by 18 Li^+ (**Figure 1B**). These Li^+ occupy these positions, and the other half are empty spaces through which Li+ may migrate in the structure (Kraft et al., 2017). In addition to the lithium-ion vacancies, the introduction of different halogen elements also has a great influence on the lithium-ion diffusion in argyrodite SSEs. The difference in conductivity among Li_6PS_5Cl (1.9×10^{-3} S cm^{-1}), Li_6PS_5Br (6.8×10^{-4} S cm^{-1}), and Li_6PS_5I (4.6×10^{-7} S cm^{-1}) depends on the degree of S-X disorder. Since the ionic radii of halogens Cl^-, Br^- are similar to S^{2-}, the introduction of Cl^-, Br^- has an obvious site-specific disorder. While I^- exhibits an ordered distribution with S^{2-} because of its larger ionic radius, which leads to the room temperature conductivity of Li_6PS_5I is not as high as the other. Baktash et al. (2020) found that increasing the S-Cl disorder can substantially increase the Li_6PS_5Cl ionic conductivity. Nazar et al. (Zhou et al., 2019a) further found that the activation energy barrier to reduce the mobility of lithium ions is the key to the disordered distribution of Li^+. In addition, their work shows that the use of other elements (Ge, Si, etc.) in partial substitution of phosphorus in addition to halogen atoms can also cause Li^+ site disorder. From the above research work, it can be found that anion disorder and the resulting lithium disorder is the key to achieve rapid diffusion of lithium ions (**Figure 1C**).

INTERFACES BETWEEN ARGYRODITE SOLID-STATE ELECTROLYTES AND LITHIUM-METAL ANODE

Although argyrodite SSEs have high ionic conductivity and relatively good stability at the interface with the anode. However, compared with conventional liquid electrolytes, argyrodite SSEs have ineligible interfacial problems with the anode. Interfacial problems are mainly divided into two aspects as following: one is the growth of lithium dendrites, and the other one is the interfacial reactions. In conventional liquid batteries, the lithium metal is well infiltrated by the liquid electrolyte, which helps to induce relatively smooth lithium deposition. The argyrodite SSEs will have a critical current density in the process of cycling with the lithium anode. When the current density is exceeded the critical current density during plating or stripping, dendritic lithium deposition will form and cause short circuit. When the current density of the stripped lithium exceeds its own rate of replenishment, the lithium metal forms voids at the interface and aggravate the uneven deposition of lithium. (Koerver et al., 2017; Manalastas et al., 2019) Bruce et al. (Kasemchainan et al., 2019) found that these voids will only be partially eliminated in the following cycles, and the remainder will gradually accumulate as the cycles increase. The accumulation of these voids reduces the contact area at the interface and increases the local current density, which eventually leads to the generation of lithium dendrites (**Figure 1D**). In further work, they also found a close relationship between the magnitude of the critical current density leading to lithium dendrite generation and pressure. When the applied pressure is greater than 0.81 MPa, the lithium metal is deformed plastically, and creep rather than diffusion of the lithium metal is the main mechanism for lithium transport to the interface. Ning et al. (2021) proposed that lithium dendrites are inextricably linked to cracks of SSEs generated during cycling. Studies using *in situ* X-ray computed tomography revealed that small cracks appear first at the edges of the electrolyte during lithium deposition. The current density is enhanced at the edges of these cracks, inducing the deposition of lithium (Tang et al., 2009). With more and more lithium depositions at the cracks, the original cracks show dendritic expansion. The formation of lithium dendrites has a great relationship with the local current density, so that the control of the local current density can inhibit the generation of lithium dendrites.

In addition to the lithium dendrite issue, the interfacial reactions induced by the thermodynamic instability between argyrodite SSEs and anode are also worth of attention. Juergen et al.(Wenzel et al., 2018) dopted X-ray photoelectron spectroscopy to confirm that Li_6PS_5X will decompose at interface due to the strong reduction of lithium. Some of the Li_6PS_5X decomposed on the surface of lithium metal to form solid electrolyte interphase (SEI) with the ingredient of decomposition products such as Li_3P, Li_2S and LiX (**Figure 1E**). The SEI leads to an increase in interfacial resistance and hinders the conduction of lithium ion. Further study by Wagemaker et al. (Schwietert et al., 2020) revealed that the thermodynamic decomposition reaction of argyrodite SSEs with the anode side is not instantaneous. Taking argyrodite Li_6PS_5Cl as an example, it was first reduced to the unstable $Li_{11}PS_5Cl$, and then $Li_{11}PS_5Cl$ was further reduced to Li_2S, LiCl and Li_3P. In this process, the generated intermediate phases such as S, Li_2S and LiCl not only produce a large volume expansion, but also leading to the destabilization of the kinetics. The continued decomposition of argyrodite SSEs at the interface as the cycle proceeds is the main reason for the increase in interfacial resistance. Our group (Zheng et al., 2021) used *in situ* Raman energy spectroscopy and *in situ* electrochemical impedance spectroscopy to find “self-healing” effect of Li_6PS_5Cl after decomposition. The Li_6PS_5Cl self-healing mechanism is mainly attributed to the reversible redox reaction that can be achieved by Li_6PS_5Cl and the consumption of the deposited lithium metal during the redox reaction. The discovery of the self-healing mechanism of argyrodite SSEs provides a new idea and theoretical basis to tackle interface problems.

STRATEGIES FOR THE INTERFACIAL ISSUES

Considering the complex interfacial problem between argyrodite SSEs and Li-metal anode, strategies were proposed from different perspectives. The researchers firstly proposed using an alloy to react with the lithium anode or building a suitable 3D collector to solve the interfacial problem of lithium dendrite. Secondly, the argyrodite SSEs are doped with different elements to artificially construct SEI during the contact with the lithium anode, or to make the argyrodite SSEs flexible or three-dimensional structure to suppress the interfacial reaction.

Alloyed Anode and 3D Current Collectors

Lithium metal has been a popular anode material because of its high specific capacity and the lowest redox potential. However, in practical applications, the generation of lithium dendrites at the interface has hindered its practical application and development. The method of synthesizing alloy anode by lithium and alloy can effectively regulate the growth of lithium dendrites and induce the uniform deposition of lithium during the cycling process. By studying the nucleation mechanism of lithium on different metals, Cui et al. (Yan et al., 2016) found that lithium is deposited on different metals with different overpotentials. The selection of different alloy substrates can be used to tune the lithium metal deposition. Wang et al. (Zhang et al., 2021) concluded from the binary phase diagram to explain that lithium exhibits good structural stability during alloying with silver and can form lithium-silver alloys in different ratios. After cycling to lithium stripping, the de-lithiumed porous silver particles can be used as a carrier material to induce the next lithium deposition. While gold and lithium form a lithium-saturated material with limited ability to retain lithium and cannot regulate the deposition of excess lithium, leading to structural instability. Based on the above study, silver is an excellent alloy conductor, which can form various types of lithium-silver solid solutions with lithium continuously and regulating the deposition of lithium. Therefore, Kim et al. (Choi et al., 2022) proposed a Ag-Li alloy anode could be made in large quantities by roll pressing (**Figure 1F**). In contrast to previous reports, *in situ* formation of silver-rich silver-lithium intermetallic compounds can induce uniform deposition of lithium after simple roll aging. The Ag-Li spacer can play a role in inducing a uniform deposition of lithium during the cycling process, rather than concentrating on one spot, thus maintaining a more stable SE/Ag-Li interface. By adding a layer of Ag-Li between the lithium anode and Li_6PS_5Cl, normal cycling at very high current density (12C) was achieved and the growth of lithium dendrites was well suppressed. In addition to the use of alloy anode, lithium-free graphite can also inhibit the growth of lithium dendrites due to its inherent 3D structure. Han et al. (Lee et al., 2020) designed an Ag-C anode that achieves 1000 cycles at high energy density with a Coulombic efficiency of more than 99.8%. Using Ag-C composite anode, the problems of low energy density and cycle life of conventional argyrodite batteries are well solved by the regulation of lithium dendrites of Ag and the 3D structure of graphite to accommodate the volume expansion. Li et al. (Ye and Li, 2021) constructed a sandwich structure of LPSCl-LGPS-LPSCl to overcome the instability between LGPS and Li. The “expansion screw effect” of the LGPS decomposition is used to fill the empty space created by the decomposition of the LPSCL. This property can inhibit the growth of lithium dendrites.

In addition to the widespread use of silver and lithium to form lithium-silver alloys to regulate the growth of lithium dendrites, other alloying elements also have their advantages in regulating lithium dendrites. Zhang et al. (Luo et al., 2021) took advantage of the inherent good deformability of the Li-In alloy to assemble the cell under high pressure to make a tighter fit between the electrolyte and the negative electrode of the alloy (**Figure 1H**). The close contact between the electrolyte and the anode eliminates the voids at the interface and suppresses the generation of lithium dendrites. Hayashi et al. (Kato et al., 2018) took advantage of the fact that Au can form a lithium-gold alloy with lithium to add a layer of gold foil between the electrolyte and the lithium anode, increasing the sites for lithium deposition, while the resulting lithium-gold alloy can fill the gap formed after the lithium is stripped well. Due to the greater binding energy with lithium than the electrolyte, alloying elements will preferentially combine with lithium metal to form Li-alloy anode, thereby leading to uniform deposition of lithium and avoiding lithium dendrite generation.

Modification of the Argyrodite Solid-State Electrolytes

In addition to the formation of lithium dendrites due to the inhomogeneous deposition of lithium, another serious interfacial problem between lithium metal anode and argyrodite SSEs is the interfacial reaction (Xu et al., 2018a; Zhang et al., 2019b). Due to the high reduction of lithium metal anode, argyrodite SSEs easily reduced by lithium metal at the interface and decomposed into intermediate phases such as Li_2S, Li_3P. The passivation layer composed of these intermediate phases will increase the interfacial impedance as the battery cycle progresses, resulting in degradation of the battery performance. It has been previously reported (Xu et al., 2018b)' (Fan et al., 2018) that pretreatment of lithium metal surfaces with chemicals containing I or F can effectively reduce interfacial resistance and inhibit interfacial reactions (Zhang et al., 2020b). In order to improve the stability of the lithium metal anode/argyrodite interface, Sun et al. (Zhao et al., 2020) proposed the fluorination of Li_6LP_5Cl. The fluorinated $LPSCl_{0.3}F_{0.7}$ electrolyte was synthesized by introducing the element F into the Li_6LP_5Cl electrolyte using a solid-state synthesis method. During the cycling process, a dense and well-conducting LiF is *in situ* generated at the interface between $LPSCl_{0.3}F_{0.7}$ and lithium metal (**Figure 1H**). The sheet-like LiF prevents the contact between the electrolyte and the lithium metal, thus inhibiting the interfacial reactions. Tu et al. (Liu et al., 2021) synthesized LPSNCl by solid-phase method using partial substitution of N atoms for S atoms and discovered that the tetrahedral position occupied by N atoms in the crystal could make the crystal structure more stable. During the cycling process, the electrolyte generates a LiN-rich SEI layer *in situ* on the surface of the lithium anode, successfully curbing the continual occurrence of interfacial reactions. Apart from doping of other elements to induce the *in situ* generation of SEI to suppress the interfacial reaction, the construction of three-dimensional and flexible electrolytes can also contain the interfacial reaction. Zhu et al. (Cao et al., 2021) synthesized flexible and highly ion-conductive electrolyte films using ethylcellulose and LPSCl. The electrolyte film can fully contact with the lithium metal anode, inhibit the growth of lithium dendrites under high pressure, and its own excellent thermal stability can inhibit the decomposition of the electrolyte film during cycling. Cui et al. (Wang et al., 2021) synthesized a three-dimensional porous LPSCl skeleton using SeS_2 as pore-forming agent, which reduced the problem of poor solid-solid contact between electrolyte and anode by means of *in situ* polymerization and greatly reduced the interfacial resistance.

SUMMARY AND OUTLOOK

Argyrodite SSEs are attracting more and more attention because of their high ionic conductivity and their self-healing mechanism when reacting with lithium metal anode. Nevertheless, the complex interface problems between argyrodite SSEs and lithium metal anode limit their practical use. Growth of lithium dendrites due to excessive local current density from voids created during lithium stripping/deposition when matched with argyrodite SSEs. Because of the strong reduction of lithium, the increasing interfacial resistance due to the continuous decomposition of argyrodite SSEs at the Li-metal anode interface is another interface problem which limits the practical application of argyrodite SSEs. In response to these obvious interface problems, a number of solutions have been proposed. The construction of the alloy anode can effectively guide the uniform deposition of lithium, thus reducing the growth of lithium dendrites due to uneven deposition during lithium stripping. Elemental doping of argyrodite SSEs allows the electrolyte to generate a dense SEI film *in situ* with the lithium metal anode during cycling, which can inhibit the continual occurrence of interfacial reactions. Although many interface issues still need to be resolved, the future of argyrodite batteries is still worthy of anticipation. We present our outlook on interface issues from the following perspectives.

1) Mechanism of interfacial lithium deposition need to be furtherly explored. Although a large amount of work has been done to summarize the mechanism of lithium ion transport at the interface. The issues such as the preferred sites for lithium deposition during deposition, the connection between the voids created by exfoliation and the deposition sites, still lack in-depth studies. We expect to use more three-dimensional and clearer characterization tools to characterize the whole process of lithium dendrite growth. Combining these characterization tools with the study of interfacial mechanisms will lead to more specific solutions.
2) Development of novel argyrodite SSEs. For argyrodite SSEs, the behavior of spontaneous decomposition during contact with lithium metal limits their use. The application of various elemental covalently generates a dense SEI layer *in situ* to suppress the interfacial reaction while maintaining the ionic conductivity.

AUTHOR CONTRIBUTIONS

YG and WZ contributed to conception of this mini review. BP wrote the first draft of the manuscript. YG, YX, HH, and XH wrote sections of the manuscript. All authors contributed to manuscript revision, read, and approved the submitted version.

FUNDING

The authors would like to thank the financial support by the National Natural Science Foundation of China (No. U20A20253 and 21972127), the Natural Science Foundation of Zhejiang Province (No. LY21E020005), and Zhejiang Provincial Special Support Program for High-level Talents (No. 2020R51004).

REFERENCES

Baktash, A., Reid, J. C., Roman, T., and Searles, D. J. (2020). Diffusion of Lithium Ions in Lithium-Argyrodite Solid-State Electrolytes. *Npj Comput. Mater.* 6 (1), 162. doi:10.1038/s41524-020-00432-1

Boulineau, S., Courty, M., Tarascon, J.-M., and Viallet, V. (2012). Mechanochemical Synthesis of Li-Argyrodite Li6PS5X (X=Cl, Br, I) as Sulfur-Based Solid Electrolytes for All Solid State Batteries Application. *Solid State Ionics* 221, 1–5. doi:10.1016/j.ssi.2012.06.008

Bron, P., Johansson, S., Zick, K., Dehnen, S., Schmedt auf der Günne, J., and Roling, B. (2013). Li10SnP2S12: An Affordable Lithium Superionic Conductor. *J. Am. Chem. Soc.* 135 (42), 15694–15697. doi:10.1021/ja407393y

Cao, D., Li, Q., Sun, X., Wang, Y., Zhao, X., Cakmak, E., et al. (2021). Amphipathic Binder Integrating Ultrathin and Highly Ion-Conductive Sulfide Membrane for Cell-Level High-Energy-Density All-Solid-State Batteries. *Adv. Mater.* 33 (52), 2105505. doi:10.1002/adma.202105505

Choi, H. J., Kang, D. W., Park, J.-W., Park, J.-H., Lee, Y.-J., Ha, Y.-C., et al. (2022). *In Situ* Formed Ag-Li Intermetallic Layer for Stable Cycling of All-Solid-State Lithium Batteries. *Adv. Sci.* 2022 (9), 2103826. doi:10.1002/advs.202103826

Deiseroth, H.-J., Kong, S.-T., Eckert, H., Vannahme, J., Reiner, C., Zaiß, T., et al. (2008). Li6PS5X: A Class of Crystalline Li-Rich Solids with an Unusually High Li+ Mobility. *Angew. Chem. Int. Ed.* 47 (4), 755–758. doi:10.1002/anie.200703900

Fan, X., Ji, X., Han, F., Yue, J., Chen, J., Chen, L., et al. (2018). Fluorinated Solid Electrolyte Interphase Enables Highly Reversible Solid-State Li Metal Battery. *Sci. Adv.* 4 (12), eaau9245. doi:10.1126/sciadv.aau9245

Ge, Q., Zhou, L., Lian, Y.-m., Zhang, X., Chen, R., and Yang, W. (2018). Metal-phosphide-doped Li7P3S11 Glass-Ceramic Electrolyte with High Ionic Conductivity for All-Solid-State Lithium-Sulfur Batteries. *Electrochemistry Commun.* 97, 100–104. doi:10.1016/j.elecom.2018.10.024

Goodenough, J. B., Hong, H. Y.-P., and Kafalas, J. A. (1976). Fast Na+-Ion Transport in Skeleton Structures. *Mater. Res. Bull.* 11 (2), 203–220. doi:10.1016/0025-5408(76)90077-5

Janek, J., and Zeier, W. G. (2016). A Solid Future for Battery Development. *Nat. Energ.* 1 (9), 16141. doi:10.1038/nenergy.2016.141

Kamaya, N., Homma, K., Yamakawa, Y., Hirayama, M., Kanno, R., Yonemura, M., et al. (2011). A Lithium Superionic Conductor. *Nat. Mater* 10 (9), 682–686. doi:10.1038/nmat3066

Kanno, R., and Murayama, M. (2001). Lithium Ionic Conductor Thio-LISICON: The Li 2S-GeS 2-P 2S 5 System. *J. Electrochem. Soc. - J ELECTROCHEM SOC* 148. 1379028. doi:10.1149/1.1379028

Kasemchainan, J., Zekoll, S., Spencer Jolly, D., Ning, Z., Hartley, G. O., Marrow, J., et al. (2019). Critical Stripping Current Leads to Dendrite Formation on Plating in Lithium Anode Solid Electrolyte Cells. *Nat. Mater.* 18 (10), 1105–1111. doi:10.1038/s41563-019-0438-9

Kato, A., Kowada, H., Deguchi, M., Hotehama, C., Hayashi, A., and Tatsumisago, M. (2018). XPS and SEM Analysis between Li/Li3PS4 Interface with Au Thin Film for All-Solid-State Lithium Batteries. *Solid State Ionics* 322, 1–4. doi:10.1016/j.ssi.2018.04.011

Koerver, R., Dursun, I., Leichtwei?, T., Dietrich, C., Zhang, W., Binder, J., et al. (2017). Capacity Fade in Solid-State Batteries: Interphase Formation and Chemomechanical Processes in Nickel-Rich Layered Oxide Cathodes and Lithium Thiophosphate Solid Electrolytes. *Chem. Mater.* 29 (13), 5574–5582. doi:10.1021/acs.chemmater.7b00931

Kong, S. T., Gün, Ö., Koch, B., Deiseroth, H. J., Eckert, H., and Reiner, C. (2010). Structural Characterisation of the Li Argyrodites Li7PS6 and Li7PSe6 and Their Solid Solutions: Quantification of Site Preferences by MAS-NMR Spectroscopy. *Chem. Eur. J.* 16 (17), 5138–5147. doi:10.1002/chem.200903023

Kraft, M. A., Culver, S. P., Calderon, M., Böcher, F., Krauskopf, T., Senyshyn, A., et al. (2017). Influence of Lattice Polarizability on the Ionic Conductivity in the Lithium Superionic Argyrodites Li6PS5X (X = Cl, Br, I). *J. Am. Chem. Soc.* 139 (31), 10909–10918. doi:10.1021/jacs.7b06327

Lee, Y.-G., Fujiki, S., Jung, C., Suzuki, N., Yashiro, N., Omoda, R., et al. (2020). High-energy Long-Cycling All-Solid-State Lithium Metal Batteries Enabled by Silver-Carbon Composite Anodes. *Nat. Energ.* 5 (4), 299–308. doi:10.1038/s41560-020-0575-z

Liu, Y., Su, H., Li, M., Xiang, J., Wu, X., Zhong, Y., et al. (2021). *In Situ* formation of a Li3N-Rich Interface between Lithium and Argyrodite Solid Electrolyte Enabled by Nitrogen Doping. *J. Mater. Chem. A.* 9 (23), 13531–13539. doi:10.1039/d1ta03343c

Luo, S., Wang, Z., Li, X., Liu, X., Wang, H., Ma, W., et al. (2021). Growth of Lithium-Indium Dendrites in All-Solid-State Lithium-Based Batteries with Sulfide Electrolytes. *Nat. Commun.* 12 (1), 6968. doi:10.1038/s41467-021-27311-7

Manalastas, W., Jr, Rikarte, J., Chater, R. J., Brugge, R., Aguadero, A., Buannic, L., et al. (2019). Mechanical Failure of Garnet Electrolytes during Li Electrodeposition Observed by In-Operando Microscopy. *J. Power Sourc.* 412 (FEB.1), 287–293. doi:10.1016/j.jpowsour.2018.11.041

Mercier, R., Malugani, J.-P., Fahys, B., and Robert, G. (1981). Superionic Conduction in Li 2 S - P 2 S 5 - LiI - Glasses. *Solid State Ionics* 5, 663–666. doi:10.1016/0167-2738(81)90341-6

Mercier, R., Malugani, J. P., Fahys, B., Douglande, J., and Robert, G. (1982). Synthese, structure cristalline et analyse vibrationnelle de l'hexathiohypodiphosphate de lithium Li4P2S6. *J. Solid State. Chem.* 43 (2), 151–162. doi:10.1016/0022-4596(82)90224-9

Minami, T., Hayashi, A., and Tatsumisago, M. (2000). Preparation and Characterization of Lithium Ion-Conducting Oxysulfide Glasses. *Solid State Ionics* 136-137, 1015–1023. doi:10.1016/s0167-2738(00)00555-5

Minami, K., Hayashi, A., and Tatsumisago, M. (2011). Crystallization Process for Superionic Li7P3S11 Glass-Ceramic Electrolytes. *J. Am. Ceram. Soc.* 94 (6), 1779–1783. doi:10.1111/j.1551-2916.2010.04335.x

Ning, Z., Jolly, D. S., Li, G., De Meyere, R., Pu, S. D., Chen, Y., et al. (2021). Visualizing Plating-Induced Cracking in Lithium-Anode Solid-Electrolyte Cells. *Nat. Mater.* 20 (8), 1121–1129. doi:10.1038/s41563-021-00967-8

Schwietert, T. K., Arszelewska, V. A., Wang, C., Yu, C., Vasileiadis, A., de Klerk, N. J. J., et al. (2020). Clarifying the Relationship between Redox Activity and Electrochemical Stability in Solid Electrolytes. *Nat. Mater.* 19 (4), 428–435. doi:10.1038/s41563-019-0576-0

Tang, M., Albertus, P., and Newman, J. (2009). Two-Dimensional Modeling of Lithium Deposition during Cell Charging. *J. Electrochem. Soc.* 156 (5), A390. doi:10.1149/1.3095513

Tang, H., Deng, Z., Lin, Z., Wang, Z., Chu, I.-H., Chen, C., et al. (2018). Probing Solid-Solid Interfacial Reactions in All-Solid-State Sodium-Ion Batteries with First-Principles Calculations. *Chem. Mater.* 30 (1), 163–173. doi:10.1021/acs.chemmater.7b04096

Tatsumisago, M., Hama, S., Hayashi, A., Morimoto, H., Minami, T., and Ionics, T. J. S. S. (2002). New Lithium Ion Conducting Glass-Ceramics Prepared from Mechanochemical Li2S–P2s5 Glasses. *Solid State Ionics* 154, 635–640. doi:10.1016/S0167-2738(02)00509-X

Wang, Y., Ju, J., Dong, S., Yan, Y., Jiang, F., Cui, L., et al. (2021). Facile Design of Sulfide-Based All Solid-State Lithium Metal Battery: *In Situ* Polymerization within Self-Supported Porous Argyrodite Skeleton. *Adv. Funct. Mater.* 31, 2101523. doi:10.1002/adfm.202101523

Wenzel, S., Sedlmaier, S. J., Dietrich, C., Zeier, W. G., and Janek, J. (2018). Interfacial Reactivity and Interphase Growth of Argyrodite Solid Electrolytes at Lithium Metal Electrodes. *Solid State Ionics* 318, 102–112. doi:10.1016/j.ssi.2017.07.005

Xu, R.-c., Xia, X.-h., Wang, X.-l., Xia, Y., and Tu, J.-p. (2017). Tailored Li2S-P2S5glass-Ceramic Electrolyte by MoS2doping, Possessing High Ionic Conductivity for All-Solid-State Lithium-Sulfur Batteries. *J. Mater. Chem. A.* 5 (6), 2829–2834. doi:10.1039/c6ta10142a

Xu, L., Tang, S., Cheng, Y., Wang, K., Liang, J., Liu, C., et al. (2018). Interfaces in Solid-State Lithium Batteries. *Joule* 2 (10), 1991–2015. doi:10.1016/j.joule.2018.07.009

Xu, R., Han, F., Ji, X., Fan, X., Tu, J., and Wang, C. (2018). Interface Engineering of Sulfide Electrolytes for All-Solid-State Lithium Batteries. *Nano Energy* 53, 958–966. doi:10.1016/j.nanoen.2018.09.061

Yamane, H., Shibata, M., Shimane, Y., Junke, T., Seino, Y., Adams, S., et al. (2007). Crystal Structure of a Superionic Conductor, Li7P3S11. *Solid State Ionics* 178 (15), 1163–1167. doi:10.1016/j.ssi.2007.05.020

Yan, K., Lu, Z., Lee, H.-W., Xiong, F., Hsu, P.-C., Li, Y., et al. (2016). Selective Deposition and Stable Encapsulation of Lithium through Heterogeneous Seeded Growth. *Nat. Energ.* 1 (3), 16010. doi:10.1038/nenergy.2016.10

Ye, L., and Li, X. (2021). A Dynamic Stability Design Strategy for Lithium Metal Solid State Batteries. *Nature* 593 (7858), 218–222. doi:10.1038/s41586-021-03486-3

Yu, C., Hageman, J., Ganapathy, S., van Eijck, L., Zhang, L., Adair, K. R., et al. (2019). Tailoring Li6PS5Br Ionic Conductivity and Understanding of its Role in Cathode Mixtures for High Performance All-Solid-State Li-S Batteries. *J. Mater. Chem. A.* 7 (17), 10412–10421. doi:10.1039/c9ta02126d

Zhang, Z., and Kennedy, J. H. (1990). Synthesis and Characterization of the B2S3Li2S, the P2S5Li2S and the B2S3P2S5Li2S Glass Systems. *Solid State Ionics* 38 (3), 217–224. doi:10.1016/0167-2738(90)90424-p

Zhang, J., Zhong, H., Zheng, C., Xia, Y., Liang, C., Huang, H., et al. (2018). All-solid-state Batteries with Slurry Coated LiNi0.8Co0.1Mn0.1O2 Composite Cathode and Li6PS5Cl Electrolyte: Effect of Binder Content. *J. Power Sourc.* 391 (JUL.1), 73–79. doi:10.1016/j.jpowsour.2018.04.069

Zhang, J., Zheng, C., Lou, J., Xia, Y., Liang, C., Huang, H., et al. (2019). Poly(ethylene Oxide) Reinforced Li6PS5Cl Composite Solid Electrolyte for All-Solid-State Lithium Battery: Enhanced Electrochemical Performance, Mechanical Property and Interfacial Stability. *J. Power Sourc.* 412, 78–85. doi:10.1016/j.jpowsour.2018.11.036

Zhang, Q., Cao, D., Ma, Y., Natan, A., Aurora, P., and Zhu, H. (2019). Sulfide-Based Solid-State Electrolytes: Synthesis, Stability, and Potential for All-Solid-State Batteries. *Adv. Mater.* 31 (44), 1901131. doi:10.1002/adma.201901131

Zhang, J., Zheng, C., Li, L., Xia, Y., Huang, H., Gan, Y., et al. (2020). Unraveling the Intra and Intercycle Interfacial Evolution of Li 6 PS 5 Cl-Based All-Solid-State Lithium Batteries. *Adv. Energ. Mater.* 10 (4), 1903311. doi:10.1002/aenm.201903311

Zhang, J., Li, L., Zheng, C., Xia, Y., Gan, Y., Huang, H., et al. (2020). Silicon-Doped Argyrodite Solid Electrolyte Li6PS5I with Improved Ionic Conductivity and Interfacial Compatibility for High-Performance All-Solid-State Lithium Batteries. *ACS Appl. Mater. Inter.* 12 (37), 41538–41545. doi:10.1021/acsami.0c11683

Zhang, S., Yang, G., Liu, Z., Weng, S., Li, X., Wang, X., et al. (2021). Phase Diagram Determined Lithium Plating/Stripping Behaviors on Lithiophilic Substrates. *ACS Energ. Lett.* 6 (11), 4118–4126. doi:10.1021/acsenergylett.1c02127

Zhao, F., Sun, Q., Yu, C., Zhang, S., Adair, K., Wang, S., et al. (2020). Ultrastable Anode Interface Achieved by Fluorinating Electrolytes for All-Solid-State Li Metal Batteries. *ACS Energ. Lett.* 5 (4), 1035–1043. doi:10.1021/acsenergylett.0c00207

Zheng, C., Zhang, J., Xia, Y., Huang, H., Gan, Y., Liang, C., et al. (2021). Unprecedented Self-Healing Effect of Li 6 PS 5 Cl-Based All-Solid-State Lithium Battery. *Small* 17 (37), 2101326. doi:10.1002/smll.202101326

Zhou, L., Assoud, A., Zhang, Q., Wu, X., and Nazar, L. F. (2019). New Family of Argyrodite Thioantimonate Lithium Superionic Conductors. *J. Am. Chem. Soc.* 141 (48), 19002–19013. doi:10.1021/jacs.9b08357

Zhou, L., Park, K.-H., Sun, X., Lalère, F., Adermann, T., Hartmann, P., et al. (2019). Solvent-Engineered Design of Argyrodite Li6PS5X (X = Cl, Br, I) Solid Electrolytes with High Ionic Conductivity. *ACS Energ. Lett.* 4 (1), 265–270. doi:10.1021/acsenergylett.8b01997

Conflict of Interest: The authors declare that the research was conducted in the absence of any commercial or financial relationships that could be construed as a potential conflict of interest.

ORIGINAL RESEARCH
published: 02 February 2022
doi: 10.3389/fchem.2021.834418

Architecting Hierarchical WO_3 Agglomerates Assembled With Straight and Parallel Aligned Nanoribbons Enabling High Capacity and Robust Stability of Lithium Storage

Xiaotong Dong[1], Yongshuai Liu[1], Shikai Zhu[1], Yike Ou[1], Xiaoyu Zhang[1], Wenhao Lan[1], Haotian Guo[2], Cunliang Zhang[2]*, Zhaoguo Liu[1], Shuai Ju[1], Yuan Miao[1], Yongcheng Zhang[1]* and Hongsen Li[1]*

[1]Center for Marine Observation and Communications, College of Physics, Qingdao University, Qingdao, China, [2]School of Chemistry and Chemical Engineering, Henan Engineering Center of New Energy Battery Materials, Henan Key Laboratory of Bimolecular Reorganization and Sensing, Shangqiu Normal University, Shangqiu, China

Edited by:
Xifei Li,
Xi'an University of Technology, China

Reviewed by:
Ya You,
Wuhan University of Technology, China
Xianhong Rui,
Guangdong University of Technology, China

***Correspondence:**
Hongsen Li
hsli@qdu.edu.cn
Yongcheng Zhang
qdzhyc@163.com
Cunliang Zhang
zcliang@126.com

Specialty section:
This article was submitted to Electrochemistry, a section of the journal Frontiers in Chemistry

Received: 13 December 2021
Accepted: 27 December 2021
Published: 02 February 2022

Citation:
Dong X, Liu Y, Zhu S, Ou Y, Zhang X, Lan W, Guo H, Zhang C, Liu Z, Ju S, Miao Y, Zhang Y and Li H (2022) Architecting Hierarchical WO_3 Agglomerates Assembled With Straight and Parallel Aligned Nanoribbons Enabling High Capacity and Robust Stability of Lithium Storage. Front. Chem. 9:834418. doi: 10.3389/fchem.2021.834418

The pursuit of electrochemical energy storage has led to a pressing need on materials with high capacities and energy densities; however, further progress is plagued by the restrictive capacity (372 mAh g^{-1}) of conventional graphite materials. Tungsten trioxide (WO_3)-based anodes feature high theoretical capacity (693 mAh g^{-1}), suitable potential, and affordable cost, arousing ever-increasing attention and intense efforts. Nonetheless, developing high-performance WO_3 electrodes that accommodate lithium ions remains a daunting challenge on account of sluggish kinetics characteristics and large volume strain. Herein, the well-designed hierarchical WO_3 agglomerates assembled with straight and parallel aligned nanoribbons are fabricated and evaluated as an anode of lithium-ion batteries (LIBs), which exhibits an ultra-high capacity and excellent rate capability. At a current density of 1,000 mA g^{-1}, a reversible capacity as high as 522.7 mAh g^{-1} can be maintained after 800 cycles, corresponding to a high capacity retention of ~80%, demonstrating an exceptional long-durability cyclic performance. Furthermore, the mechanistic studies on the lithium storage processes of WO_3 are probed, providing a foundation for further optimizations and rational designs. These results indicate that the well-designed hierarchical WO_3 agglomerates display great potential for applications in the field of high-performance LIBs.

Keywords: WO_3, hierarchical structure, nanoribbons, lithium-ion batteries, high performances

INTRODUCTION

The commercialization of electrochemical energy storage (EES) systems, especially lithium-ion batteries (LIBs), has brought revolutionary changes in the industrial structure of energy storage (Abakumov et al., 2020; Liu L. et al., 2020; Eum et al., 2020; Gao et al., 2020). However, in spite of the mature technology of LIBs, which undergoes uncasting optimization for decades, the LIB systems are still seriously bottlenecked by conventional graphite materials on account of their low theoretical capacities, thus severely restricting the overall energy density of EES devices (Zhang and Qi, 2016; Qu et al., 2019). In this respect, considerable efforts were devoted to design and exploit novel alternative anode materials with larger reversible capacity and energy density (Li H. et al., 2021; Li Q. et al., 2021; Yue et al., 2022). As a renowned part of the potential electrode material family, tungsten trioxide (WO_3) has attracted tremendous attention due to its excellent chemical stability, high theoretical capacity (693 mAh g^{-1}), and low cost (Yao et al., 2017; Bekarevich et al., 2020).

Although WO_3 has been widely investigated as hosts for energy storage, the applications of WO_3 in LIBs are still hindered by its intrinsic inferior conductivity and large volume strain, resulting in poor rate capabilities, sluggish kinetics, and rapid capacity fading in practical applications, thus seriously inhibiting its further development (Sasidharan et al., 2012; Yoon et al., 2014; Bekarevich et al., 2020; Xiao Y. et al., 2021; Rastgoo-Deylami et al., 2021; Hou et al., 2022). To conquer the obstacles above, various strategies have been approached in recent reports, in which the well-known examples of one-dimension (1D) structure offered the natural starting point (Luo et al., 2021). 1D single crystal WO_3 nanowires fabricated by Gu et al. delivered a discharge capacity of 218 mAh g^{-1} for the first cycle under a current of 50 mA g^{-1}, and a capacity retention of 75.2% after 50 cycles, which can be largely attributed to the robust structural stability given by the 1D structure (Gu et al., 2007; Huang et al., 2020; Li et al., 2020). On the other hand, hierarchical structures have demonstrated their favorable Li-ion storage properties (Zhao et al., 2019; Liang et al., 2022). Duan et al. prepared biconical hexagonal (h-WO_3) mesocrystals by an ionic liquid-assisted hydrothermal route; the specific capacity of h-WO_3 mesocrystals can be maintained at 426 mAh g^{-1} at 50 mA g^{-1} after 50 cycles, benefiting from its inherent uniform porosity associated with well-defined nanoparticle orientation (Duan et al., 2015; Liu C. et al., 2020). However, noticeable capacity degradation was observed (1,379 mAh g^{-1} for initial discharge and 30.9% capacity retention on 50th cycle). Beyond these, vacancy engineering (Tu et al., 2018; Li et al., 2019) or developing hybridization of WO_3 with conductive carbon-based materials (Yu et al., 2013; Di et al., 2019; Lee et al., 2021) have also been used to lower the bandgap and diffusion barriers, but the capacity retention is still limited during prolonged cycling. In this respect, despite these attempts, it remains an enormous challenge to improve the specific capacity and cyclic stability concurrently to satisfy future large-scale commercial applications (Xiao Z. et al., 2021; Du et al., 2021).

In light of the above consideration, herein, the well-designed WO_3 agglomerates assembled with straight and parallel aligned nanoribbons are prepared *via* a one-step hydrothermal method for high-performance LIBs. Benefiting from the unique hierarchical structure of WO_3 agglomerates with high electrode–electrolyte contact area, short Li-ion pathway, and good strain accommodation, the electrode exhibits dramatically enhanced Li-ion storage properties in cyclic stability, specific capacity concurrently, along with a high capacity retention of ~80% (661.5 mAh g^{-1} for initial discharge and 522.7 mAh g^{-1} after 800 cycles at 1,000 mA g^{-1}), remarkably higher than those of the state-of-the-art WO_3-based anodes. Moreover, kinetics analysis and Li-ion diffusion chemistry of the hierarchical WO_3 agglomerates are investigated, providing a deeper insight into the mechanical origins of the improvement on Li-ion storage properties. These intriguing findings showcase the intrinsic desirable Li-ion storage performance of the hierarchical WO_3 agglomerates and open new opportunities for the applications of high-performance LIBs by informing more rational designs.

EXPERIMENTAL SECTION

Synthesis of Hierarchical WO_3 Agglomerates

All the chemicals were used as received without further purifications. In a typical synthesis of hierarchical WO_3 agglomerates, 0.3 g of $(NH_4)_{10}W_{12}O_{41}\cdot xH_2O$ and 0.2 g of $C_2H_2O_4\cdot 2H_2O$ dispersed in 30 ml of deionized water. After stirring for 30 min, the homogeneous solution was transferred into a 60-ml Teflon-lined autoclave and hydrothermal reaction proceeded at 180°C for 8 h in an electric oven. After cooling to room temperature, the obtained products were washed sequentially with deionized water and ethanol for three times, and they were finally dried overnight at 60°C. For comparison, pure WO_3 with different morphologies were synthesized *via* the same route except that the hydrothermal time was set as 4 and 12 h, respectively.

Material Characterization

The phase purity of the products was detected by powder X-ray diffraction (XRD, Bruker D8 Advance, Germany) with a Cu Kα radiation. X-ray photoelectron spectroscopy (XPS) measurements were performed by an ESCALAB250Xi system using a monochromatic Al Ka1 source. The surface morphology of materials was explored by field-emission scanning electron microscopy (FESEM, ZEISS, Sigma-300) and transmission electron microscopy (TEM, JEOL, JEM-2100F).

Electrochemical Measurement

The working electrode slurries were obtained by mixing the active materials, Super P, and carboxyl methyl cellulose (CMC) (weight ratio = 7:2:1) in deionized water. The obtained slurries were coated on the copper foil; 1 M solution of $LiPF_6$ in ethylene carbonate (EC)/dimethyl carbonate (DMC)/diethyl carbonate (DEC) with a volume ratio of 1:1:1 was employed as the electrolyte, and the Celgard 2,250 film (Whatman) was selected as separator. The galvanostatic discharge–charge measurements were performed on a multichannel battery tester (LAND-CT2001A). The cyclic voltammetry (CV) and electrochemical impedance spectroscopic (EIS) curves were conducted on an electrochemical workstation (IVIUM technologies, Vertex).

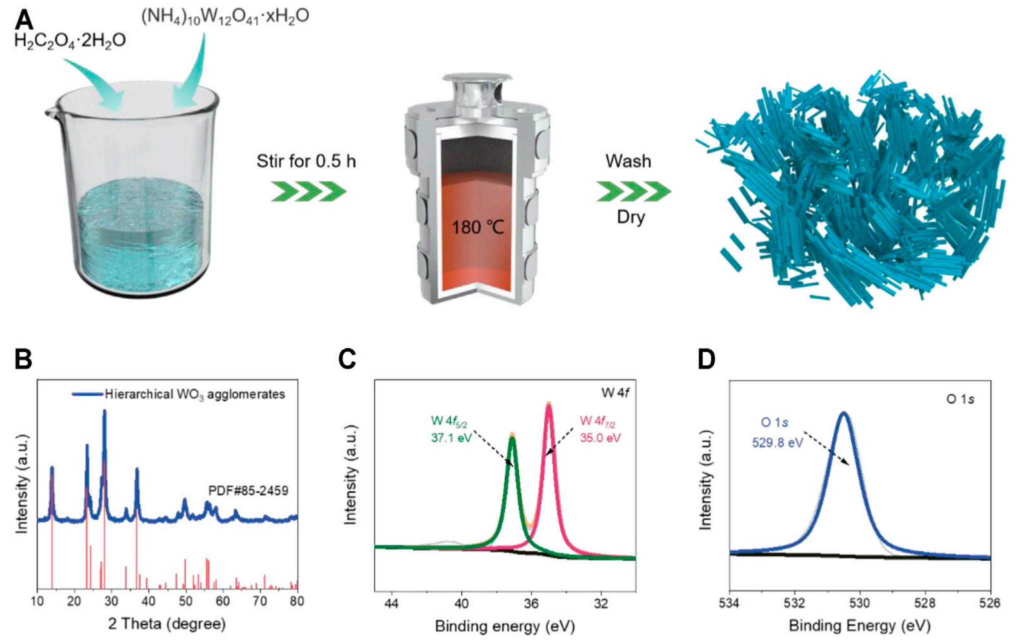

FIGURE 1 | (A) Synthetic route of the prepared WO_3 product. **(B)** The XRD patterns of the hierarchical WO_3 agglomerates. **(C)** W 4*f* spectra and **(D)** O 1*s* spectra of the hierarchical WO_3 agglomerates.

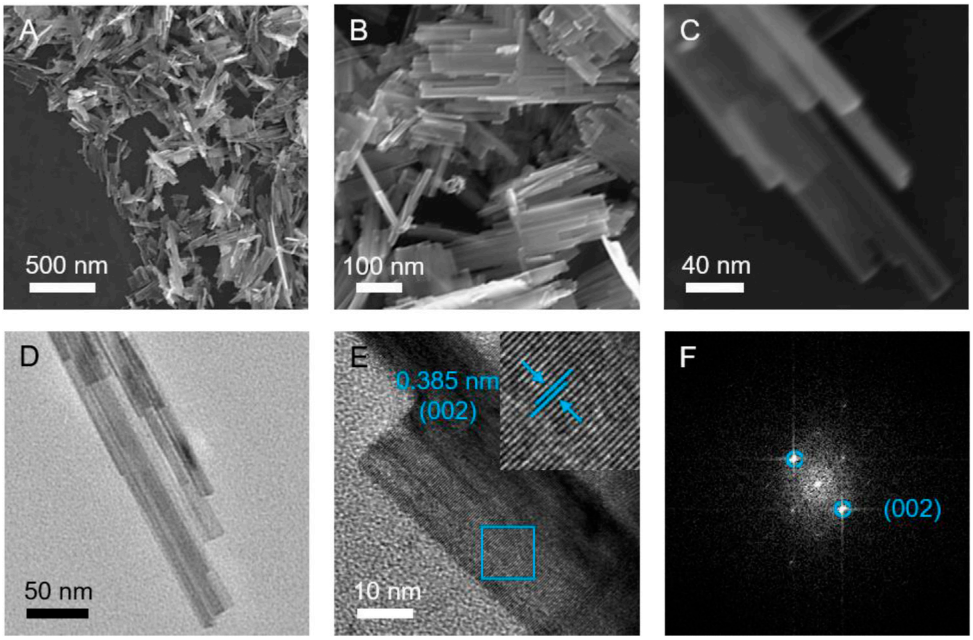

FIGURE 2 | (A–C) FESEM, **(D)** TEM, and **(E)** HRTEM images of the hierarchical WO_3 agglomerates assembled with straight and parallel aligned nanoribbons. **(F)** The corresponding FFT patterns.

RESULTS AND DISCUSSION

Figure 1A provides a schematic description of the synthesis strategy of the hierarchical WO_3 agglomerates, which was prepared *via* a simple one-step hydrothermal method using $(NH_4)_{10}W_{12}O_{41} \cdot xH_2O$ as the tungsten source (details are described in the Experimental section). Through regulating the hydrothermal time, the pure WO_3 products with controllable

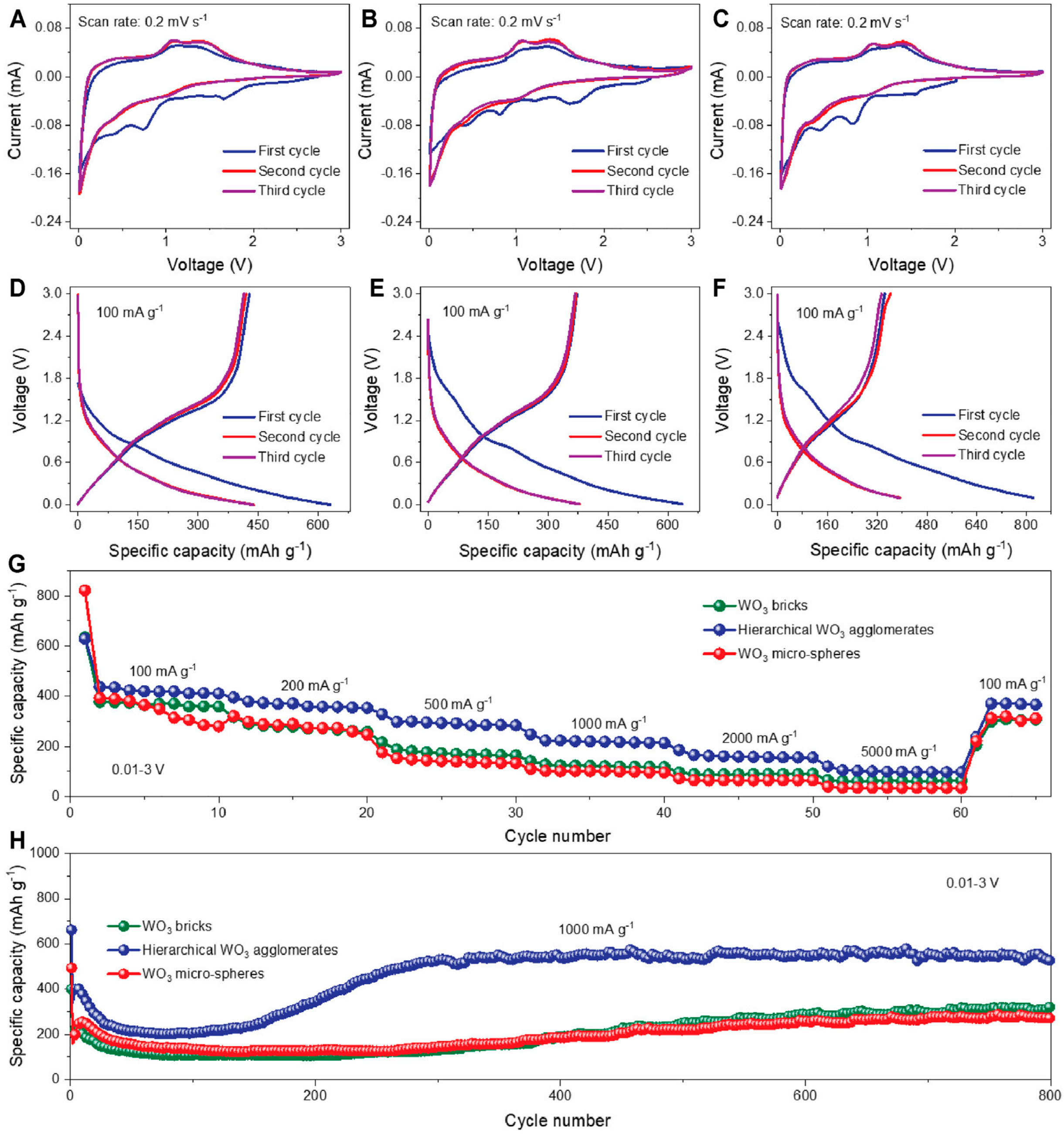

FIGURE 3 | Electrochemical performance of the prepared WO_3 products. **(A–C)** CV curves of the hierarchical WO_3 agglomerates, WO_3 bricks, and WO_3 micro-spheres at a scan rate of 0.2 mV s^{-1}, respectively. **(D–F)** Galvanostatic charge/discharge profiles of the hierarchical WO_3 agglomerates, WO_3 bricks, and WO_3 micro-spheres at 100 mA g^{-1} during the first three cycles, respectively. **(G)** Rate performance of these prepared WO_3 samples at various current densities from 100 to 5,000 mA g^{-1}. **(H)** Cycling performances of these three prepared WO_3 samples at 1,000 mA g^{-1}.

morphology could be obtained. The XRD testing was first carried out to investigate the phase purity of the as-prepared products. As shown in **Figure 1B**, the green lines stand for the final products. The obvious sharp and strong diffraction peaks indicates high-crystallinity of WO_3, which can be well indexed to typical hexagonal (JCPDS No. 85-2459) phase without any unknown impurity peaks (Pachfule et al., 2016). The XPS spectrum was also performed to analyze the elemental composition and surface chemical bonding state of the products (Tong et al., 2016). The survey spectrum shows that the prepared WO_3 consists of C, O, and W elements (**Supplementary Figure S1**). The high-resolution XPS of W 4*f* (**Figure 1C**) exhibits two characteristic peaks located at 35.0 and 37.1 eV that correspond to the W $4f_{7/2}$ and W $4f_{5/2}$ levels (Grugeon et al., 2001). The O 1*s* XPS spectra in

Figure 1D shows the peaks at 529.8 eV, which is ascribed to the W-O bonding mode of WO_3 (Poizot et al., 2000). The XPS results further confirm the phase purity of WO_3, in keeping with the above XRD analysis.

To study the morphologies and microstructures of the prepared WO_3 products, FESEM and TEM were conducted (**Figure 2**). As displayed in **Figures 2A–C**, the structure of product consists of straight and parallel aligned nanoribbons with a periodic stacking. These secondary 1D nanoribbons have a diameter of approximately 20 nm, offering abundant active sites for lithium ions/electrons exchange between the electrode and the electrolyte, (Liu L. et al., 2020), which is conducive to achieving good electrochemical performances. **Supplementary Figure S2** and **Supplementary Figure S3** exhibit the FESEM images of the contrast samples synthesized under different hydrothermal time. Interestingly, with the decrease of the hydrothermal time, the product features a multilayer brick morphology (**Supplementary Figure S2**, denoted as WO_3 bricks); however, when the hydrothermal time increases, a micro-sphere assembled with some irregular nanoribbons can be obtained (**Supplementary Figure S3**, denoted as WO_3 micro-spheres). It can be seen that the hydrothermal time plays a key role in the formation of the different structures of the WO_3 electrode. In addition, the XRD patterns of the above-mentioned WO_3 bricks and WO_3 micro-spheres were also tested, which can be found in **Supplementary Figure S4** and **Supplementary Figure S5**, respectively. TEM and high-resolution TEM (HRTEM) images of the hierarchical WO_3 agglomerates (shown in **Figures 2D,E**) further reveal the crystallographic orientation and unique stacking straight and parallel aligned nanoribbons structure (Chen et al., 2019). The lattice-resolved HRTEM image exhibits the clear lattice with a spacing of 0.385 nm for the (002) planes of WO_3 (**Figure 2E**). Moreover, the corresponding fast Fourier transform (FFT) pattern (**Figure 2F**) also shows the existence of (002) facets, further confirming the high purity of the prepared WO_3.

To explore the potential of these as-prepared WO_3 products for Li-ion storage, half-cells were assembled with Li metal as the counter and reference electrodes. The CV curves of the hierarchical WO_3 agglomerates at a scan rate of $0.2\ \mathrm{mV\,s^{-1}}$ in the voltage window of 0.01–3.0 V (*vs.* Li/Li^+) are presented in **Figure 3A**. Apparently, the reduction peaks between 0.3 and 2 V in the cathodic polarization process are observed in the first cycle, which can be ascribed to the decomposition of the electrolyte and the formation of the solid–electrolyte interface (SEI) (Dahbi et al., 2016; Wang et al., 2018; Yao et al., 2018; Huang et al., 2020). On the following cycles, the broad reduction peak at ~1.0 V on the cathodic scan and the corresponding oxidation peak at ~1.5 V on the reversible anodic scan are related to the Li^+ intercalation–deintercalation processes (Yoon et al., 2014; Li B. et al., 2016; Pathak et al., 2018; Huang et al., 2020). Additionally, the reduction peak observed below 0.25 V can be associated with the conversion of W^{6+} to W^0, which could cause the destruction of WO_3 lattice structure to a certain extent (Rastgoo-Deylami et al., 2021). The CV curves of the pure WO_3 bricks and WO_3 micro-spheres are also shown in **Figures 3B,C**, which exhibits similar shapes to that of hierarchical WO_3 agglomerates. For further comparison, **Figures 3D–F** illustrate the charge/discharge curves of hierarchical WO_3 agglomerates, WO_3 bricks, and WO_3 micro-spheres under a stationary current density of $100\ \mathrm{mA\,g^{-1}}$ within the voltage range of 0.01–3.0 V (vs. Li/Li^+). Note that, from all the three electrodes, the difference in discharge-specific capacity is quite obvious between the first two cycles, but achieves stability in the subsequent cycles, which can be possibly explained by the stable surface state and electrochemical reversibility after the initial activation process (Liang et al., 2021a; Wang et al., 2021). However, the hierarchical WO_3 agglomerate electrode exhibits a higher discharge capacity of $487.6\ \mathrm{mAh\,g^{-1}}$ after the first cycle, much better than WO_3 bricks ($377.7\ \mathrm{mAh\,g^{-1}}$) and WO_3 micro-spheres ($393.6\ \mathrm{mAh\,g^{-1}}$). The superior performance of the hierarchical WO_3 agglomerates was also observed in rate capability tests under various current densities, which is plotted in **Figure 3G**. A highly reversible capacity of $437.7\ \mathrm{mAh\,g^{-1}}$ at $100\ \mathrm{mA\,g^{-1}}$ is obtained, maintaining $121.4\ \mathrm{mAh\,g^{-1}}$ when the current density reaches as high as $5{,}000\ \mathrm{mA\,g^{-1}}$, demonstrating the best sustainable high current endurance of the hierarchical WO_3 agglomerates among all the samples. Regarding the long-term cycling stability (**Figure 3H**), reversible capacities of 522.7, 325.9, and $272.3\ \mathrm{mAh\,g^{-1}}$ are retained for the hierarchical WO_3 agglomerate, WO_3 brick, and WO_3 micro-sphere electrodes, respectively, after 800 cycles at a high current density of $1{,}000\ \mathrm{mA\,g^{-1}}$, indicating an outstanding long cycle life of the prepared hierarchical WO_3 agglomerates. We further compared the performance parameter with state-of-the-art representatively reported congeneric LIBs, which are shown in **Supplementary Figure S6** and **Supplementary Table S1**.

To study the dynamic characteristics of the hierarchical WO_3 agglomerate, WO_3 brick, and WO_3 micro-sphere electrodes, the EIS measurement was carried out (see **Figure 4A**). The depressed semicircle in high-frequency regions represents the charge transfer resistance at the interface of electrode/electrolyte, while the inclined line in low-frequency regions associated with the mass transfer process (Shaibani et al., 2020; Jiang et al., 2021). Obviously, the EIS result reveals that the hierarchical WO_3 agglomerate electrode shows significant smaller charge transfer resistance compared to that of WO_3 brick and WO_3 micro-sphere electrodes, which could be ascribed to the larger specific surface area and structural integrity of the hierarchical WO_3 agglomerate electrode. To seek an in-depth understanding of the electrode kinetics of the hierarchical WO_3 agglomerate electrode materials, the galvanostatic intermittent titration technique (GITT) is conducted to analyze the Li-ion diffusion coefficient (D_{Li+}) during lithiation and delithiation. Of note, the cell was given five cycles at $100\ \mathrm{mA\,g^{-1}}$ to reach its thermal equilibrium state (Chen et al., 2019). In addition, the batteries alternately discharged for 15 min, rested for 60 min, and then charged for 15 min in the same way. D_{Li+} can be calculated *via*

$$D_{Li+} = \frac{4}{\pi\tau}\left(\frac{mV_m}{MA}\right)^2\left(\frac{\Delta E_s}{\Delta E_\tau}\right)^2 \tag{1}$$

where τ represents the relaxation time, and m, M, V_m, and A represent the active material mass, molar mass, molar volume,

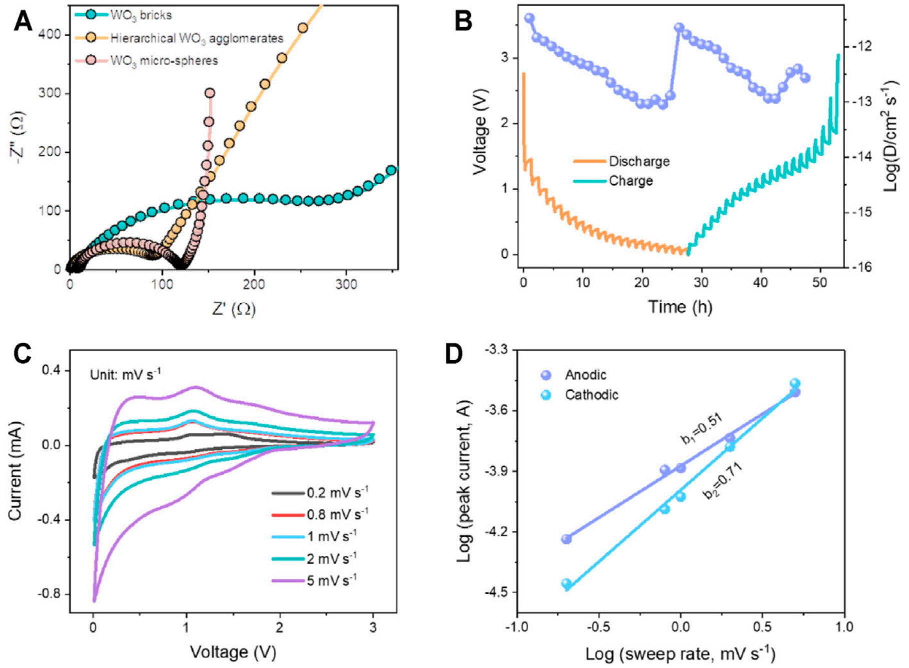

FIGURE 4 | (A) Nyquist impedance plots for the hierarchical WO_3 agglomerates, WO_3 bricks, and WO_3 micro-sphere electrodes, respectively. **(B)** GITT curves of the hierarchical WO_3 agglomerates and the corresponding diffusion coefficients versus state of charge and discharge. **(C)** CV curves of the hierarchical WO_3 agglomerate electrodes at different scan rates. **(D)** Corresponding plots of log(*i*) versus log(*v*) at cathodic and anodic peaks.

and the electrode geometric area, respectively. ΔE_s denotes the voltage changes during the relaxation period, and ΔE_τ is the variation during the current pulse. As shown in **Figure 4B**, the calculated D_{Li+} of Li^+ is in the order of $10^{-11.5}$–$10^{-13.1}$ $cm^2\ s^{-1}$, which is highly comparable to those well-designed metal oxide-based electrode materials (Zhao et al., 2020). CV curves were also tested to explore the reaction kinetics of the hierarchical WO_3 agglomerate electrode. **Figure 4C** demonstrates the CV curves of the hierarchical WO_3 agglomerate electrode at various sweep rates from 0.2 to 5 mV s^{-1} within a voltage range of 0.01–3 V. As the scan rates increase, the CV profiles remain similar except that the cathodic and anodic peaks slightly shift and gradually broaden. A power-law (i = av^b) can be used to describe the relationship between the peak current (i) and scan rate (v), where a and b are defined as adjustable parameters (He et al., 2014; Liu et al., 2021). In principle, a b value of 0.5 means that the current is controlled by semi-infinite diffusion, while 1.0 indicates a surface capacitive-controlled behavior (Wang et al., 2019; Fu et al., 2020). By fitting the profiles of log(i) as a function of log(v) (**Figure 4D**), the calculated b values of 0.71 and 0.51 are computed for the cathodic and anodic peaks, respectively, indicating that the charge storage of the hierarchical WO_3 agglomerates is mainly dominated by the joint effect of diffusion and capacitive-controlled processes (Hwang et al., 2019; Liang et al., 2021b).

To reveal the charge storage mechanism of the hierarchical WO_3 agglomerates, the *ex situ* XPS analyses are conducted at fully discharged/charged states to explore the valence state of tungsten and oxygen elements. The high-resolution XPS of W 4*f* presented in **Figure 5A** shows that two peaks appeared at binding energies of 35.1 and 37.1 eV at the fully discharged state, which can be ascribed to the $W4f_{7/2}$ and $W4f_{5/2}$ of W^{6+}, respectively (Tong et al., 2016). In addition, two other small W 4*f* core level peaks centered at 32.1 and 33.5 eV also emerge in the XPS spectra, indicative of the formation of elemental tungsten as a result of Li^+ intercalation (Tong et al., 2016). After being fully charged (**Figure 5B**), the doublet at 34.9 and 37.1 eV are detected in the high-resolution XPS of W 4*f*, which corresponds to the $W4f_{7/2}$ and $W4f_{5/2}$ of W^{6+}. **Figures 5C,D** show the O 1*s* XPS spectra of the hierarchical WO_3 agglomerates at fully discharged and charged stages. As demonstrated, the XPS measurement shows a stable typical peak located at 529.8 eV, which is attributed to the W-O bonding mode of WO_3 (Li P. et al., 2016), indicating that oxygen does not participate in charge compensation during cycling. According to previous works (Kumagai et al., 1996; Gu et al., 2007; Huang et al., 2008), the energy storage in WO_3 has been proved to be highly associated with lithium intercalation/de-intercalation during the cycling process. Combining with the XPS results, we further confirm that the charge storage mechanism of the prepared hierarchical WO_3 agglomerates firstly occurs with Li^+ intercalation and then the conversion of partial tungsten elements during the discharging process, which can also be found in other metal oxides (Poizot et al., 2000; Grugeon et al., 2001).

Based on the above analysis and discussions, the reaction mechanism of the hierarchical WO_3 agglomerates in the charge/

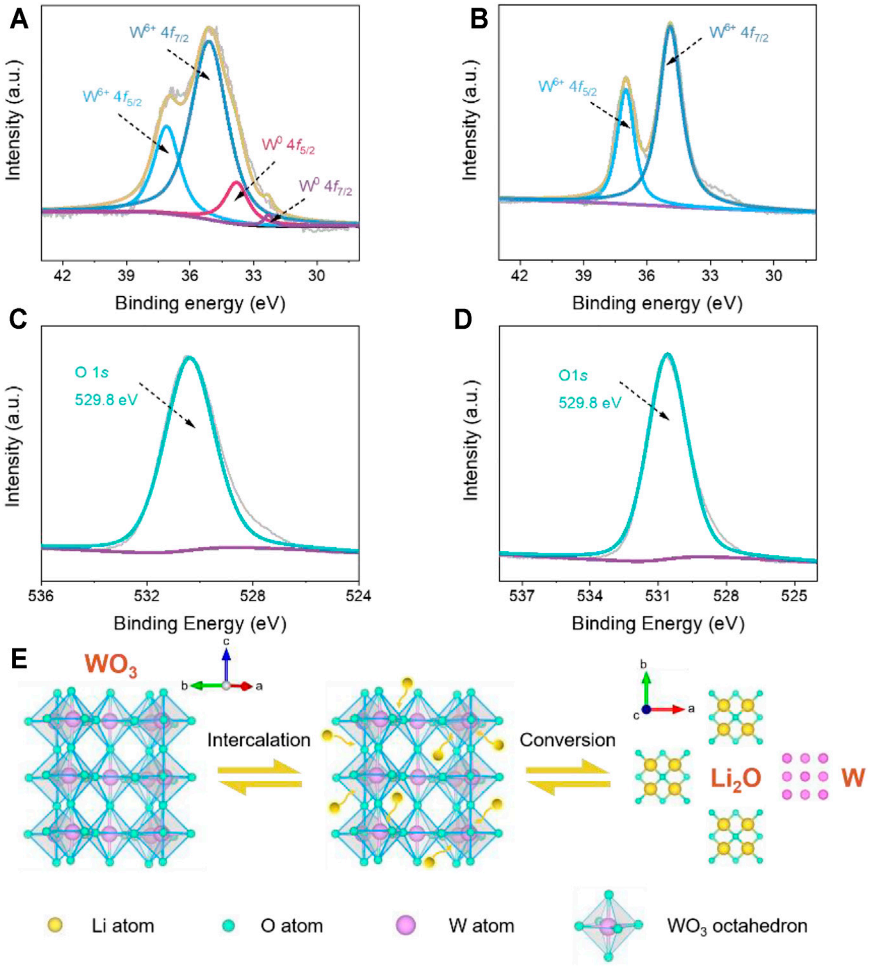

FIGURE 5 | (A, B) *Ex situ* XPS spectra of the W 4*f* region of fully discharged and charged hierarchical WO_3 agglomerate electrodes. **(C, D)** O 1*s* region of fully discharged and charged hierarchical WO_3 agglomerate electrodes. **(E)** Schematic illustration of the proposed charge storage mechanism for WO_3-based LIBs.

discharge processes can be schematically illustrated in **Figure 5E**, and the proposed mechanisms can be approximately expressed as follows (Wu and Yao, 2017; Wang et al., 2019):

$$WO_3 + xLi^+ + xe^- \leftrightarrow Li_xWO_3 \quad (2)$$

$$Li_xWO_3 + (6-x)Li^+ + (6-x)e^- \leftrightarrow W + 3Li_2O \quad (3)$$

The Li^+ insertion and extraction reaction are represented by **Eq. 2**, and x represents the ratio of lithium ion to tungsten oxide. **Eq. 3** shows that the typical conversion reaction occurs at the electrode, where the zero-valent tungsten can be generated. The mechanistic insights into the energy storage processes in WO_3-based materials are helpful to design and prepare advanced electrode structures in enhancing the Li storage performances for high-energy LIBs.

CONCLUSION

To summarize, hierarchical WO_3 agglomerates assembled with straight and parallel aligned nanoribbons have been successfully prepared by a facile hydrothermal approach, and introduced as a novel promising anode material for LIBs. The unique hierarchical agglomerate structure building by secondary 1D nanoribbons with a large interior space can effectively increase the electrode/electrolyte contact area, provide sufficient accessible active sites, and enable rapid transport of both Li ions and electrons. Electrochemical tests demonstrate that the prepared hierarchical WO_3 agglomerates show remarkable Li storage properties including high reversible specific capacity, outstanding rate capability, and excellent cycling stability, making it a very attractive anode for LIBs. This study paves the way to develop transition-metal-based electrode materials with well-designed architecture for applications in high-performance LIBs.

DATA AVAILABILITY STATEMENT

The original contributions presented in the study are included in the article/**Supplementary Material**. Further inquiries can be directed to the corresponding authors.

AUTHOR CONTRIBUTIONS

XD and YL contributed equally to this work. All authors listed have made a substantial, direct, and intellectual contribution to the work and approved it for publication.

FUNDING

HL acknowledges the support from the National Natural Science Foundation of China (51804173) and the Undergraduate Innovation and Entrepreneurship Training Program. CZ acknowledges the support from Henan New Engineering Research and Practice Project (2020JGLX067).

SUPPLEMENTARY MATERIAL

The Supplementary Material for this article can be found online at: https://www.frontiersin.org/articles/10.3389/fchem.2021.834418/full#supplementary-material

REFERENCES

Abakumov, A. M., Fedotov, S. S., Antipov, E. V., and Tarascon, J.-M. (2020). Solid State Chemistry for Developing Better Metal-Ion Batteries. *Nat. Commun.* 11 (1), 4976. doi:10.1038/s41467-020-18736-7

Bekarevich, R., Pihosh, Y., Tanaka, Y., Nishikawa, K., Matsushita, Y., Hiroto, T., et al. (2020). Conversion Reaction in the Binder-free Anode for Fast-Charging Li-Ion Batteries Based on WO_3 Nanorods. *ACS Appl. Energ. Mater.* 3 (7), 6700–6708. doi:10.1021/acsaem.0c00844

Chen, M., Hua, W., Xiao, J., Cortie, D., Chen, W., Wang, E., et al. (2019). NASICON-type Air-Stable and All-Climate Cathode for Sodium-Ion Batteries with Low Cost and High-Power Density. *Nat. Commun.* 10 (1), 1480. doi:10.1038/s41467-019-09170-5

Dahbi, M., Yabuuchi, N., Fukunishi, M., Kubota, K., Chihara, K., Tokiwa, K., et al. (2016). Black Phosphorus as a High-Capacity, High-Capability Negative Electrode for Sodium-Ion Batteries: Investigation of the Electrode/Electrolyte Interface. *Chem. Mater.* 28 (6), 1625–1635. doi:10.1021/acs.chemmater.5b03524

Di, J., Xu, H., Gai, X., Yang, R., and Zheng, H. (2019). One-step Solvothermal Synthesis of Feather Duster-like CNT@WO_3 as High-Performance Electrode for Supercapacitor. *Mater. Lett.* 246, 129–132. doi:10.1016/j.matlet.2019.03.070

Du, Q.-k., Wu, Q.-x., Wang, H.-x., Meng, X.-j., Ji, Z.-k., Zhao, S., et al. (2021). Carbon Dot-Modified Silicon Nanoparticles for Lithium-Ion Batteries. *Int. J. Miner Metall. Mater.* 28 (10), 1603–1610. doi:10.1007/s12613-020-2247-1

Duan, X., Xiao, S., Wang, L., Huang, H., Liu, Y., Li, Q., et al. (2015). Ionic Liquid-Modulated Preparation of Hexagonal Tungsten Trioxide Mesocrystals for Lithium-Ion Batteries. *Nanoscale* 7 (6), 2230–2234. doi:10.1039/C4NR05717A

Eum, D., Kim, B., Kim, S. J., Park, H., Wu, J., Cho, S.-P., et al. (2020). Voltage Decay and Redox Asymmetry Mitigation by Reversible Cation Migration in Lithium-Rich Layered Oxide Electrodes. *Nat. Mater.* 19 (4), 419–427. doi:10.1038/s41563-019-0572-4

Fu, Q., Zhu, X., Li, R., Liang, G., Luo, L., Chen, Y., et al. (2020). A Low-Strain $V_3Nb_{17}O_{50}$ Anode Compound for superior Li+ Storage. *Energ. Storage Mater.* 30, 401–411. doi:10.1016/j.ensm.2020.05.012

Gao, Y., Rojas, T., Wang, K., Liu, S., Wang, D., Chen, T., et al. (2020). Low-temperature and High-Rate-Charging Lithium Metal Batteries Enabled by an Electrochemically Active Monolayer-Regulated Interface. *Nat. Energ.* 5 (7), 534–542. doi:10.1038/s41560-020-0640-7

Grugeon, S., Laruelle, S., Herrera-Urbina, R., Dupont, L., Poizot, P., and Tarascon, J.-M. (2001). Particle Size Effects on the Electrochemical Performance of Copper Oxides toward Lithium. *J. Electrochem. Soc.* 148 (4), A285. doi:10.1149/1.1353566

Gu, Z., Li, H., Zhai, T., Yang, W., Xia, Y., Ma, Y., et al. (2007). Large-scale Synthesis of Single-crystal Hexagonal Tungsten Trioxide Nanowires and Electrochemical Lithium Intercalation into the Nanocrystals. *J. Solid State. Chem.* 180 (1), 98–105. doi:10.1016/j.jssc.2006.09.020

He, X., Wang, J., Kloepsch, R., Krueger, S., Jia, H., Liu, H., et al. (2014). Enhanced Electrochemical Performance in Lithium Ion Batteries of a Hollow Spherical Lithium-Rich Cathode Material Synthesized by a Molten Salt Method. *Nano Res.* 7 (1), 110–118. doi:10.1007/s12274-013-0378-7

Hou, R., Li, H., Diao, M., Sun, Y., Liang, Y., Yu, Z., et al. (2022). Fast Electrochemical Activation of the Broadband Saturable Absorption of Tungsten Oxide Nanoporous Film. *Nano Res.* 15 (1), 326–332. doi:10.1007/s12274-021-3478-9

Huang, K., Pan, Q., Yang, F., Ni, S., Wei, X., and He, D. (2008). Controllable Synthesis of Hexagonal WO_3 nanostructures and Their Application in Lithium Batteries. *J. Phys. D: Appl. Phys.* 41 (15), 155417. doi:10.1088/0022-3727/41/15/155417

Huang, Y., Lu, R., Wang, M., Sakamoto, J., and Poudeu, P. F. P. (2020). Hexagonal-WO_3 Nanorods Encapsulated in Nitrogen and Sulfur Co-doped Reduced Graphene Oxide as a High-Performance Anode Material for Lithium Ion Batteries. *J. Solid State. Chem.* 282, 121068. doi:10.1016/j.jssc.2019.121068

Hwang, C. H., Kim, H.-e., Nam, I., and Bang, J. H. (2019). Polygonal Multi-Polymorphed $Li_4Ti_5O_{12}$@rutile TiO_2 as Anodes in Lithium-Ion Batteries. *Nano Res.* 12 (4), 897–904. doi:10.1007/s12274-019-2320-0

Jiang, Q., Zhang, W.-q., Zhao, J.-c., Rao, P.-h., and Mao, J.-f. (2021). Superior Sodium and Lithium Storage in Strongly Coupled Amorphous Sb_2S_3 Spheres and Carbon Nanotubes. *Int. J. Miner Metall. Mater.* 28 (7), 1194–1203. doi:10.1007/s12613-021-2259-5

Kumagai, N., Kumagai, N., Umetzu, Y., Tanno, K., and Pereira-Ramos, J. P. (1996). Synthesis of Hexagonal Form of Tungsten Trioxide and Electrochemical Lithium Insertion into the Trioxide. *Solid State Ionics* 86-88, 1443–1449. doi:10.1016/0167-2738(96)00327-X

Lee, S.-K., Kim, H., Bang, S., Myung, S.-T., and Sun, Y.-K. (2021). WO_3 Nanowire/Carbon Nanotube Interlayer as a Chemical Adsorption Mediator for High-Performance Lithium-Sulfur Batteries. *Molecules* 26 (2), 377. doi:10.3390/molecules26020377

Li, B., Li, X., Li, W., Wang, Y., Uchaker, E., Pei, Y., et al. (2016a). Mesoporous Tungsten Trioxide Polyaniline Nanocomposite as an Anode Material for High-Performance Lithium-Ion Batteries. *ChemNanoMat* 2 (4), 281–289. doi:10.1002/cnma.201500208

Li, H., Hu, Z., Xia, Q., Zhang, H., Li, Z., Wang, H., et al. (2021a). Operando Magnetometry Probing the Charge Storage Mechanism of CoO Lithium-Ion Batteries. *Adv. Mater.* 33 (12), 2006629. doi:10.1002/adma.202006629

Li, H., Zhang, X., Zhao, Z., Hu, Z., Liu, X., and Yu, G. (2020). Flexible Sodium-Ion Based Energy Storage Devices: Recent Progress and Challenges. *Energ. Storage Mater.* 26, 83–104. doi:10.1016/j.ensm.2019.12.037

Li, P., Li, X., Zhao, Z., Wang, M., Fox, T., Zhang, Q., et al. (2016b). Correlations Among Structure, Composition and Electrochemical Performances of WO_3 Anode Materials for Lithium Ion Batteries. *Electrochimica Acta* 192, 148–157. doi:10.1016/j.electacta.2016.01.199

Li, Q., Li, H., Xia, Q., Hu, Z., Zhu, Y., Yan, S., et al. (2021b). Extra Storage Capacity in Transition Metal Oxide Lithium-Ion Batteries Revealed by *In Situ* Magnetometry. *Nat. Mater.* 20, 76–83. doi:10.1038/s41563-020-0756-y

Li, Y., Chang, K., Tang, H., Li, B., Qin, Y., Hou, Y., et al. (2019). Preparation of Oxygen-Deficient WO_3- Nanosheets and Their Characterization as Anode Materials for High-Performance Li-Ion Batteries. *Electrochimica Acta* 298, 640–649. doi:10.1016/j.electacta.2018.12.137

Liang, H., Hu, Z., Zhao, Z., Chen, D., Zhang, H., Wang, H., et al. (2021a). Dendrite-structured FeF_2 Consisting of Closely Linked Nanoparticles as Cathode for High-Performance Lithium-Ion Capacitors. *J. Energ. Chem.* 55, 517–523. doi:10.1016/j.jechem.2020.07.031

Liang, H., Zhang, H., Zhao, L., Chen, Z., Huang, C., Zhang, C., et al. (2022). Layered $Fe_2(MoO_4)_3$ Assemblies with Pseudocapacitive Properties as Advanced Materials for High-Performance Sodium-Ion Capacitors. *Chem. Eng. J.* 427, 131481. doi:10.1016/j.cej.2021.131481

Liang, H., Zhang, Y., Hao, S., Cao, L., Li, Y., Li, Q., et al. (2021b). Fast Potassium Storage in Porous CoV_2O_6 Nanosphere@graphene Oxide towards High-Performance Potassium-Ion Capacitors. *Energ. Storage Mater.* 40, 250–258. doi:10.1016/j.ensm.2021.05.013

Liu, C., Wang, C., Meng, X., Li, X., Qing, Q., Wang, X., et al. (2020a). Tungsten Nitride Nanoparticles Anchored on Porous Borocarbonitride as High-Rate Anode for Lithium Ion Batteries. *Chem. Eng. J.* 399, 125705. doi:10.1016/j.cej.2020.125705

Liu, L., Zhao, Z., Hu, Z., Lu, X., Zhang, S., Huang, L., et al. (2020b). Designing Uniformly Layered $FeTiO_3$ Assemblies Consisting of Fine Nanoparticles Enabling High-Performance Quasi-Solid-State Sodium-Ion Capacitors. *Front. Chem.* 8, 371. doi:10.3389/fchem.2020.00371

Liu, Z., Luo, X., Qin, L., Fang, G., and Liang, S. (2021). Progress and prospect of Low-Temperature Zinc Metal Batteries. *Adv. Powder Mater*. doi:10.1016/j.apmate.2021.10.002

Luo, Y., Wang, C., and Wang, X. (2021). Fast Energy Storage Performance of $CoFe_2O_4$/CNTs Hybrid Aerogels for Potassium Ion Battery. *J. Colloid Interf. Sci.* 600, 820–827. doi:10.1016/j.jcis.2021.05.088

Pachfule, P., Shinde, D., Majumder, M., and Xu, Q. (2016). Fabrication of Carbon Nanorods and Graphene Nanoribbons from a Metal-Organic Framework. *Nat. Chem* 8 (7), 718–724. doi:10.1038/nchem.2515

Pathak, R., Gurung, A., Elbohy, H., Chen, K., Reza, K. M., Bahrami, B., et al. (2018). Self-recovery in Li-Metal Hybrid Lithium-Ion Batteries via WO_3 Reduction. *Nanoscale* 10 (34), 15956–15966. doi:10.1039/c8nr01507d

Poizot, P., Laruelle, S., Grugeon, S., Dupont, L., and Tarascon, J.-M. (2000). Nano-sized Transition-Metal Oxides as Negative-Electrode Materials for Lithium-Ion Batteries. *Nature* 407 (6803), 496–499. doi:10.1038/35035045

Qu, G., Wang, J., Liu, G., Tian, B., Su, C., Chen, Z., et al. (2019). Vanadium Doping Enhanced Electrochemical Performance of Molybdenum Oxide in Lithium-Ion Batteries. *Adv. Funct. Mater.* 29 (2), 1805227. doi:10.1002/adfm.201805227

Rastgoo-Deylami, M., Javanbakht, M., Omidvar, H., Hooshyari, K., Salarizadeh, P., and Askari, M. B. (2021). Nickel-doped Monoclinic WO_3 as High Performance Anode Material for Rechargeable Lithium Ion Battery. *J. Electroanalytical Chem.* 894, 115383. doi:10.1016/j.jelechem.2021.115383

Sasidharan, M., Gunawardhana, N., Yoshio, M., and Nakashima, K. (2012). WO_3 Hollow Nanospheres for High-Lithium Storage Capacity and Good Cyclability. *Nano Energy* 1 (3), 503–508. doi:10.1016/j.nanoen.2012.03.003

Shaibani, M., Mirshekarloo, M. S., Singh, R., Easton, C. D., Cooray, M. C. D., Eshraghi, N., et al. (2020). Expansion-tolerant Architectures for Stable Cycling of Ultrahigh-Loading Sulfur Cathodes in Lithium-Sulfur Batteries. *Sci. Adv.* 6 (1), eaay2757. doi:10.1126/sciadv.aay2757

Tong, H., Xu, Y., Cheng, X., Zhang, X., Gao, S., Zhao, H., et al. (2016). One-pot Solvothermal Synthesis of Hierarchical WO_3 Hollow Microspheres with superior Lithium Ion Battery Anode Performance. *Electrochimica Acta* 210, 147–154. doi:10.1016/j.electacta.2016.05.154

Tu, J., Lei, H., Yu, Z., and Jiao, S. (2018). Ordered WO_3–x Nanorods: Facile Synthesis and Their Electrochemical Properties for Aluminum-Ion Batteries. *Chem. Commun.* 54 (11), 1343–1346. doi:10.1039/C7CC09376D

Wang, H., Jiang, Y., and Manthiram, A. (2018). Long Cycle Life, Low Self-Discharge Sodium-Selenium Batteries with High Selenium Loading and Suppressed Polyselenide Shuttling. *Adv. Energ. Mater.* 8 (7), 1701953. doi:10.1002/aenm.201701953

Wang, H., Zhao, L., Zhang, H., Liu, Y., Yang, L., Li, F., et al. (2021). Revealing the Multiple Cathodic and Anodic Involved Charge Storage Mechanism in an $FeSe_2$ Cathode for Aluminium-Ion Batteries by *In Situ* Magnetometry. *Energy Environ. Sci* 15, 311–319. doi:10.1039/D1EE03070A

Wang, L., Huang, K.-W., Chen, J., and Zheng, J. (2019). Ultralong Cycle Stability of Aqueous Zinc-Ion Batteries with Zinc Vanadium Oxide Cathodes. *Sci. Adv.* 5 (10), eaax4279. doi:10.1126/sciadv.aax4279

Wu, X., and Yao, S. (2017). Flexible Electrode Materials Based on WO_3 Nanotube Bundles for High Performance Energy Storage Devices. *Nano Energy* 42, 143–150. doi:10.1016/j.nanoen.2017.10.058

Xiao, Y., Jiang, M., and Cao, M. (2021a). Developing WO_3 as High-Performance Anode Material for Lithium-Ion Batteries. *Mater. Lett.* 285, 129129. doi:10.1016/j.matlet.2020.129129

Xiao, Z., Yu, Z., Ma, X., and Xu, C. (2021b). S, N-Codoped Carbon Capsules with Microsized Entrance: Highly Stable S Reservoir for Li-S Batteries. *Adv. Powder Techn.* 32 (5), 1757–1765. doi:10.1016/j.apt.2021.03.031

Yao, S., Qu, F., Wang, G., and Wu, X. (2017). Facile Hydrothermal Synthesis of WO_3 Nanorods for Photocatalysts and Supercapacitors. *J. Alloys Compd.* 724, 695–702. doi:10.1016/j.jallcom.2017.07.123

Yao, Y., Chen, M., Xu, R., Zeng, S., Yang, H., Ye, S., et al. (2018). CNT Interwoven Nitrogen and Oxygen Dual-Doped Porous Carbon Nanosheets as Free-Standing Electrodes for High-Performance Na-Se and K-Se Flexible Batteries. *Adv. Mater.* 30 (49), 1805234. doi:10.1002/adma.201805234

Yoon, S., Woo, S.-G., Jung, K.-N., and Song, H. (2014). Conductive Surface Modification of Cauliflower-like WO_3 and its Electrochemical Properties for Lithium-Ion Batteries. *J. Alloys Compd.* 613, 187–192. doi:10.1016/j.jallcom.2014.06.010

Yu, M., Sun, H., Sun, X., Lu, F., Hu, T., Wang, G., et al. (2013). 3D WO_3 Nanowires/graphene Nanocomposite with Improved Reversible Capacity and Cyclic Stability for Lithium Ion Batteries. *Mater. Lett.* 108, 29–32. doi:10.1016/j.matlet.2013.06.067

Yue, L., Ma, C., Yan, S., Wu, Z., Zhao, W., Liu, Q., et al. (2022). Improving the Intrinsic Electronic Conductivity of $NiMoO_2$ Anodes by Phosphorous Doping for High Lithium Storage. *Nano Res.* 15 (1), 186–194. doi:10.1007/s12274-021-3455-3

Zhang, F., and Qi, L. (2016). Recent Progress in Self-Supported Metal Oxide Nanoarray Electrodes for Advanced Lithium-Ion Batteries. *Adv. Sci.* 3 (9), 1600049. doi:10.1002/advs.201600049

Zhao, Z., Hu, Z., Jiao, R., Tang, Z., Dong, P., Li, Y., et al. (2019). Tailoring Multi-Layer Architectured FeS_2@C Hybrids for superior Sodium-, Potassium- and Aluminum-Ion Storage. *Energ. Storage Mater.* 22, 228–234. doi:10.1016/j.ensm.2019.01.022

Zhao, Z., Hu, Z., Li, Q., Li, H., Zhang, X., Zhuang, Y., et al. (2020). Designing Two-Dimensional WS_2 Layered Cathode for High-Performance Aluminum-Ion Batteries: From Micro-assemblies to Insertion Mechanism. *Nano Today* 32, 100870. doi:10.1016/j.nantod.2020.100870

Conflict of Interest: The authors declare that the research was conducted in the absence of any commercial or financial relationships that could be construed as a potential conflict of interest.

frontiers in Chemistry

ORIGINAL RESEARCH
published: 03 February 2022
doi: 10.3389/fchem.2021.812274

Hydrothermal Preparation and High Electrochemical Performance of NiS Nanospheres as Anode for Lithium-Ion Batteries

Lin-Hui Wang[1†], **Long-Long Ren**[2†], **Yu-Feng Qin**[1*] **and Qiang Li**[3]

[1]College of Information Science and Engineering, Shandong Agricultural University, Taian, China, [2]College of Mechanical and Electronic Engineering, Shandong Agricultural University, Taian, China, [3]College of Physics, University-Industry Joint Center for Ocean Observation and Broadband Communication, Qingdao University, Qingdao, China

Nickel sulfide has been widely studied as an anode material for lithium-ion batteries due to its environmental friendliness, low cost, high conductivity, and high theoretical capacity. A simple hydrothermal method was used to prepare NiS nanospheres materials with the size in the range of 100–500 nm. The NiS nanospheres electrodes exhibited a high reversible capacity of 1402.3 mAh g^{-1} at 200 mA g^{-1} after 280 cycles and a strong rate capability of 814.8 mAh g^{-1} at 0.8 A g^{-1} and 1130.5 mAh g^{-1} when back to 0.1 A g^{-1}. Excellent electrochemical properties and the simple preparation method of the NiS nanospheres make it possible to prepare NiS on a large scale as the anode of lithium-ion batteries.

Keywords: anodes, lithium-ion batteries, hydrothermal method, NiS nanospheres, electrochemical performance

Edited by:
Jun Zhang,
Zhejiang University of Technology,
China

Reviewed by:
Xiao-Dong Zhu,
Qingdao University of Science and
Technology, China
Yongfeng Yuan,
Zhejiang Sci-Tech University, China

***Correspondence:**
Yu-Feng Qin
qinyufeng@sdau.edu.cn

[†]*These authors have contributed equally to this work*

Specialty section:
This article was submitted to
Electrochemistry,
a section of the journal
Frontiers in Chemistry

Received: *10 November 2021*
Accepted: *16 December 2021*
Published: *03 February 2022*

Citation:
Wang L-H, Ren L-L, Qin Y-F and Li Q (2022) Hydrothermal Preparation and High Electrochemical Performance of NiS Nanospheres as Anode for Lithium-Ion Batteries.
Front. Chem. 9:812274.
doi: 10.3389/fchem.2021.812274

INTRODUCTION

With the gradual exhaustion of fossil energy and the resulting emission of carbon oxides, the development of new green and sustainable energy, such as wind energy and solar energy, presents a strong trend, which puts forward higher requirements for energy storage and conversion technology (Li S. et al., 2021). As new energy storage devices, lithium-ion batteries (LIBs) have been widely studied due to their long service life, no memory effect, high charging efficiency, and environmental friendliness (Hong and Song, 2018; Hou et al., 2020; Li W. et al., 2020; Teng et al., 2020; Zheng et al., 2020; Gao et al., 2021; Li H. et al., 2021; Li Z. et al., 2021; Wang L et al., 2021). Since LIBs were commercialized by Sony in 1991, graphite has been the main anode of LIBs for a long period (Park and Lee, 2019). Although graphite has high conductivity and good cycling stability, its poor rate performance and low theoretical capacity will limit its application and development in the future (Dong et al., 2019; Ren et al., 2021; Xia et al., 2021).

Nanomaterials have shown excellent physical and chemical properties in many fields due to their larger specific surface area and higher activity (Wang et al., 2014; Wang et al., 2017; Li H. et al., 2019; Zhou et al., 2019; Gu et al., 2021; Wang X et al., 2021; Zhao et al., 2021; Liang et al., 2022; Wang et al., 2022). Transition metal sulfide (TMS) nanomaterials have been extensively researched in the field of the anode materials of LIBs due to low redox potential, good conductivity, strong cycling stability, and high theoretical capacity (Zhao et al., 2018; Wang et al., 2020; Yang et al., 2021). Among them, NiS is an excellent choice to replace graphite anodes because of its good stability, high theoretical capacity (590 mAh g^{-1}), and high conductivity (Ren et al., 2021). Recently, Lee et al. synthesized hierarchical carbon-coated NiS with a discharge capacity of 606 mAh g^{-1} after 100 cycles (Park and Lee, 2019). Gao et al. prepared porous NiS@NSC tubules using biological templates, which showed a

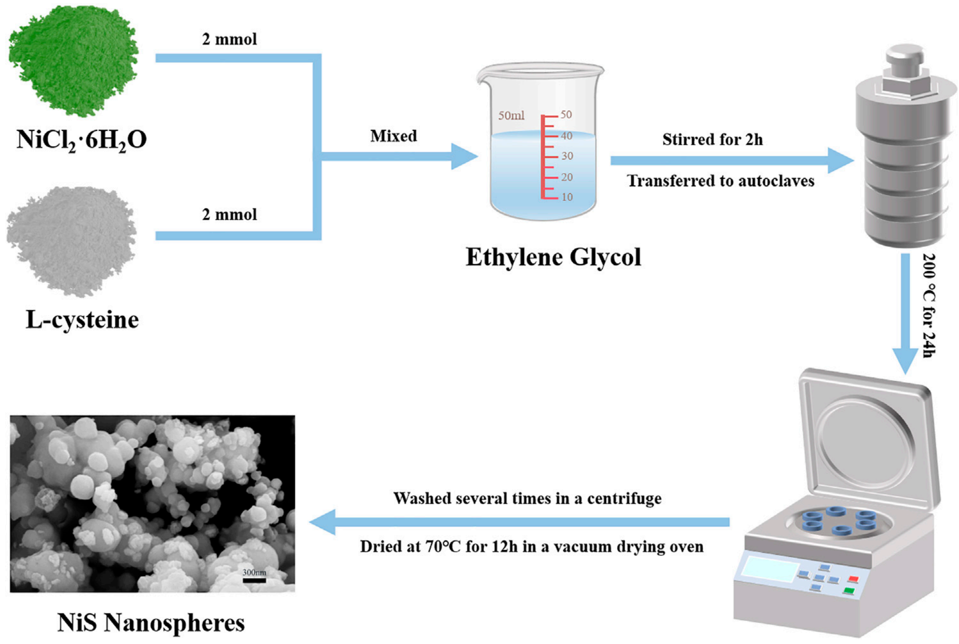

FIGURE 1 | The schematic diagram of preparing NiS nanospheres.

discharge capacity of 715.9 mAh g^{-1} at the 200th cycle (Dong et al., 2019). Wang et al. prepared NiS/C nanomaterials with biomass biochar, exhibiting a reversible capacity of 411.6 mAh g^{-1} at the 100th cycle (Xia et al., 2021). However, most NiS nanomaterials have not shown the satisfying reversible capacity and cycle stability, and complex preparations restricted its mass production.

In this work, NiS nanospheres were prepared by a hydrothermal method and showed outstanding performance as anodes for LIBs. The initial discharge and charge capacities reached 1418.5 mAh g^{-1} and 778.3 mAh g^{-1} at 0.2 A g^{-1}, respectively. The reversible capacity was up to 1402.3 mAh g^{-1} after 280 charging-discharging cycles. The discharge specific capacity of NiS nanospheres reached 814.8 mAh g^{-1} at 0.8 A g^{-1}, and it increased to 1130.5 mAh g^{-1} when back to 0.1 A g^{-1}, indicating an enhanced rate capability. The outstanding electrochemical performance indicated that the NiS nanosphere materials are more potential anodes for LIBs.

METHODS OF PREPARATION AND CHARACTERIZATION

Preparation of NiS Nanospheres

The schematic diagram of the preparation process of NiS nanospheres is shown in **Figure 1**. There were 244.85 mg (2 mmol) of L-cysteine and 475.38 mg (2 mmol) of $NiCl_2·6H_2O$ added into ethylene glycol (35 ml) and stirred by a magnetic stirrer for more than 2 h. The mixture was transferred to a Teflon-sealed autoclave and thoroughly reacted for 24 h at 200°C. The black powder samples were acquired after alternately washing 6 times with deionized water and ethanol in a centrifuge (10,000 rpm for 10 min) and drying at 70°C in a vacuum for 12 h.

Characterization of NiS Nanospheres

X-ray diffraction (XRD, SmartLab, Rigku Japan) and scanning electron microscope (SEM, GeminiSEM300, Zeiss, Germany) were used to characterize the composition, structure, and morphology of the black powder. The scan rate of the Cu Kα radiation is 5°/min in the range of 20°–80° for the XRD measurements.

Electrochemical Test of NiS Nanospheres

The anodes were made of carboxymethyl cellulose (CMC), carbon black, and NiS nanospheres powders (mass ratio 7:2:1). After coating the mixed paste on copper foil uniformly, the copper foil was dried for 12 h at 70°C under vacuum and cut into discs (113 mm^2). The CR-2032 cells were assembled in argon with Celgard 2250 films used as the diaphragm, 1M LiPF6 solution with dimethyl ethyl carbonate and ethyl carbonate (v/v = 1:1) used as the electrolyte, and lithium disks used as counter-electrodes.

Land-CT3001A battery testing systems were used for the cycle performance test of NiS nanospheres at several different current densities. The electrochemical impedance spectroscopy (EIS, 10^{-2}–10^5 Hz) and the cyclic voltammetry (CV, 0.1–1.5 mV s^{-1}) curves were determined by a CHI660E electrochemical workstation. The electrochemical tests were realized at room temperature between 0.01 and 3.0 V.

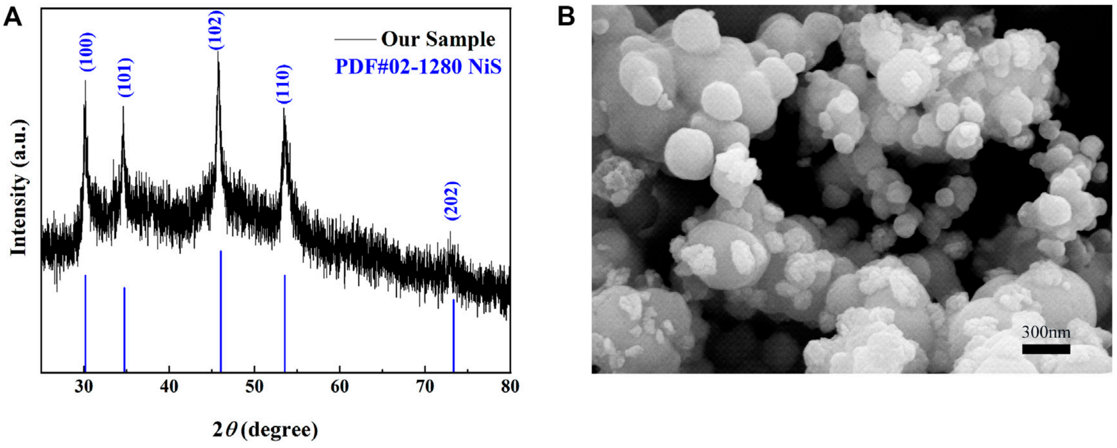

FIGURE 2 | (A) XRD patterns and **(B)** the SEM image of the material.

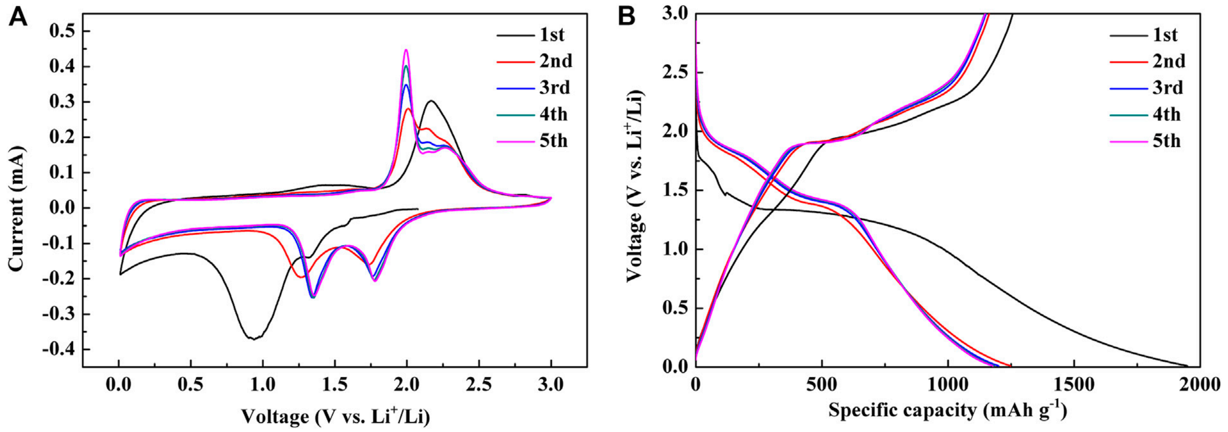

FIGURE 3 | (A) Initial five CV curves. **(B)** Initial five discharge and charge curves.

RESULTS AND DISCUSSION

Structure and Morphology of NiS Nanospheres

The XRD patterns of the materials shown in **Figure 2A** have a high degree of matching with the standard card PDF No. 02-1280, which shows that the sample is pure NiS and no other components exist. The sharp diffraction peaks indicate that the samples are crystalline. In addition, the different peaks at 30.167°, 34.742°, 46.034°, 53.546°, and 73.327°, respectively, corresponded to the (100), (101), (102), (110), and (202) crystal planes of NiS. To further investigate the morphology, the NiS material was tested by SEM. The materials consisted of nanospheres with sizes between 100 and 500 nm as shown in **Figure 2B**.

Electrochemical Performance of NiS Nanospheres

The initial five CV curves were measured at 0.1 mV s^{-1}, as is shown in **Figure 3A**. In CV curves, three reduction peaks existed near 0.94, 1.32, and 1.58 V during the first cathode sweep (lithiation). The peak at 0.94 V denotes the formation of the solid electrolyte interphase (SEI) layer, which can be seen from the fact that this peak no longer exists in the second circle (Duan et al., 2015; Fan et al., 2017; Jin et al., 2017; Dong et al., 2019). The reduction peaks at 1.58 and 1.32 V represent the reduction process from NiS to Ni, which corresponds to the two reactions of **Equations 1** and **2**, respectively (Wang et al., 2011; Dong et al., 2019; Xia et al., 2021).

$$\mathbf{3NiS} + \mathbf{2Li}^{+} + \mathbf{2e}^{-} \rightarrow \mathbf{Ni_3S_2} + \mathbf{Li_2S} \tag{1}$$

$$\mathbf{Ni_3S_2} + \mathbf{4Li}^{+} + \mathbf{4e}^{-} \rightarrow \mathbf{3Ni} + \mathbf{2Li_2S} \tag{2}$$

In the second cycle, the two peaks shifted to 1.74 and 1.27 V, while in the third cycle, they shifted to 1.77 and 1.35 V, which was due to the activation of the materials (Ni et al., 2012). The two reduction peaks in subsequent cycles almost completely coincide with that in the third cycle, which indicates the stable reduction reaction process.

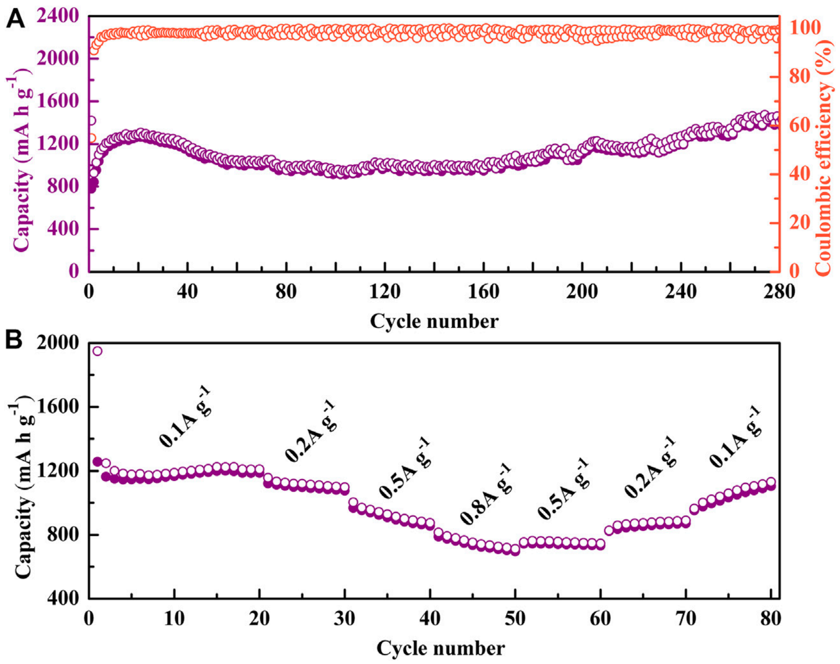

FIGURE 4 | (A) Cycle performance of NiS nanospheres. **(B)** Rate capabilities of NiS nanospheres.

Two oxidation peaks can be observed near 1.46 and 2.17 V during the first anode sweep (delithiation). The peak at 1.46 V, which vanishes in following cycles, represents the decomposition of the SEI layer (Vadivazhagan et al., 2021; Xia et al., 2021), and the peak at 2.17 V relates to the reaction of Ni to NiS (Vadivazhagan et al., 2021), which corresponds to **Equation 3** (Vadivazhagan et al., 2021).

$$\mathbf{Ni + Li_2S \rightarrow NiS} + 2\mathbf{Li}^{+} + 2\mathbf{e}^{-} \tag{3}$$

The oxidation peak at 2.17 V split into three peaks at 1.99, 2.14, and 2.27 V in the second cycle, which also represents the production of NiS (Han et al., 2017; Ren et al., 2021; Xia et al., 2021). In the subsequent cycles, the peak positions of the oxidation processes almost completely coincide with that in the second cycle, which shows the stable oxidation reaction process and cycle stability.

The initial five constant current discharge-charge curves of NiS nanospheres were measured at 100 mA g^{-1}, as shown in **Figure 3B**. There is a small platform between 1.6 and 1.7 V and a large platform between 1.0 and 1.5 V during the first discharge process. The small platform corresponds to the reduction process of NiS to Ni_3S_2, while the large platform signifies the formation of the SEI layer as well as the reduction process of Ni_3S_2 to Ni, which completely corresponds to the CV curves. There is a small platform near 1.4 V and a large platform near 2.0 V in the first charge process, which corresponds very well to the oxidation peaks in the CV curves. As shown in **Figure 3B**, the discharge and charge capacities of the first cycle are 1949 mAh g^{-1} and 1257 mAh g^{-1} respectively. The discharge and charge capacities can be stable around 1200 mAh g^{-1} in the following four cycles, which are much higher than the theoretical capacity of NiS (Li Q. et al., 2020; Kim et al., 2020). The phenomenon could originate from the reversible formation of polymeric gel-like films around the transition metal particles (Laruelle et al., 2002), the interface lithium storage (Zhukovskii et al., 2006), and the surface conversion of LiOH to Li_2O and LiH (Hu et al., 2013). It is worth noting that the discharge-charge curves almost completely coincide after the first circle, which shows the great electrochemical stability and reversibility.

The cycle performance and the rate capabilities of NiS nanospheres were measured, as shown in **Figure 4**. The initial discharge and charge capacities at 200 mA g^{-1} are up to 1418.5 mAh g^{-1} and 778.3 mAh g^{-1}, respectively. The initial Coulomb efficiency is 54.9% and increases rapidly to more than 90% in the second cycle, and then remains near 100% to the 280th cycle. The cycle curve has two upward trends. The first upward trend during the initial 20 cycles could be ascribed to the active process of NiS nanospheres in the first few redox reaction cycles (Li L. et al., 2019; Li S. et al., 2019), and the second upward trend during the 160th to 280th cycle could be due to the increase of active sites caused by the rupture of the NiS nanospheres during cycles (Duan et al., 2015; Wang et al., 2020, Wang L et al., 2021) and/or the reversible growth of a polymeric gel-like film resulting from the kinetically activated electrolyte degradation (Feng et al., 2013; Rui et al., 2014; Duan et al., 2015). After 280 discharge-charge cycles, the high specific capacity of 1402.3 mAh g^{-1} is obtained, which shows that the NiS nanosphere materials have good reversibility and stability as the anode of LIBs. The comparison of electrochemical

TABLE 1 | Comparison of electrochemical properties between NiS_2 nanospheres and other reported NiS-based materials.

NiS-based materials	Initial discharge capacity (mAh g^{-1})	Discharge capacity (mAh g^{-1})	Current density (mA g^{-1})	References
NiS	1418.5	1402.3 (280 cycles)	200	This work
HCNS	1132	606 (97 cycles)	100	Park and Lee (2019)
NiS@NSC	1075.4	715.9 (200 cycles)	100	Dong et al. (2019)
CSF-NiS/C	1522.8	411.6 (100 cycles)	100	Xia et al. (2021)
rGO@NiS	1520.6	1328.7 (120 cycles)	100	Ren et al. (2021)
NS@CNT	—	644 (100 cycles)	300	Fan et al. (2017)
CNTs@C@NiS	860	649 (100 cycles)	100	Jin et al. (2017)
NiS/CPC	1249	650 (50 cycles)	100	Vadivazhagan et al. (2021)
NiS@OLC	889	546 (100 cycles)	100	Han et al. (2017)
NiS/N-rGO	1240	467 (100 cycles)	0.5C	Lee et al. (2020)
NiO@β-NiS@Ni_3S_2	853.1	498.5 (100 cycles)	500	Wu et al. (2019)
NiS_2	753	580.6 (400 cycles)	0.2C	Zhang et al. (2018)
CNF@NiS-2	1768.9	1020.6 (100 cycles)	100	Zhang et al. (2016)
NiS-PPy-CNF	806	669 (30 cycles)	100	Li et al. (2016)

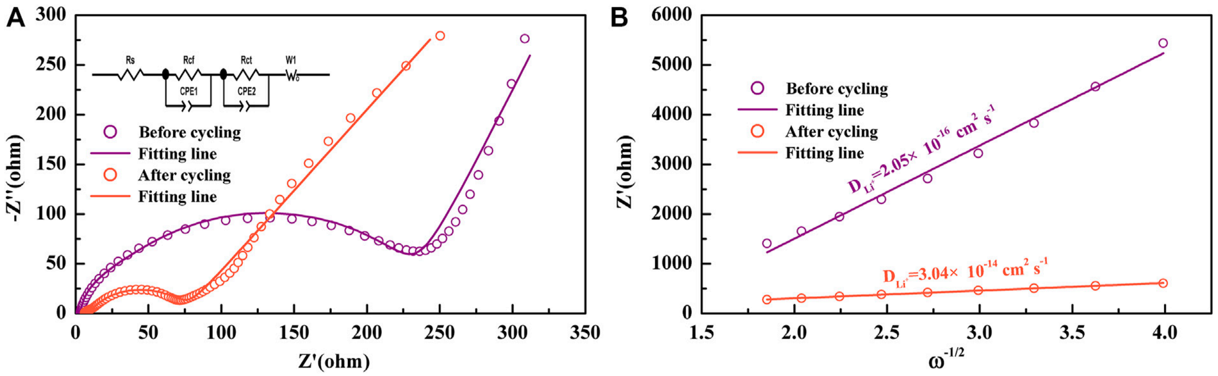

FIGURE 5 | (A) EIS of NiS nanosphere electrodes before and after cycles; the inset is the equivalent circuit. **(B)** $Z' - \omega^{-1/2}$ plots in the low-frequency range of the NiS nanosphere electrodes before and after the cycling performance test.

properties between this work and other NiS-based electrode materials is shown in **Table 1**, which shows the outstanding electrochemical performance of the NiS nanospheres materials.

It can be seen from **Figure 4B** that the specific capacities are 1224.3 mAh g^{-1}, 1157.1 mAh g^{-1}, 1003.6 mAh g^{-1}, and 814.8 mAh g^{-1} at 0.1 A g^{-1}, 0.2 A g^{-1}, 0.5 A g^{-1}, and 0.8 A g^{-1}, respectively. The specific capacity returns to 1130.5 mAh g^{-1} when back to 0.1 A g^{-1}, which shows that the NiS nanosphere electrodes have good reversibility and stability.

Kinetics Characterizations of NiS Nanospheres

To study the kinetic characteristics of NiS nanospheres as anodes of LIBs, the EIS of NiS nanospheres electrodes was measured before and after the cycle test, as shown in **Figure 5A**. The Nyquist curves are both made up of a straight line and two semicircles. The intercept denotes the resistance of the electrolyte and the electrode (R_s), the diameters of the small and large semicircles denote the resistance of the SEI layer to lithium-ions migration (R_{cf}) and the charge transfer resistance (R_{ct}), respectively. It is obvious from **Figure 5A** that both the diameters before the cycle test are much larger than those after the cycle test, which shows that electrons and lithium-ions can move more easily and the NiS nanospheres electrodes have good conductivity during cycles. The insert of **Figure 5A** shows the equivalent circuit of the EIS curves, and all the parameters can be quantitatively fitted by it. The fitted values of R_s, R_{cf}, and R_{ct} are shown in **Table 2**. R_s changes a little before and after the cycle test, but R_{cf} and R_{ct} decrease significantly after the cycle test, which is more conducive to improving reversible capacity and cycle stability (Teng et al., 2020; Ren et al., 2021).

TABLE 2 | Kinetics parameters of NiS nanosphere electrodes.

Parameters	Before cycling	After cycling
R_s (Ohm)	3.438	6.25
R_{cf} (Ohm)	193.2	64.24
R_{ct} (Ohm)	27.81	3.847

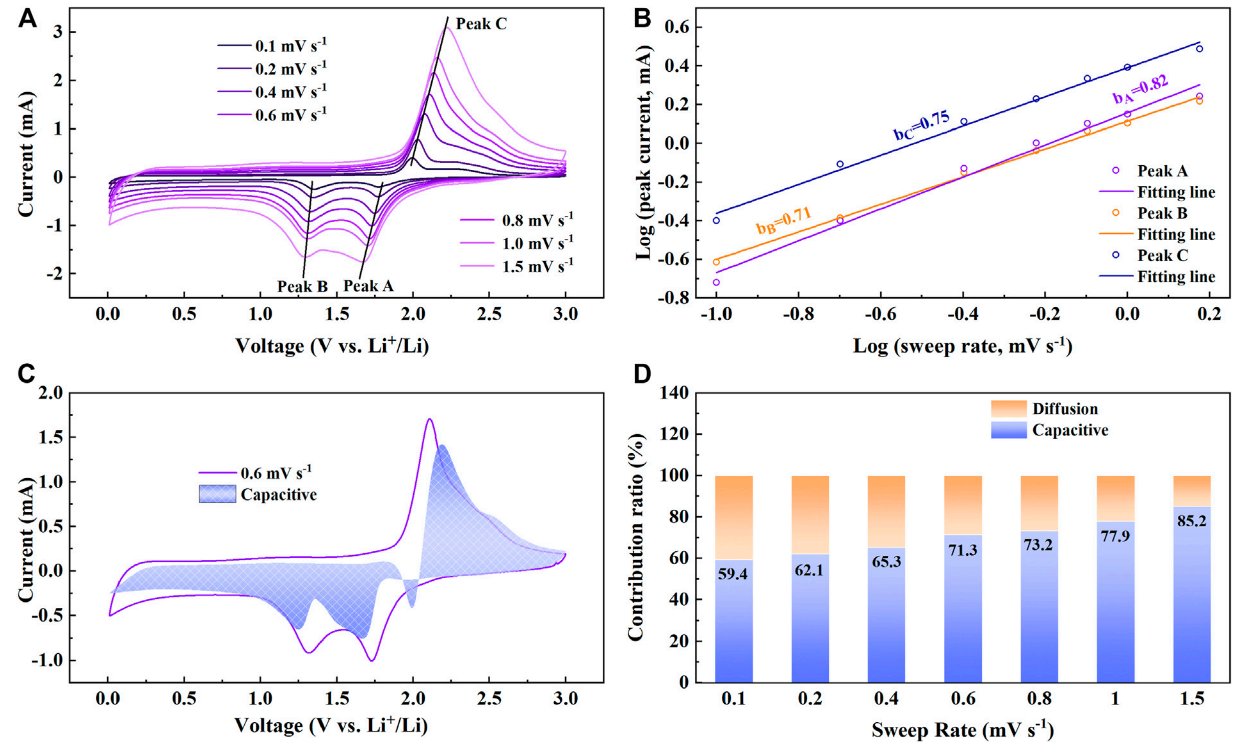

FIGURE 6 | (A) CV curves at different sweep rates. **(B)** The corresponding plots of log(*i*) vs. log(*v*) at three redox peaks. **(C)** The CV curves and the voltage distribution (shaded part) at the sweep rate of 0.6 mV s^{-1}. **(D)** Contribution ratio of capacitive at various sweep rates.

The diffusion coefficient of lithium-ions can be obtained by the following equations (Chen et al., 2018; Teng et al., 2020):

$$Z' = R_s + R_{ct} + R_t + \sigma\omega^{-1/2} \tag{4}$$

$$D_{\mathrm{Li}^+} = \frac{R^2T^2}{2A^2n^4F^4C^2\sigma^2} \tag{5}$$

where R represents the gas constant, T represents the thermodynamic temperature, here is the room temperature, A represents the surface area of the electrode, n stands for the number of electrons transferred in the oxidation or reduction reaction per molecule, f represents the Faraday constant, C represents the concentration of lithium-ions, and σ represents the slopes of $Z' - \omega^{-1/2}$ plots in **Figure 5B**. By calculation, the diffusion coefficients of lithium-ions before and after the cyclic test are $2.05 \times 10^{-16}\,\mathrm{cm}^2\,\mathrm{s}^{-1}$ and $3.04 \times 10^{-14}\,\mathrm{cm}^2\,\mathrm{s}^{-1}$, respectively. With the increase of ion activity, the diffusion rate of lithium-ions and electrons is faster after the cycle test, which may also be one of the reasons for the increase of reversible capacity of NiS nanospheres electrodes during cycling.

To further study the dynamic characteristics of the NiS nanospheres, CV curves at different sweep rates were measured. The shapes of CV curves in **Figure 6A** are very similar, only the intensities of the peaks increase with the increase of sweep rates, which shows that NiS nanosphere electrodes have good cyclic reversibility in the process of lithium and delithium (Ren et al., 2021). The contribution proportions of ion diffusion and capacitance effect in the cycles at different sweep rates can be roughly estimated by the following two equations (Ge et al., 2018; Li W. et al., 2020).

$$i = av^b \tag{6}$$

$$\log(i) = b\log(v) + \log(a) \tag{7}$$

where i represents the peak current, and v represents the sweep rate. It indicates that the charge-discharge process is dominated by ion diffusion when b approaches 0.5, while when b approaches 1, the charge-discharge process mainly depends on the capacitance effect. The b values corresponding to the three peaks of redox reactions are 0.82, 0.71, and 0.75, respectively, as shown in **Figure 6B**, which shows that the current is the result of the joint action of ion diffusion and capacitance effect in these three reaction processes.

To further research the role of capacitance effect in NiS nanospheres electrodes, the following equation can be used to quantitatively calculate the current contribution proportion of capacitance effect (Wang et al., 2007; Ge et al., 2018).

$$i(V) = k_1 v + k_2 v^{1/2} \tag{8}$$

where $k_1 v$ represents the current contribution of capacitance effect and $k_2 v^{1/2}$ represents the current contribution of the ion diffusion. **Figure 6C** shows the voltage distribution (shaded part) of capacitive current at 0.6 mV s^{-1}. The proportion of capacitive current is great at 0.6 mV s^{-1}, reaching 71.3%. **Figure 6D** shows

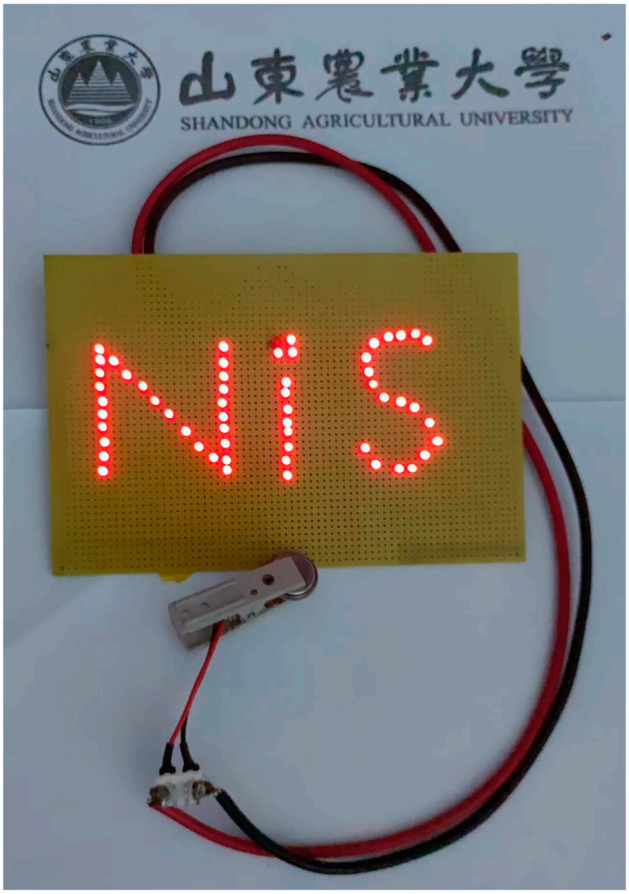

FIGURE 7 | The LED lamps of "NiS" illuminated by two cells in series.

the proportions of capacitance effect and ion diffusion in current contribution at different sweep rates. The current contribution proportion of capacitance effect increases from 59.4 to 85.2% with the increases of sweep rate from 0.1 mV s^{-1} to 1.5 mV s^{-1}. The large current contribution of the capacitance effect also shows that NiS nanosphere electrodes have good rate capability. Two cells in series were used to light up the LED lamps of "NiS", as shown in **Figure 7**, which indicates the potential application of NiS nanosphere material as anode for LIBs.

CONCLUSION

In this paper, NiS nanospheres were successfully synthesized by a simple hydrothermal method. The NiS nanosphere materials used as the anode of LIBs are not only simple to manufacture but also show outstanding electrochemical performance. After 280 charging-discharging circles, a high reversible specific capacity of 1402.3 mAh g^{-1} at 200 mA g^{-1} was obtained. In addition, the NiS nanosphere electrodes display a good rate capability. The reversible capacity still reaches 814.8 mAh g^{-1} even at 0.8 A g^{-1}. In addition, the reversible capacity can still reach 1130.5 mAh g^{-1} when back to 0.1 A g^{-1}. Furthermore, the conductivity after the cycle test is higher than that before the cycle test, which may be one of the reasons why the reversible capacity of NiS nanosphere electrodes increases during cycling. The proportion of capacitance contribution reaches 85.2% at 1.5 mV s^{-1}, showing a strong rate capability of NiS nanospheres electrodes. The outstanding cycling stability and rate capability indicated that the NiS nanosphere materials are more promising anodes for LIBs.

DATA AVAILABILITY STATEMENT

The raw data supporting the conclusion of this article will be made available by the authors, without undue reservation.

AUTHOR CONTRIBUTIONS

All authors listed have made a substantial, direct, and intellectual contribution to the manuscript writing, editing, and reviewing work, and approved it for publication.

FUNDING

This work was funded by the National Natural Science Foundation of China No. 22179066, and the Project of Shandong Province Higher Educational Science and Technology Program (No. J17KA184).

REFERENCES

Chen, H., Zhang, B., Wang, X., Dong, P., Tong, H., Zheng, J.-c., et al. (2018). CNT-decorated $Na_3V_2(PO_4)_3$ Microspheres as a High-Rate and Cycle-Stable Cathode Material for Sodium Ion Batteries. *ACS Appl. Mater. Inter.* 10, 3590–3595. doi:10.1021/acsami.7b16402

Dong, X., Deng, Z.-P., Huo, L.-H., Zhang, X.-F., and Gao, S. (2019). Large-Scale Synthesis of NiS@N and S Co-doped Carbon Mesoporous Tubule as High Performance Anode for Lithium-Ion Battery. *J. Alloys Compounds.* 788, 984–992. doi:10.1016/j.jallcom.2019.02.326

Duan, W., Yan, W., Yan, X., Munakata, H., Jin, Y., and Kanamura, K. (2015). Synthesis of Nanostructured Ni_3S_2 with Different Morphologies as Negative Electrode Materials for Lithium Ion Batteries. *J. Power Sourc.* 293, 706–711. doi:10.1016/j.jpowsour.2015.05.098

Fan, P., Liu, H., Liao, L., Fu, J., Wang, Z., Lv, G., et al. (2017). Flexible and High Capacity Lithium-Ion Battery Anode Based on a Carbon Nanotube/Electrodeposited Nickel Sulfide Paper-like Composite. *RSC Adv.* 7, 49739–49744. doi:10.1039/c7ra08239h

Feng, N., Hu, D., Wang, P., Sun, X., Li, X., and He, D. (2013). Growth of Nanostructured Nickel Sulfide Films on Ni Foam as High-Performance Cathodes for Lithium Ion Batteries. *Phys. Chem. Chem. Phys.* 15, 9924–9930. doi:10.1039/c3cp50615k

Gao, M., Zhou, W.-Y., Mo, Y.-X., Sheng, T., Deng, Y., Chen, L., et al. (2021). Outstanding Long-Cycling Lithium−Sulfur Batteries by Core-Shell Structure of S@Pt Composite with Ultrahigh Sulfur Content. *Adv. Powder Mater.* doi:10.1016/j.apmate.2021.09.006

Ge, P., Hou, H., Li, S., Huang, L., and Ji, X. (2018). Three-Dimensional Hierarchical Framework Assembled by Cobblestone-Like $CoSe_2$@C Nanospheres for Ultrastable Sodium-Ion Storage. *ACS Appl. Mater. Inter.* 10, 14716–14726. doi:10.1021/acsami.8b01888

Gu, Z. Y., Guo, J. Z., Zhao, X. X., Wang, X. T., Xie, D., Sun, Z. H., et al. (2021). High-ionicity Fluorophosphate Lattice via Aliovalent Substitution as Advanced Cathode Materials in Sodium-ion Batteries. *InfoMat.* 3, 694–704. doi:10.1002/inf2.12184

Han, D., Xiao, N., Liu, B., Song, G., and Ding, J. (2017). One-pot Synthesis of Core/Shell-Structured NiS@onion-Like Carbon Nanocapsule as a High-Performance Anode Material for Lithium-Ion Batteries. *Mater. Lett.* 196, 119–122. doi:10.1016/j.matlet.2017.03.042

Hong, S.-H., and Song, M. Y. (2018). Syntheses of Nano-Sized Co-Based Powders by Carbothermal Reduction for Anode Materials of Lithium Ion Batteries. *Ceramics Int.* 44, 4225–4229. doi:10.1016/j.ceramint.2017.12.002

Hou, X., Li, W., Wang, Y., Li, S., Meng, Y., Yu, H., et al. (2020). Sodium-Based Dual-Ion Batteries via Coupling High-Capacity Selenium/Graphene Anode with High-Voltage Graphite Cathode. *Chin. Chem. Lett.* 31, 2314–2318. doi:10.1016/j.cclet.2020.04.021

Hu, Y.-Y., Liu, Z., Nam, K.-W., Borkiewicz, O. J., Cheng, J., Hua, X., et al. (2013). Origin of Additional Capacities in Metal Oxide Lithium-Ion Battery Electrodes. *Nat. Mater.* 12, 1130–1136. doi:10.1038/nmat3784

Jin, R., Jiang, Y., Li, G., and Meng, Y. (2017). Amorphous Carbon Coated Multiwalled Carbon Nanotubes@transition Metal Sulfides Composites as High Performance Anode Materials for Lithium Ion Batteries. *Electrochimica Acta.* 257, 20–30. doi:10.1016/j.electacta.2017.10.078

Kim, H., Choi, W., Yoon, J., Um, J. H., Lee, W., Kim, J., et al. (2020). Exploring Anomalous Charge Storage in Anode Materials for Next-Generation Li Rechargeable Batteries. *Chem. Rev.* 120, 6934–6976. doi:10.1021/acs.chemrev.9b00618

Laruelle, S., Grugeon, S., Poizot, P., Dolle´, M., Dupont, L., and Tarascon, J.-M. (2002). On the Origin of the Extra Electrochemical Capacity Displayed by MO/Li Cells at Low Potential. *J. Electrochem. Soc.* 149, A627–A634. doi:10.1149/1.1467947

Lee, Y.-J., Ha, T.-H., Cho, G.-B., Kim, K.-W., Ahn, J.-H., and Cho, K.-K. (2020). Fabrication of Nickel Sulfide/Nitrogen-Doped Reduced Graphene Oxide Nanocomposite as Anode Material for Lithium-Ion Batteries and its Electrochemical Performance. *J. Nanosci. Nanotechnol.* 20, 6782–6787. doi:10.1166/jnn.2020.18783

Li, H., Guo, S., Shin, K., Wong, M. S., and Henkelman, G. (2019). Design of a Pd-Au Nitrite Reduction Catalyst by Identifying and Optimizing Active Ensembles. *ACS Catal.* 9, 7957–7966. doi:10.1021/acscatal.9b02182

Li, L., Wang, L., Zhang, M., Huang, Q., Chen, L., and Wu, F. (2019). High-Performance Lithium-Ion Battery Anodes Based on Mn_3O_4/Nitrogen-Doped Porous Carbon Hybrid Structures. *J. Alloys Compounds.* 775, 51–58. doi:10.1016/j.jallcom.2018.10.106

Li, S., Li, B., Zhong, Y., Pan, Z., Xu, M., Qiu, Y., et al. (2019). Mn_2O_3@C Yolk-Shell Nanocubes as Lithium-Storage Anode with Suppressed Surface Electrolyte Decomposition. *Mater. Chem. Phys.* 222, 256–262. doi:10.1016/j.matchemphys.2018.10.015

Li, H., Hu, Z., Xia, Q., Zhang, H., Li, Z., Wang, H., et al. (2021). Operando Magnetometry Probing the Charge Storage Mechanism of CoO Lithium-Ion Batteries. *Adv. Mater.* 33, 2006629. doi:10.1002/adma.202006629

Li, S., Gu, Z.-Y., Guo, J.-Z., Hou, X.-K., Yang, X., Zhao, B., et al. (2021). Enhanced Electrode Kinetics and Electrochemical Properties of Low-Cost $NaFe_2PO_4(SO_4)_2$ via Ca^{2+} Doping as Cathode Material for Sodium-Ion Batteries. *J. Mater. Sci. Technology.* 78, 176–182. doi:10.1016/j.jmst.2020.10.047

Li, Z., Zhang, Y., Li, X., Gu, F., Zhang, L., Liu, H., et al. (2021). Reacquainting the Electrochemical Conversion Mechanism of FeS2 Sodium-Ion Batteries by Operando Magnetometry. *J. Am. Chem. Soc.* 143, 12800–12808. doi:10.1021/jacs.1c06115

Li, Q., Li, H., Xia, Q., Hu, Z., Zhu, Y., Yan, S., et al. (2020). Extra Storage Capacity in Transition Metal Oxide Lithium-Ion Batteries Revealed by *In Situ* Magnetometry. *Nat. Mater.* 20, 76–83. doi:10.1038/s41563-020-0756-y

Li, W, Liang, H.-J., Hou, X.-K., Gu, Z.-Y., Zhao, X.-X., Guo, J.-Z., et al. (2020). Feasible Engineering of Cathode Electrolyte Interphase Enables the Profoundly Improved Electrochemical Properties in Dual-Ion Battery. *J. Energ. Chem.* 50, 416–423. doi:10.1016/j.jechem.2020.03.043

Li, X., Chen, Y., Zou, J., Zeng, X., Zhou, L., and Huang, H. (2016). Stable Freestanding Li-Ion Battery Cathodes by *In Situ* Conformal Coating of Conducting Polypyrrole on NiS-Carbon Nanofiber Films. *J. Power Sourc.* 331, 360–365. doi:10.1016/j.jpowsour.2016.09.067

Liang, H., Zhang, H., Zhao, L., Chen, Z., Huang, C., Zhang, C., et al. (2022). Layered $Fe_2(MoO_4)_3$ Assemblies with Pseudocapacitive Properties as Advanced Materials for High-Performance Sodium-Ion Capacitors. *Chem. Eng. J.* 427, 131481–131489. doi:10.1016/j.cej.2021.131481

Ni, S., Yang, X., and Li, T. (2012). Fabrication of a Porous NiS/Ni Nanostructured Electrode via a Dry Thermal Sulfuration Method and its Application in a Lithium Ion Battery. *J. Mater. Chem.* 22, 2395–2397. doi:10.1039/c2jm15394g

Park, J. H., and Lee, J. W. (2019). Visualized Pulverization via *Ex Situ* Analyses: Nickel Sulfide Anode Caged in a Hierarchical Carbon. *J. Electrochem. Soc.* 166, A838–A847. doi:10.1149/2.1071904jes

Ren, H., Wang, J., Cao, Y., Luo, W., and Sun, Y. (2021). Nickel Sulfide Nanoparticle Anchored Reduced Graphene Oxide with Improved Lithium Storage Properties. *Mater. Res. Bull.* 133, 111047–111057. doi:10.1016/j.materresbull.2020.111047

Rui, X., Tan, H., and Yan, Q. (2014). Nanostructured Metal Sulfides for Energy Storage. *Nanoscale.* 6, 9889–9924. doi:10.1039/c4nr03057e

Teng, X., Zhang, F., Li, Q., Wang, X., Ye, W., Li, H., et al. (2020). Interfacial Engineering of Self-Supported SnO_2 Nanorod Arrays as Anode for Flexible Lithium-Ion Batteries. *J. Electrochem. Soc.* 167, 120515–120524. doi:10.1149/1945-7111/abac86

Vadivazhagan, M., Shakkeel, N. K., and Nallathamby, K. (2021). Demonstration of Biocarbon-Added NiS Porous Nanospheres as a Potential Anode for Lithium-Ion Batteries. *Energy Fuels.* 35, 8991–9000. doi:10.1021/acs.energyfuels.1c00582

Wang, J., Polleux, J., Lim, J., and Dunn, B. (2007). Pseudocapacitive Contributions to Electrochemical Energy Storage in TiO_2 (Anatase) Nanoparticles. *J. Phys. Chem. C.* 111, 14925–14931. doi:10.1021/jp074464w

Wang, K., Li, L., Zhang, T., and Liu, Z. (2014). Nitrogen-doped Graphene for Supercapacitor with Long-Term Electrochemical Stability. *Energy.* 70, 612–617. doi:10.1016/j.energy.2014.04.034

Wang, L.-H., Dai, Y.-K., Qin, Y.-F., Chen, J., Zhou, E.-L., Li, Q., et al. (2020). One-Pot Synthesis and High Electrochemical Performance of CuS/$Cu_{1.8}S$ Nanocomposites as Anodes for Lithium-Ion Batteries. *Materials.* 13, 3797–3808. doi:10.3390/ma13173797

Wang, L, Teng, X.-L., Qin, Y.-F., and Li, Q. (2021). High Electrochemical Performance and Structural Stability of CoO Nanosheets/CoO Film as Self-Supported Anodes for Lithium-Ion Batteries. *Ceramics Int.* 47, 5739–5746. doi:10.1016/j.ceramint.2020.10.160

Wang, X., Liu, W., Wang, C., Zhang, S., Ding, M., and Xu, X. (2021). Enhanced Formaldehyde Gas Sensing Performance of Ternary $CuBi_2O_4$ Oxides through Oxygen Vacancy Manipulation and Surface Platinum Decoration. *Sensors Actuators B: Chem.* 344, 130190–130199. doi:10.1016/j.snb.2021.130190

Wang, X., Liu, W., Wang, T., Zhao, Y., Zhao, G., Zhang, S., et al. (2022). Synthesis of Multishelled SnOx/Co_3O_4 Amorphous/Crystalline Heterophase with Galvanic Replacement Reaction for superior HCHO Sensing. *Sensors Actuators B: Chem.* 350, 130876–130886. doi:10.1016/j.snb.2021.130876

Wang, X., Zhang, S., Shao, M., Huang, J., Deng, X., Hou, P., et al. (2017). Fabrication of ZnO/$ZnFe_2O_4$ Hollow Nanocages Through Metal Organic Frameworks Route with Enhanced Gas Sensing Properties. *Sensors Actuators B: Chem.* 251, 27–33. doi:10.1016/j.snb.2017.04.114

Wang, Y., Zhu, Q., Tao, L., and Su, X. (2011). Controlled-Synthesis of NiS Hierarchical Hollow Microspheres with Different Building Blocks and Their Application in Lithium Batteries. *J. Mater. Chem.* 21, 9248–9254. doi:10.1039/c1jm10271k

Wu, X., Li, S., Xu, Y., Wang, B., Liu, J., and Yu, M. (2019). Hierarchical Heterostructures of NiO Nanosheet Arrays Grown on pine Twig-like β-NiS@Ni_3S_2 Frameworks as Free-Standing Integrated Anode for High-Performance Lithium-Ion Batteries. *Chem. Eng. J.* 356, 245–254. doi:10.1016/j.cej.2018.08.187

Xia, G., Li, X., He, J., Wang, Y., Gu, Y., Liu, L., et al. (2021). A Biomass-Derived Biochar-Supported NiS/C Anode Material for Lithium-Ion Batteries. *Ceramics Int.* 47, 20948–20955. doi:10.1016/j.ceramint.2021.04.093

Yang, Z. Y., Yuan, Y. F., Zhu, M., Yin, S. M., Cheng, J. P., and Guo, S. Y. (2021). Superior Rate-Capability and Long-Lifespan Carbon Nanotube-In-nanotube@

Sb_2S_3 Anode for Lithium-Ion Storage. *J. Mater. Chem. A.* 9, 22334–22346. doi:10.1039/d1ta06708g

Zhang, L., Huang, Y., Zhang, Y., Gu, H., Fan, W., and Liu, T. (2016). Flexible Electrospun Carbon Nanofiber@NiS Core/Sheath Hybrid Membranes as Binder-free Anodes for Highly Reversible Lithium Storage. *Adv. Mater. Inter.* 3, 1500467–1500476. doi:10.1002/admi.201500467

Zhang, Y., Lu, F., Pan, L., Xu, Y., Yang, Y., Bando, Y., et al. (2018). Improved Cycling Stability of NiS_2 Cathodes Through Designing a "Kiwano" Hollow Structure. *J. Mater. Chem. A.* 6, 11978–11984. doi:10.1039/c8ta01551a

Zhao, J., Zhang, Y., Wang, Y., Li, H., and Peng, Y. (2018). The Application of Nanostructured Transition Metal Sulfides as Anodes for Lithium Ion Batteries. *J. Energ. Chem.* 27, 1536–1554. doi:10.1016/j.jechem.2018.01.009

Zhao, W. C., Yuan, Y. F., Du, P. F., Yin, S. M., and Guo, S. Y. (2021). Intimately Coupled MoP Nanocrystalline@carbon Nanosheets-Assembled Hierarchical Mesoporous Nanospheres for High-Performance Sodium-Ion Storage. *Electrochimica Acta.* 389, 138712. doi:10.1016/j.electacta.2021.138712

Zheng, Y. Q., Yuan, Y. F., Tong, Z. W., Yin, H., Yin, S. M., and Guo, S. Y. (2020). Watermelon-like TiO_2 Nanoparticle (P25)@microporous Amorphous Carbon Sphere with Excellent Rate Capability and Cycling Performance for Lithium-Ion Batteries. *Nanotechnology.* 31, 215407. doi:10.1088/1361-6528/ab73be

Zhou, Y., Huang, Y., Pang, J., and Wang, K. (2019). Remaining Useful Life Prediction for Supercapacitor Based on Long Short-Term Memory Neural Network. *J. Power Sourc.* 440, 227149–227157. doi:10.1016/j.jpowsour.2019.227149

Zhukovskii, Y. F., Balaya, P., Kotomin, E. A., and Maier, J. (2006). Evidence for Interfacial-Storage Anomaly in Nanocomposites for Lithium Batteries from First-Principles Simulations. *Phys. Rev. Lett.* 96, 058302. doi:10.1103/PhysRevLett.96.058302

Conflict of Interest: The authors declare that the research was conducted in the absence of any commercial or financial relationships that could be construed as a potential conflict of interest.

frontiers
in Chemistry

ORIGINAL RESEARCH
published: 10 February 2022
doi: 10.3389/fchem.2021.830485

Energy-Saving Synthesis of Functional CoS_2/rGO Interlayer With Enhanced Conversion Kinetics for High-Performance Lithium-Sulfur Batteries

Junan Feng[1†], Yahui Li[1†], Jinshi Yuan[1], Yuling Zhao[1], Jianmin Zhang[2], Fengyun Wang[1], Jie Tang[3] and Jianjun Song[1]**

[1]College of Physics, Qingdao University, Qingdao, China, [2]National Engineering Research Center for Intelligent Electrical Vehicle Power System (Qingdao), College of Mechanical and Electrical Engineering, Qingdao University, Qingdao, China, [3]National Institute for Materials Science, Tsukuba, Japan

Edited by:
Pan Xiong,
Nanjing University of Science and Technology, China

Reviewed by:
Borui Liu,
The University of Sydney, Australia
Tao Yang,
Hangzhou Dianzi University, China

***Correspondence:**
Jie Tang
tang.jie@nims.go.jp
Jianjun Song
Jianjun.song@qdu.edu.cn

†These authors have contributed equally to this work

Specialty section:
This article was submitted to Electrochemistry,
a section of the journal
Frontiers in Chemistry

Received: *07 December 2021*
Accepted: *22 December 2021*
Published: *10 February 2022*

Citation:
Feng J, Li Y, Yuan J, Zhao Y, Zhang J, Wang F, Tang J and Song J (2022) Energy-Saving Synthesis of Functional CoS_2/rGO Interlayer With Enhanced Conversion Kinetics for High-Performance Lithium-Sulfur Batteries. Front. Chem. 9:830485.
doi: 10.3389/fchem.2021.830485

Lithium sulfur (Li-S) battery has exhibited great application potential in next-generation high-density secondary battery systems due to their excellent energy density and high specific capacity. However, the practical industrialization of Li-S battery is still affected by the low conductivity of sulfur and its discharge product (Li_2S_2/Li_2S), the shuttle effect of lithium polysulfide (Li_2S_n, $4 \leq n \leq 8$) during charging/discharging process and so on. Here, cobalt disulfide/reduced graphene oxide (CoS_2/rGO) composites were easily and efficiently prepared through an energy-saving microwave-assisted hydrothermal method and employed as functional interlayer on commercial polypropylene separator to enhance the electrochemical performance of Li-S battery. As a physical barrier and second current collector, the porous conductive rGO can relieve the shuttle effect of polysulfides and ensure fast electron/ion transfer. Polar CoS_2 nanoparticles uniformly distributed on rGO provide strong chemical adsorption to capture polysulfides. Benefitting from the synergy of physical and chemical constraints on polysulfides, the Li-S battery with CoS_2/rGO functional separator exhibits enhanced conversion kinetics and excellent electrochemical performance with a high cycling initial capacity of 1,122.3 mAh g^{-1} at 0.2 C, good rate capabilities with 583.9 mAh g^{-1} at 2 C, and long-term cycle stability (decay rate of 0.08% per cycle at 0.5 C). This work provides an efficient and energy/time-saving microwave hydrothermal method for the synthesis of functional materials in stable Li-S battery.

Keywords: cobalt disulfide, microwave hydrothermal, conversion kinetics, shuttle effect, lithium-sulfur battery

INTRODUCTION

Lithium-ion batteries systems have played a crucial role in the field of energy storage over the past two decades (Lu, et al., 2013; Manthiram, 2017; Ma, et al., 2021a). However, traditional lithium-ion battery electrode materials ($LiCoO_2$, $LiMn_2O_4$, $LiFePO_4$, etc.) cannot satisfy the requirement for high energy density in practical applications due to their limited energy density (Wang et al., 2015; Liu et al., 2020b; Zhang F. et al., 2021). With the development of energy technology in electronic devices and new energy vehicles, energy storage systems with low prices, that are environment friendly, and with excellent energy density have attracted great attention (Manthiram, et al., 2014; Bhargav, et al., 2020; Guo, et al., 2022). Lithium-sulfur (Li-S) battery has exhibited great application potential in next-generation high-density battery systems due to its high specific capacity (1,672 mAh g^{-1}) and gratifying theoretical energy density (2,567 Wh kg^{-1}) (Pang et al., 2016; Li Y. et al., 2018). However, the commercial viability of high-efficiency Li-S battery is limited by a series of shortcomings. Due to the low conductivity of sulfur and Li_2S_2/Li_2S (Chung and Manthiram, 2018; Zhao Z. et al., 2020), the serious shuttle effect of polysulfides soluble in electrolyte (LiPSs) (Li_2S_n, $4 \le n \le 8$) during charging/discharging, and inevitable growth of lithium dendrites (Zhou et al., 2021), the cycle stability of Li-S battery is unsatisfactory, which seriously hinders the development of Li-S battery (Xu et al., 2018; Hu et al., 2020). So far, numerous methods have been developed to solve these problems, including designing suitable cathode materials (Chen et al., 2017; You et al., 2019; Yan et al., 2020), modifying separators (Bai et al., 2016; Guo et al., 2019; Hu et al., 2021), and optimizing electrolytes (Agostini et al., 2015; Wang et al., 2016; Wan, et al., 2021). Among them, the simplest and most direct strategy is to modify the separator by constructing a reasonable functional interlayer to limit the severe shuttle effect (Rana et al., 2019; Wei et al., 2020).

As a key component of Li-S battery, the separator mainly prevents internal short circuits and provides a transmission path for ions (Ghazi et al., 2017). However, the conventional separator cannot suppress the shuttle effect of polysulfides owing to its highly micron-scale pore structure. In this case, coating a thin functional interlayer separator on the cathode side has proven to be a rational method, which can significantly immobilize polysulfides, improve the utilization of sulfur, and prevent the growth of lithium dendrite on the anode side (Li et al., 2017; Zhao et al., 2021). The functional separator facing the cathode electrode is the first barrier to limit the polysulfide, greatly increasing the utilization rate of sulfur species, and has attracted widespread attention in recent years (Zhang et al., 2015; Song et al., 2016; Liu et al., 2021). A variety of materials have been studied as functional interlayers for preventing the shuttle of polysulfides (LiPSs). First, one-dimensional (1D) (Chung and Manthiram, 2014; Gu, et al., 2020; Lin, et al., 2021) or two-dimensional (2D) (Wu et al., 2016; Lei et al., 2018; Zhang et al., 2018; Song et al., 2019) materials are introduced as the physical function coating to functionalize the conventional separator. Considering that polar materials can lead to chemical bonding with polysulfides, some polar transition metal compounds (CeO_2, MnO_2, CoS_2, Co_9S_8, MoS_2, Ni_2P, etc.) were subsequently studied (Zhou et al., 2016; Li G. et al., 2018; Song et al., 2018; Tan et al., 2018; Li et al., 2020; Zhang H. et al., 2021), which can not only provide strong chemical interaction with soluble polysulfides but also play a role in electrochemical catalysis to promote redox reaction kinetics and reduce electrochemical polarization.

In this work, for the first time, we report an energy-saving synthesis of 3D porous CoS_2/rGO composites as functional interlayer through an efficient microwave-assisted hydrothermal method to improve the electrochemical performance of Li-S battery. The microwave hydrothermal method has the advantages of fast nucleation speed, short reaction time, and energy conservation, and thus it is beneficial to improve the synthesis efficiency of composite materials (Kim et al., 2016; Yuan et al., 2016). The porous conductive graphene can serve as both the first barrier to physically block LiPSs and a second current collector to reduce electrochemical resistance, promoting electron/ion transfer (Zhang et al., 2020). Meanwhile, CoS_2 particles which are *in situ* grown in the network of reduced graphene oxide (rGO) could not only improve adsorption ability for LiPSs but also act as catalytic centers to ensure the fast electrochemical redox conversion kinetics, further minimizing the loss of active materials (Abdul Razzaq et al., 2020). Therefore, as illustrated in **Scheme 1**, due to the double blocking of physical barrier and chemical interaction, compared with the traditional polypropylene (PP) separators, the functional CoS_2/rGO modified separator effectively eases the shuttle effect of LiPSs, accelerates the redox reaction kinetics, and thus improves the cycle stability and rate performance of the Li-S battery.

EXPERIMENTAL SECTION

Preparation of CoS_2/rGO Composite

Graphene oxide (GO) was synthesized by a modified Hummers method. Disperse 30 mg GO into 40 ml solution and sonicate for 1 h. Add 40 mg $CoCl_2 \cdot 6H_2O$ and 80 mg CH_4N_2S into the above

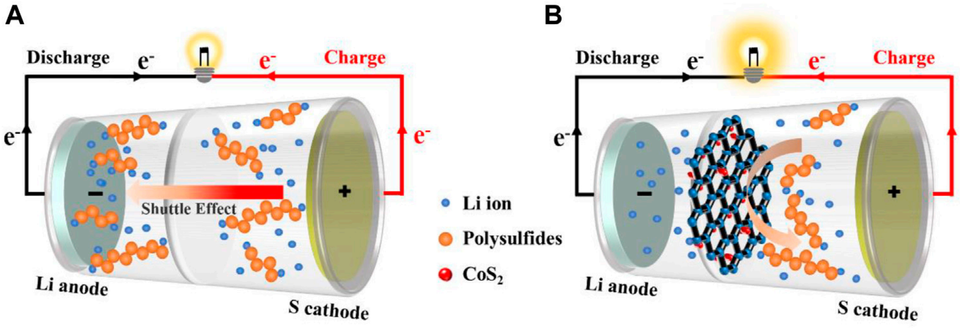

SCHEME 1 | Schematic diagram of the cells without **(A)** and with **(B)** functional CoS_2/rGO interlayer.

dispersion and stir for 10 min. Then, pour it into a digestion tank and allow to react for 5 min under microwave hydrothermal process. After the reaction, the product was repeatedly washed several times and then freeze-dried for 24 h to obtain CoS_2/rGO composites. In addition, the rGO was also synthesized according to the same route without the addition of $CoCl_2 \cdot 6H_2O$ and CH_4N_2S.

Preparation of Cathode

Sulfur and carbon black (sulfur:carbon black = 7:3) are mixed and ground uniformly and then transferred to a polytetrafluoroethylene container for reaction at 155°C for 12 h to obtain sulfur and carbon black (S/C) composites. The S/C cathode slurry was prepared by uniformly mixing 80% S/C, 10% carbon black additive, and 10% polyvinylidene difluoride (PVDF) in *N*-methyl-2-pyrrolidone (NMP) and then was evenly coated on the aluminum foil and dried under vacuum at 60°C for 12 h. The dried aluminum foil electrode is cut into a disc with a diameter of 12 mm, and the S loading of the cathode is 1 mg cm^{-2}.

Preparation of CoS_2/rGO or rGO Modified Separator

The CoS_2/rGO composite or rGO prepared by the microwave hydrothermal method was mixed with PVDF with a mass ratio of 9:1 in NMP. The slurry was ground uniformly then coated on one side of the commercial PP separator and dried under vacuum at 60°C for 12 h. The modified separators are cut into 19 mm discs, and the mass loading of CoS_2/rGO or rGO is only about 0.19 mg cm^{-2}.

Electrochemical Measurements

Li-S batteries (CR 2032) are assembled in a glovebox filled with inert gas (H_2O, $O_2 < 0.1$ ppm). Lithium foil as the anode, S/C composites as cathode, and 1.0 M LiTFSI dissolved in a DOL/DME (volume ratio is 1:1) mixed solvent with 0.1 M $LiNO_3$ additive as electrolyte. The amount of electrolyte used in each cell is 15 μl. For high sulfur loading of 3.1 mg cm^{-2}, a low electrolyte/sulfur (E/S) ratio of ~5 μl mg^{-1} was used.

Materials Characterization and Electrochemical Analysis

The crystal phase, morphologies, and microstructure of the different samples were characterized with X-ray diffraction (XRD, Ultima IV, CuKα radiation), scanning electron microscope (SEM, Sigma500), and transmission electron microscope (TEM, JSM-2100 Plus), respectively. X-ray photoelectron spectrometer (XPS, PHI 5000) was used to survey the composition of elements and chemical state. Thermogravimetric analysis (TGA, TG 209 F3) was used to estimate the S content of the S/KB cathode. Electrochemical workstation (CHI 760E) was used to measure the original date of cyclic voltammetry (CV, the voltage range is 1.7–2.8 V with 0.1 mV S^{-1} scan rate) and electrochemical impedance spectroscopy (EIS, the AC voltage amplitude is 5 mV and the frequency range is 0.01 Hz–100 kHz). The electrochemical performance and constant current charge/discharge curve were gauged by Land CT 2001A battery test system in the 1.7–2.8 V voltage range.

RESULTS AND DISCUSSION

Figures 1A, B show the morphologies and microstructure of rGO and CoS_2/rGO composites investigated by SEM; CoS_2/rGO composites present a highly 3D porous structure, ensuring enough space to store LiPSs and accelerate ion diffusion (Zhao M. et al., 2020). CoS_2 particles were evenly distributed on rGO sheet without any agglomeration, which is conducive to chemical adsorption of LiPSs. **Supplementary Figures S1A,B** show the rGO has a similar porous structure to CoS_2/rGO composites. The high conductivity porous rGO framework forms the second current collector and ensures the rapid supply of electrons for electrochemical reactions (Chong et al., 2018). The TEM images of the CoS_2/rGO composites in **Figures 1C, D** clearly show that the CoS_2 particles with a diameter of about 50 nm were uniformly attached to the rGO sheet, matching well with the SEM images results. The high-resolution TEM (HRTEM) images in **Figures 1E, F** exhibit that the parallel lattice fringe is 0.32 nm, which can be indexed to the (111) crystal plane of CoS_2 particle.

The phase of CoS_2/rGO was studied *via* XRD, as shown in **Figure 2A**; the sharp diffraction peaks in the CoS_2/rGO matched well with the characteristic peak of cubic CoS_2 (PDF#41-1,471). No other impurity phases exist except for the characteristic peak of rGO at ~25°. For confirming the chemical valence and element of GO and CoS_2/rGO composites, XPS test result is shown in **Figure 2B**; the fitting curves present the presence of Co, S, and C components in CoS_2/rGO materials, consistent with the XRD results. In particular, **Figure 2C** exhibits the C 1s HR-XPS spectrum of GO, four peaks at 289.1, 287.2, 286.8, and 284.6 eV, representing O-C=O, C=O, C-O, and C=C, respectively (Yuan, et al., 2015). As expected, the peak intensity ratio of these oxygen-containing functional groups in the CoS_2/rGO is much lower than the peak intensity ratio in the GO sample (**Figure 2D**); this comparison demonstrated that GO can be effectively reduced to rGO during the microwave hydrothermal process. As shown in **Figure 2E**, the Co $2p_{1/2}$ and Co $2p_{3/2}$ characteristic peaks of CoS_2 were located at 794.4 and 779.4 eV in the HR-XPS of Co 2p, respectively. (Xu, et al., 2021). The satellite peak signal is 781.8, 786.1, 797.5, and 803.4 eV (Wang, et al., 2018). The fitting results of **Figure 2F** for the HR-XPS of S 2p of the characteristic peak of S $2p_{1/2}$ and S $2p_{3/2}$ are shown at 164.4 and 163.2 eV, which corresponds to S $2p_{1/2}$ and S $2p_{3/2}$ of CoS_2. The HR-XPS of S 2p detected peaks at 168.1 and 169.3 eV indicating the presence of sulfur oxides (Liu et al., 2020c). Therefore, the results demonstrate the successful preparation of CoS_2/rGO material by the microwave hydrothermal method.

Figure 3A shows a uniform coating surface and good mechanical flexibility of the CoS_2/rGO modified separator. The cross-sectional image indicates that the coating thickness of CoS_2/rGO functional interlayer is about 4.8 μm (**Figure 3B**). **Figure 3C** shows the top view SEM morphology of PP separator, and it can be seen that the PP separator possesses abundant pores

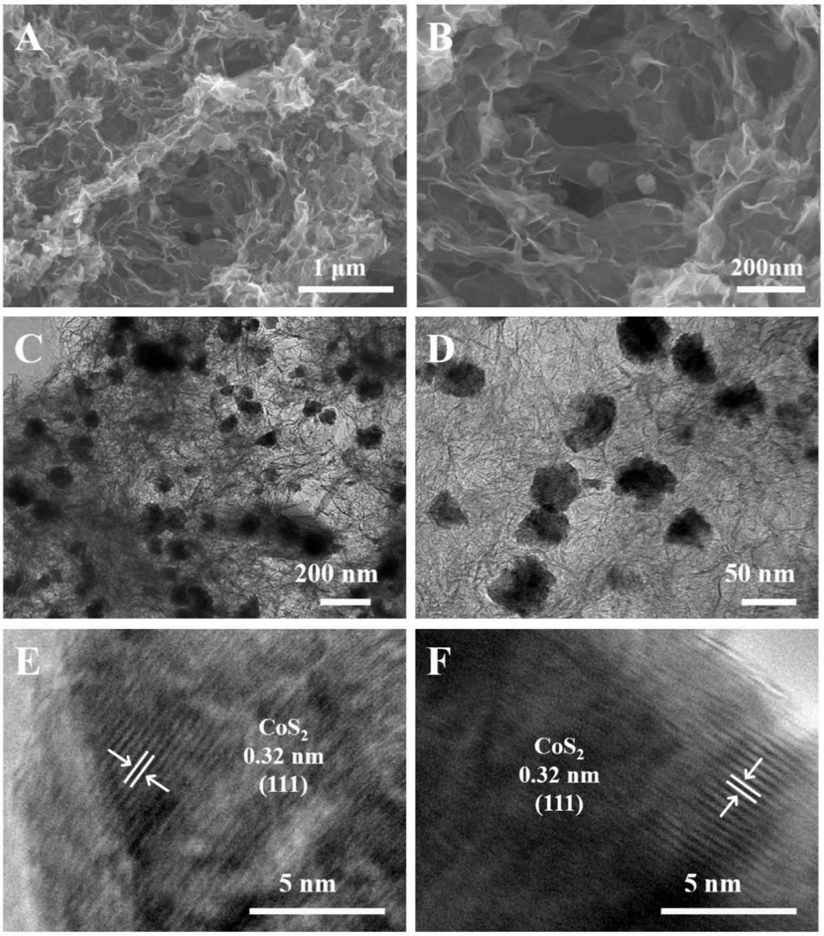

FIGURE 1 | (A,B) SEM, **(C,D)** TEM, and **(E,F)** HRTEM images of the CoS_2/rGO.

with a size of 100–200 nm in width and micron scale in length, which is conducive to the rapid transmission of ions in electrolyte, while inevitably allowing the shuttle of soluble LiPSs in the pores, resulting in the existence of side reactions and irreversible loss of sulfur active substances. (Balach, et al., 2015; Xiong, et al., 2021). However, the top view SEM image of CoS_2/rGO modified separator in **Figure 3D** indicates that the CoS_2/rGO functional interlayer is evenly covered on the surface of PP separator to form a compact physical layer to block the migration of LiPSs and retains abundant pores to ensure fast ion transfer, which is similar with the surface of rGO layer (**Supplementary Figure S2B**).

The Li-S batteries with PP separator, rGO, and CoS_2/rGO modified separators were subjected to the corresponding electrochemical tests for proving the superiority of CoS_2/rGO modified separator in electrochemical performance. The S/C compound is used as the cathode electrode. TGA confirms the content of S in the S/C precursor is 70% (**Figure 4A**). **Figure 4B** shows the CV curves of the Li-S batteries with a PP separator, rGO modified separator, and CoS_2/rGO modified separator between the voltages of 1.7 and 2.8 V at the scanning rate of 0.1 mV S^{-1}. Two typical cathodic peaks were located at 2.33 and 2.02 V, which corresponds to the reduction process from solid S_8 to soluble LiPSs and then further to solid-phase Li_2S_2/Li_2S (Fan et al., 2019), while the continuous anodic peak at 2.36–2.40 V was attributed to the reversible oxidation of sulfur species to S_8 (Zhuang et al., 2020). It can be seen from **Figure 4B** that, compared with PP separator and rGO modified separator, the Li-S battery with CoS_2/rGO modified separator shows sharper redox peaks and higher peak current responses, which can be owing to the robust interaction for LiPSs and the accelerated redox kinetics by the electrochemical catalytic ability of CoS_2 (Li et al., 2021; Yuan et al., 2017). At the same time, **Figure 4C** shows the CV curves of a Li-S battery with a CoS_2/rGO modified separator for four cycles. The well-overlapped curves with each other further proved the good reversibility and the strong immobilization ability of LiPSs (Liu, et al., 2019). EIS of the Li-S batteries with PP separator, rGO, and CoS_2/rGO modified separators before cycling and after 50 cycles was conducted and shown in **Figure 4D**; the diameter of the semicircle in the low-frequency region represents the charge transfer resistance (R_{ct}) (Deng et al., 2013; Cui et al., 2021). It can be seen that fresh cells with CoS_2/rGO modified separator exhibited the smallest R_{ct} value when compared with PP separator and rGO modified

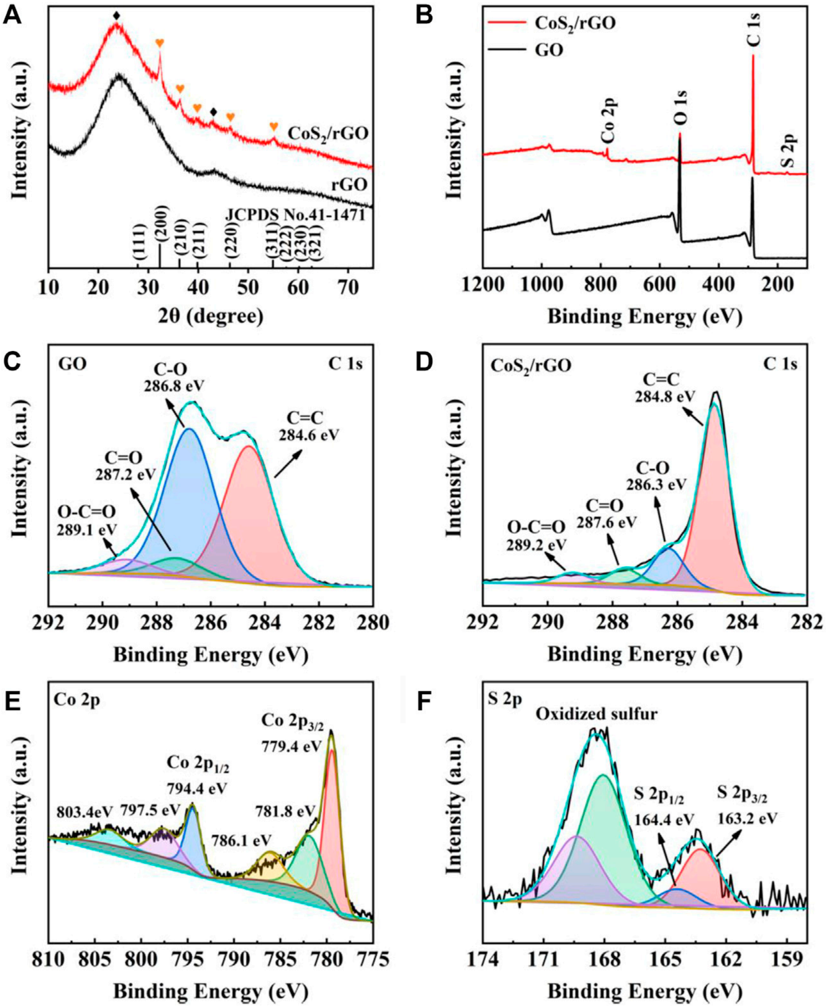

FIGURE 2 | (A) XRD patterns of rGO and CoS$_2$/rGO; **(B)** full XPS spectrum of GO and CoS$_2$/rGO; high-resolution XPS (HR-XPS) spectra of C 1s **(C)** for GO; C 1s **(D)**, Co 2p **(E)**, and S 2p **(F)** for CoS$_2$/rGO.

separator, which indicates that CoS$_2$ uniformly attached in rGO could effectively ensure fast transmission for Li$^+$ migration and reduce the charge transfer resistance. After cycling at 1 C for 50 cycles, the values of R$_{ct}$ show an increase, which can be ascribed to the redistribution of S and the accumulation of Li$_2$S and Li$_2$S$_2$ in porous structure. Li-S battery with CoS$_2$/rGO modified separator still shows the smallest R$_{ct}$ value. change than that of the other two cells after cycling, suggesting that CoS$_2$/rGO modified separator could effectively ease the accumulation of LiPSs and improve the utilization of sulfur active materials (Liu et al., 2020a; Ma et al., 2021b).

Figure 5A appraises the cycle stability of the Li-S batteries with different separators for 100 cycles at 0.2 C. The cells with CoS$_2$/rGO modified separator show the highest first discharge capacity of 1,122.3 mAh g^{-1}. It is worth noting that the specific capacity remains at 897.8 mAh g^{-1} with a capacity retention rate of 80% after 100 cycles. In contrast, the initial discharge capacity of the batteries with rGO and PP separator are 970.7 and 646.9 mAh g^{-1} at 0.2 C; after 100 cycles, the capacity only remains at 631.2 and 275.9 mAh g^{-1}, respectively (the capacity retention rates are 65% and 42%). In addition, the Li-S battery with CoS$_2$/rGO modified separator also exhibits excellent rate performance. As shown in **Figure 5B**. The discharge capacity of Li-S battery with CoS$_2$/rGO modified separator at 0.1–1 C is 1,218.3, 1,093, 930.2, and 760.1 mAh g^{-1}, respectively. Even at a high current density of 2 C, the corresponding capacity is still 583.9 mAh g^{-1}. When the current density is converted back to 0.1 C, the reversible discharge capacity is 1,110.5 mAh g^{-1}, indicating its high reversibility. Furthermore, the charge/discharge profiles of batteries with different separators at 0.1–2 C current density are also investigated; the Li-S battery with CoS$_2$/rGO modified separator shows a more stable and flatter potential platform than Li-S batteries and other separators at different current densities (**Figure 5C**) at different current rates of charge and discharge, and the platform reflects its better electrochemical accessibility. Besides, the degree of electrochemical polarization gradually intensifies with the increases

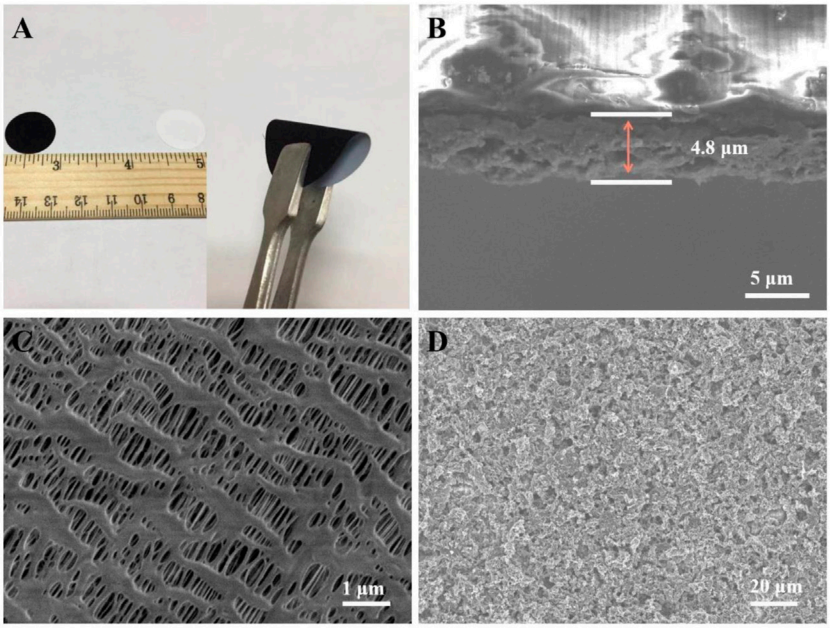

FIGURE 3 | **(A)** Digital images of the CoS_2/rGO modified separator; **(B)** cross-sectional SEM image of the CoS_2/rGO modified separator; **(C,D)** top-view SEM image of the PP separator and CoS_2/rGO modified separator, respectively.

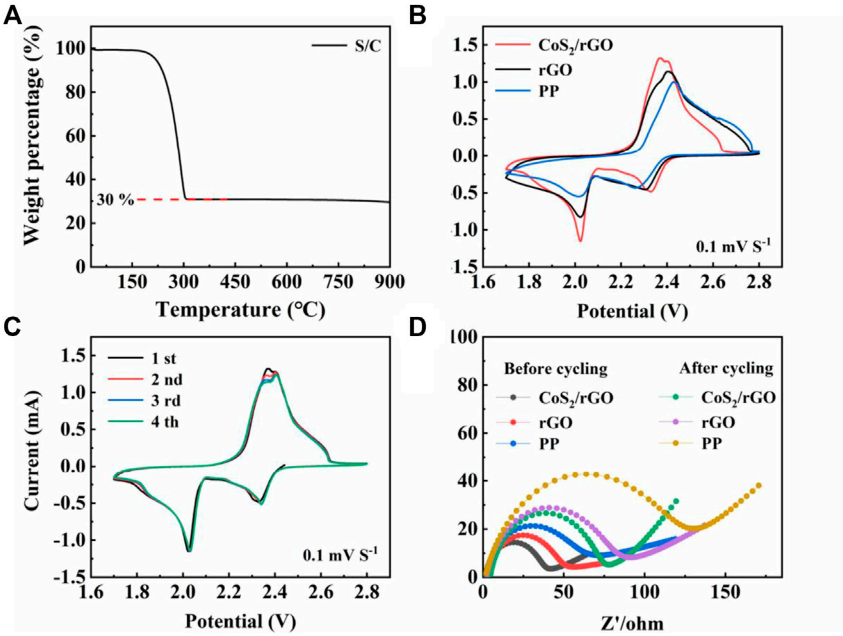

FIGURE 4 | **(A)** TGA curves of S/C; **(B)** CV curves of the Li-S cells with different separators under 0.1 mV S^{-1}; **(C)** CV curves of Li-S cell with CoS_2/rGO modified separator for four cycles at the scan rate of 0.1 mV S^{-1}; **(D)** Nyquist plots of Li-S cells with different separators before and after cycling.

of current density; as shown in **Figures 5C–E**, the Li-S battery using CoS_2/rGO modified separator shows the lowest potential plateau gaps between different charge/discharge profiles than others, with platform potential difference of 168, 187, 248, 303, and 410 mV at 0.1–2 C, suggesting the excellent electrocatalysis of polar CoS_2 nanoparticles could alleviate electrochemical polarization. The above results demonstrate that the CoS_2/rGO modified separator could effectively capture LiPSs and catalyze its conversion to Li_2S_2/Li_2S, thus achieving fast redox reaction kinetics and suppressed shuttle effect.

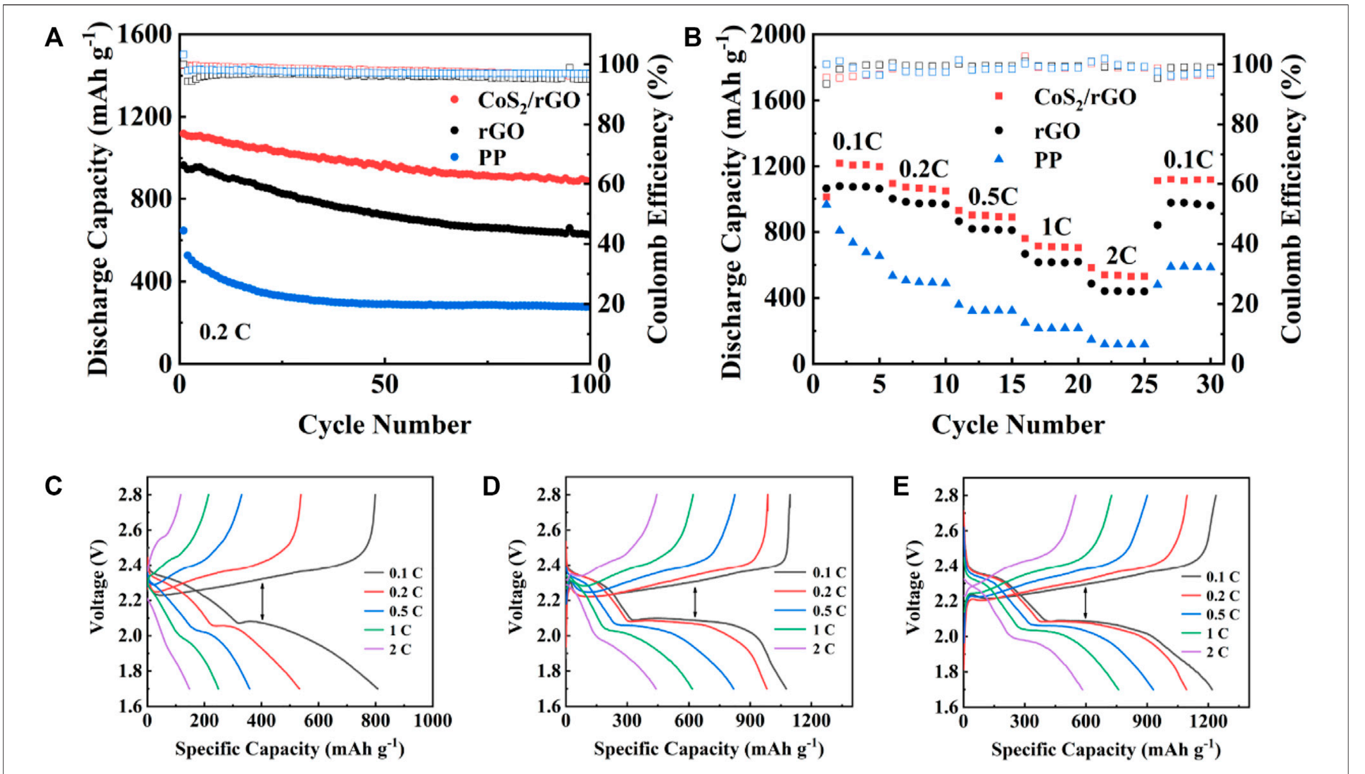

FIGURE 5 | (A,B) Cycling and rate performance of the Li-S batteries with CoS_2/rGO, rGO, and PP separator at 0.2 C; discharge/charge profiles of cells with PP **(C)**, rGO **(D)**, and CoS_2/rGO **(E)** separators at different rates.

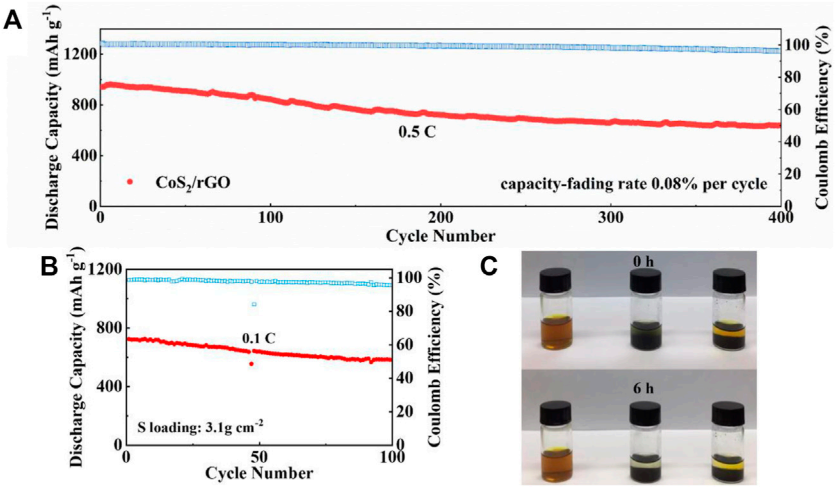

FIGURE 6 | (A) The long cycling performance of the Li-S battery with CoS_2/rGO separator at 0.5 C for 400 cycles; **(B)** cycle stability of the Li-S battery with CoS_2/rGO separator of high S loading at 0.1 C; **(C)** digital images of Li_2S_6 adsorption test for 0 and 6 h, respectively.

The long-term cyclabilities of the Li-S battery with CoS_2/rGO modified separator were further evaluated in **Figure 6A**. At a discharge current density of 0.5 C, the first discharge capacity of the Li-S battery with the CoS_2/rGO modified separator is 963.2 mAh g^{-1}. After 400 cycles, the discharge capacity remains at 640.8 mAh g^{-1}, and the average capacity decay rate per cycle is only 0.08%; meanwhile, the average Coulombic efficiency of 98.3% was achieved. The stable Coulombic efficiency indicates that the CoS_2/rGO interlayer effectively inhibits the shuttle effect and the irreversible wastage of lithium metal. More satisfyingly, after four cycles activated at 0.02 C, the battery can deliver reliable stability under high S loading of 3.1 mg cm^{-2}; the capacity reaches 725.1 mAh g^{-1} at 0.1 C and remains at 583.4 mAh g^{-1} after 100 cycles with a high capacity retention ratio of about 80% (**Figure 6B**). This shows that the Li-S battery with CoS_2/rGO modified separator has great potential for practical applications. Meanwhile, a plain visual Li_2S_6 adsorption test was used to measure the capability of the CoS_2/rGO to capture LiPSs. With the same mass of CoS_2/rGO and rGO immersed in equal volume brown Li_2S_6 solution, in **Figure 6C**, after static holding for 6 h, the color of the solution in the bottle containing rGO retains pale yellow, indicating that rGO only has poor physical adsorption to LiPSs. In sharp contrast, the color of the solution for CoS_2/rGO changed from brown to nearly transparent, which clearly confirms the effective chemical interaction of CoS_2/rGO with LiPSs.

CONCLUSION

In summary, we report a simple and energy-saving synthesis of CoS_2/rGO composites *via* a facile microwave hydrothermal method and applied it as an efficient mediator to trap LiPSs and accelerate its reaction kinetics to reinforce the electrochemical performance of Li-S battery. In this structure, high conductivity rGO network can shorten the path of ion migration and therefore reduce the internal resistance of cells. The porous structure of rGO combining the polar sites of CoS_2 nanoparticles could fix the soluble LiPSs on the cathode side through physical and chemical adsorption and enhance redox kinetics as an efficient electrochemical catalyst, thereby efficiently alleviating the shuttle effect of the LiPSs through the separator. Therefore, the Li-S battery with CoS_2/rGO modified separator exhibits excellent rate performance and stable cycling performance under high sulfur loading of 3.1 mg cm^{-2}.

DATA AVAILABILITY STATEMENT

The raw data supporting the conclusion of this article will be made available by the authors, without undue reservation.

AUTHOR CONTRIBUTIONS

JF: Investigation, methodology, formal analysis, data curation, writing—original draft. YL: Investigation, methodology, formal analysis, data curation, writing—original draft. JY: Review and editing, data curation. YZ: Review and editing, data curation. JZ: Review and editing, data curation. FW: Review and editing. JT: Project administration, resources, funding acquisition, writing—review and editing, supervision. JS: Project administration, resources, funding acquisition, writing—review and editing, supervision.

FUNDING

This work was financially supported by Taishan Oversea Scholar Program of Shandong Province, China, the Natural Science Foundation of Shandong Province, China (ZR2021QE192), China Postdoctoral Science Foundation (2018M63074), Source Innovation Project of Qingdao (19-6-2-19-cg), and Qingdao Postdoctoral Applied Research Project.

SUPPLEMENTARY MATERIAL

The Supplementary Material for this article can be found online at: https://www.frontiersin.org/articles/10.3389/fchem.2021.830485/full#supplementary-material

REFERENCES

Abdul Razzaq, A., Yuan, X., Chen, Y., Hu, J., Mu, Q., Ma, Y., et al. (2020). Anchoring MOF-Derived CoS_2 on Sulfurized Polyacrylonitrile Nanofibers for High Areal Capacity Lithium–Sulfur Batteries. *J. Mater. Chem. A.* 8, 1298–1306. doi:10.1039/c9ta11390h

Agostini, M., Xiong, S., Matic, A., and Hassoun, J. (2015). Polysulfide-containing Glyme-Based Electrolytes for Lithium Sulfur Battery. *Chem. Mater.* 27, 4604–4611. doi:10.1021/acs.chemmater.5b00896

Bai, S., Liu, X., Zhu, K., Wu, S., and Zhou, H. (2016). Metal–organic Framework-Based Separator for Lithium–Sulfur Batteries. *Nat. Energ.* 1, 16094. doi:10.1038/nenergy.2016.94

Balach, J., Jaumann, T., Klose, M., Oswald, S., Eckert, J., and Giebeler, L. (2015). Functional Mesoporous Carbon-Coated Separator for Long-Life, High-Energy Lithium-Sulfur Batteries. *Adv. Funct. Mater.* 25, 5285–5291. doi:10.1002/adfm.201502251

Bhargav, A., He, J., Gupta, A., and Manthiram, A. (2020). Lithium-Sulfur Batteries: Attaining the Critical Metrics. *Joule* 4, 285–291. doi:10.1016/j.joule.2020.01.001

Chen, T., Ma, L., Cheng, B., Chen, R., Hu, Y., Zhu, G., et al. (2017). Metallic and Polar Co_9S_8 Inlaid Carbon Hollow Nanopolyhedra as Efficient Polysulfide Mediator for Lithium−sulfur Batteries. *Nano Energy* 38, 239–248. doi:10.1016/j.nanoen.2017.05.064

Chong, W. G., Xiao, Y., Huang, J.-Q., Yao, S., Cui, J., Qin, L., et al. (2018). Highly Conductive Porous Graphene/sulfur Composite Ribbon Electrodes for Flexible Lithium–Sulfur Batteries. *Nanoscale* 10, 21132–21141. doi:10.1039/C8NR06666C

Chung, S. H., and Manthiram, A. (2014). High-performance Li-S Batteries with an Ultra-lightweight MWCNT-Coated Separator. *J. Phys. Chem. Lett.* 5, 1978–1983. doi:10.1021/jz5006913

Chung, S.-H., and Manthiram, A. (2018). Designing Lithium-Sulfur Cells with Practically Necessary Parameters. *Joule* 2, 710–724. doi:10.1016/j.joule.2018.01.002

Cui, J., Chen, X., Zhou, Z., Zuo, M., Xiao, Y., Zhao, N., et al. (2021). Effect of Continuous Pressures on Electrochemical Performance of Si Anodes. *Mater. Today Eng.* 20, 100632. doi:10.1016/j.mtener.2020.100632

Deng, Z., Zhang, Z., Lai, Y., Liu, J., Li, J., and Liu, Y. (2013). Electrochemical Impedance Spectroscopy Study of a Lithium/sulfur Battery: Modeling and Analysis of Capacity Fading. *J. Electrochem. Soc.* 160, A553–A558. doi:10.1149/2.026304jes

Fan, L., Li, M., Li, X., Xiao, W., Chen, Z., and Lu, J. (2019). Interlayer Material Selection for Lithium-Sulfur Batteries. *Joule* 3, 361–386. doi:10.1016/j.joule.2019.01.003

Ghazi, Z. A., He, X., Khattak, A. M., Khan, N. A., Liang, B., Iqbal, A., et al. (2017). MoS_2/Celgard Separator as Efficient Polysulfide Barrier for Long-Life Lithium-Sulfur Batteries. *Adv. Mater.* 29, 1606817. doi:10.1002/adma.201606817

Gu, X., Kang, H., Shao, C., Ren, X., and Liu, X. (2020). A typha Angustifolia-like MoS_2/carbon Nanofiber Composite for High Performance Li-S Batteries. *Front. Chem.* 8, 149. doi:10.3389/fchem.2020.00149

Guo, P., Sun, K., Shang, X., Liu, D., Wang, Y., Liu, Q., et al. (2019). Nb_2O_5/RGO Nanocomposite Modified Separators with Robust Polysulfide Traps and

Ctalytic Centers for Boosting Performance of Lithium-Sulfur Batteries. *Small* 15, 1902363. doi:10.1002/smll.201902363

Guo, X., Wang, S., Yu, L., Guo, C., Yan, P., Gao, H., et al. (2022). Dense SnS_2 Nanoplates Vertically Anchored on a Graphene Aerogel for Pseudocapacitive Sodium Storage. *Mater. Chem. Front.* doi:10.1039/D1QM01369F

Hu, Y., Chen, W., Lei, T., Jiao, Y., Huang, J., Hu, A., et al. (2020). Strategies toward High-loading Lithium–Sulfur Battery. *Adv. Energ. Mater.* 10, 2000082. doi:10.1002/aenm.202000082

Hu, S., Yi, M., Huang, X., Wu, D., Lu, B., Wang, T., et al. (2021). Cobalt-Doped Porphyrin-Based Porous Organic Polymer-Modified Separator for High-Performance Lithium–Sulfur Batteries. *J. Mater. Chem. A.* 9, 2792–2805. doi:10.1039/d0ta10607k

Kim, I. T., Song, M. J., Kim, Y. B., and Shin, M. W. (2016). Microwave-hydrothermal Synthesis of boron/nitrogen Co-doped Graphene as an Efficient Metal-free Electrocatalyst for Oxygen Reduction Reaction. *Int. J. Hydrogen Energ.* 41, 22026–22033. doi:10.1016/j.ijhydene.2016.08.069

Lei, T., Chen, W., Lv, W., Huang, J., Zhu, J., Chu, J., et al. (2018). Inhibiting Polysulfide Shuttling with a Graphene Composite Separator for Highly Robust Lithium-Sulfur Batteries. *Joule* 2, 2091–2104. doi:10.1016/j.joule.2018.07.022

Li, J., Huang, Y., Zhang, S., Jia, W., Wang, X., Guo, Y., et al. (2017). Decoration of Silica Nanoparticles on Polypropylene Separator for Lithium-Sulfur Batteries. *ACS Appl. Mater. Inter.* 9, 7499–7504. doi:10.1021/acsami.7b00065

Li, X., Zhang, Y., Wang, S., Liu, Y., Ding, Y., He, G., et al. (2020). Scalable High-Areal-Capacity Li-S Batteries Enabled by sandwich-structured Hierarchically Porous Membranes with Intrinsic Polysulfide Adsorption. *Nano Lett.* 20, 6922–6929. doi:10.1021/acs.nanolett.0c03088

Li, Y., Li, J., Yuan, J., Zhao, Y., Zhang, J., Liu, H., et al. (2021). 3D CoS_2/rGO Aerogel as Trapping-Catalyst Sulfur Host to Promote Polysulfide Conversion for Stable Li-S Batteries. *J.Alloy. Compd.* 873, 159780. doi:10.1016/j.jallcom.2021.159780

Li, G., Wang, S., Zhang, Y., Li, M., Chen, Z., and Lu, J. (2018). Revisiting the Role of Polysulfides in Lithium-Sulfur Batteries. *Adv. Mater.* 30, 1705590. doi:10.1002/adma.201705590

Li, Y., Shi, B., Liu, W., Guo, R., Pei, H., Ye, D., et al. (2018). Hollow polypyrrole@MnO_2 Spheres as Nano-Sulfur Hosts for Improved Lithium-Sulfur Batteries. *Electrochim. Acta* 260, 912–920. doi:10.1016/j.electacta.2017.12.068

Lin, J.-X., Qu, X.-M., Wu, X.-H., Peng, J., Zhou, S.-Y., Li, J.-T., et al. (2021). $NiCo_2O_4$/CNF Separator Modifiers for Trapping and Catalyzing Polysulfides for High-Performance Lithium–Sulfur Batteries with High Sulfur Loadings and Lean Electrolytes. *ACS Sust. Chem. Eng.* 9, 1804–1813. doi:10.1021/acssuschemeng.0c08049

Liu, B., Bo, R., Taheri, M., Di Bernardo, I., Motta, N., Chen, H., et al. (2019). Metal-organic Frameworks/conducting Polymer Hydrogel Integrated Three-Dimensional Free-Standing Monoliths as Ultrahigh Loading Li-S Battery Electrodes. *Nano Lett.* 19, 4391–4399. doi:10.1021/acs.nanolett.9b01033

Liu, B., Taheri, M., Torres, J. F., Fusco, Z., Lu, T., Liu, Y., et al. (2020a). Janus Conductive/insulating Microporous Ion-Sieving Membranes for Stable Li-S Batteries. *ACS Nano* 14, 13852–13864. doi:10.1021/acsnano.0c06221

Liu, X., Tan, Y., Wang, W., Li, C., Seh, Z. W., Wang, L., et al. (2020b). Conformal Prelithiation Nanoshell on $LiCoO_2$ Enabling High-Energy Lithium-Ion Batteries. *Nano Lett.* 20, 4558–4565. doi:10.1021/acs.nanolett.0c01413

Liu, X., Xu, H., Ma, H., Tan, Z., Wang, Y., Liu, Q., et al. (2020c). One Pot Synthesis and Capacitive Sodium Storage Properties of rGO Confined CoS_2 Anode Materials. *J.Alloy. Compd.* 813, 151598. doi:10.1016/j.jallcom.2019.07.310

Liu, Y., Chen, M., Su, Z., Gao, Y., Zhang, Y., and Long, D. (2021). Direct Trapping and Rapid Conversing of Polysulfides via a Multifunctional Nb_2O_5-CNT Catalytic Layer for High Performance Lithium-Sulfur Batteries. *Carbon* 172, 260–271. doi:10.1016/j.carbon.2020.10.022

Lu, L., Han, X., Li, J., Hua, J., and Ouyang, M. (2013). A Review on the Key Issues for Lithium-Ion Battery Management in Electric Vehicles. *J. Power Sourc.* 226, 272–288. doi:10.1016/j.jpowsour.2012.10.060

Ma, L., Hou, B., Shang, N., Zhang, S., Wang, C., Zong, L., et al. (2021a). The Precise Synthesis of Twin-Born Fe3O4/FeS/carbon Nanosheets for High-Rate Lithium-Ion Batteries. *Mater. Chem. Front.* 5, 4579–4588. doi:10.1039/d1qm00153a

Ma, L., Yu, L.-J., Liu, J., Su, Y.-Q., Li, S., Zang, X., et al. (2021b). Construction of Ti_4O_7/TiN/carbon Microdisk Sulfur Host with Strong Polar N–Ti–O Bond for Ultralong Life Lithium–Sulfur Battery. *Energ. Storage Mater.* 44, 180–189. doi:10.1016/j.ensm.2021.09.024

Manthiram, A., Fu, Y., Chung, S. H., Zu, C., and Su, Y. S. (2014). Rechargeable Lithium-Sulfur Batteries. *Chem. Rev.* 114, 11751–11787. doi:10.1021/cr500062v

Manthiram, A. (2017). An Outlook on Lithium Ion Battery Technology. *ACS Cent. Sci.* 3, 1063–1069. doi:10.1021/acscentsci.7b00288

Pang, Q., Liang, X., Kwok, C. Y., and Nazar, L. F. (2016). Advances in Lithium–Sulfur Batteries Based on Multifunctional Cathodes and Electrolytes. *Nat. Energ.* 1, 16132. doi:10.1038/nenergy.2016.132

Rana, M., Li, M., Huang, X., Luo, B., Gentle, I., and Knibbe, R. (2019). Recent Advances in Separators to Mitigate Technical Challenges Associated with Re-chargeable Lithium Sulfur Batteries. *J. Mater. Chem. A.* 7, 6596–6615. doi:10.1039/c8ta12066h

Song, J., Su, D., Xie, X., Guo, X., Bao, W., Shao, G., et al. (2016). Immobilizing Polysulfides with MXene-Functionalized Separators for Stable Lithium-Sulfur Batteries. *ACS Appl. Mater. Inter.* 8, 29427–29433. doi:10.1021/acsami.6b09027

Song, X., Chen, G., Wang, S., Huang, Y., Jiang, Z., Ding, L. X., et al. (2018). Self-assembled Close-Packed MnO_2 Nanoparticles Anchored on a Polyethylene Separator for Lithium-Sulfur Batteries. *ACS Appl. Mater. Inter.* 10, 26274–26282. doi:10.1021/acsami.8b07663

Song, J., Guo, X., Zhang, J., Chen, Y., Zhang, C., Luo, L., et al. (2019). Rational Design of Free-Standing 3D Porous MXene/rGO Hybrid Aerogels as Polysulfide Reservoirs for High-Energy Lithium–Sulfur Batteries. *J. Mater. Chem. A.* 7, 6507–6513. doi:10.1039/c9ta00212j

Tan, L., Li, X., Wang, Z., Guo, H., and Wang, J. (2018). Lightweight Reduced Graphene oxide@MoS_2 Interlayer as Polysulfide Barrier for High-Performance Lithium-Sulfur Batteries. *ACS Appl. Mater. Inter.* 10, 3707–3713. doi:10.1021/acsami.7b18645

Wan, H., Liu, S., Deng, T., Xu, J., Zhang, J., He, X., et al. (2021). Bifunctional Interphase-Enabled $Li_{10}GeP_2S_{12}$ Electrolytes for Lithium–Sulfur Battery. *ACS Energ. Lett.* 6, 862–868. doi:10.1021/acsenergylett.0c02617

Wang, H.-Q., Lai, F.-Y., Li, Y., Zhang, X.-H., Huang, Y.-G., Hu, S.-J., et al. (2015). Excellent Stability of Spinel $LiMn_2O_4$-Based Cathode Materials for Lithium-Ion Batteries. *Electrochim. Acta* 177, 290–297. doi:10.1016/j.electacta.2015.02.027

Wang, L., Liu, J., Yuan, S., Wang, Y., and Xia, Y. (2016). To Mitigate Self-Discharge of Lithium–Sulfur Batteries by Optimizing Ionic Liquid Electrolytes. *Energy Environ. Sci.* 9, 224–231. doi:10.1039/c5ee02837j

Wang, J.-Y., Ouyang, T., Li, N., Ma, T., and Liu, Z.-Q. (2018). S, N Co-doped Carbon Nanotube-Encapsulated Core-Shelled CoS_2@Co Nanoparticles: Efficient and Stable Bifunctional Catalysts for Overall Water Splitting. *Sci. Bull.* 63, 1130–1140. doi:10.1016/j.scib.2018.07.008

Wei, Z., Ren, Y., Sokolowski, J., Zhu, X., and Wu, G. (2020). Mechanistic Understanding of the Role Separators Playing in Advanced Lithium-sulfur Batteries. *InfoMat* 2, 483–508. doi:10.1002/inf2.12097

Wu, F., Qian, J., Chen, R., Ye, Y., Sun, Z., Xing, Y., et al. (2016). Light-weight Functional Layer on a Separator as a Polysulfide Immobilizer to Enhance Cycling Stability for Lithium–Sulfur Batteries. *J. Mater. Chem. A.* 4, 17033–17041. doi:10.1039/c6ta06516c

Xiong, P., Zhang, F., Zhang, X., Liu, Y., Wu, Y., Wang, S., et al. (2021). Atomic-scale Regulation of Anionic and Cationic Migration in Alkali Metal Batteries. *Nat. Commun.* 12, 4184. doi:10.1038/s41467-021-24399-9

Xu, Z.-L., Kim, J.-K., and Kang, K. (2018). Carbon Nanomaterials for Advanced Lithium Sulfur Batteries. *Nano Today* 19, 84–107. doi:10.1016/j.nantod.2018.02.006

Xu, J., Yang, L., Cao, S., Wang, J., Ma, Y., Zhang, J., et al. (2021). Sandwiched Cathodes Assembled from CoS_2 -modified Carbon Clothes for High-Performance Lithium-Sulfur Batteries. *Adv. Sci.* 8, 2101019. doi:10.1002/advs.202101019

Yan, Y., Zhang, P., Qu, Z., Tong, M., Zhao, S., Li, Z., et al. (2020). Carbon/sulfur Aerogel with Adequate Mesoporous Channels as Robust Polysulfide Confinement Matrix for Highly Stable Lithium-Sulfur Battery. *Nano Lett.* 20, 7662–7669. doi:10.1021/acs.nanolett.0c03203

You, Y., Ye, Y., Wei, M., Sun, W., Tang, Q., Zhang, J., et al. (2019). Three-dimensional MoS_2/rGO Foams as Efficient Sulfur Hosts for High-Performance Lithium-Sulfur Batteries. *Chem. Eng. J.* 355, 671–678. doi:10.1016/j.cej.2018.08.176

Yuan, S., Guo, Z., Wang, L., Hu, S., Wang, Y., and Xia, Y. (2015). Leaf-like Graphene-Oxide-Wrapped Sulfur for High-Performance Lithium–Sulfur Battery. *Adv. Sci.* 2, 1500071. doi:10.1002/advs.201500071

Yuan, D., Huang, G., Zhang, F., Yin, D., and Wang, L. (2016). Facile Synthesis of CuS/rGO Composite with Enhanced Electrochemical Lithium-Storage

Properties through Microwave-Assisted Hydrothermal Method. *Electrochim. Acta* 203, 238–245. doi:10.1016/j.electacta.2016.04.042

Yuan, H., Kong, L., Li, T., and Zhang, Q. (2017). A Review of Transition Metal Chalcogenide/graphene Nanocomposites for Energy Storage and Conversion. *Chin. Chem. Lett.* 28, 2180–2194. doi:10.1016/j.cclet.2017.11.038

Zhang, Z., Wang, G., Lai, Y., Li, J., Zhang, Z., and Chen, W. (2015). Nitrogen-doped Porous Hollow Carbon Sphere-Decorated Separators for Advanced Lithium–Sulfur Batteries. *J. Power Sourc.* 300, 157–163. doi:10.1016/j.jpowsour.2015.09.067

Zhang, Y., Gao, Z., Song, N., He, J., and Li, X. (2018). Graphene and its Derivatives in Lithium–Sulfur Batteries. *Mater. Today Eng.* 9, 319–335. doi:10.1016/j.mtener.2018.06.001

Zhang, Y., Wang, Y., Luo, R., Yang, Y., Lu, Y., Guo, Y., et al. (2020). A 3D Porous FeP/rGO Modulated Separator as a Dual-Function Polysulfide Barrier for High-Performance Lithium Sulfur Batteries. *Nanoscale Horiz* 5, 530–540. doi:10.1039/c9nh00532c

Zhang, F., Li, Z., Cao, T., Qin, K., Xu, Q., Liu, H., et al. (2021). Multishelled Ni_2P Microspheres as Multifunctional Sulfur Host 3D-Printed Cathode Materials Ensuring High Areal Capacity of Lithium–Sulfur Batteries. *ACS Sust. Chem. Eng.* 9, 6097–6106. doi:10.1021/acssuschemeng.1c01580

Zhang, H., Li, J., Luo, L., Zhao, J., He, J., Zhao, X., et al. (2021). Hierarchically Porous MXene Decorated Carbon Coated $LiFePO_4$ as Cathode Material for High-Performance Lithium-Ion Batteries. *J.Alloy. Compd.* 876, 160210. doi:10.1016/j.jallcom.2021.160210

Zhao, Q., Hao, Z., Tang, J., Xu, X., Liu, J., Jin, Y., et al. (2021). Cation-selective Separators for Addressing the Lithium-Sulfur Battery Challenges. *ChemSusChem* 14, 792–807. doi:10.1002/cssc.202002152

Zhao, M., Li, B. Q., Peng, H. J., Yuan, H., Wei, J. Y., and Huang, J. Q. (2020). Lithium-sulfur Batteries under Lean Electrolyte Conditions: Challenges and Opportunities. *Angew. Chem. Int. Ed.* 59, 12636–12652. doi:10.1002/anie.201909339

Zhao, Z., Pathak, R., Wang, X., Yang, Z., Li, H., and Qiao, Q. (2020). Sulfiphilic FeP/rGO as a Highly Efficient Sulfur Host for Propelling Redox Kinetics toward Stable Lithium-Sulfur Battery. *Electrochim. Acta* 364, 137117. doi:10.1016/j.electacta.2020.137117

Zhou, J., Lin, N., Cai, W. l., Guo, C., Zhang, K., Zhou, J., et al. (2016). Synthesis of S/CoS_2 Nanoparticles-Embedded N-Doped Carbon Polyhedrons from Polyhedrons ZIF-67 and Their Properties in Lithium-Sulfur Batteries. *Electrochim. Acta* 218, 243–251. doi:10.1016/j.electacta.2016.09.130

Zhou, Z., Sun, T., Cui, J., Shen, X., Shi, C., Cao, S., et al. (2021). A Homogenous Solid Polymer Electrolyte Prepared by Facile spray Drying Method Is Used for Room-Temperature Solid Lithium Metal Batteries. *Nano Res.* doi:10.1007/s12274-021-3683-6

Zhuang, Z., Kang, Q., Wang, D., and Li, Y. (2020). Single-Atom Catalysis Enables Long-Life, High-Energy Lithium-Sulfur Batteries. *Nano Res.* 13, 1856–1866. doi:10.1007/s12274-020-2827-4

Conflict of Interest: The authors declare that the research was conducted in the absence of any commercial or financial relationships that could be construed as a potential conflict of interest.

frontiers in Chemistry

REVIEW
published: 14 February 2022
doi: 10.3389/fchem.2022.827563

Research Progresses and Challenges of Flexible Zinc Battery

Yunfei Xu, Xin Xu, Mei Guo, Guoxin Zhang and Yaqun Wang**

Department of Energy Storage Technology, Shandong University of Science and Technology, Qingdao, China

Flexible zinc batteries have great potential in wearable electronic devices due to their high safety, low cost, and environmental friendliness. In the past few years, a great deal of work on flexible zinc batteries has been reported, with exciting results. Therefore, many solutions have been proposed in electrode design and electrolyte preparation to ensure the desired flexibility without sacrificing the capacity. This paper reviews the recent progress of flexible zinc batteries. We discuss the differences between various anode materials, cathode materials, and electrolytes, introduce the differences of electrode preparation methods of active materials on flexible substrates and their influence on the performance of the battery. Finally, the challenges and future research trends of flexible zinc batteries in capacity and mechanical properties are pointed out.

Keywords: flexible, zinc ion battery, zinc-air battery, mechanical property, flexible substrate, *in situ* growth, inkjet printing, screen printing

Edited by:
Yu Ding,
University of Maryland, United States

Reviewed by:
Kangning Zhao,
Swiss Federal Institute of Technology Lausanne, Switzerland
Yumin Qian,
Beijing Institute of Technology, China

****Correspondence:***
Guoxin Zhang
zhanggx@sdust.edu.cn
Yaqun Wang
yqwang@sdust.edu.cn

Specialty section:
This article was submitted to Electrochemistry, a section of the journal Frontiers in Chemistry

Received: *02 December 2021*
Accepted: *25 January 2022*
Published: *14 February 2022*

Citation:
Xu Y, Xu X, Guo M, Zhang G and Wang Y (2022) Research Progresses and Challenges of Flexible Zinc Battery. Front. Chem. 10:827563. doi: 10.3389/fchem.2022.827563

INTRODUCTION

With the development of miniaturization of electronic chips, it is possible to integrate electric devices, such as implantable medical devices, wearable health monitoring systems, flexible displays, and intelligent clothing, which have attracted the attention of researchers all over the world. (Yu et al., 2017; Liu et al., 2018; Sumboja et al., 2018; Zhang et al., 2018; Dong et al., 2021).As an indispensable part of the flexible electronic equipment, the battery needs to have good cycling and safety performance to meet the requirements. Especially when the flexible battery follows the deformation of the flexible electronic devices, the mechanical and electrochemical properties are required to be higher.

As an electrode material, zinc has the advantages of lower cost, more content in the crust and lower redox equilibrium potential than lithium. Moreover, using environmentally insensitive zinc makes zinc-based batteries manufacture easier and package cheaper than lithium-based batteries. (Fang et al., 2018). At present, conventional zinc-based batteries such as Zn-MnO_2, Zn-Ni and Zn-Air have already been commercialized, but they are mainly rigid and used in non-flexible electronic devices. Many researches have been done to make these batteries flexible. In addition, Zinc ion batteries (ZIBs) because of its high energy density, low cost, environmental friendliness, safety and other advantages are gradually coming into people's horizons, have good prospects in portable devices. ZIB, as a promising alternative to lithium ion battery, has attracted widespread attention. (Tan et al., 2017; Li et al., 2019a; Yu et al., 2019; Zhang et al., 2020a).

At present, great progresses have been made in electrode materials selection, flexible electrode preparation and electrolyte design of flexible zinc ion batteries. (Li et al., 2019a). In this review, the latest research progresses in electrode materials, electrolytes, and adhesion methods of active material are reviewed. Lastly, some concluding remarks were prospected to outline the challenges and future research trends for flexible zinc batteries.

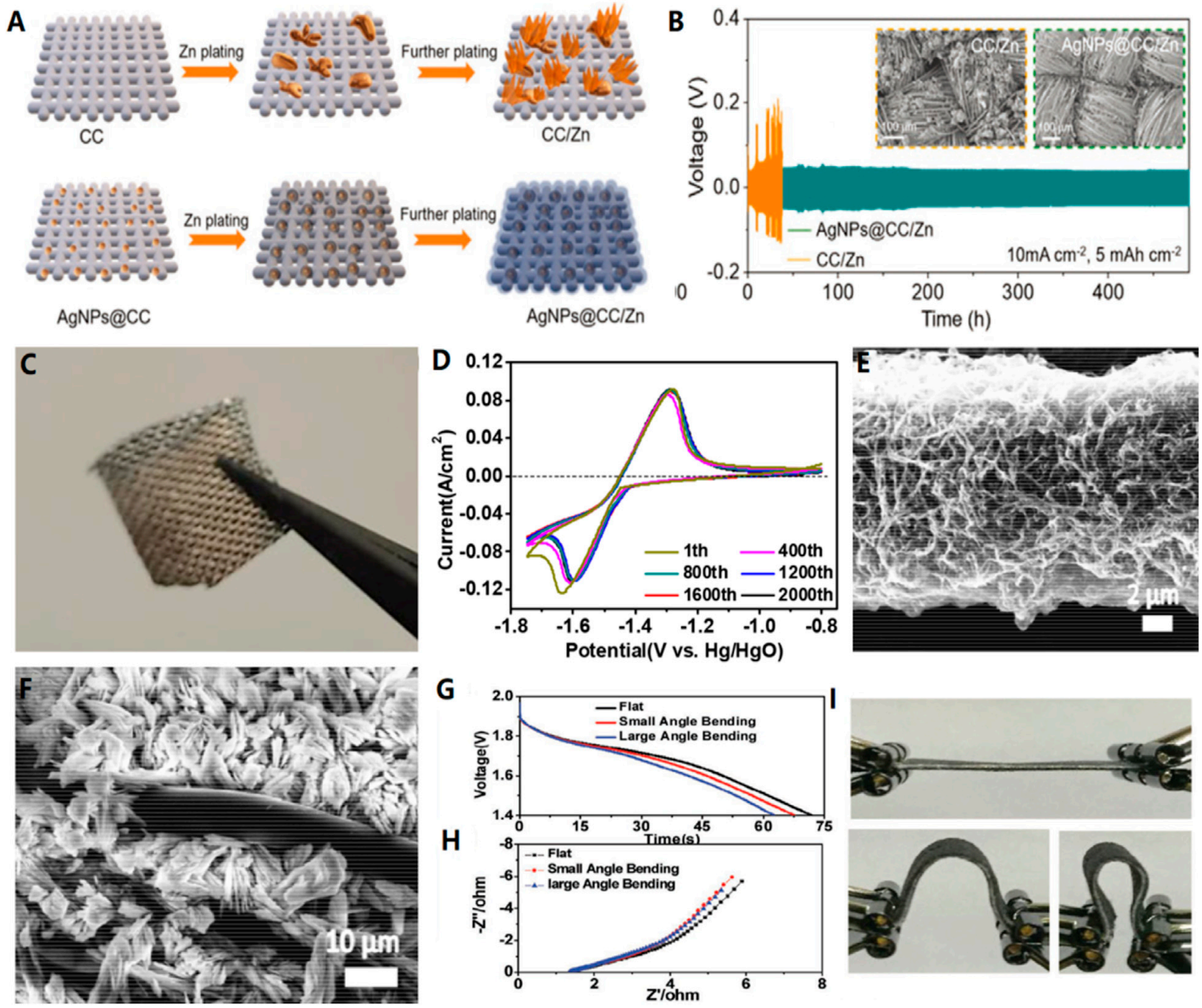

FIGURE 1 | (A) Schematic diagram of Zn deposition on bare CC and AgNPs@CC scaffolds. **(B)** The capacity is 5 mA h/cm^2 at 10 mA h/cm^2 current density. Inset: SEM images of CC/Zn and AgNPs@CC/Zn electrodes after circulation. **(C)** Flexible AgNPs@CC/Zn electrode under bending.Copyright 2021 Wiley-VCH GmbH. **(D)** CV curves of the CC-CF@120ZnO at different cycles. SEM images of **(E)** CC-CF@ZnO and **(F)** CC-ZnO after cycling test, showing the importance of CFs for preventing the Zn dendrite growth. **(G–I)** Discharge curves and EIS results of solid-state batteries under different bending conditions. Copyright 2016 WILEY-VCH Verlag GmbH & Co. KGaA, Weinheim.

COMMON MATERIALS FOR FLEXIBLE ZINC BATTERIES

Anode Materials

Zinc metal anodes are of particular interest to the flexible battery market due to their low material cost, high theoretical capacity (820 mA h/g, 5,854 mA h/cm^3), (Kaveevivitchai and Manthiram, 2016), good rechargeability and safe chemistry. The most common anode in flexible zinc ion battery is zinc foil, because of its good mechanical properties. However, the stiffness of heavy metal zinc foil anodes reduces the energy density, making it impossible to apply to industrial flexible, wearable energy storage systems. (Pan et al., 2016). In addition, the main challenges faced by zinc metal anodes are the mechanical stability of the electrode during long-term deformation and uncontrollable dendrite growth during cycling, resulting in poor cycle performance and coulomb efficiency of the battery, which severely limits the service life of flexible zinc ion batteries and hinders their practical application. (Lao-atiman et al., 2017; Han et al., 2018a; Li et al., 2018a; Ma et al., 2018; Tang et al., 2019; Zeng et al., 2019; Li et al., 2020a; Nguyen et al., 2020). In order to solve these problems of Zn anode, there are several strategies, including:

a) Method for constructing composite zinc anode.

Chen and his colleagues proposed a heterogeneous metal seed-mediated strategy. (Chen et al., 2021a). The basic idea is through the inkjet printing on the main chain of the three dimensional conductive printing silver nanoparticles, in order to induce the homogeneous nucleation of zinc, and avoid initial electroplating phase of the dendrite growth. Therefore, AgNPs@CC/Zn anode has excellent performance at a high current density of 10 mA/cm^2, with cycle performance exceeding 480 h. (**Figures 1A,B**)

b) Deposition of zinc materials on a highly conductive substrate.

Zinc oxide nanoparticles are deposited on a three-dimensional layered carbon cloth-carbon nanofiber (CC-CF) substrate as an anode (CC-CF@ZnO). (**Figures 1D,E**) The device exhibits excellent stability, maintaining up to 91.45% initial capacity after 1,000 cycles and 72.90% initial capacity after 2,400 cycles. The significant increase in cyclic capacity is due to the uniform deposition of nano particles on the three-dimensional highly conductive nano-carbon fibers, which alleviates the shape change during the electrochemical reaction. In particular, it avoids the uneven distribution of current and zinc deposition, thus preventing the formation of zinc dendrite. (Liu et al., 2016).

Pang (Guo et al., 2021) prepared zinc nanosheets/CC (Zn/CC) by electrodeposition, and Zn nanosheets were uniformly deposited on the surface of CC fiber. Form a three-dimensional network interconnected with recent nano piece, insert for the ion-extraction process provides a rich active site. Compared with the same amount of conventional metal zinc anode foil, nanostructures zinc and CC skeleton integration enhances the flexibility of the anode, the formation of the surface of the more active, which helps the development of high performance flexible device.

c) Coating inert material on zinc anode.

For example, (Alfaruqi et al., 2018), constructed a Sn-doped $NaTi_2(PO_4)_3$ (NTP/Sn) protective layer on the surface of zinc anode (Zn@NTP/Sn) to improve the cyclic stability of zinc anode. Using Sn doping $NaTi_2$ (PO_4) $_3$ through the structure design and high performance of zinc anode interface features, is helpful to accelerate the transfer of Zn^{2+}, increase the interface performance. At the current density of 0.4 mA/cm^2, the average voltage lag of Zn@NTP/Sn symmetric cells is only 17.4 mV, which is much lower than that of exposed Zn symmetric cells (75.8 mV) and Zn@NTP symmetric cells (43.7 mV). In addition, it has been reported that the zinc electrode surface was coated with Al_2O_3 coating (Lee et al., 2013) and Bi alloying (Jo et al., 2017) to improve HER overpotential and reduce self-discharge caused by hydrogen release, thus improving the cycle performance of the battery.

d) Use appropriate electrolytes.

For example, ionic liquid based zinc salt electrolyte is an effective way to solve the hydrogen evolution reaction (HER) and zinc dendrite growth of zinc ion batteries. (Ma et al., 2020) developed polyvinylidene fluoride hexafluoropropylene (PVDF-HFP)+5% poly (ethylene oxide) (PEO)+ILZE electrolyte (1-ethyl-3-methylimidazolium tetrafluoroboric acid ([EMIM]BF_4) ionic liquid) using 2 M zinc tetrafluoroborate ($Zn(BF_4)_2$) as carrier. The final product is represented as PHP-ILZE. The electrolyte developed can achieve hydrogen-free, dendrite-free galvanizing/stripping in 1,500 h (3,000 cycles) at 2 mA/cm^2 with a Coulomb efficiency of nearly 100%. At the same time, oxygen-induced corrosion and passivation were effectively inhibited. This is the first demonstration of an all-solid-state zinc-ion battery based on a newly developed electrolyte, which simultaneously solves the problems of deep hydrogen evolution and dendrite growth of conventional zinc-ion batteries.

Li and his colleagues have developed a polyethylene glycol 600 (PEG 600) and polysorbate 20 (Tween 20) compound additive, as the organic inhibitors in alkaline electrolyte, mainly by inhibiting the hydrogen evolution reaction to a certain extent, inhibit the corrosion of zinc. Because Tween 20 is more polar than PEG 600, it absorbs zinc better. Because of Tween 20 highly branched structure, zinc cannot be Tween 20 complete coverage, and linear polyethylene glycol (peg) can be adsorbed on the rest of the active site, thus two kind of corrosion inhibitor for zinc corrosion synergy effect, the corrosion of the composite inhibitor is better than single corrosion inhibitor. (Liang et al., 2011).

The combination of these methods enables advanced flexible zinc anodes to be better designed with less dendrite growth, higher corrosion and passivation resistance, and less hydrogen evolution, suitable for quasi-solid zinc-based aqueous batteries.

Cathode Materials

The cathode materials commonly used in flexible zinc ion battery include various transition metal compounds, such as manganese (Qiu et al., 2017; Huang et al., 2019; Zu et al., 2019; Zhang et al., 2020b; Zhang et al., 2020c), cobalt, nickel (Liu et al., 2016; Wan et al., 2018) or molybdenum-based oxides/sulfides, Prussian blue analogues and conducting polymers (Eftekhari et al., 2017; Yao et al., 2020; Cong et al., 2021). (**Table 1**) Here, we will focus on the last 5 years of research.

Manganese Based Materials

Manganese based compounds have been widely used as cathode materials for ZIB due to their advantages of abundant resources, low cost and non-toxicity. (Pan et al., 2016; Zhang et al., 2016). MnO_2 is considered as the most promising cathode material among many manganese based compounds. MnO_2 is a material with a polymorphic crystal shape. Under different preparation conditions, the crystal shape, morphology, particle size, porosity, specific surface area are different, and then show different capacity and charge-discharge characteristics. (Xu et al., 2012; Alfaruqi et al., 2018). Huang and his colleagues have provided new insights into the energy storage mechanism of Waterborne zinc-manganese battery with the participation of Mn^{2+}. (Huang et al., 2019). In the first discharge process, the combination of Zn^{2+} and H^+ insert promoted the MnO_2 to Zn_xMnO_4, MnOOH and Mn_2O_3 transformation, at the same time, raised the pH of the electrolyte, formation of $ZnSO_4{\cdot}3Zn(OH)_2{\cdot}5H_2O$ (noted as "BZSP"). Later in the charging process, Zn_xMnO_4, MnOOH and Mn_2O_3 by extracting Zn^{2+} and H^+ reduction for alpha MnO_2, BZSP and Mn^{2+} reacts $ZnMn_3O_7$ $\cdot 3H_2O$. Besides the electrochemical reaction, Zn^{2+} can also be in alpha MnO_2, ZnxMnO$_4$ and $ZnMn_3O_7{\cdot}3H_2O$ in the reversible insert and

TABLE 1 | Comparison of electrochemical properties of different cathode materials.

Cathode materials	Electrolyte	Capacity	Cycling stability	Power density	Energy density	References
CC-CF@NiO	PVA + ZnO + KOH	0.39 mAh cm^{-2} at 5 mA cm^{-2}	91.45% after 1,000 cycles	57.5 W kg^{-1}	19.7 Wh kg^{-1}	Liu et al. (2016)
N-CC@MnO_2	(PVA)+LiCl + $ZnCl_2$+$MnSO_4$	353 mA h g^{-1} at 0.5 A g^{-1}	93.6% after 1,000 cycles	7.9 kW kg^{-1}	440 W h kg^{-1}	Zu et al. (2019)
Ag_2O	KOH + LiOH + polyacrylic acid	3.78 mA h cm^{-2}				Eftekhari et al. (2017)
AgO	KOH + PVA + $Ca(OH)_2$	>54 mAh cm^{-2}				Cong et al. (2021)
CC-PANI-FeCN	$ZnSO_4$+PVA	238 mAh/g at 0.2A/g	71% at 1,000 cycles			Zhang et al. (2015)
ZnHCF@MnO_2	$ZnSO_4$+PVA	89 mA h/g at 100 mA/g	~71% at 500 cycles			Wang et al. (2017)
CoFe(CN)6	PAM + poly (ethylene oxide)$_{53}$-poly (propylene oxide)$_{34}$-poly (ethylene oxide)$_{53}$ (F77) +$Zn(OTf)_2$	173.4 mAh g^{-1} at 0.3A/g	93.4% after 2000 cycles			Javed et al. (2020)
AgNPs@CC	$Zn(CF_3SO_3)_2$	255mAh/g at 5.0 mA/g	184 mAh/g at 1,200 cycles			Chen et al. (2021a)
P-MnO_{2-x}@VMG	PVA + $ZnCl_2$+$MnSO_4$	284.2 mA h/g at 0.5A/g	> 87% at 500 cycles		369.5 Wh kg^{-1}	Chamoun et al. (2018)
t-CNTs-PA-PE	$ZnSO_4$+PAM	238 mA h/g at 0.2 A/g	~100% at 1,500 cycles			Jia et al. (2015)
CC-MOF derived Ag nanowires	KOH + PVA	1.605 mA h/cm^2 at	CC-MOF derived Ag nanowires	2.8 mW/cm^2	1.87 mWh/cm^2	Tehrani et al. (2015)
MnO_2	$ZnSO_4$+ $MnSO_4$	19.3 mAh/cm3 (corresponding to 393 mA h/g) at7.5 mA/cm^3	83.9% at 1,300 cycles		38.1 mW h cm^{-3}	Wang et al. (2018b)
PANI/mCC	PVA + $Zn(CF_3SO_3)_2$	156.4 mAh g^{-1}	80% after 1,000 cycles	9742 W kg^{-1}	185.7 Wh kg^{-1}	Guo et al. (2021)
CNT/MnO_2-PPy	$ZnSO_4$+ $MnSO_4$	222.7 mAh/g at 0.3A/g	87.4% after 1,000 times		341.6 Wh kg^{-1}	Yin et al. (2021)
V_2O_5-Ti	Zn (CF_3SO_3) $_2$ + PVA	377.5 mAh g^{-1} at 4A g^{-1}	68.21% after 500 cycles	6.4 kW kg^{-1}	622 Wh kg^{-1}	Song et al. (2016)
binder-free V_2O_5 nanorods	PAM + $ZnSO_4$	362.01 mAh g^{-1} at 0.13 A g^{-1}	81.9% after 600 cycles	33.4 mW cm −3	10.5 mWh-cm^{-3}	Lin et al. (2020)

extract, under the participation of Mn^{2+}, BZSP, $Zn_2Mn_3O_8$ and $ZnMn_2O_4$ reciprocal transformation (**Figure 2B**).

On the other hand, the slow kinetics and rapid capacity decay caused by the strong electrostatic repulsion between the divalent zinc ions and the manganese based host crystal structure is one of the important challenges for the practical application of zinc ion batteries. Li's team proposed *in-situ* growth of manganese dioxide nanorods arrays on three-dimensional porous surface nitrogen-doped carbon cloth (N-CC) (**Figure 2C**). It is not only better than the other nanostructures has higher specific surface area, more active site and better permeability, and can maintain the stability of the structure and electrochemical significantly improve the conductivity at the same time. In addition, it allows a strong covalent coupling based on the nanoscale active material and N-CC, leading to a fast electron transfer from the active material to the collector. Thus, Under the current density of 0.5 g/A, flexible-CC@ MnO_2/N-CC@Zn battery can produce a high capacity of 353 mA h/g (**Figures 2D,E**). In addition, the CV curve of our assembled state N -CC@MnO_2//N-CC@Zn battery hardly changes after 1,000 cycles, which also proves that the cell has good cycle stability. Further, the prepared devices can be bent and twisted in different states without affecting their electrochemical performance (**Figures 2F,G**). (Qiu et al., 2017)

In addition, many researchers believe that the oxygen vacancy generation and ion intercalation are another effective method to improve the electrochemical performance of Zn/MnO_2 battery. There are two main reasons: On the one hand, as shallow bodies, oxygen vacancies can fundamentally improve the electrical conductivity of manganese-based materials, influence the embedding and de-embedding of metal ions in material layers, reduce the stress and electrostatic repulsion between adjacent layers, directly overcome migration and diffusion barriers, and promote the diffusion and charge transfer of ions during the embedding of metal ions; on the other hand, the electrode material with oxygen vacancy can also generate more electrochemically active sites, increase the surface energy of the system, promote the electrochemical phase transition, and thus possess better charge storage capacity. (Zu et al., 2019; Zhang et al., 2020b).

Zhang's team reported a simple phosphorylation process that introduces oxygen vacancies into phosphate ion intercalated manganese dioxide/vertical multilayer graphene (VMG) arrays to form complete P-MnO_{2-x}@VMG cathodes (**Figure 2H**). By

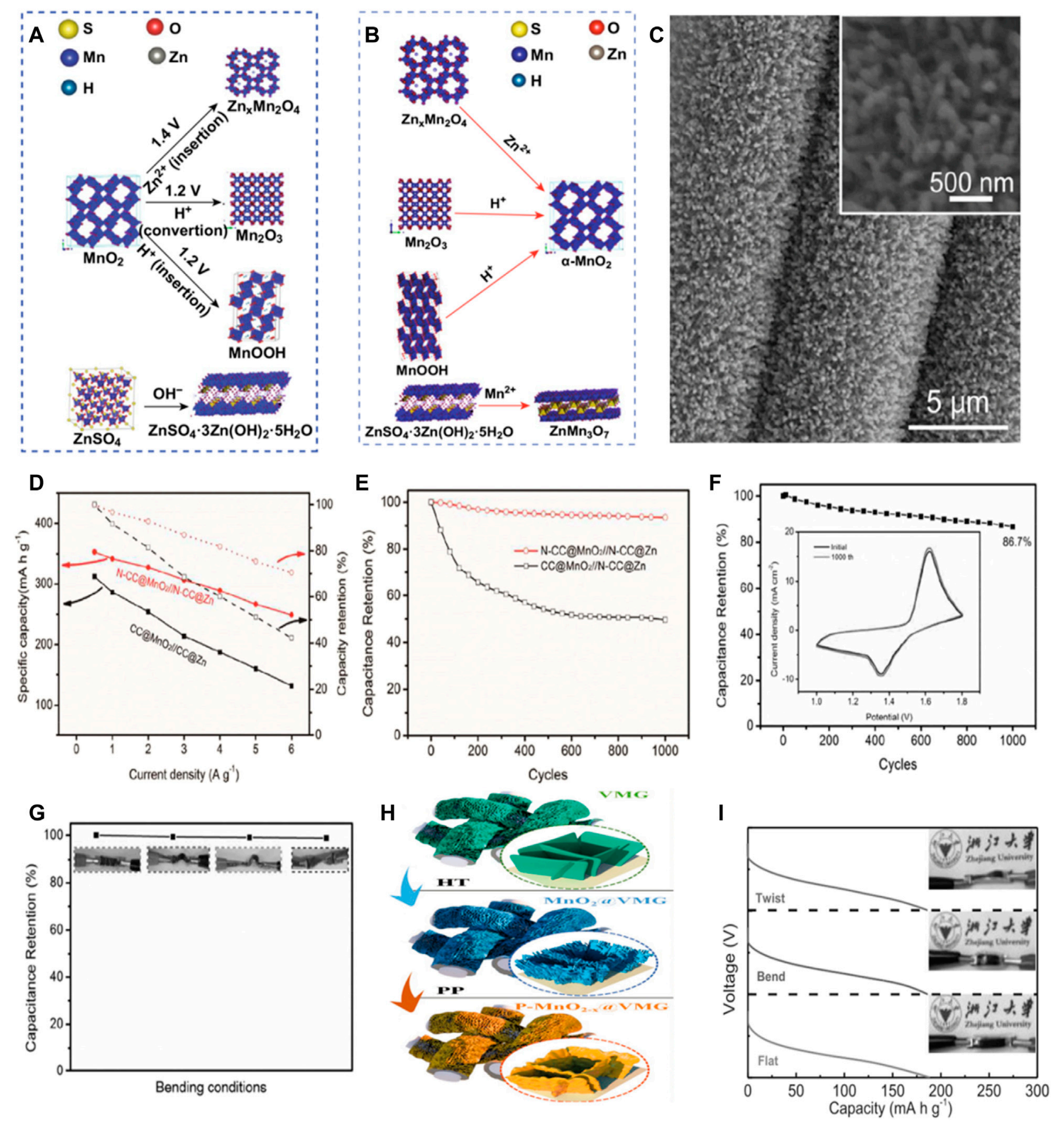

FIGURE 2 | Phase evolution of cathode during the first discharge process **(A)** and charge process **(B)**. Copyright 2019 Springer. **(C)**SEM images of the N-CC@ MnO_2; inset is the corresponding magnifed SEM image. **(D)** N-CC@MnO_2//N-CC@Zn and CC@MnO_2//N-CC@Zn the specific capacity and capacity retention rate of the battery as a function of current density **(E)** Cycling performance of the N-CC@MnO_2//N-CC@Zn and CC@MnO_2//N-CC@Zn batteries collected at 1 A/g for 1,000 cycles. **(F)** Capacity retention rate of the battery after 1,000 cycles at the current density of 1 A/g N-CC@MnO_2//N-CC@Zn. The CV curves of the first and 1000th cycles are illustrated. **(G)** At different bending conditions N-CC@MnO_2//N-CC@Zn battery capacity retention rate.Copyright 2017 Journal of Materials Chemistry A. **(H)** For the synthesis of MnO_{2-x} @ VMG shell/core array. (HT, hydrothermal method; PP, phosphorization process). **(I)** Discharge curves of the device under flat, bending and twisting conditions at 3 A/g current density. Copyright 2020 WILEY-VCH Verlag GmbH & Co. KGaA, Weinheim.

phosphorylation, the oxygen vacancy and phosphorus ion intercalation are realized simultaneously, which improves the electrical conductivity of MnO_2 and expands its layer spacing to accelerate ion transfer. In addition, the flexible VMG conductive network provides good peripheral charge transfer and imparts good mechanical strength to the cathode. Thanks to these advantages, at the current density of 0.5 A/g, P-MnO_{2-x}@VMG cathodes shows a high capacity of 302.8 mA h/g in aqueous electrolytes, and the capacity retention rate is more than 90% after 1,000 cycles at the current density of 2 A/g, which proves its long-term cycling stability. In addition, by comparing the 3 A/g discharge curves of the battery under flat, bent and twisted conditions, it can be seen that the difference between the three curves is negligible, which proves that the battery has great potential in flexible wearable electronic devices. (**Figure 2I**). (Zhang et al., 2020c) Mai et al. reported the generation of oxygen vacancies in tunnel α -MnO_2 via surface gradient Ti doping using defect engineering for long-life Zn-MnO_2 batteries. (Lian et al., 2019). Interestingly, the introduction of surface gradient Ti doping leads to the contraction of the interlayer, but at the same time, the reduction of Mn valence state leads to the formation of oxygen vacancies compensated by electrons. In addition, Ti substitution and the resulting oxygen vacancy open the [MnO_6] octahedral wall, resulting in an unbalanced charge distribution and local electric fields in the crystal structure, accelerating ion/electron migration rates. Therefore, the diffusion coefficients of Zn^{2+} and H^+ in Ti-MnO_2 nanowires are improved. Therefore, Ti-MnO_2 nanowires show improved H^+ and Zn^{2+} storage capacities in Zn/MnO_2 batteries, and achieve excellent high rate capacity and ultra-long cycle stability.

Also, in $ZnSO_4$ electrolytes widely studied, MnO_2 usually suffers volume loss due to Mn^{3+} disambiguation dissolving Mn^{2+} [39]. Mn^{2+} is added to the electrolyte to inhibit the disproportionation of Mn^{3+}, which can effectively inhibit the dissolution of manganese base materials and improve the stability of cathode materials (Pan et al., 2016; Chamoun et al., 2018), but the mechanism is still unclear. For example, in a Zn-MnO_2 cell, dissolution of α -MnO_2 is alleviated when $MnSO_4$ is added to a $ZnSO_4$ electrolyte because it can alter the dissolution balance of Mn^{2+} from the α-MnO_2 electrode. (Lian et al., 2019). Zhang and his colleagues reported MnO_2 based anode and cathode, zinc added $Mn(CF_3SO_3)_2$ additives of $Zn(CF_3SO_3)_2$ electrolytic Zn-MnO_2 water of high performance rechargeable batteries. It is found that $Mn(CF_3SO_3)_2$ can inhibit the dissolution of Mn^{2+} and form uniform porous MnO_x nanosheets on the cathode surface, which helps to maintain the integrity of the electrode. It is important to note that beta MnO_2 has the high irreversible capacity, stable high rate capability and cycle performance. (Zhang et al., 2017). In addition, coating can also be used to alleviate the dissolution of mangan-based materials. For example, Yang et al. prepared an independent flexible film (Designated as CNT/MnO_2-PPY) composed of carbon nanotubes and polypyrrole coated manganese dioxide nanowire through *in-situ* reactive self-assembly and vacuum filtration. The Polypyrrole (PPy) coating improves the conductivity of MnO_2 NWs, alleviates the dissolution of cathode materials and provides a strong buffer to accommodate large volume changes during repeated cycles. (Zhang et al., 2020d).

Silver-Based Materials

Zinc-silver batteries have the following advantages: high specific energy (theoretical specific capacity: 432 mAh/g), high discharge efficiency, moderate charging efficiency, smooth discharge voltage, small self-discharge rate, long dry storage life and good mechanical properties. (Kumar et al., 2019; Tan et al., 2018). At the same time, zinc-silver batteries also have obvious shortcomings, which are as follows: very high cost, short life, poor low-temperature performance and not resistant to overcharging. The silver oxide button battery has widely used in electronic watches, calculators, small instruments and other micro electrical appliances as power supply because of their above-mentioned advantages. In recent years, a lot of research has been done to make these batteries flexible. In addition, Wang's team has developed a printable, polymer-based zinc-silver oxide (AgO-Zn) battery with flexibility, rechargeability, high area capacity and low impedance. The redox reactiondepends on the zinc ions (Zn^{2+}) and silver ions dissolved in alkaline electrolyte (Ag) and the supersaturated induced precipitation. In addition, due to the high oxidation state, make full use of line printing batteries can realize >54 mA h/cm^2 area of high capacity (**Figure 3A**) while maintaining a low internal resistance (**Figure 3B**). The battery can still charge and discharge normally without multiple deformations affecting its rechargeability (**Figures 3C,D**). Overall, printed thin film AgO-Zn thin film batteries combine superior electrochemical and mechanical properties and prove to be well suited for reliably and sustainably powering a wide variety of wearable and flexible electronic devices. In addition, Meng and his colleagues used polystyrene block polyisoprene block polystyrene (SIS) as a hyperelastic adhesive for printing inks to print a Zn-Ag_2O battery with high ductility and a reversible capacity density of 2.5 mA h/cm^2 even after repeated 100% stretching.Two stretchable battery with "NANO" design printed directly on the seal on the spandex thermoplastic polyurethane (PU) the top of the head (**Figure 3E**). On the "NANO" current collector, electrodes are printed separately to form two "NA" and "NO" batteries designed to be connected in series to power the 3V wearable LED (**Figure 3F**). Regardless of the serious torsional strain (**Figure 3G**), indentation (**Figure 3H**), 100% uniaxial tensile (**Figure 3I**) and biaxial stretching, stretching "NANO" to the battery can keep constant LED brightness (**Figure 3J**). The battery energy provided so far reported the highest reversible capacity of the inherent scalability battery size and discharge current density. New stress wear-resisting printing inks for the wide application of flexible paved the way to the further development of the electronic products. The new printed battery based on SIS can withstand severe bending caused by the wearer's movement. (Kumar et al., 2016).

Conductive Polymers

Compared with metal oxides, conductive polymers exhibit higher conductivity due to their long π -electron conjugated system (Shi et al., 2018), and also has the advantages of low cost, easy synthesis, and excellent mechanical properties (Cong et al., 2021), are excellent cathode materials for Zn batteries, and show promising energy storage behavior. Therefore, conductive polymers have attracted wide attention in the field of electric energy storage, especially in wearable electronic devices. Polyaniline (PANI) is one of the most common type of conductive polymers. Polyaniline is easy

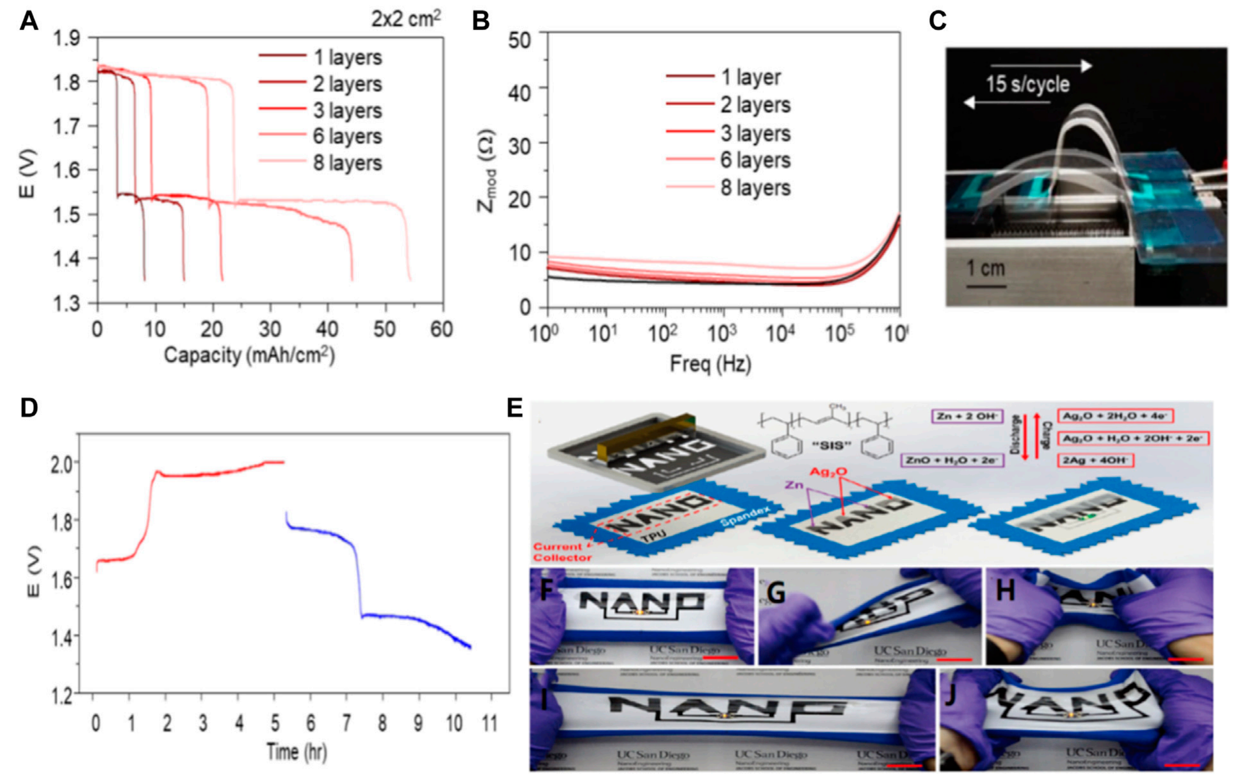

FIGURE 3 | (A) Electrochemical performance of AgO-Zn batteries as galvanic cells. The active material load is the capacity of the 2 × 2 cm^2 battery with 1-8 layers. **(B)** Bode plot reflecting the corresponding impedance of the 2 × 2 cm^2 cells with different areal loading. **(C)** Diagram of a cell controlled by a linear stage at a speed of 15 s/cycle under repeated 180° bending cycles, and **(D)** corresponding volt-time curves for charging (red) and discharging (blue) of the cell during approximately ~2,500 repeated bending cycles. Copyright 2020 ResearchGate. **(E)** Screen printing steps for Zn-Ag_2O cells on stretchable fabric using SIS adhesive. Illustration: REDOX charging-discharging reaction. Photographs of the sealed cell during **(F)** horizontal stretching, **(G)** distortion, **(H)** indentation strain, **(I)** 100% stretching and **(J)** biaxial stretching. Copyright 2016 Advanced Energy Materials.

to synthesize and has high electrical conductivity and electrochemical activity. (Eftekhari et al., 2017). It as a stream of zinc ion battery cathode material has been widely studied. However, it suffers from rapid deactivation and consequent performance deterioration due to spontaneous deprotonation during charging/discharging, and has the disadvantage of poor cycling stability in high pH solutions, which limits its further application in polyaniline zinc batteries. Therefore, Yang's group reported a strategy to introduce $[Fe\ (CN)_6]^{4-}$, in which the nitrogen atoms on the polyaniline chain may also interact with $[Fe(CN)_6]^{3-}$/$[Fe(CN)_6]^{4-}$ to affect the electrochemical stability of polyaniline. Considering these factors, $[Fe(CN)_6]^{3-}$/$[Fe(CN)_6]^{4-}$ and polyaniline chain between the REDOX reaction and hydrogen bonding may be beneficial to the electrochemical properties of polyaniline, which can greatly improve the cycle stability of the polyaniline electrode, at the same time maintain its initial high specific capacity (**Figure 4A**). After 1,000 times charging and discharging cycle, CC–PANI–FeCN capacity retention rate of about 71%, and the capacity of the CC–PANI retention rate is only 17% (**Figures 4B,C**). Assembly of quasi solid flexible zinc ion battery under the condition of different bending the specific capacity and coulomb efficiency is close to 100%, suggest that the potential of as flexible energy storage device (**Figure 4D**). (Yao et al., 2020)

In addition, Huang's team reported a method to improve the electrochemical reactivity and stability of the polyaniline cathode by constructing a pile-electron conjugate system between PEDOT: PSS on polyaniline and carbon nanotubes. The cathode can provide a high capacity of 238 mA h/g at a current density of 0.2 A/g, with good rate performance and good cycle stability (**Figure 4E**). Zinc ion batteries based on post-treated CNT PANI PEDOT: PSS (t-CNTs-PA-PE)showed good cycle stability and almost 100% cycle efficiency in 1,500 cycles. Moreover, Solid ZIBs in the bending and hammering process, the capacity loss is not obvious, keep in more than 90% of the original capacity (**Figures 4F,G**). This work demonstrates that conductive polymer cathodes can be used in high-performance ZIBs to meet the needs of flexible electronics. (Liu et al., 2019a).

Prussian Blue Materials

PBA with the formula of $A_xM_y\ [B(CN)_6]_z mH_2O$ (x, y, z, m = stoichiometric numbers; A, B = alkaline metal; M = Zn^{2+}, Ni^{2+}, Cu^{2+}, etc.) is constructed by a 3D network of zeolitic struc-ture. (Xu et al., 2017). It has open skeleton structure, sufficient REDOX

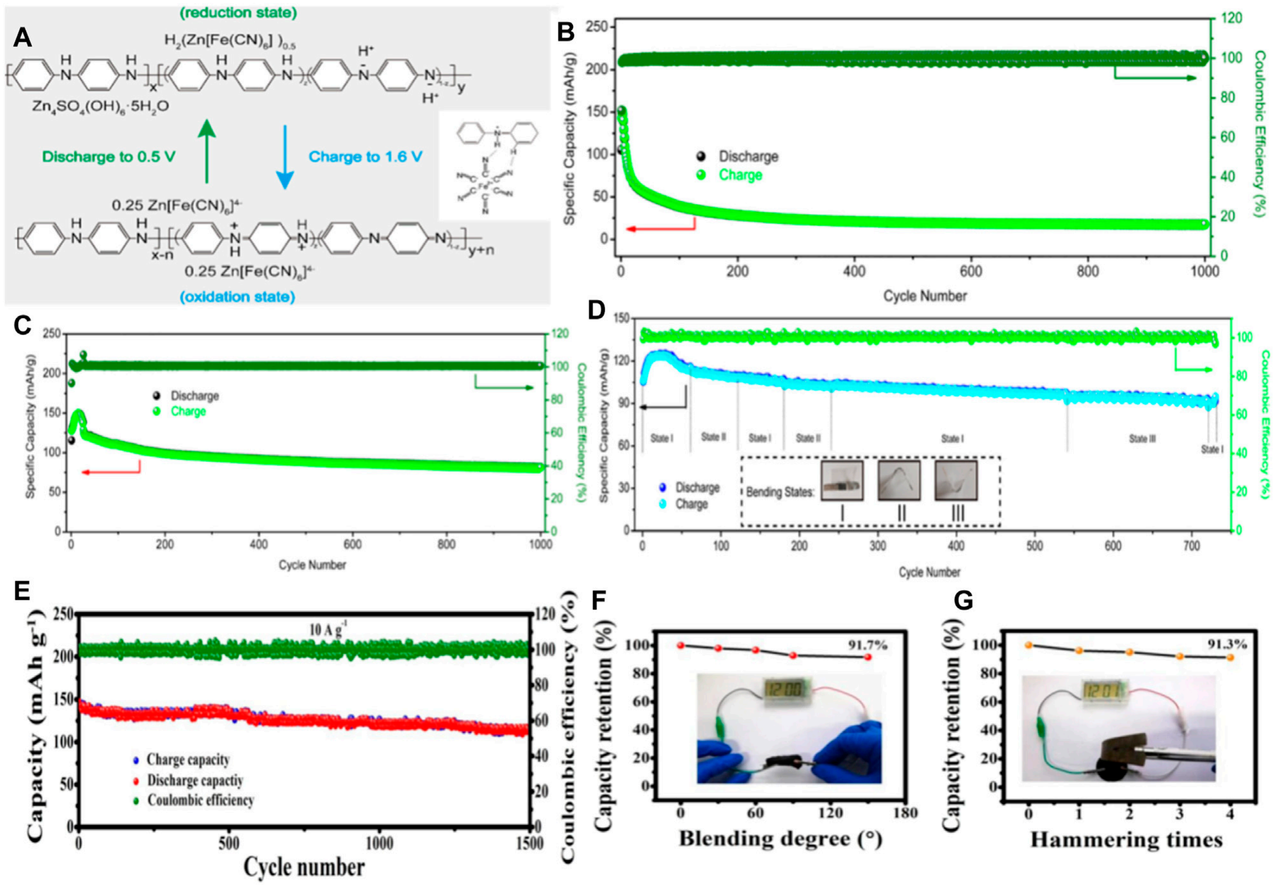

FIGURE 4 | (A) REDOX mechanism of CC-PANI-FeCN. Illustration$[Fe(CN)_6]^{4-}$ Schematic diagram of interaction with PANI. Cyclic properties of CC-PANI **(B)** and CC-PANI-FeCN **(C)** at current density 5 A/g. **(D)** The optical images ofquasi-solid-stateflexible batteries in different bending states. Copyright 2020 Chemical Engineering Journal. **(E)** Cycling performance of t-CNT-PA-PE cathode in ZIBs at current density of 10 A/g. Capacity retention of solid ZIBs under different destructive tests, including **(F)** bending test and **(G)** hammer testCopyright 2019 ACS Appl Mater Interfaces.

active center and relatively strong structural stability (Jia et al., 2015; Zhang et al., 2015; Song et al., 2018). The open framework endows PBA to be promising candidate for Zn^{2+} storage. However, Prussian blue analogues have a low capacity (less than 100 mAh/g) because the active sites are underutilized and in most cases are single-atom REDOX (Ma et al., 2019a). It is still challenging to further improve the specific capacity and cycling stability of PBA cathodes.

Lu and his colleagues prepared manganese oxide coated zinc ferrite (ZnHCF) nanocubes (ZnHCF@MnO_2) by *in situ* coprecipidation method (Lu et al., 2017). The composite has a unique structure that has a synergistic effect by combining the capacitive and intercalated properties of the two components with the REDOX reaction, thus regulating the storage of Zn ions. Therefore, ZnHCF nanocubes encapsulated by MnO_2 nanocubes have a high capacity of Zn ion storage and discharge, and their working voltage can reach ~1.7V. In order to demonstrate the practical application of zinc ion battery in the field of flexible wearable electronics, a flexible quasi-solid-state battery was prepared by coupling ZnHCF@MnO_2 with Zn thin foil in $ZnSO_4$/PVA gel electrolyte. At different bending angles, the battery's current changes are negligible, showing excellent flexibility (**Figure 5A**). In addition, the discharge capacities of the flexible device at 100, 200, 400, 500 and 800 mA/g are 89, 78, 67, 58, and 53 mAh/g, respectively (**Figure 5B**). In addition to higher discharge capacity, quasi-solid state batteries also have higher rate capacity (**Figure 5C**). When the current density increases from 100 mA/g to 800 mA/g, the discharge capacity can still exceed 49 mA h/g, and the capacity retention rate is 55%. At the same time, flexible battery can be stable cycle more than 500 times, can maintain about 71 percent of the capacity. Even flexible battery folding can power LED bulbs (drive voltage is 1.8V). (**Figure 5D**).

Zhi and his colleagues incorporated Co(II)/Co(III) and Fe(II)/Fe(III) REDOX reactions into cobalt hexocyanate ($CoFe(CN)_6$), which is a breakthrough to realize the combination of high capacity and high voltage water-bearing zinc ion batteries. (Ma et al., 2019a). The Zn/$CoFe(CN)_6$ battery utilizes two pairs of Co(II)/Co(III) and Fe(II)/Fe(III) REDOX reactions to provide a high operating voltage platform of 1.75 V and a high capacity of 173.4 mA h/g

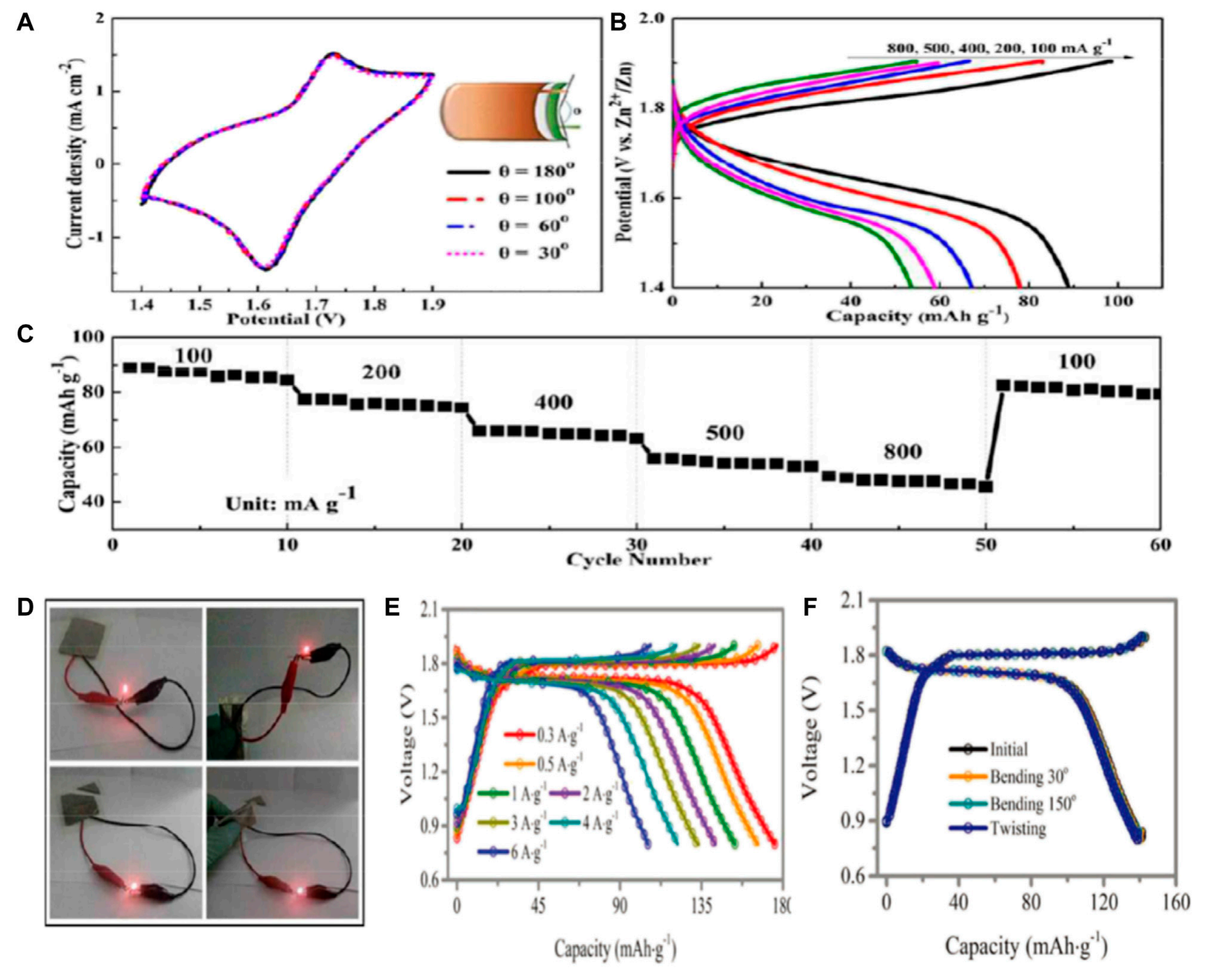

FIGURE 5 | Performance of flexible solid-state rechargeable zinc ion battery with ZnHCF@MnO_2 nickel foil as cathode **(A)** CV curves under different bending conditions at 1 mV/s; **(B)** Charge-discharge curves under different current densities; **(C)** Multiplier performance of flexible cells; **(D)** Photographs of the flexible zinc batteries powering the LED bulbs in their original and cut state respectively Copyright 2017 J. Mater. Chem. A. Electrochemical performance of Zn/$CoFe(CN)_6$ cells with 4 m $Zn(OTf)_2$ electrolyte **(E)** constant current charge-discharge curves under different current densities; **(F)** Solid-state cable battery: constant current charge-discharge curve and torsional deformation of battery at different bending angles of 60° and 150° when the fixed device length is 10 cm and bending radius is 1 cm.

at 0.3 A/g. The 3D open structure of the battery provides A sufficiently high discharge capacity of 109.5 mA h/g, even at an extremely fast charge/discharge rate of 6 A/g. (**Figure 5E**). In addition, the Zn/$CoFe(CN)_6$ battery achieved excellent cycle performance of 2,200 times and coulomb efficiency of nearly 100%. Furthermore, sol-gel of hydrogel electrolyte has been developed to prepare high-performance flexible cable batteries. The battery has excellent electrochemical performance, uniform torsional deformation and excellent mechanical properties at bending degrees of 60° and 150°. (**Figure 5F**). This strategy enables the active material to fully contact the electrolyte, thus improving the electrochemical performance (capacity increase of ≈18.73%) and mechanical stability of the solid-state device.

Vanadium Base Material

Vanadium cathode because of its excellent REDOX chemistry, can promote the open of insert/take off layer response the main structure and high specific capacity and aroused people's great interest. (Wang et al., 2017; Guo et al., 2018). Among various vanadium based oxides, V_2O_5 has good potential as ZB cathode material due to its high theoretical capacity (589 mA h/g) based on double electron transfer. The main challenge facing V_2O_5 cathode is that the V_2O_5 cathode synthesized by traditional methods has insufficient active sites, low conductivity, making its ultra-fast charging performance and high rate performance far below expectations.

Mai and colleagues designed a novel cathode material by growing two-dimensional V_2O_5 nanosheets directly on a

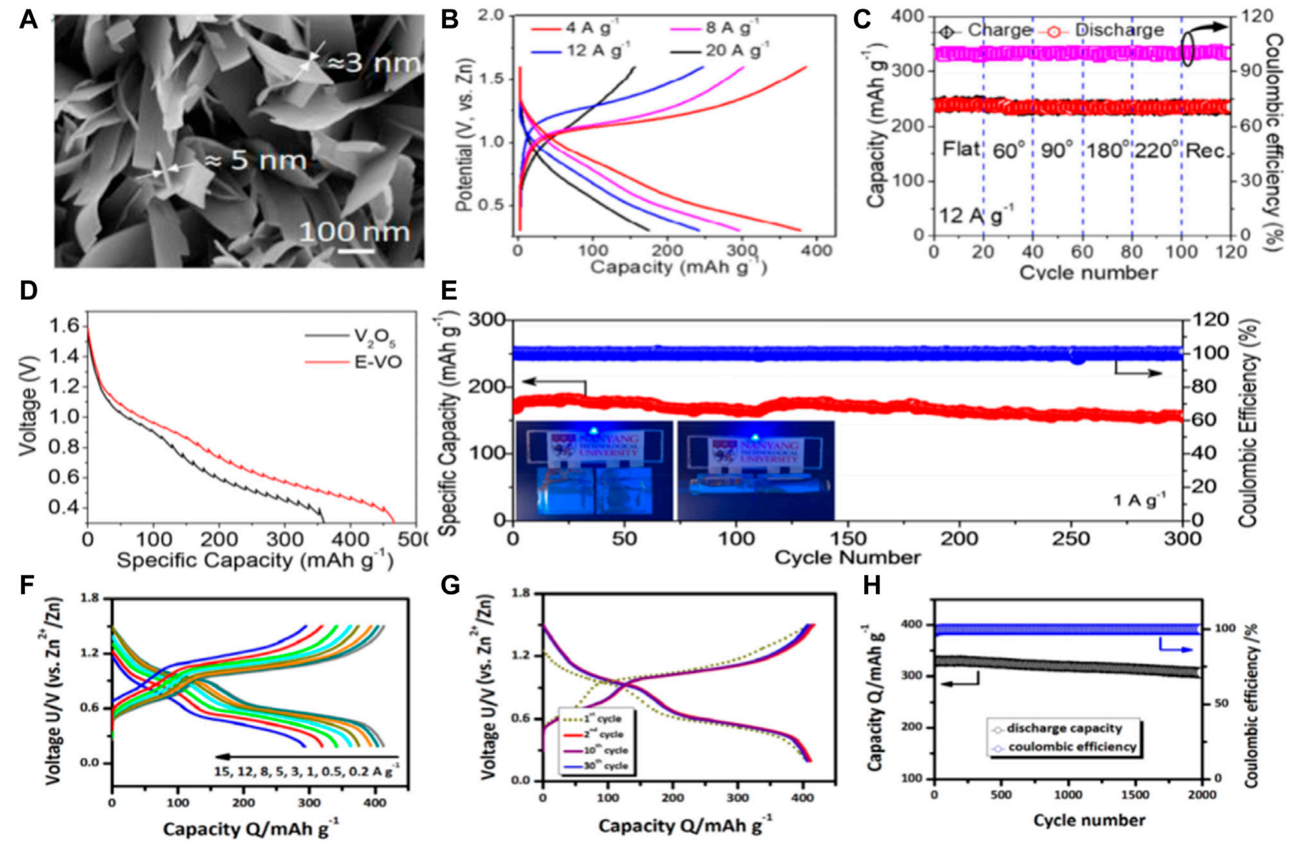

FIGURE 6 | (A) High power FESEM images of V_2O_5 nanosheets grown directly on titanium substrates, **(B)** Charge-discharge curves of at various current densities in potential window of 0.3–1.6 V, **(C)** Charge-discharge profiles during different bending states at constant current density of 12 A/g. Copyright *2020 Elsevier Ltd.* **(D)** Discharge GITT curves at a current density of 0.05 A/g,**(E)** Cycling stability and Coulombic efficiency at 1 A/g. Inset in **(E)** shows the blue LED light up by two flat or bending state flexible quasi-solid-state Zn/E-VO batteries. Copyright 2019 NANOEN 3724. **(F)** Charge/discharge curves of the DVOC sample at different current densities. **(G)** Charge/discharge curves of the DVOC sample during the initial thirty cycles. **(H)** High-rate long-term cycling properties of the DVOC sample at 10 A/g. Copyright 2020 ChemSusChem.

flexible titanium (Ti) substrate. (Javed et al., 2020). The resistance of 2D V_2O_5 nanosheets is greatly reduced and provides more active sites to facilitate electrochemical reactions in zinc ion batteries. Meanwhile, the improvement of the electrochemical performance of V_2O_5-Ti cathode is due to the unique structure of vertically arranged ultra-thin nanosheets (**Figure 6A**) which ensures that Zn^{2+} has a larger embedding space and a shorter diffusion length, thus improving the electrochemical performance and providing ultra-fast charging performance. An ultra-fast and flexible quasi - solid F-V_2O_5-Ti//Zn battery was developed. The capacity, power density and energy density parameters are better than those of the previously reported water-based/flexible zinc ion battery. (**Figures 6B,C**).

Yan and colleagues propose a simple *in situ* method that simultaneously introduces polyvalence to increase the interlayer water content and enlarge the interlayer distance of hydrated V_2O_5. (Zhao et al., 2019). These structural adjustment makes the layered expansion V_2O_5 2.2 H_2O (E-VO) nano piece has faster charge transfer kinetics, Zn^{2+}storage space and more than precursor V_2O_5 higher structural stability. (**Figure 6D**). As cathode of water-based ZIB, E-VO has the high irreversible capacity (450 mA h/g at 0.1 A/g), good ability of ratio (222 mA h/g at 10 A/g) and long term stability (72% of the capacity to keep 3,000 cycle, at 5 A/g). (**Figure 6E**).

In addition, the structure crushing and chemical dissolution during the charge-discharge cycle are the main reasons for the electrochemical instability of vanadium oxide. (Yu et al., 2015; Song et al., 2016). In order to solve these problems, regulating the V^{4+} and the ratio of the V^{5+} to enhance the electrochemical reaction of reversibility, effectively improve the capacity and stability of the vanadium oxide. An oxygen defect modulated unbonded V_2O_5 nanorods (PVO@C) for water/quasi-solid zinc ion batteries were constructed. (Liang et al., 2021). The structure of PVO@C electrode is stable due to oxygen deficiency and phosphorus doping, and the diffusion rate and electronic conductivity of Zn^{2+} ions are improved. Aqueous PVO@C//Zn cells have significantly increased capacity (362.01 mA h/g at 0.13 A/g1) and have remarkable long-term durability (86.7% capacity after 5,000 cycles and nearly 100% Coulomb efficiency) compared to the original VO//Zn or PVO//Zn cells. In addition, a stable flexible quasi-solid PVO@C//Zn cell (SS ZIB) was proposed based on flexible PVO@C cathode, elastic Zn anode and PAM gel electrolyte. This SS ZIB device achieves an impressive energy density of 10.5 mWh/cm^3 at a high power density of 33.4 W/cm^3, exceeding most solid-state batteries previously recorded. After 600 cycles, it has a capacity retention capacity of 81.9%.

Vanadate based materials have the advantages of various element valence states, large theoretical capacity, stable structure and abundant resources, so they are the most widely studied. (Li et al., 2020b; Liao et al., 2020). However, due to strong electrostatic interaction with divalent zinc ion the vanadate cathode has slow kinetics and poor cyclic stability. Deng and colleagues (Lin et al., 2020) constructed a novel vanadate oxide structure and successfully designed a defection-rich (V_6O_{13}-δ)/C nanovortex to prepare a fibrous flexible DVOC/SWNT@CNTF electrode (SWNT: single-walled carbon nanotube; Carbon nanotube fiber CNTF was prepared). Based on SWNT network and substrate are provided based on CNTF bicontinuous electronic path, promoted the fast dynamics and excellence rate capability (**Figures 6F–H**).

In addition, the pre-insertion strategy is also an effective method to improve the cycling performance of vanadium-based zinc ion batteries. Linda F. Nazar and colleagues report a vanadium oxide bronze supported by interlaminar Zn^{2+} ions and water ($Zn_{0.25}V_2O_5$•nH_2O) as the positive electrode of a zinc battery. (vKundu et al., 2016). A reversible Zn^{2+} ion (de) intercalation storage process with high speed and more than one Zn^{2+} per formula unit (capacity up to 300 mAh/g). The zinc battery has an energy density of 450 W/L and a capacity retention rate of more than 80 percent in 1,000 cycles. No dendrites form on the zinc electrode. In order to solve the problem, the preintercalated ions can easily lose the combination with the skeleton and deintercalated into the electrolyte, leading to the collapse of the structure again.Xu reported that the cyclic stability of a zinc ion cell can be improved by preintercalation of tetrapalent tin ions into Pyrovanadate $Sn_{1.5}V_2O_7(OH)_2$•$3.3H_2O$ (denoted as SnVO). (Xu et al., 2021). Compared with Pure vanadium pentoxide, the tetradvalent tin in SnVO can strongly bind to $V_2O_7^{4-}$ layer, supporting high mechanical stability during zinc ion intercalation. In addition, the tin oxide tetrahedron in the V_4O_{10} layer can further expand the size of the cavity between Pyrovanadate $V_2O_7^{4-}$, promoting the rapid kinetics of zinc ion diffusion, thus improving the rate performance of ZIB.

Electrolytes

Electrolyte is another important component of flexible zinc ion battery, which is the "blood" of flexible zinc ion battery and plays an important role in determining its performance in terms of discharge operating time, cycling performance and shelf life. There are two types of electrolytes, one is liquid electrolyte (Hilder et al., 2009), which has a certain disadvantage compared with gel electrolyte because of its fluidity and is prone to side leakage when encapsulating flexible batteries. Next is the solid electrolyte, which contains three main types: hydrogel, ionic conductive inorganic solid and organic polymer. Gel polymer electrolyte is a kind of intermediate state between liquid and solid, which is composed of polymer object and liquid electrolyte. Due to its relatively high ionic conductivity, flexibility and good interfacial contact with electrodes, it has been widely used in flexible zinc ion batteries. In general, the performance of gel electrolytes depends largely on the choice of gelatin and the ratio of each element. The gelatins used to build electrolytes are generally polyvinyl alcohol (PVA), polyethylene oxide (PEO), and polyacrylic acid (PAA) (Li et al., 2019a). Polyvinyl alcohol (PVA) is a commonly used polymer matrix with good water retention capacity, which has the characteristics of high hydrophilicity and good film forming ability, excellent chemical stability, electrochemical inertness, durability, non-toxicity and ease of manufacture. (Li et al., 2019b; Fan et al., 2019).

As the evaporation of water, the electrolyte becomes more and more concentrated and the performance of battery deteriorates. To reduce water loss of the electrolyte, thereby improving the ionic conductivity of the electrolyte and the cycle life of battery, Zhong's team has proposed a polymer electrolyte for the body that uses tetraethylammonium hydroxide (TEAOH) as an ionic conductor and polyvinyl alcohol (PVA) as a polymer, with good water retention (**Figures 7A,B**). The prepared polymer electrolyte maintained a high ionic conductivity of 30 mS/cm after 2 weeks. In addition, with the commonly used KOH-PVA electrolytic liquid ratio, TEAOH - PVA assembly zinc air battery has excellent discharge properties and cycle life, found no significant degradation in 2 weeks. (Li et al., 2019b).

In addition, the internal pores of the gel electrolyte play a key role in the absorption of electrolytes, electrolytes can be retained in the porous gel electrolytes, and polyethylene glycol as a pore-forming agent improves the doping ability and obtain high ionic conductivity. The prepared porous photovoltaic nanocomposite GPE has high ionic conductivity of 57.3 mS/cm, excellent water retention performance and good thermal and mechanical properties under environmental conditions, while the assembled flexible ZAB has excellent cycle stability, discharge performance and power density. (Fan et al., 2019).

In addition to the ionic conductivity and mechanical strength of the hydrogel, certain properties of the polymer electrolyte may have a particular impact on the performance of flexible zinc ion batteries. (Li et al., 2018b). For example, Cui's team reported a novel strategy using thermally reversible polymer hydrogels as functional electrolytes, i.e., using poly (ethylene oxide)-poly (propylene oxide)-poly (ethylene oxide) (PEO-PPO-PEO), with significant structural polymorphism in polar solvents, to provide intelligent cooling recovery for flexible zinc ion batteries. When the cell system is exposed to extreme deformation, a simple cooling process can repair the fractured electrode-electrolyte interface, resulting in *in-situ* recovery of electrochemical performance compared to conventional flexible cells (**Figure 7C**). This process can be repeated even after multiple strong folding events, and this cooling-recovery strategy requires only external temperature stimulation without any side effects involving phase transitions. (Zhao et al., 2017).

Soorathep Kheawhom's group also reported a transparent alkaline GPE film, which is polymerized by polyacrylic acid, potassium hydroxide and water as a quasi-solid electrolyteused in zinc-manganese dioxide batteries. The GPE film has high ionic

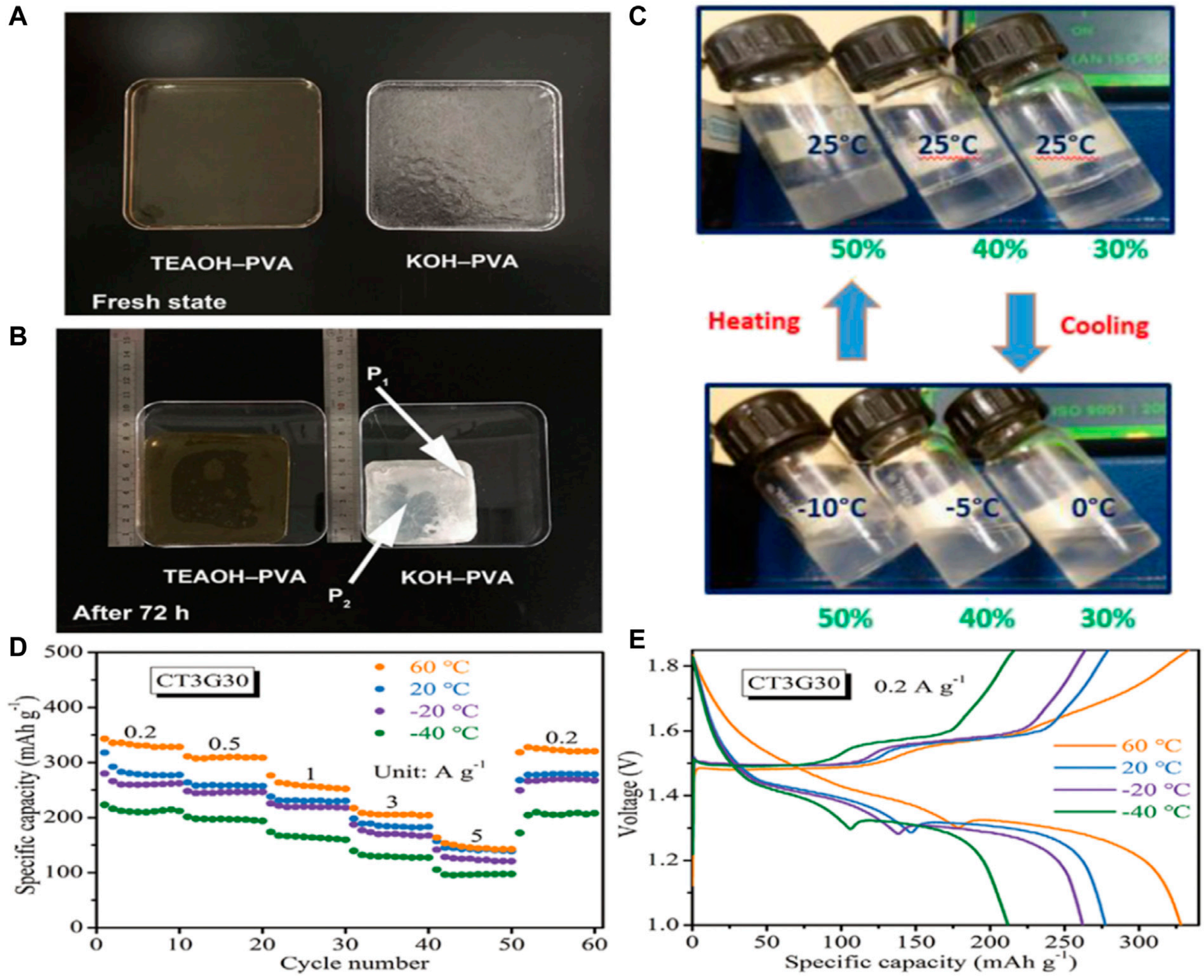

FIGURE 7 | Optical photos of **(A)** freshly prepared electrolytes and **(B)** electrolytes stored in the open ambient environment (RH = 30%, 20°C) for 72 h.Copyright 2019 Nano Energy. **(C)** Photographs of PHEs with polymer concentration ranging from 30% (w/w) to 50% (w/w) at varied temperatures, showing the thermoreversible gelation behavior. Copyright 2017 Angewandte Chemie International Edition. **(D)** Rate performance, **(E)** GCD curves at 0.2 A/g. Copyright 2021 Wiley-VCH GmbH.

conductivity, improveing the cycle life and performance of the battery. (Gaikwad et al., 2011; Lao-atiman et al., 2017).

The application of organic electrolytes in zinc ion batteries is still the least explored field in stable zinc anodes. Due to the higher thermodynamic stability of Zn to organic solvents, the application of organic solvents may reduce side reactions that may solve the lower Coulombic efficiency (CE) problem by simplifying electrochemistry at the Anode and reducing electrode passivation, thereby reducing dendrite problems.

Wang and colleagues reported that a highly stable and dendrite-free zinc anode was obtained by using triethyl phosphate (TEP) as a cosolvent in aqueous solution. In more than 3,000 h stable galvanized iron/zinc, CE value of 99.68%. The electrolyte and zinc ion battery of zinc anode and six iron acid potassium cyanide copper (KCuHCf) positive electrode showed a good compatibility. The full battery has longer cycle stability and higher rate performance. (Naveed et al., 2019).

However, compared with stream electrolytes, organic electrolytes are less safe, so stream electrolytes are the most widely studied. The flexible zinc ion battery also requires that the electrolyte can withstand the test of bending and folding, and has a certain self-healing ability.

Wong and colleagues developed a simple and economical method to construct a versatile hydrogel electrolyte using cotton as raw material, tetraethyl orthosilicate as crosslinking agent, and glycerin as antifreeze agent (Chen et al., 2021b). The resulting hydrogel electrolyte has high ionic conductivity, excellent mechanical properties (such as high tensile strength and elasticity), ultra-low freezing point, good self-healing ability, high adhesion and good heat resistance. It is worth noting that this water gel electrolyte under - 40°C can provide a record of 19.4 mS/cm high ionic conductivity. Secondly, the hydrogel electrolyte can significantly inhibit zinc dendrite growth and hydrogen evolution side reactions at -40–60°C (**Figures 7D,E**). Using this hydrogel electrolyte, a flexible quasi-solid Zn-MnO_2 cell was assembled, which showed significant energy density in the -40–60°C range. The battery also shows excellent cycle durability, with high durability in a wide range of harsh conditions. In addition, it can be in >60% of compression deformation restored to its initial state, shows that it has good elasticity. Zhi's team reported cathodes based on nanofibrillated cellulose (NFC)/polyacrylamide (PAM) hydrogels, electrodeposited Zinc nanoplate anodes, and carbon nanotube (CNT)/α-MnO_2 sewable Zn-MnO_2 cells (Wang et al., 2018a). The designed NFC/PAM hydrogel has high mechanical strength and great tensile properties. The prefabricated NFC bone network stabilizes the large pore as a channel for electrolyte diffusion. In addition, the influence of sewing on improving shear resistance of solid battery was analyzed. The sutured Zn-MnO_2 battery retains 88.5% capacity after 120 stitches and can withstand a large shear force of 43 N.

In order to effectively solve the disadvantage of rapid water loss of hydrogel electrolyte, Liu and colleagues report a solid-state battery based on a self-standing gelatin-based hydrogel electrolyte (GHE) (Han et al., 2018b), whose high ionic conductivity, strong mechanical strength, and tight contact with the electrode enable reversible and stable circulation of Zn metal anodes and $LiMn_2O_4$ cathodes. Benefiting from superior stability to water, GHE's flexibility and a carefully designed battery structure, the Zn/GHE/$LiMn_2O_4$ solid state full battery delivers a high specific capacity of 110.2 mA h/g and is resistant to cutting, flooding, bending, twisting and crimping. These characteristics of gelatin electrolyte proved beneficial to the battery components and battery performance. When heated, gelatine powder dissolved in AE, which promoted *in-situ* coating of GHE on the electrode. Using the fast cooling technology after cooling, gelatin solidifies into a solid layer of thin film, to provide mechanical strength to suppress the formation of zinc dendrite.

In a word, the research of flexible zinc ion battery electrolyte mainly focuses on how to alleviate the problem of zinc negative dendrite, hydrogen evolution and solve the problem of hydrogel electrolyte water loss. High performance electrolytes have great influence on the cycle stability, rate performance and energy storage capacity of batteries. (Liu et al., 2019b; Ma et al., 2019b). Therefore, it is of great significance to study electrolytes of flexible Zn-ion batteries.

METHOD OF COMBINING ACTIVE MATERIALS WITH FLEXIBLE SUBSTRATES

In order to improve the mechanical flexibility of electrodes for wearable electronic devices so that the active material can better adhere to the flexible substrates, flexible electrodes are usually prepared by two ways: one method is to grow the active material directly on the flexible substrate, which is typically carbon cloth, polymer elastomers or textiles. Direct growth of active materials without using any binder, such as catalytic *in-situ* growth, electrodeposition (Liu et al., 2020; Yza et al., 2022), etc. Another method is to load active material with the help of instrument. This includes loading of electrically active material onto flexible substrates by screen printing with the help of adhesives, or loading the active material by inkjet printing, 3D printing, or laser etching with a pre-designed electrode pattern.

In situ Growth Method

In the preparation of zinc ion batteries, the use of polymer binders and conductive additives results in high contact resistance, which reduces the specific capacity and diversity performance of the battery. An effective strategy to solve this problem is to directly grow the active material *in-situ* on flexible substrates or collectors as binder-free electrodes. (Wan et al., 2018). This strategy not only ensures fast charge transfer between the active material and the collector, but also enables a uniform distribution of the active material over the collector fluid. Therefore, the prepared flexible electrodes will provide better electrochemical performance, including high capacity, good rate performance and high capacity under deformation conditions.

Yao's team constructed a planar flexible quasi-solid aqueous rechargeable silver-zinc battery using silver nanowires made from a metal-organic framework (MOF) as an unbonded cathode on a carbon cloth. The results show that the ag-Zn battery has a significant energy density of 1.87 mWh/cm^2 due to the abundant reaction sites and short electron and ion diffusion paths provided by the MOF Silver nanowires (**Figure 8A**). After bending 135° and cycling 100 times, its capacity remained above 93% (**Figure 8B**), which further demonstrates the superb mechanical properties of the prepared devices (**Figure 8C**). (Li et al., 2018c) In addition, Cai and colleagues prepared three-dimensional (3D) integrated binder-free dual-functional oxygen electrodes composed of $NiCo_2O_4$@NiCoFe-hydroxide ($NiCo_2O_4$@NiCoFe-OH) nanoarrays supported by carbon cloth (**Figure 8D**). The three-dimensional porous structure and good hydrophilicity of the nitrate-treated carbon cloth substrate facilitated the directional growth of $NiCo_2O_4$ nanocrystals. Therefore, the nickel-iron-hydroxide can randomly anchore and cover on the NiFe surface. Using this controllable and cost-effective *in-situ* synthesis strategy, the core/shell structure of $NiCo_2O_4$@NiCoFe-OH nanoarrays is tightly attached to the 3D interconnected carbon microfibers. (**Figure 8E**).The manufactured monolithic binderless oxygen electrode is freestanding and highly flexible/bendable, inheriting a high mechanical strength carbon skeleton. (Li et al., 2020c).

Screen Printing Method

Many flexible batteries rely on complex, low-production and high-cost manufacturing processes that hinder their transition from the lab to the marketplace, so printed high-performance batteries offer ideas for mass production of flexible batteries. Screen printing is considered to be a cost-effective, easy-to-operate and mass-productable method for the rapid construction of flexible zinc ion cells with precise control performance, flexibility and integration with printed microelectronics. (Guo et al., 2018). Screen printing allows active design control and can potentially combine deterministic and stochastic composites. In order to meet the need for flexibility and scalability while maintaining low cost and using low-cost thick film manufacturing techniques, flexible cell modules can be printed sheet by sheet or roll by roll using traditional and low-maintenance screen printing or scraper casting equipment, thus achieving low-cost mass production of

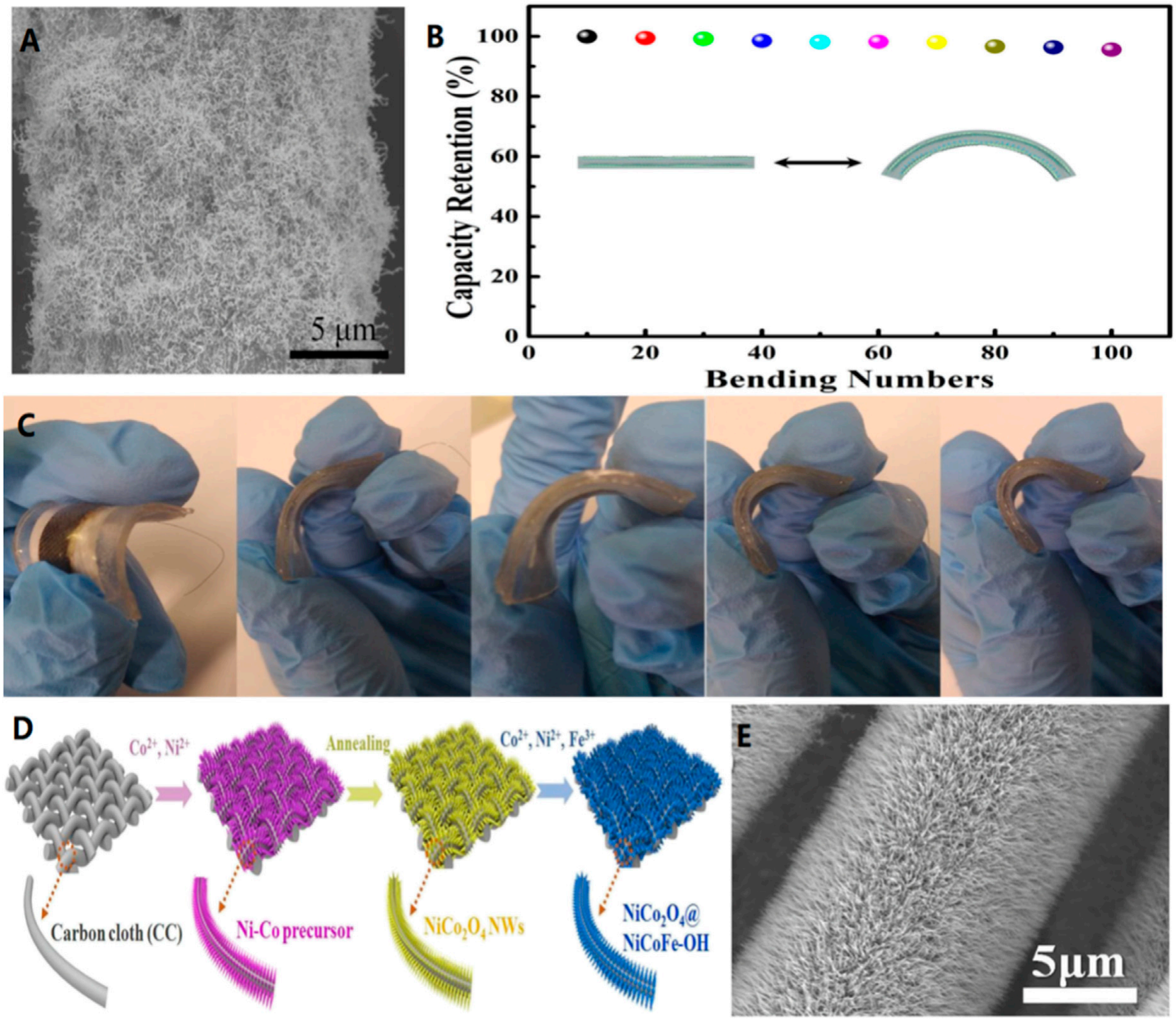

FIGURE 8 | (A) SEM of MOF derived Ag nanowires/CC at Ar/NH_3. **(B)** Normalized capacity of the quasi-solid-state Ag-Zn battery bent 135°for 100 cycles. **(C)** The photographs of bent quasi-solid-state Ag-Zn battery.Copyright 2018 American Chemical Society. **(D)** Scheme of the synthetic process of $NiCo_2O_4$@NiCoFe-OH. SEM images of $NiCo_2O_4$ NWs **(E)** grown on CC. Copyright 2020 Journal of Materials Chemistry A.

flexible batteries (**Figures 9A,B**). (Kumar et al., 2016; Yin et al., 2021)

Wu's team reports on a cost-effective and industrially applicable screen printing strategy for the rapid and scalable production of rechargeable zinc-manganese dioxide planar batteries with high performance, superior flexibility, scalable applicability and high safety. With zinc ink as anode (6.4 µm thick) and MnO_2 ink as cathode (9.8 µm thick), high-quality graphene ink was used as metal-free collector in neutral electrolyte (2 M $ZnSO_4$ and 0.5 m $MnSO_4$). Planar unbaffled Zn//MnO_2 MBs, tested in neutral aqueous solution, has a high capacity of 19.3 mA h/cm^3 (corresponding to 393 mA h/g) at a current density of 7.5 mA/cm^3, and a significant volume energy density of 17.3 mWh/cm^3, superior to lithium film battery (≤10 mWh/cm^3). In addition, the battery has stable cycling performance, with a capacity retention rate of 83.9% after 1,300 cycles under 5C, which is better than the previously reported stacked Zn//MnO_2 battery (**Figures 9C,D**). (Wang et al., 2020)

Screen printing solves the requirement of high volume production of flexible electrodes at low cost, but faces another difficulty, which is to select or develop the ink formulation and choose the mesh size, as well as the thickness of each layer of ink film forming the anode and cathode, according to the requirements of the amount of active material, electrical properties, electrode stability and electrolyte permeability. (Tehrani et al., 2015). The selection of the mesh is based on the particle size of the mass of active material to be printed. A mesh with too large an aperture loses the significance of screen printing, while a mesh with too small aperture leads to uneven printing of the active material, which in turn affects the electrochemical properties. The right printing template will allow the active substance to be printed more evenly and firmly and to meet the required amount of active substance.

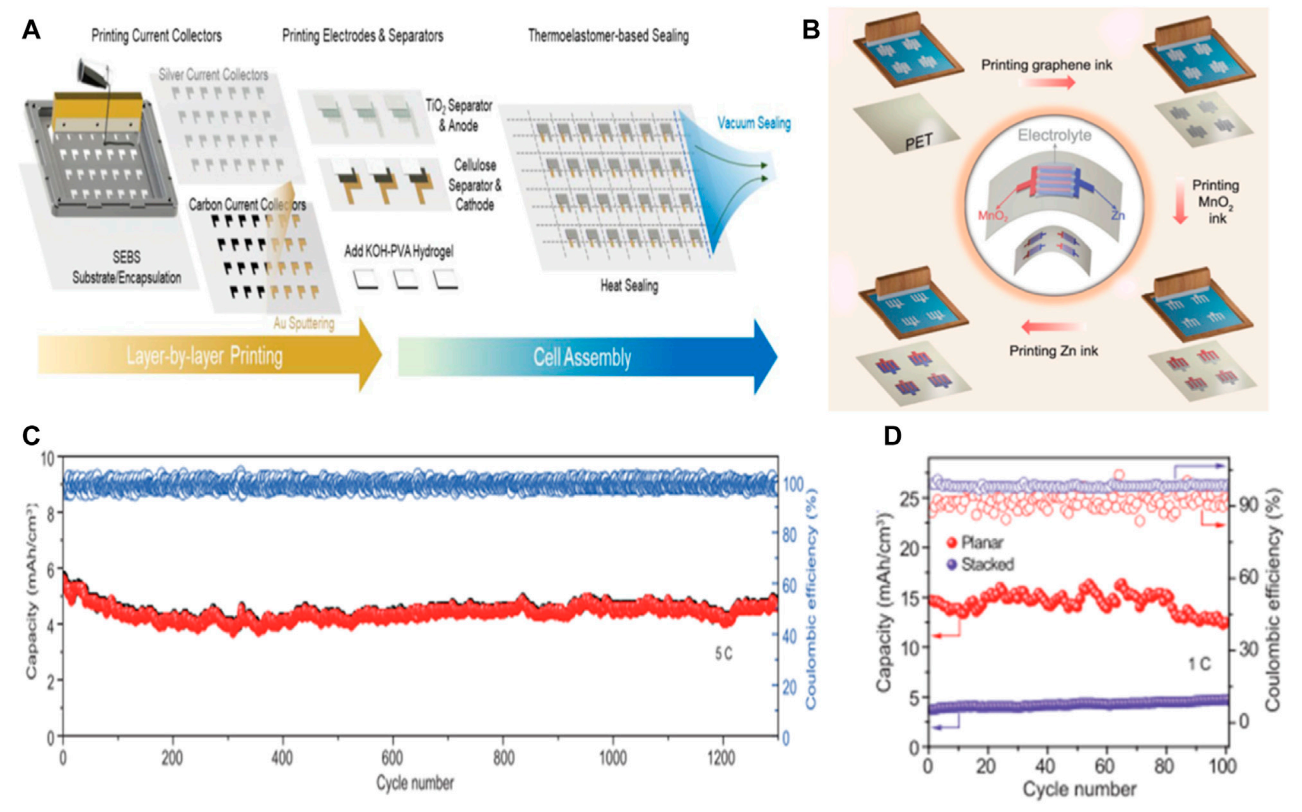

FIGURE 9 | (A) The process of assembling the flexible, rechargeable, and high-capacity AGO-Zn battery is silkscreen printed layer by layer and vacuum sealed. Copyright 2019 ResearchGate. **(B)** Zn//MnO_2 planar MBs was prepared by printing. Schematic diagram of printing zinc//MNO_2MB by screen printing method: Blank PETsubstrate, printing graphene collector electrode, printing MnO_2 cathode and Zn anode. Electrochemical performance of printed Zn//MnO_2 planar MBs **(C)** cycling stabilities of printed Zn//MnO_2 MBs with planar and sandwich-like stacked geometries, measured at a rate of 1 C; **(D)** long-term cycle stability of Zn//MnO_2 planar MBs, with a high rate of 5C over 1,300 cycles. Copyright 2020 Natl Sci Rev.

The rheology of the ink is controlled by a complex formulation of reactive materials, binders and specific solvents. The role of the binder is to bond the ink components and the collector fluid together and to influence whether the active substance will come off. Ink with different ratios of the same active material can also have a great impact on the battery performance. Somenath Mitra's team reported the preparation of printable composite electrodes embedded with multi-walled carbon nanotubes (CNTs) for flexible Ni-Zn batteries. (Wang et al., 2018b). Carbon nanotubes function for electron transport pathways, resulting in better performance than physical mixing of active materials. However, excessive amounts of carbon nanotubes can lead to cracking of the active material. Therefore, it is extremely important to test a suitable ink formulation, which is an inevitable requirement for the preparation of cells with excellent electrochemical properties.

Inkjet Printing Method

Inkjet printing, as an environmentally friendly and low-cost method for direct deposition of functional nanomaterials, has received widespread attention. Non-contact printing can be achieved on various substrates by programming the print pattern to be printed and then controlling the movement of the print nozzle. The modes of operation for inkjet printing are (i) drop-on-demand (DoD) printing, which delivers droplets caused by thermal bubbles or piezoelectric actuators, and (ii) continuous inkjet (CIJ) printing, which produces a continuous stream of ink through the nozzle by means of an electrostatic field or magnetic field. (Zhang et al., 2020e; Yan et al., 2020).

Ink-jet printing provides the advantage of flexible and wearable electronics manufacturing, such as design of high-throughput, large-scale, good performance, biocompatibility, and on the infinite basal precision deposition. In addition, due to droplet deposition and programmable pattern design, inkjet printing methods greatly reduce the waste of expensive ink materials (**Figure 10A**).

Chen and his colleagues proposed a heterogeneous metal seed-mediated strategy. The basic idea is to print silver nanoparticles on a three-dimensional conductive backbone by inkjet printing and use them as heterogeneous metal seeds to induce uniform nucleation of zinc and avoid dendrite growth during the initial electroplating stage.At the same time, the reaction of Ag with Zn produces a zinc-friendly $AgZn_3$ alloy as a Zn resource to compensate for the irreversible loss of active Zn during the recycling process. In the first 15 cycles, the capacity of the AgNPs@CC/Zn anode cell increased from 182 mA/g to 237 mA/g and maintained a

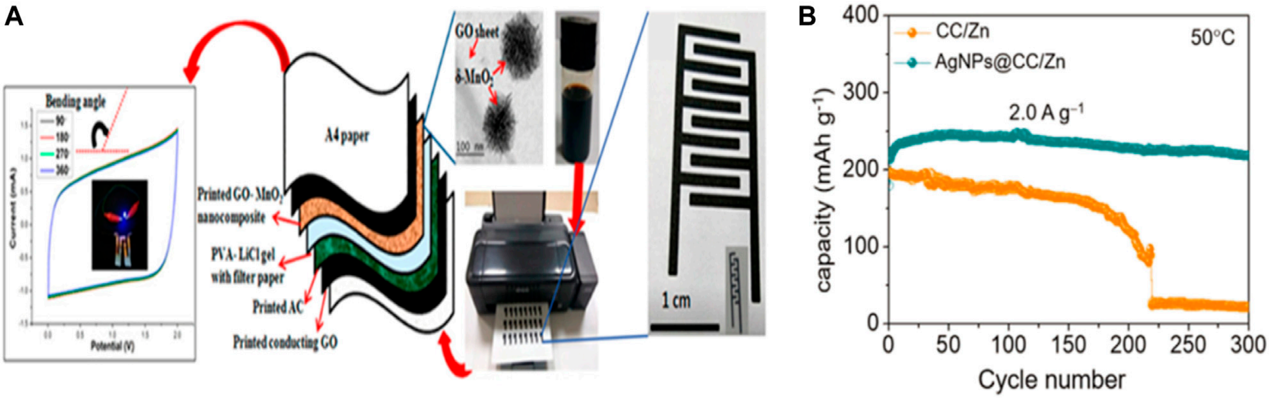

FIGURE 10 | (A) Schematic of inkjet-printed MnO_2/GO-based flexible supercapacitors on A4 paper substrates using an EPSON L130 printer. Left: CV curves of the flexible supercapacitors under various bending angles. Reproduced with permission from P. Copyright 2017 American Chemical Society. **(B)** Use the CC/zinc and AgNPs @ CC/zinc anode NVO lots zinc battery cycle stability under the condition of 50°C.Copyright 2021 Advanced Functional Materials.

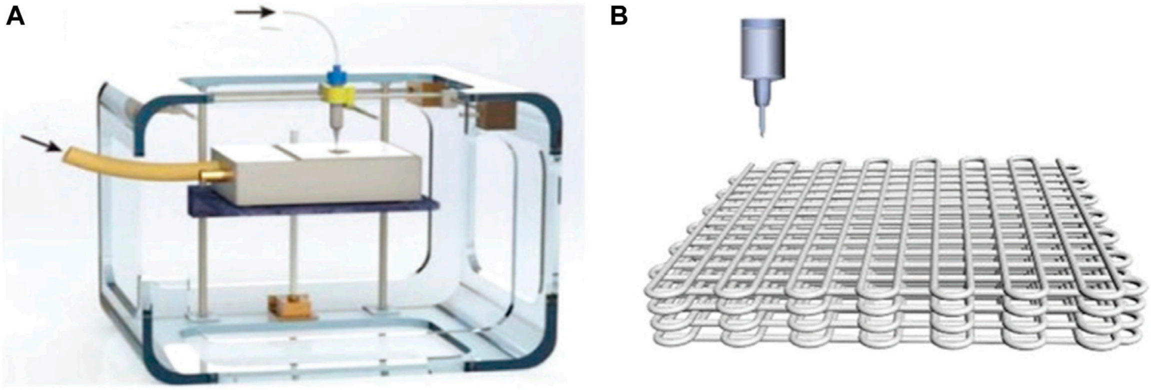

FIGURE 11 | (A) Schematic of the 3D “drop-on-demand” ink jet printer.Copyright 2019, Elsevier. **(B)** Schematic illustration of 3DP-Zn-E. Copyright 2019, Advanced Functional Materials.

reversible capacity of 218 mA/g, corresponding to a capacity retention rate of 92% (**Figure 10B**). (Chen et al., 2021a)

However, at present, there are still many challenges that the technology is relatively bad. These challenges include preventing nozzle clogging, inhibiting coffee ring effect, and enhancing ink dispersion,etc. (Yan et al., 2020)

Other Methods

Those climb from claiming 3D printing (3DP) innovation Concerning illustration An revolutionary manufacturing system has created a great attraction for the fabrication of functional electrodes in the field of energy storage and conversion. The printing process usually combines digital programming and manufacturing procedures to rationally design a 3D functional structural model of the object, followed by the use of special software to obtain sliced layers of the model, which are printed using digital technology material printers, i.e. by adding each two-dimensional (2D) layer to the previous one, enabling the construction of a 3D structure, thus enabling precise control of the spatial geometry and architecture of the device from the macro to the nano scale (**Figure 11A**). (Pang et al., 2019) Yang’s team has demonstrated a 3D printing system for those development of practical electrodes for zinc-air batteries. The printed anode comprises for large portions minor zinc balls. to enhance the utilization of zinc. The self-supporting air cathode made by 3D printing has a hierarchical porous structure with high specific surface area, which allows the electrode to have high electrocatalytic activity and fast reaction diffusion channels (**Figure 11B**). Thanks to these advantages, the assembled zinc-air battery achieves a high releasing capacity of 670 mA h/g at a current density of 5 mA/cm^2 and a long period cycle stability of at least 350 cycles. (Zhang et al., 2020f).

Laser engraving processing is based on the use of CNC technology and laser as the processing medium. The physical denaturation of the electrode material by instantaneous melting and vaporization under laser engraving irradiation enables laser engraving to achieve the processing purpose, which in turn completes the preparation of flexible electrodes.Wang’s team used a high-precision, simple and low-cost laser engraving technique to prepare finger-shaped cathodes and anodes for ZIMB. Suspended finger-like multi-walled carbon nanotube MnO_2 (MWCNTs-MnO_2) cathodes were prepared by laser engraving machine (JL-K3020) and MWCNTs-Zn anodes based on zinc nanosheets were prepared by laser etching with further acknowledge the full adaptability from claiming ZIMB. The flexible conductive substrate prepared by laser engraving allows ZIMB to exhibit excellent flexibility, resulting in high reliability and stability of ZIMB. The concept proves that the capacity maintenance of ZIMB is up to 96.5% of the beginning capacity at 120° bending angle, and even after the 5th self-healing cycle, the capacity retention is still up to 90.2%. This worth of effort gives new plans for outlining another era of high-efficiency, high-reliability and high-stability micro-energy storage devices. (Du et al., 2020).

SUMMARY AND OUTLOOK

In the era of electronic information technology, electronic devices are developing towards miniaturization and flexibility. Those ever-growing enthusiasm from both academic Group What's more shopper showcase will be activating those fast advancement of new helter skelter execution adaptable vitality stockpiling gadgets. In the research of flexible power supply, flexible zinc ion batteries have been noticed by researchers and have achieved some promising results. In this paper, the research progress of flexible zinc batteries in recent years is reviewed from the following aspects: the differences between different anode, cathode materials and electrolytes in flexible zinc batteries; the method of loading active materials on flexible electrodes are discussed and compared. Although many progresses have been made in this area, it is still highly desirable to solve the following challenges and problems in time to promote the application of flexible zinc batteries.

First of all, the performance of the active materials has a critical impact on the cycling performance and flexibility of the battery. The research of zinc anodes mainly focuses on the material of metal zinc anodes. The primary goal is to reduce the generation of zinc dendrites during long-term cycling, so as to improve the lifetime and electrochemical performance of the battery. Most studies have used zinc foil directly, and some studies have cast zinc and zinc oxide particles on flexible substrates or grow zinc *in situ* instead of zinc foil in order to obtain better mechanical properties and stability. The research of cathodes is mainly to try to obtain materials with high capacity, high cycling performance, low cost and good mechanical properties, including ion embedding and oxygen vacancy generation for some cathode materials to improve the battery performance. Moreover, the research on the electrolyte of flexible zinc ion battery mainly focuses on the gel electrolyte. It consists of polymer body and liquid electrolyte, which has relatively excellent flexibility performance and can basically meet the needs of flexible zinc ion battery, and also has relatively good ionic conductivity to improve the multiplication performance of flexible zinc ion battery, as well as can make good interfacial contact with electrode.

Secondly, the main technologies for loading active materials onto flexible electrodes include *in-situ* growth method, screen printing, and inkjet printing and so on. Among them, the *in-situ* growth of active materials does not require binder, which ensures rapid charge transfer between active materials and collectors, makes the active material evenly distributed on the collector, so that the prepared flexible electrodes have better electrochemical performance. Screen printing is a sheet-by-sheet or roll-by-roll printing method for flexible cell, which is considered to be a cost-effective, easy-to-handle and mass-producible process. Inkjet printing can programmed according to the pattern to be printed, enabling non-contact printing on a variety of substrates, resulting in low-cost, high-precision, high-efficiency electrode printing, which can be used for artificial intelligence equipment, special-shaped battery and private customization.

With the innovation of technology, flexible zinc ion battery has a wide application prospect in flexible electronic devices due to its excellent performance. The development of wearable/implantable electronic devices such as flexible display devices, health monitors and electronic sensors has attracted more and more attention from academia and industry. One of the biggest challenges in the development of flexible electronic devices is to develop flexible, light, thin and safe portable energy storage devices. Flexible water zinc ion batteries are safe, can meet safety performance, and can be designed to fit into clothing and other wearable devices. The batteries must better fit the shape of wearable devices to avoid being bulky. Therefore, the development prospect of flexible zinc ion battery is broad.

Despite the advantages of flexible zinc batteries, there are still many problems for researchers to continue to study: (1) compared with the high theoretical capacity of the zinc metal anode, the cathode active material with higher capacity need to be explored; (2) the stability of the zinc negative electrode at high current and high capacity needs to improved; (3) in flexible batteries, with movements such as bending, the loaded active material usually cracks or flakes off, leading to a rapid decline in electrochemical performance. Therefore, it is necessary to design the ideal electrode material structure or improve the process method of loaded active material, and then further improve the mechanical properties of the electrode; (4) to further increase the actual capacity of flexible zinc batteries while improving the mechanical properties of electrodes. How to encourage the capacity of zinc ion batteries by increasing the amount of loaded active substance, which in turn has wider practicality.

AUTHOR CONTRIBUTIONS

All authors listed have made a substantial, direct, and intellectual contribution to the work and approved it for publication.

FUNDING

This work was financially supported by the National Natural Science Foundation of China (61904097), the Shandong Scientific Research Awards Foundation for Outstanding Young Scientists (No. ZR2018BEM030), Scientific Research Foundation of Shandong University of Science and Technology for Recruited Talents (No. 2017RCJJ058) and the Program for Tsingtao Al-ion Power and Energy-storage Battery Research Team in the University.

REFERENCES

Alfaruqi, M. H., Islam, S., Putro, D. Y., Mathew, V., Kim, S., Jo, J., et al. (2018). Structural Transformation and Electrochemical Study of Layered MnO2 in Rechargeable Aqueous Zinc-Ion Battery. *Electrochimica Acta* 276, 1–11. doi:10.1016/j.electacta.2018.04.139

Chamoun, M., Brant, W. R., Tai, C.-W., Karlsson, G., and Noréus, D. (2018). Rechargeability of Aqueous Sulfate Zn/MnO2 Batteries Enhanced by Accessible Mn2+ Ions. *Energ. Storage Mater.* 15, 351–360. doi:10.1016/j.ensm.2018.06.019

Chen, M., Chen, J., Zhou, W., Han, X., Yao, Y., and Wong, C. P. (2021). Realizing an All-Round Hydrogel Electrolyte toward Environmentally Adaptive Dendrite-free Aqueous Zn-MnO_2 Batteries. *Adv. Mater.* 33 (9), e2007559. doi:10.1002/adma.202007559

Chen, T., Wang, Y., Yang, Y., Huang, F., Zhu, M., Wei Ang, B. T., et al. (2021). Heterometallic Seed-Mediated Zinc Deposition on Inkjet Printed Silver Nanoparticles toward Foldable and Heat-Resistant Zinc Batteries. *Adv. Funct. Mater.* 31 (24). doi:10.1002/adfm.202101607

Cong, Z., Guo, W., Zhang, P., Sha, W., Guo, Z., Chang, C., et al. (2021). Wearable Antifreezing Fiber-Shaped Zn/PANI Batteries with Suppressed Zn Dendrites and Operation in Sweat Electrolytes. *ACS Appl. Mater. Inter.* 13 (15), 17608–17617. doi:10.1021/acsami.1c02065

Dong, H., Li, J., Guo, J., Lai, F., Zhao, F., Jiao, Y., et al. (2021). Insights on Flexible Zinc-Ion Batteries from Lab Research to Commercialization. *Adv. Mater.* 33 (20), e2007548. doi:10.1002/adma.202170158

Du, X., Shi, J., Chen, Z., Ni, T., Li, J., Ruan, L., et al. (2020). A Laser Etched Zinc Ion Microbattery with Excellent Flexibility and Self-Healability. *Sustainable Energ. Fuels* 4 (9), 4713–4721. doi:10.1039/d0se00843e

Eftekhari, A., Li, L., and Yang, Y. (2017). Polyaniline Supercapacitors. *J. Power Sourc.* 347, 86–107. doi:10.1016/j.jpowsour.2017.02.054

Fan, X., Liu, J., Song, Z., Han, X., Deng, Y., Zhong, C., et al. (2019). Porous Nanocomposite Gel Polymer Electrolyte with High Ionic Conductivity and superior Electrolyte Retention Capability for Long-Cycle-Life Flexible Zinc–Air Batteries. *Nano Energy* 56, 454–462. doi:10.1016/j.nanoen.2018.11.057

Fang, G., Zhou, J., Pan, A., and Liang, S. (2018). Recent Advances in Aqueous Zinc-Ion Batteries. *ACS Energ. Lett.* 3 (10), 2480–2501. doi:10.1021/acsenergylett.8b01426

Gaikwad, A. M., Whiting, G. L., Steingart, D. A., and Arias, A. C. (2011). Highly Flexible, Printed Alkaline Batteries Based on Mesh-Embedded Electrodes. *Adv. Mater.* 23 (29), 3251–3255. doi:10.1002/adma.201100894

Guo, F., Gao, S., Ji, C., Mi, H., Li, H., Zhang, W., et al. (2021). Finely Crafted Polyaniline Cathode for High-Performance Flexible Quasi-Solid-State Zn-Ion Battery. *Solid State Ionics* 364, 115612. doi:10.1016/j.ssi.2021.115612

Guo, X., Fang, G., Zhang, W., Zhou, J., Shan, L., Wang, L., et al. (2018). Mechanistic Insights of Zn^{2+} Storage in Sodium Vanadates. *Adv. Energ. Mater.* 8 (27). doi:10.1002/aenm.201801819

Han, J., Wang, K., Liu, W., Li, C., Sun, X., Zhang, X., et al. (2018). Rational Design of Nano-Architecture Composite Hydrogel Electrode towards High Performance Zn-Ion Hybrid Cell. *Nanoscale* 10 (27), 13083–13091. doi:10.1039/c8nr03889a

Han, Q., Chi, X., Zhang, S., Liu, Y., Zhou, B., Yang, J., et al. (2018). Durable, Flexible Self-Standing Hydrogel Electrolytes Enabling High-Safety Rechargeable Solid-State Zinc Metal Batteries. *J. Mater. Chem. A* 6 (45), 23046–23054. doi:10.1039/c8ta08314b

Hilder, M., Winther-Jensen, B., and Clark, N. B. (2009). Paper-based, Printed Zinc–Air Battery. *J. Power Sourc.* 194 (2), 1135–1141. doi:10.1016/j.jpowsour.2009.06.054

Huang, Y., Mou, J., Liu, W., Wang, X., Dong, L., Kang, F., et al. (2019). Novel Insights into Energy Storage Mechanism of Aqueous Rechargeable Zn/MnO2 Batteries with Participation of Mn2+. *Nano-micro Lett.* 11 (1), 49. doi:10.1007/s40820-019-0278-9

Javed, M. S., Lei, H., Wang, Z., Liu, B-t., Cai, X., and Mai, W. (2020). 2D V_2O_5 Nanosheets as a Binder-free High-Energy Cathode for Ultrafast Aqueous and Flexible Zn-Ion Batteries. *Nano Energy* 70, 104573. doi:10.1016/j.nanoen.2020.104573

Jia, Z., Wang, B., and Wang, Y. (2015). Copper Hexacyanoferrate with a Well-Defined Open Framework as a Positive Electrode for Aqueous Zinc Ion Batteries. *Mater. Chem. Phys.* 149-150, 601–606. doi:10.1016/j.matchemphys.2014.11.014

Jo, Y. N., Prasanna, K., Kang, S. H., Ilango, P. R., Kim, H. S., Eom, S. W., et al. (2017). The Effects of Mechanical Alloying on the Self-Discharge and Corrosion Behavior in Zn-Air Batteries. *J. Ind. Eng. Chem.* 53, 247–252. doi:10.1016/j.jiec.2017.04.032

Kaveevivitchai, W., and Manthiram, A. (2016). High-capacity Zinc-Ion Storage in an Open-Tunnel Oxide for Aqueous and Nonaqueous Zn-Ion Batteries. *J. Mater. Chem. A.* 4 (48), 18737–18741. doi:10.1039/c6ta07747a

Kumar, R., Johnson, K. M., Williams, N. X., and Subramanian, V. (2019). Scaling Printable Zn–Ag_2O Batteries for Integrated Electronics. *Adv. Energ. Mater.* 9 (13). doi:10.1002/aenm.201803645

Kumar, R., Shin, J., Yin, L., You, J. M., Meng, Y. S., and Wang, J. (2016). All-Printed, Stretchable Zn-Ag_2O Rechargeable Battery via Hyperelastic Binder for Self-Powering Wearable Electronics. *Adv. Energ. Mater.* 7 (8). doi:10.1002/aenm.201602096

Lao-atiman, W., Julaphatachote, T., Boonmongkolras, P., and Kheawhom, S. (2017). Printed Transparent Thin Film Zn-MnO2Battery. *J. Electrochem. Soc.* 164 (4), A859–A863. doi:10.1149/2.1511704jes

Lee, S.-M., Kim, Y.-J., Eom, S.-W., Choi, N.-S., Kim, K.-W., and Cho, S.-B. (2013). Improvement in Self-Discharge of Zn Anode by Applying Surface Modification for Zn-Air Batteries with High Energy Density. *J. Power Sourc.* 227, 177–184. doi:10.1016/j.jpowsour.2012.11.046

Li, C., Zhang, Q., Sun, J., Li, T., Songfeng, E., Zhu, Z., et al. (2018). High-Performance Quasi-Solid-State Flexible Aqueous Rechargeable Ag–Zn Battery Based on Metal–Organic Framework-Derived Ag Nanowires. *ACS Energ. Lett.* 3 (11), 2761–2768. doi:10.1021/acsenergylett.8b01675

Li, H., Han, C., Huang, Y., Huang, Y., Zhu, M., Pei, Z., et al. (2018). An Extremely Safe and Wearable Solid-State Zinc Ion Battery Based on a Hierarchical Structured Polymer Electrolyte. *Energy Environ. Sci.* 11 (4), 941–951. doi:10.1039/c7ee03232c

Li, M., Liu, B., Fan, X., Liu, X., Liu, J., Ding, J., et al. (2019). Long-Shelf-Life Polymer Electrolyte Based on Tetraethylammonium Hydroxide for Flexible Zinc-Air Batteries. *ACS Appl. Mater. Inter.* 11 (32), 28909–28917. doi:10.1021/acsami.9b09086

Li, R., Li, L., Jia, R., Jiang, K., Shen, G., and Chen, D. (2020). A Flexible Concentric Circle Structured Zinc-Ion Micro-Battery with Electrodeposited Electrodes. *Small Methods* 4 (9). doi:10.1002/smtd.202000363

Li, S., Yang, X., Yang, S., Gao, Q., Zhang, S., Yu, X., et al. (2020). An Amorphous Trimetallic (Ni–Co–Fe) Hydroxide-Sheathed 3D Bifunctional Electrode for superior Oxygen Evolution and High-Performance cable-type Flexible Zinc–Air Batteries. *J. Mater. Chem. A* 8 (11), 5601–5611. doi:10.1039/d0ta00888e

Li, T., Wang, J., Li, X., Si, L., Zhang, S., and Deng, C. (2020). Unlocking the Door of Boosting Biodirected Structures for High-Performance VNxOy/C by Controlling the Reproduction Mode. *Adv. Sci. (Weinh).* 7 (5), 1903276. doi:10.1002/advs.201903276

Li, X., Tang, Y., Lv, H., Wang, W., Mo, F., Liang, G., et al. (2019). Recent Advances in Flexible Aqueous Zinc-Based Rechargeable Batteries. *Nanoscale* 11 (39), 17992–18008. doi:10.1039/c9nr06721c

Li, Y., Fu, J., Zhong, C., Wu, T., Chen, Z., Hu, W., et al. (2018). Recent Advances in Flexible Zinc-Based Rechargeable Batteries. *Adv. Energ. Mater.* 9 (1). doi:10.1002/aenm.201802605

Lian, S., Sun, C., Xu, W., Huo, W., Luo, Y., Zhao, K., et al. (2019). Built-in Oriented Electric Field Facilitating Durable Zn MnO2 Battery. *Nano Energy* 62, 79–84. doi:10.1016/j.nanoen.2019.04.038

Liang, M., Zhou, H., Huang, Q., Hu, S., and Li, W. (2011). Synergistic Effect of Polyethylene Glycol 600 and Polysorbate 20 on Corrosion Inhibition of Zinc Anode in Alkaline Batteries. *J. Appl. Electrochem.* 41, 991–997. doi:10.1007/s10800-011-0328-6

Liang, X., Yan, L., Li, W., Bai, Y., Zhu, C., Qiang, Y., et al. (2021). Flexible High-Energy and Stable Rechargeable Vanadium-Zinc Battery Based on Oxygen Defect Modulated V_2O_5 Cathode. *Nano Energy* 87, 106164. doi:10.1016/j.nanoen.2021.106164

Liao, M., Wang, J., Ye, L., Sun, H., Wen, Y., Wang, C., et al. (2020). A Deep-Cycle Aqueous Zinc-Ion Battery Containing an Oxygen-Deficient Vanadium Oxide

Cathode. *Angew. Chem. Int. Ed. Engl.* 59 (6), 2273–2278. doi:10.1002/anie.201912203

Lin, Y., Zhou, F., Xie, M., Zhang, S., and Deng, C. (2020). V_6O_{13}-delta @C Nanoscrolls with Expanded Distances between Adjacent Shells as a High-Performance Cathode for a Knittable Zinc-Ion Battery. *ChemSusChem* 13 (14), 3696–3706. doi:10.1002/cssc.202000699

Liu, J., Guan, C., Zhou, C., Fan, Z., Ke, Q., Zhang, G., et al. (2016). A Flexible Quasi-Solid-State Nickel-Zinc Battery with High Energy and Power Densities Based on 3D Electrode Design. *Adv. Mater.* 28 (39), 8732–8739. doi:10.1002/adma.201603038

Liu, T., Mou, J., Wu, Z., Lv, C., Huang, J., and Liu, M. (2020). A Facile and Scalable Strategy for Fabrication of Superior Bifunctional Freestanding Air Electrodes for Flexible Zinc–Air Batteries. *Adv. Funct. Mater.* 30 (36). doi:10.1002/adfm.202003407

Liu, Y., Xie, L., Zhang, W., Dai, Z., Wei, W., Luo, S., et al. (2019). Conjugated System of PEDOT:PSS-Induced Self-Doped PANI for Flexible Zinc-Ion Batteries with Enhanced Capacity and Cyclability. *ACS Appl. Mater. Inter.* 11 (34), 30943–30952. doi:10.1021/acsami.9b09802

Liu, Z., Liang, G., Zhan, Y., Li, H., Wang, Z., Ma, L., et al. (2019). A Soft yet Device-Level Dynamically Super-tough Supercapacitor Enabled by an Energy-Dissipative Dual-Crosslinked Hydrogel Electrolyte. *Nano Energy* 58, 732–742. doi:10.1016/j.nanoen.2019.01.087

Liu, Z., Mo, F., Li, H., Zhu, M., Wang, Z., Liang, G., et al. (2018). Advances in Flexible and Wearable Energy-Storage Textiles. *Small Methods* 2 (11). doi:10.1002/smtd.201800124

Lu, K., Song, B., Zhang, Y., Ma, H., and Zhang, J. (2017). Encapsulation of Zinc Hexacyanoferrate Nanocubes with Manganese Oxide Nanosheets for High-Performance Rechargeable Zinc Ion Batteries. *J. Mater. Chem. A.* 5 (45), 23628–23633. doi:10.1039/c7ta07834j

Ma, L., Chen, S., Li, N., Liu, Z., Tang, Z., Zapien, J. A., et al. (2020). Hydrogen-Free and Dendrite-free All-Solid-State Zn-Ion Batteries. *Adv. Mater.* 32 (14), e1908121. doi:10.1002/adma.201908121

Ma, L., Chen, S., Long, C., Li, X., Zhao, Y., Liu, Z., et al. (2019). Achieving High-Voltage and High-Capacity Aqueous Rechargeable Zinc Ion Battery by Incorporating Two-Species Redox Reaction. *Adv. Energ. Mater.* 9 (45). doi:10.1002/aenm.201902446

Ma, L., Chen, S., Wang, D., Yang, Q., Mo, F., Liang, G., et al. (2019). Super-Stretchable Zinc–Air Batteries Based on an Alkaline-Tolerant Dual-Network Hydrogel Electrolyte. *Adv. Energ. Mater.* 9 (12). doi:10.1002/aenm.201803046

Ma, L., Chen, S., Li, H., Ruan, Z., Tang, Z., Liu, Z., et al. (2018). Initiating a Mild Aqueous Electrolyte Co3O4/Zn Battery with 2.2 V-High Voltage and 5000-cycle Lifespan by a Co(iii) Rich-Electrode. *Energ. Environ. Sci.* 11 (9), 2521–2530. doi:10.1039/c8ee01415a

Naveed, A., Yang, H., Yang, J., Nuli, Y., and Wang, J. (2019). Highly Reversible and Rechargeable Safe Zn Batteries Based on a Triethyl Phosphate Electrolyte. *Angew. Chem. Int. Ed. Engl.* 58 (9), 2760–2764. doi:10.1002/anie.201813223

Nguyen, T. T., Balamurugan, J., Kim, D. H., Kim, N. H., and Lee, J. H. (2020). Hierarchical 3D Oxygenated Cobalt Vanadium Selenide Nanosheets as Advanced Electrode for Flexible Zinc-Cobalt and Zinc-Air Batteries. *Small* 16 (48), e2004661. doi:10.1002/smll.202004661

Pan, H., Shao, Y., Yan, P., Cheng, Y., Han, K. S., Nie, Z., et al. (2016). Reversible Aqueous Zinc/manganese Oxide Energy Storage from Conversion Reactions. *Nat. Energ.* 1, 16039. doi:10.1038/nenergy.2016.39

Pang, Y., Cao, Y., Chu, Y., Liu, M., Snyder, K., Mackenzie, D., et al. (2019). Additive Manufacturing of Batteries. *Adv. Funct. Mater.* 30 (1). doi:10.1002/adfm.201906244

Qiu, W., Li, Y., You, A., Zhang, Z., Li, G., Lu, X., et al. (2017). High-performance Flexible Quasi-Solid-State Zn-MnO2 Battery Based on MnO2 Nanorod Arrays Coated 3D Porous Nitrogen-Doped Carbon Cloth. *J. Mater. Chem. A.* 5 (28), 14838–14846. doi:10.1039/c7ta03274a

Shi, H.-Y., Ye, Y.-J., Liu, K., Song, Y., and Sun, X. (2018). A Long-Cycle-Life Self-Doped Polyaniline Cathode for Rechargeable Aqueous Zinc Batteries. *Angew. Chem. Int. Ed.* 57 (50), 16359–16363. doi:10.1002/anie.201808886

Song, H., Liu, C., Zhang, C., and Cao, G. (2016). Self-doped V^{4+}–V_2o_5 Nanoflake for 2 Li-Ion Intercalation with Enhanced Rate and Cycling Performance. *Nano Energy* 22, 1–10. doi:10.1016/j.nanoen.2016.02.004

Song, M., Tan, H., Chao, D., and Fan, H. J. (2018). Recent Advances in Zn-Ion Batteries. *Adv. Funct. Mater.* 28 (41). doi:10.1002/adfm.201802564

Sumboja, A., Liu, J., Zheng, W. G., Zong, Y., Zhang, H., and Liu, Z. (2018). Electrochemical Energy Storage Devices for Wearable Technology: a Rationale for Materials Selection and Cell Design. *Chem. Soc. Rev.* 3047 (15), 5919–5945. doi:10.1039/c8cs00237a

Tan, P., Chen, B., Xu, H., Cai, W., He, W., Zhang, H., et al. (2018). Integration of Zn-Ag and Zn-Air Batteries: A Hybrid Battery with the Advantages of Both. *ACS Appl. Mater. Inter.* 10 (43), 36873–36881. doi:10.1021/acsami.8b10778

Tan, P., Chen, B., Xu, H., Zhang, H., Cai, W., Ni, M., et al. (2017). Flexible Zn- and Li-Air Batteries: Recent Advances, Challenges, and Future Perspectives. *Energ. Environ. Sci.* 10 (10), 2056–2080. doi:10.1039/c7ee01913k

Tang, B., Shan, L., Liang, S., and Zhou, J. (2019). Issues and Opportunities Facing Aqueous Zinc-Ion Batteries. *Energ. Environ. Sci.* 12 (11), 3288–3304. doi:10.1039/c9ee02526j

Tehrani, Z., Korochkina, T., Govindarajan, S., Thomas, D. J., Mahony, J. O., Kettle, J., et al. (2015). Ultra-thin Flexible Screen Printed Rechargeable Polymer Battery for Wearable Electronic Applications. *Org. Electronics* 26, 386–394. doi:10.1016/j.orgel.2015.08.007

vKundu, D., Adams, B. D., Duffort, V., Vajargah, S. H., and Nazar, L. F. (2016). A High-Capacity and Long-Life Aqueous Rechargeable Zinc Battery Using a Metal Oxide Intercalation Cathode. *Nat. Energ.* 1 (10). doi:10.1038/nenergy.2016.119

Wan, F., Zhang, L., Dai, X., Wang, X., Niu, Z., and Chen, J. (2018). Aqueous Rechargeable Zinc/sodium Vanadate Batteries with Enhanced Performance from Simultaneous Insertion of Dual Carriers. *Nat. Commun.* 9 (1), 1656. doi:10.1038/s41467-018-04060-8

Wang, D., Li, H., Liu, Z., Tang, Z., Liang, G., Mo, F., et al. (2018). A Nanofibrillated Cellulose/Polyacrylamide Electrolyte-Based Flexible and Sewable High-Performance Zn-MnO_2 Battery with Superior Shear Resistance. *Small* 14 (51), e1803978. doi:10.1002/smll.201803978

Wang, H., Bi, X., Bai, Y., Wu, C., Gu, S., Chen, S., et al. (2017). Open-Structured $V_2O_5{\cdot}nH_2O$ Nanoflakes as Highly Reversible Cathode Material for Monovalent and Multivalent Intercalation Batteries. *Adv. Energ. Mater.* 7 (14). doi:10.1002/aenm.201770077

Wang, X., Zheng, S., Zhou, F., Qin, J., Shi, X., Wang, X., et al. (2020). Scalable Fabrication of Printed Zn//MnO_2 Planar Micro-batteries with High Volumetric Energy Density and Exceptional Safety. *Natl. Sci. Rev.* 7 (1), 64–72. doi:10.1093/nsr/nwz070

Wang, Z., Meng, X., Chen, K., and Mitra, S. (2018). Synthesis of Carbon Nanotube Incorporated Metal Oxides for the Fabrication of Printable, Flexible Nickel-Zinc Batteries. *Adv. Mater. Inter.* 5 (4). doi:10.1002/admi.201701036

Xu, C., Li, B., Du, H., and Kang, F. (2012). Energetic Zinc Ion Chemistry: the Rechargeable Zinc Ion Battery. *Angew. Chem. Int. Ed.* 51 (4), 933–935. doi:10.1002/anie.201106307

Xu, W., Sun, C., Wang, N., Liao, X., Zhao, K., Yao, G., et al. (2021). Sn Stabilized Pyrovanadate Structure Rearrangement for Zinc Ion Battery. *Nano Energy* 81, 105584. doi:10.1016/j.nanoen.2020.105584

Xu, Y., Zheng, S., Tang, H., Guo, X., Xue, H., and Pang, H. (2017). Prussian Blue and its Derivatives as Electrode Materials for Electrochemical Energy Storage. *Energ. Storage Mater.* 9, 11–30. doi:10.1016/j.ensm.2017.06.002

Yan, K., Li, J., Pan, L., and Shi, Y. (2020). Inkjet Printing for Flexible and Wearable Electronics. *APL Mater.* 8 (12). doi:10.1063/5.0031669

Yao, H., Li, Q., Zhang, M., Tao, Z., and Yang, Y. (2020). Prolonging the Cycle Life of Zinc-Ion Battery by Introduction of $[Fe(CN)_6]^{4-}$ to PANI via a Simple and Scalable Synthetic Method. *Chem. Eng. J.* 392, 123653. doi:10.1016/j.cej.2019.123653

Yin, L., Scharf, J., Ma, J., Doux, J.-M., Redquest, C., Le, V. L., et al. (2021). High Performance Printed AgO-Zn Rechargeable Battery for Flexible Electronics. *Joule* 5, 228–248. doi:10.1016/j.joule.2020.11.008

Yu, M., Lin, D., Feng, H., Zeng, Y., Tong, Y., and Lu, X. (2017). Boosting the Energy Density of Carbon-Based Aqueous Supercapacitors by Optimizing the Surface Charge. *Angew. Chem. Int. Ed.* 56 (20), 5454–5459. doi:10.1002/anie.201701737

Yu, M., Zeng, Y., Han, Y., Chen, X., Zhao, W., Liang, C., et al. (2015). Valence-optimized Vanadium Oxide Supercapacitor Electrodes Exhibit Ultrahigh Capacitance and Super-long Cyclic Durability of 100000 Cycles. *Adv. Funct. Mater.* 25, 3534–3540. doi:10.1002/adfm.201501342

Yu, P., Zeng, Y., Zhang, H., Yu, M., Tong, Y., and Lu, X. (2019). Flexible Zn-Ion Batteries: Recent Progresses and Challenges. *Small* 15 (7), e1804760. doi:10.1002/smll.201804760

Yza, B., Gl, A., and Cz, A. (2022). Low-cost MgFe X $Mn_{2-x}O_4$ Cathode Materials for High-Performance Aqueous Rechargeable Magnesium-Ion Batteries. *Chem. Eng. J.* 392.

Zeng, Y., Zhang, X., Qin, R., Liu, X., Fang, P., Zheng, D., et al. (2019). Dendrite-Free Zinc Deposition Induced by Multifunctional CNT Frameworks for Stable Flexible Zn-Ion Batteries. *Adv. Mater.* 31 (36), e1903675. doi:10.1002/adma.201903675

Zhang, J., Li, X. L., Fan, S., Huang, S., Yan, D., Liu, L., et al. (2020). 3D-printed Functional Electrodes towards Zn-Air Batteries. *Mater. Today Energ.* 16. doi:10.1016/j.mtener.2020.100407

Zhang, L., Chao, D., and Yang, P. (2020). Flexible Pseudocapacitive Electrochromics via Inkjet Printing of Additive-Free Tungsten Oxide Nanocrystal Ink. *Adv. Energ. Mater.* 10 (17). doi:10.1002/aenm.202000142

Zhang, L., Chen, L., Zhou, X., and Liu, Z. (2015). Towards High-Voltage Aqueous Metal-Ion Batteries beyond 1.5 V: The Zinc/Zinc Hexacyanoferrate System. *Adv. Energ. Mater.* 5 (2). doi:10.1002/aenm.201400930

Zhang, N., Cheng, F., Liu, J., Wang, L., Long, X., Liu, X., et al. (2017). Rechargeable Aqueous Zinc-Manganese Dioxide Batteries with High Energy and Power Densities. *Nat. Commun.* 8 (1), 405. doi:10.1038/s41467-017-00467-x

Zhang, N., Cheng, F., Liu, Y., Zhao, Q., Lei, K., Chen, C., et al. (2016). Cation-Deficient Spinel ZnMn2O4 Cathode in Zn(CF3SO3)2 Electrolyte for Rechargeable Aqueous Zn-Ion Battery. *J. Am. Chem. Soc.* 138 (39), 12894–12901. doi:10.1021/jacs.6b05958

Zhang, W., Zuo, C., Tang, C., Tang, W., Lan, B., Fu, X., et al. (2020). The Current Developments and Perspectives of V_2O_5 as Cathode for Rechargeable Aqueous Zinc-Ion Batteries. *Energ. Technology* 9 (2). doi:10.1002/ente.202000789

Zhang, Y., Deng, S., Pan, G., Zhang, H., Liu, B., Wang, X. L., et al. (2020). Introducing Oxygen Defects into Phosphate Ions Intercalated Manganese Dioxide/Vertical Multilayer Graphene Arrays to Boost Flexible Zinc Ion Storage. *Small Methods* 4 (6). doi:10.1002/smtd.201900828

Zhang, Y., Tao, L., Xie, C., Wang, D., Zou, Y., Chen, R., et al. (2020). Defect Engineering on Electrode Materials for Rechargeable Batteries. *Adv. Mater.* 32 (7), e1905923. doi:10.1002/adma.201905923

Zhang, Y., Xu, G., Liu, X., Wei, X., Cao, J., and Yang, L. (2020). Scalable *In Situ* Reactive Assembly of Polypyrrole-Coated MnO 2 Nanowire and Carbon Nanotube Composite as Freestanding Cathodes for High Performance Aqueous Zn-Ion Batteries. *ChemElectroChem* 7 (13), 2762–2770. doi:10.1002/celc.202000253

Zhang, Z., Cui, L., Shi, X., Tian, X., Wang, D., Gu, C., et al. (2018). Textile Display for Electronic and Brain-Interfaced Communications. *Adv. Mater.* 30 (18), e1800323. doi:10.1002/adma.201800323

Zhao, J., Sonigara, K. K., Li, J., Zhang, J., Chen, B., Zhang, J., et al. (2017). A Smart Flexible Zinc Battery with Cooling Recovery Ability. *Angew. Chem. Int. Ed. Engl.* 56, 7871–7875. doi:10.1002/anie.201704373

Zhao, J., Ren, H., Liang, Q., Yuan, D., Xi, S., Wu, C., et al. (2019). High-performance Flexible Quasi-Solid-State Zinc-Ion Batteries with Layer-Expanded Vanadium Oxide Cathode and Zinc/stainless Steel Mesh Composite Anode. *Nano Energy* 62, 94–102. doi:10.1016/j.nanoen.2019.05.010

Zu, D., Wang, H., Lin, S., Ou, G., Wei, H., Sun, S., et al. (2019). Oxygen-deficient Metal Oxides: Synthesis Routes and Applications in Energy and Environment. *Nano Res.* 12 (9), 2150–2163. doi:10.1007/s12274-019-2377-9

Conflict of Interest: The authors declare that the research was conducted in the absence of any commercial or financial relationships that could be construed as a potential conflict of interest.

frontiers in Chemistry

MINI REVIEW
published: 14 February 2022
doi: 10.3389/fchem.2022.832972

Recent Developments of Cathode Materials for Thermal Batteries

Renyi Li, Wei Guo and Yumin Qian**

Key Lab of Advanced Optoelectronic Quantum Architecture and Measurement (MOE), School of Physics, Beijing Institute of Technology, Beijing, China

Big progress has been made in batteries based on an intercalation mechanism in the last 20 years, but limited capacity in batteries hinders their further increase in energy density. The demand for more energy intensity makes research communities turn to conversion-type batteries. Thermal batteries are a special kind of conversion-type battery, which are thermally activated primary batteries composed mainly of cathode, anode, separator (electrolyte), and heating mass. Such kinds of battery employ an internal pyrotechnic source to make the battery stack reach its operating temperature. Thermal batteries have a long history of research and usage in military fields because of their high specific capacity, high specific energy, high thermal stability, long shelf life, and fast activation. These experiences and knowledge are of vital importance for the development of conversion-type batteries. This review provides a comprehensive account of recent studies on cathode materials. The paper covers the preparation, characterization of various cathode materials, and the performance test of thermal batteries. These advances have significant implications for the development of high-performance, low-cost, and mass production conversion-type batteries in the near future.

Keywords: thermal batteries, cathode materials, metal chlorides, metal fluorides, metal sulfides

INTRODUCTION

Thermal batteries are a special kind of primary batteries that can be stored in an inactive state for a long time and then activated generally at 350–550°C when energy is required (Guidotti and Masset, 2006; Choi et al., 2015). It was first invented and developed in the 1940s to power German weapons (Guidotti and Masset, 2006). The activation time and power density greatly affect the response speed of thermal batteries. Reserved thermal batteries with large capacity, high power, high thermal stability, long shelf lives, and fast activation are an attractive high-temperature battery system, which can be used as an effective power source for the actuator of guided weapons and the propulsion device of underwater and space vehicles (Cho et al., 2020).

From the development history, thermal battery can be divided into three stages as shown in **Figure 1**. The first-generation calcium/chromate thermal battery had a low energy density, complex reaction mechanism, dendrite formation, and unpredictable performance, which is replaced by the second-generation lithium/sulfides batteries. Currently, the Li/FeS_2 thermal battery with better power and discharging time compared with calcium/chromate counterpart, is widely used in various military weapons and environment. However, with the evolution of military action into an intelligence era and the thriving of space exploration, there are new challenges faced by batteries: energy/power density, discharging time, and activation time. Thus, the Li/FeS_2 battery cannot meet the requirement and new battery technologies are essential to fulfill these needs. In terms of anodes, Ca, Mg, and Li or corresponding alloys all have been used as anode materials

Edited by:
Yu Ding,
University of Maryland, United States

Reviewed by:
Xiao-Dong Zhu,
Qingdao University of Science and Technology, China

***Correspondence:**
Wei Guo
weiguo7@bit.edu.cn
Yumin Qian
yuminqian@bit.edu.cn

Specialty section:
This article was submitted to Electrochemistry, a section of the journal Frontiers in Chemistry

Received: 10 December 2021
Accepted: 10 January 2022
Published: 14 February 2022

Citation:
Li R, Guo W and Qian Y (2022) Recent Developments of Cathode Materials for Thermal Batteries. Front. Chem. 10:832972. doi: 10.3389/fchem.2022.832972

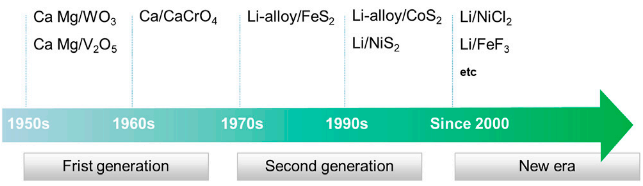

FIGURE 1 | Historic development of thermal battery.

(Guidotti and Masset, 2008). However, only Li or Li-alloy is used at present, so this review only focuses on cathode materials related to Li chemistry. Higher voltage is more practical for a battery with a high-power output. Furthermore, obtaining the same voltage requires fewer single cells with high-voltage, which is beneficial to improve the overall energy density of the battery. Due to the stronger electronegativity of halide elements, halide compounds usually show higher voltages. Thus, metal halide materials are ideal replacement of metal sulfides as cathode materials for thermal batteries. This review highlights the reported metal sulfides and halides, and finally gives a generalization for the future research direction for cathode of thermal batteries.

TRANSITION METAL SULFIDES

FeS_2

Pyrite is a relatively abundant and cheap natural mineral used as cathode material for thermal batteries (Guidotti et al., 2002). FeS_2 has a capacity of 893 mAh/g with an open circuit voltage (OCV) of 2.0 V (Ko et al., 2019). It is a typical semiconductor with a bandgap of 0.95 eV (Ennaoui et al., 1993) and begins to decompose at 550°C. The synthesis of high-purity pyrite powder from natural mineral for thermal battery requires a complex ground, sizing, and purification process with high cost. The detailed preparation, characterization, and performance tests of FeS_2 cathode are shown in **Supplementary Figures S1–S5**.

Guidotti used the plasma spraying (PS) method (Guidotti et al., 2006) to synthesize FeS_2 with LiCl-KCl eutectic electrolyte to make the composite cathode, which showed low impedance and was almost 3.5 times (Guidotti et al., 2006) that of the discrete pressed-powder. The performance of batteries with PS cathode had a linear relationship with the number of cells, and the reduced battery components facilitate the battery design by reduced chance of assembly errors. Wang et al. synthesized pyrite films to solve mechanical integrity issues of thin pellets, and the prepared pyrite thin films with several superior physical properties than that of micron pyrite pellets (Au, 2003; Wang et al., 2013). Ko prepared thin-film cathodes with good homogeneity and a reproducible thickness *via* a tape-casting process (Ko et al., 2017), which can produce a thin sheet with a thickness of 0.01 to 1.2 mm, as well as the possibility of controlling density, surface condition, and the flexibility of synthesis sheets (Park et al., 2016). Such method can be easily scaled up, but increases the internal resistance of the battery due to the presence of different polymer binders (Masset et al., 2005; Cha et al., 2018). Various studies shows the phase transformations of FeS_2 discharging process as follows (Tomczuk et al., 1982; Choi et al., 2014; Chen et al., 2017; Cha et al., 2018; Zhang and Tran, 2018; Kim et al., 2020; Zou et al., 2020; Thu et al., 2021): $FeS_2 \rightarrow Li_3Fe_2S_4 \rightarrow Li_{2+x}Fe_{1-x}S_2 \rightarrow Fe$.

CoS_2

In special high-power and long discharging time applications, FeS_2 is replaced by CoS_2 due to its excellent thermal stability (650°C), metal-like electrical conductivity, and discharge performance (Preto et al., 1983; Guidotti et al., 2002; Guidotti and Masset, 2006). The capacity of CoS_2 is 871 mAh/g, and OCV is 1.99 V[23]. The detailed preparation, characterization, and performance tests of CoS_2 cathode are shown in **Supplementary Figures S6–S8**.

Guidotti prepared CoS_2 cathode *via* an aqueous process (Guidotti et al., 2002) with improved thermal stability after heat treatment at 550°C. The performance can be enhanced by increasing the CoS_2 particle size. Guidotti also showed that thermal spraying catholyte mixtures have distinct advantages for fabrication of thin electrodes for short-life thermal batteries (Guidotti et al., 2006). Xie prepared CoS_2 and carbon nanotubes (CNTs) composite cathode using hydrothermal growth method (Xie et al., 2016). The pulse discharge performance of the CoS_2/CNTs cathode was superior to that of conventional CoS_2 due to the enhanced conductivity. Hu used the screening-printing method to prepare a film cathode (Hu et al., 2018) with a thickness of 50 μm that showed twice the capacity and active material utilization ratio. Xie prepared a novel carbon-coated CoS_2 (C@CoS_2) cathode material *via* a facile one-pot hydrothermal method (Xie et al., 2017) to prevent the CoS_2 oxidation when exposing to air (Masset and Guidotti, 2008a; Masset and Guidotti, 2008b). The decomposition temperature of C@CoS_2 was 610°C, which was 200°C higher than that of CoS_2 nanocrystal (Masset and Guidotti, 2008a). Xie used carbon-coated CoS_2 as the cathode to inhibit the higher self-discharge rate in the Li-B/CoS_2 system (Xie et al., 2018).

There are many phases in the Co-S phase diagram, such as CoS_2 (space group *Pa*-3), Co_3S_4 (space group *Fd*-3m), Co_9S_8 (*Fm-3m*), and CoS (*P6₃/mmc*) (Masset and Guidotti, 2008b). Although the electrochemical performances of CoS_2-based thermal batteries have been studied for many years, little is known about the phase evolution of CoS_2 in the discharge process of thermal batteries. Previous studies showed that the phase transformation during the discharge process of CoS_2 followed the $CoS_2 \rightarrow Co_3S_4 \rightarrow Co_9S_8 \rightarrow Co$ pathway (Masset, 2008). Payne's powder neutron diffraction study showed that the phase transformations of the CoS_2 discharging process followed the CoS_2-CoS-Co_9S_8-Co pathway (Payne et al., 2019).

NiS_2

The low-cost NiS_2 was regarded as one of the promising cathode material candidates because the thermal stability and discharge performance of NiS_2 were between FeS_2 and CoS_2[27]. However, NiS_2 cathode cannot fully react at high current density, which becomes a key problem for thermal batteries (Jin et al., 2018).

Nanocrystallization is an effective method to improve the specific capacity of cathode (Xu et al., 2014; Yu et al., 2016; Liu et al., 2017a; Yu et al., 2017). Moreover, the intermediate phase evolution and reaction speed could benefit from the merit of nanostructured cathode materials (Sen and Mitra, 2013). The more discharge steps appeared in the discharge curve, the more complete the NiS_2 cathode reaction. Jin prepared nanostructured NiS_2 using nickel carbonyl and sulfur powder as precursors by ball milling, which resulted in a double increase in specific capacity (Jin et al., 2017a).

Although nanocrystallizaiton can be used to improve the intermediate reaction rate and utilization rate of NiS_2, it decreases the decomposition temperature (Ji et al., 2014; Yang et al., 2014; Xie et al., 2016), which makes it suitable only for thermal batteries with short life time (discharge temperature ≤500°C). Jin employed hierarchical carbon modification to enhance the thermal stability and conductivity of nanostructured NiS_2 with significantly higher discharge performance than the pristine NiS_2 with much higher resistance (Jin et al., 2018). Hierarchical carbon modification not only increased the initial decomposition temperature but also prevented the further decomposition of residual NiS_2. The characterization and performance tests of the nanostructured NiS_2 powder are shown in detail in **Supplementary Figure S9**.

The Ni-S phase diagram exhibits various Ni_XS_Y ($X \le 7$, $Y \le 6$) polymorphism structures (Payne et al., 2017). However, despite years of studies, little is known about how the crystalline phases in batteries evolve at high temperatures (Payne et al., 2017).

The HRTEM measurement confirms that the phase transformations of the NiS_2 discharging process followed the $NiS_2 \rightarrow NiS \rightarrow Ni_7S_6 \rightarrow Ni_3S_2 \rightarrow Ni$ pathway (Jin et al., 2017a). Payne's *in situ* powder neutron diffraction study (Payne et al., 2017) showed that the phase transformations of NiS_2 the discharging process followed the $NiS_2 \rightarrow NiS \rightarrow Ni_2S_3 \rightarrow Ni$ pathway.

In recent years, transition metal dichalcogenides (TMDs) have received considerable attention due to their novel layer structure (Zhang et al., 2018) with unique properties, which endow great potential in catalysis (Liang et al., 2020; Sarma et al., 2020; Xu et al., 2020; Zeng et al., 2020; Wang et al., 2021), energy storage, and conversion (Gao et al., 2016; Li et al., 2019). Various TMDs have been reported as thermal battery cathode material with high decomposition temperature and capacity, such as MoS_2 (Zheng et al., 2018), WS_2 (Guo et al., 2019a), NiMoSs (Yusong Choi, 2019), and ZrS_3 (Giagloglou et al., 2016). These materials show various advantage over traditional FeS_2, which deserve detailed study in the future.

TRANSITION METAL CHLORIDE

It is urgent to develop new cathode materials for thermal batteries with high power and energy output capability, miniaturization, and micromation to adapt to the rapid development of weapon and space exploration system (Tian et al., 2021), which is difficult for these traditional cathode materials (Liu et al., 2017b). The detailed synthesis, characterization, and performance tests of $NiCl_2$ are exhibited in **Supplementary Figures S10–S12**.

$NiCl_2$ is considered an ideal substitute cathode material for FeS_2 and matches the excellent performance of Li alloy anode due to its relative high potential (2.5–3 V vs Li), high discharge current, high specific energy, and low cost (Guidotti et al., 2006; Ying et al., 2016; Liu et al., 2017b). However, the high solubility of $NiCl_2$ in molten salt electrolyte can cause short circuit. Due to the low conductivity and poor electrochemical activity of $NiCl_2$, the activation time is longer, so a certain amount of conductive additives must be added to improve its conductivity (Jai Prakash, 2000; Jin et al., 2017b; Gui et al., 2020; Tian et al., 2021).

The thermal stability of $NiCl_2$ was primarily affected by the crystal water and oxide impurities during low-temperature pre-dehydration. Thus, surface and sublimation treatment of hydrate $NiCl_2$ are necessary to modify the microstructure and make large specific surface area to boost the electrochemical performance. Jin prepared pure $NiCl_2$ by vacuum sintering after sublimation and synthesized the carbon-coated $NiCl_2$ *via* a simple solid-state reaction (Jin et al., 2017b). The carbon-coated $NiCl_2$ cathode showed drastic improvement in capacity, specific energy, and discharging time. The electrochemical mechanism was shown as follows:

$$\mathbf{2Li + NiCl_2 \rightarrow 2LiCl + Li}$$

The carbon coating enhanced the electronic conductivity and led to the reduced activation time. At the same time, the carbon coating increased the structure stability and reduced the solubility of $NiCl_2$ by protecting the $NiCl_2$ from directly contacting the electrolyte. However, it also resulted in a greater voltage delay during the initial discharge process. Hu filled sublimated $NiCl_2$ into Ni foam instead of compact stainless steel screen printing (Hu et al., 2017). The discharge voltage of the $NiCl_2$-based single cell with Ni foam substrate was 2.55 V. Compared with $NiCl_2$ cathode with stainless steel substrate, the electrochemical test showed that the $NiCl_2$/Ni foam cathode had more than twice the capacity, had almost one-third of the internal resistance, and had a power density of 10.866 kW/kg, which outweighed the sulfide batteries. Ni foam substrate can enhance the electronic conductivity, causing the fast electron transfer and reaction (Xie et al., 2017). Liu proposed a novel two-step variable temperature solid-state method to remove the crystal water from $NiCl_2$ hexahydrate (Liu et al., 2017b). The study showed that the sintering temperatures influenced the morphology of materials, which induced the reduction in discharging time and specific capacity. The two-step variable-temperature preparation method was an effective method to enhance the thermal stability of $NiCl_2$ cathode materials. The 600°C-treated cathode exhibited better specific capacities of 210.42 and 242.84 mAh/g at 0.5 and 2.0 A. Giagloglou prepared $NiCl_2$ by solid-state reaction in sealed evacuated quartz tubes, which showed enhanced performance (Giagloglou et al., 2018) and whose specific capacity was achieved at 360 mAh/g under 500°C. By using a simple hydrogen etching technique, Gui successfully modified the Ni content and surface roughness (Gui et al., 2020). At different etching conditions, the

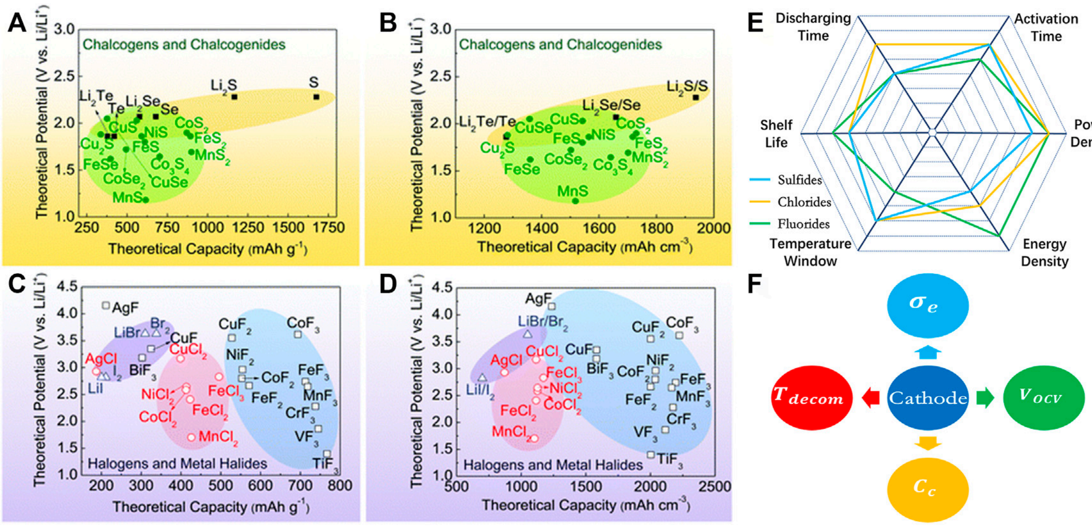

FIGURE 2 | Theoretical gravimetric and volumetric capacities and theoretical potential of selected conversion cathode materials: **(A,B)** chalcogens and chalcogenides; **(C,D)** halogens and metal halides (reproduced from Wu and Yushin, 2017, Copyright 2017 Royal Society of Chemistry). **(E)** Comparison for the various properties of thermal batteries using sulfides, chlorides, and fluorides as the cathode material. **(F)** The future development directions for the high-performance cathode material of thermal battery.

prepared $NiCl_2$ showed higher discharge voltage and significantly shorter activation time than those of the pure $NiCl_2$ cathode. The discharge voltage and specific power of the prepared $NiCl_2$ *via* hydrogen etching technique were 2.43 V and 7.59 kW/kg. The fabricated the Ni-$NiCl_2$ composite cathode material *via* hydrogen reduction by Tian et al. (2021) showed higher voltage and much shorter activation time, and half of the internal resistance and the power density was up to 11.4 kW/kg.

Additionally, $PbCl_2$ was reported as cathode material (Chen et al., 2021). Although $PbCl_2$ had a relatively low theoretical specific capacity (193 mAh/g), due to the high utilization rate, it still may increase the energy density of the battery. Giagloglou synthesized $KNiCl_3$, Li_2MnCl_4, and Li_6VCl_8 *via* solid-state reaction and used them in the thermal battery (Giagloglou et al., 2018). Compared with well-known metal disulfide, these transition metal chlorides provided greater specific power and exhibited higher voltage, which can be considered as promising alternative materials for Li thermal battery applications.

TRANSITION METAL FLUORIDES

Transition metal fluorides (TMFs) have attracted much attention because of their high voltage, specific energy, and excellent thermal stability (Yamakawa et al., 2009; Kim et al., 2010; Chun et al., 2016; Sheng Nan Guo and Wang, 2019; Chang et al., 2020). The ionic bond property of TMFs results in a high working potential (Li et al., 2012). The theoretical potential of the most attractive cathode material, CuF_2, is up to 3.55 V with a specific capacity as high as 528 mAh/g and a specific energy of 1.87 kW h/kg (Yamakawa et al., 2009). The theoretical potential of NiF_2 is 2.96 V, and the specific capacity is 554 mAh/g. Chang prepared pure NiF_2 *via* a direct and simple two-step dehydration method from commercial $NiF_2.4H_2O$ (Chang et al., 2020). The discharge mechanism was as follows:

$$\mathbf{NiF_2 + 2Li \rightarrow 2LiF + Ni}$$

Their electrochemical tests of NiF_2 cathode showed that there was a voltage platform approximately 2.4 V at 0.1 A/cm^2 under 520°C. The maximum voltage plateau can reach 2.5 V when the temperature is raised up to 580°C, and the corresponding specific power was 3.7 kW/kg, making it possible to apply in high specific power thermal batteries. The voltage plateaus dropped in succession when the current density is increased due to the enhanced concentration polarization. The discharge time decreased from 295 to 88 s when the current density is increased from 0.1 A/cm^2 to 0.5 A/cm^2, which induced a lower specific capacity. The specific power reached up to 16.2 kW/kg at a high current density of 0.5 A/cm^2, which proved that NiF_2 can be used as the cathode material with high specific power and energy. Compared to the cathode material $NiCl_2$ with long activation time and severe infiltration, the NiF_2 exhibited better electrochemical performance. The average resistance was 0.56 Ω, which was equivalent to the total polarization. Carbon coating was an effective means to further improve the thermal stability and electrochemical performance of NiF_2. The detailed synthesis, characterization, and performance tests of NiF_2 are shown in **Supplementary Figures S13, S14**.

FeF_3 is another investigated cathode material (Hua et al., 2021). During the lithiation process, two characteristic discharge voltages of FeF_3 were exhibited at about 3 V and below 2 V, and the corresponding capacities were 237 and 175 mAh/g, respectively. The electrochemical mechanism of FeF_3 follows a three-electron-transfer reaction (Badway et al., 2003):

$$\mathbf{FeF_3 + Li + e^- \rightarrow LiFeF_3}$$

$$\mathbf{LiFeF_3 + 2Li + 2e^- \rightarrow Fe^0 + 3LiF}$$

Guo synthesized the anhydrous FeF_3 by a liquid-phase method combined with a thermal treatment process of the $FeF_3.3H_2O$/MWCNTs composite (Guo et al., 2019b). During heat treatment, the $FeF_3.3H_2O$ crystal smooth surface became rough due to the release of crystal water and phase transformation, and more particles were broken into small nanoparticles. However, MWCNT fibers can still be evenly distributed among FeF_3 particles by this simple and convenient method. The large bandgap of pristine FeF_3 can hinder the transfer electrons, inducing more self-discharge reaction than electrode reaction. The electrochemical test showed that conductive MWCNTs can facilitate electron transfer, and the electrode reaction prioritized the self-discharge reaction. The additive MWCNTs led to a decrease of the total polarization of FeF_3 from 45 to 10 mΩ, proving that the MWCNTs can form a conductive network among FeF_3 particles and greatly improve the conductivity. Wang used a scalable and low-cost strategy to prepare a CoF_2/CNTs cathode nanocomposite, and the capacity was achieved at 550 mAh/g with excellent mechanical properties (Wang et al., 2015). Other TMFs, such as FeF_2 (Wang et al., 2011), TiF_3 (Kitajou et al., 2017; Kitajou et al., 2019), and MnF_3 (Read, 2012), have been successfully synthesized and exhibited excellent performance. The summary of the cathode type, size/thickness, phase, and performance of cathode materials in recent studies is shown in **Supplementary Table S1**.

SUMMARY AND OUTLOOK

Theoretic calculation is another tool for the design of high-performance cathode materials as shown in **Figures 2A–D**; many new materials have been designed to be potential candidates (Wu and Yushin, 2017). The strength and weakness of metal sulfides, chlorides, and fluorides are summarized and compared as shown in **Figure 2E**. Currently, sulfides are most studied and widely used as cathode materials for thermal batteries, but they do not meet the new challenge with the development of military weapons and space exploration in the future. Chlorides and fluorides have relatively high voltage and decomposition temperature, which make them suitable for the high-energy-density and long-discharging-time battery. However, they are still at the infancy stage; more detailed studies need to be carried out for the real application.

For the future development of cathode materials for thermal batteries, they can be improved mainly from the following four aspects, as shown in **Figure 2F**:

1) High voltage V_{ocv}: this is the most important factor that influences the power and energy density of the thermal battery. More importantly, a higher-voltage cell will use fewer series cells to achieve the demanding output voltage and a simpler battery management system. Thus, the higher effective mass ratio of active material is also helpful for further enhancement of energy density. In this respect, the metal fluoride has overall advantage over chloride, sulfide, or oxides, because of the higher electronegativity difference between fluorine and alkali metal.
2) High capacity C_c: transition metal compound with multiple valency metal and nonmetal element will have multiple electron transfer reaction with a relative higher n/M ratio, which leads to a higher capacity. Transition metals with high valency state compounds are potential materials
3) High decomposition temperature T_{decom}: thermal battery discharging time depends on the lower and upper temperature limit of the working temperature window, T_{dw} and T_{up}, which are usually determined by the melting point of electrolyte and the decomposition temperature of cathode, respectively. Usually, electrolyte is a mixture of halide salts with very high boiling temperature and decomposition temperature. So, the cathode decomposition temperature is usually T_{up}. The larger the $T_{up} - T_{dw}$ difference, the longer the discharging time. Nanostructure materials often show lower T_{decom}, but surface modification has shown increased T_{decom}.
4) High electron conductivity σ_e: the cathode that has higher electron conductivity will facilitate the ion/electron transfer and thus has low internal resistance and higher output voltage. More importantly, it can yield larger current and thus has a large output power. However, almost all these metal compounds are insulators; thus, proper surface or doping engineering is necessary to improve the conductivity.

Coating, doping, and tailoring the microstructure are effective methods to improve the discharge performance of cathode (Tan et al., 2016). Carbon modification is an effective method to improve the stability and conductivity of electrode materials (Oh et al., 2010; Chinnappan et al., 2016; Jiang et al., 2016; Li et al., 2016; Shan et al., 2016; Zhang et al., 2016; Liu et al., 2017c; Li et al., 2017). In real application, simultaneously improving these factors without hindering other factors is impossible. Optimizing the cell design or electrode designs, such as tape-casting and screening-printing, to increase the mass ratio of active material is another useful way to upgrade the energy density of batteries (Ko et al., 2017).

AUTHOR CONTRIBUTIONS

RL wrote the manuscript. YQ and WG were supervisors and proposed modifications to this work.

FUNDING

This work was supported by the National Natural Science Foundation of China (NSFC, Grant No. 51971037) and Open Research Fund of CNMGE Platform & NSCC-TJ.

SUPPLEMENTARY MATERIAL

The Supplementary Material for this article can be found online at: https://www.frontiersin.org/articles/10.3389/fchem.2022.832972/full#supplementary-material

REFERENCES

Au, M. (2003). Nanostructured thermal Batteries with High Power Density. *J. Power Sourc.* 115 (2), 360–366. doi:10.1016/S0378-7753(02)00627-4

Badway, F., Pereira, N., Cosandey, F., and Amatucci, G. G. (2003). Carbon-Metal Fluoride Nanocomposites: Structure and Electrochemistry of FeF_3:C. *J. Electrochem. Soc.* 150 (9), 1209–1218. doi:10.1149/1.1596162

Cha, Y. L., Park, I. H., Moon, K. H., Kim, D. H., Jung, S. I., and Yoon, Y. S. (2018). Simultaneous Control of Phase Transformation and Crystal of Amorphous TiO_2 Coating on MWCNT Surface. *J. Korean Ceram. Soc.* 55 (6), 618–624. doi:10.4191/kcers.2018.55.6.09

Chang, Q., Luo, Z., Fu, L., Zhu, J., Yang, W., Li, D., et al. (2020). A New Cathode Material of NiF_2 for thermal Batteries with High Specific Power. *Electrochim. Acta* 361, 137051. doi:10.1016/j.electacta.2020.137051

Chen, F., Jiang, C., Xu, L., Li, X., and Shen, Q. (2021). High Utilization Rate thermal Batteries Using $PbCl_2$ as a Cathode Material. *Mater. Lett.* 299, 130018. doi:10.1016/j.matlet.2021.130018

Chen, Y., Xu, S., Li, Y., Jacob, R. J., Kuang, Y., Liu, B., et al. (2017). FeS_2 Nanoparticles Embedded in Reduced Graphene Oxide toward Robust, High-Performance Electrocatalysts. *Adv. Energ. Mater.* 7 (19), 1700482. doi:10.1002/aenm.201700482

Chinnappan, A., Baskar, C., Kim, H., and Ramakrishna, S. (2016). Carbon Nanotube Hybrid Nanostructures: Future Generation Conducting Materials. *J. Mater. Chem. A, Mater. Energ. sustainability* 4 (24), 9347–9361. doi:10.1039/c6ta01717g

Cho, J.-H., Im, C. N., Choi, C. H., Ha, S.-h., Yoon, H.-K., Choi, Y., et al. (2020). Thermal Stability Characteristics of High-Power, Large-Capacity, reserve thermal Batteries with Pure Li and Li(Si) Anodes. *Electrochimica Acta* 353, 136612. doi:10.1016/j.electacta.2020.136612

Choi, Y.-S., Yu, H.-R., and Cheong, H.-W. (2015). Electrochemical Properties of a Lithium-Impregnated Metal Foam Anode for thermal Batteries. *J. Power Sourc.* 276, 102–104. doi:10.1016/j.jpowsour.2014.11.103

Choi, Y., Cho, S., and Lee, Y. (2014). Effect of the Addition of Carbon Black and Carbon Nanotube to FeS_2 Cathode on the Electrochemical Performance of thermal Battery. *J. Ind. Eng. Chem.* 20 (5), 3584–3589. doi:10.1016/j.jiec.2013.12.052

Chun, J., Jo, C., Sahgong, S., Kim, M. G., Lim, E., Kim, D. H., et al. (2016). Ammonium Fluoride Mediated Synthesis of Anhydrous Metal Fluoride-Mesoporous Carbon Nanocomposites for High-Performance Lithium Ion Battery Cathodes. *ACS Appl. Mater. Inter.* 8 (51), 35180–35190. doi:10.1021/acsami.6b10641

Ennaoui, A., Flechter, S., Smestad, G., and Tributsch, H. (1993). Iron Disulfide for Solar Energy Conversion. *Sol. Energ. Mat. Sol. C.* 29, 289–370. doi:10.1016/0927-0248(93)90095-K

Gao, J., Li, L., Tan, J., Sun, H., Li, B., Idrobo, J. C., et al. (2016). Vertically Oriented Arrays of ReS_2 Nanosheets for Electrochemical Energy Storage and Electrocatalysis. *Nano Lett.* 16 (6), 3780–3787. doi:10.1021/acs.nanolett.6b01180

Giagloglou, K., Payne, J. L., Crouch, C., Gover, R. K. B., Connor, P., and Irvine, J. T. S. (2018). Transition Metal Chlorides $NiCl_2$, $KNiCl_3$, Li_6VCl_8 and Li_2MnCl_4 as Alternative Cathode Materials in Primary Li Thermal Batteries. *J. Electrochem. Soc.* 165 (14), 3510–3516. doi:10.1149/2.1231814jes

Giagloglou, K., Payne, J. L., Crouch, C., Gover, R. K. B., Connor, P. A., and Irvine, J. T. S. (2016). Zirconium Trisulfide as a Promising Cathode Material for Li Primary Thermal Batteries. *J. Electrochem. Soc.* 163 (14), A3126–A3130. doi:10.1149/2.1351614jes

Gui, Y., Lin, X., Fu, L., Zhu, J., Yang, W., Li, D., et al. (2020). Shortening Activation Time of thermal Battery by Hydrogen Etching of $NiCl_2$ Cathode. *Mater. Lett.* 275, 128136. doi:10.1016/j.matlet.2020.128136

Guidotti, R. A., and Masset, P. J. (2008). Thermally Activated ("thermal") Battery Technology. *J. Power Sourc.* 183, 388–398. doi:10.1016/j.jpowsour.2008.04.090

Guidotti, R. A., and Masset, P. (2006). Thermally Activated ("thermal") Battery Technology. *J. Power Sourc.* 161 (2), 1443–1449. doi:10.1016/j.jpowsour.2006.06.013

Guidotti, R. A., Reinhardt, F. W., Dai, J., and Reisner, D. E. (2006). Performance of thermal Cells and Batteries Made with Plasma-Sprayed Cathodes and Anodes. *J. Power Sourc.* 160 (2), 1456–1464. doi:10.1016/j.jpowsour.2006.02.025

Guidotti, R. A., Reinhardt, F. W., Dai, J., Reisner, D. E., and Schwarz, R. (2002). Preparation and Characterization of Nanostructured FeS2 and CoS2 for High-Temperature Batteries. *MRS Proc.* 730. doi:10.1557/PROC-730-V7.3

Guo, S., Guo, H., Wang, X., Zhu, Y., Yang, M., Zhang, Q., et al. (2019). Synthesis and Electrochemical Performance of WS_2 Nanosheet for thermal Batteries. *Mater. Lett.* 249, 81–83. doi:10.1016/j.matlet.2019.04.030

Guo, S. N., Guo, H., Wang, X., Zhu, Y., Hu, J., Yang, M., et al. (2019). Iron Trifluoride as a High Voltage Cathode Material for Thermal Batteries. *J. Electrochem. Soc.* 166 (15), A3599–A3605. doi:10.1149/2.0371915jes

Hu, J., Chu, Y., Tian, Q., Guo, S., Yang, M., Wang, X., et al. (2017). Electrochemical Properties of the $NiCl_2$ Cathode with Nickel Foam Substrate for thermal Batteries. *Mater. Lett.* 207, 198–201. doi:10.1016/j.matlet.2017.07.082

Hu, J., Chu, Y., Tian, Q., Wang, J., Li, Y., Wu, Q., et al. (2018). Film Cathode for thermal Batteries Using a Screen-Printing Process. *Mater. Lett.* 215, 296–299. doi:10.1016/j.matlet.2017.12.114

Hua, X., Eggeman, A. S., Castillo-Martínez, E., Robert, R., Geddes, H. S., Lu, Z., et al. (2021). Revisiting Metal Fluorides as Lithium-Ion Battery Cathodes. *Nat. Mater.* 20 (6), 841–850. doi:10.1038/s41563-020-00893-1

Jai Prakash, L. R. D. R. (2000). Effect of Sodium Iodide Additive on the Electrochemical Performance of Sodium/nickel Chloride Cells. *J. Appl. Electrochemistry* 30, 1229–1233. doi:10.1023/A:1026539607417

Ji, Y., Liu, X., Liu, W., Wang, Y., Zhang, H., Yang, M., et al. (2014). A Facile Template-free Approach for the Solid-phase Synthesis of CoS_2 Nanocrystals and Their Enhanced Storage Energy in Supercapacitors. *RSC Adv.* 4 (91), 50220–50225. doi:10.1039/C4RA08614G

Jiang, B., Han, C., Li, B., He, Y., and Lin, Z. (2016). *In-Situ* Crafting of $ZnFe_2O_4$ Nanoparticles Impregnated within Continuous Carbon Network as Advanced Anode Materials. *ACS Nano* 10 (2), 2728–2735. doi:10.1021/acsnano.5b07806

Jin, C., Fu, L., Zhu, J., Yang, W., Li, D., and Zhou, L. (2018). A Hierarchical Carbon Modified Nano-NiS_2 Cathode with High thermal Stability for a High Energy thermal Battery. *J. Mater. Chem. A.* 6 (16), 7123–7132. doi:10.1039/C8TA00346G

Jin, C., Zhou, L., Fu, L., Zhu, J., and Li, D. (2017). Synthesis and Discharge Performances of $NiCl_2$ by Surface Modification of Carbon Coating as Cathode Material of thermal Battery. *Appl. Surf. Sci.* 402, 308–313. doi:10.1016/j.apsusc.2017.01.034

Jin, C., Zhou, L., Fu, L., Zhu, J., Li, D., and Yang, W. (2017). The Acceleration Intermediate Phase (NiS and Ni_3S_2) Evolution by Nanocrystallization in Li/NiS_2 thermal Batteries with High Specific Capacity. *J. Power Sourc.* 352, 83–89. doi:10.1016/j.jpowsour.2017.03.119

Kim, I. Y., Woo, S. P., Ko, J., Kang, S., Yoon, Y. S., Cheong, H., et al. (2020). Binder-Free Cathode for Thermal Batteries Fabricated Using FeS_2 Treated Metal Foam. *Front. Chem.* 7. doi:10.3389/fchem.2019.00904

Kim, S., Seo, D., Gwon, H., Kim, J., and Kang, K. (2010). Fabrication of FeF_3 Nanoflowers on CNT Branches and Their Application to High Power Lithium Rechargeable Batteries. *Adv. Mater.* 22 (46), 5260–5264. doi:10.1002/adma.201002879

Kitajou, A., Eguchi, K., Ishado, Y., Setoyama, H., Okajima, T., and Okada, S. (2019). Electrochemical Properties of Titanium Fluoride with High Rate Capability for Lithium-Ion Batteries. *J. Power Sourc.* 419, 1–5. doi:10.1016/j.jpowsour.2019.02.056

Kitajou, A., Tanaka, I., Tanaka, Y., Kobayashi, E., Setoyama, H., Okajima, T., et al. (2017). Discharge and Charge Reaction of Perovskite-type MF_3 (M = Fe and Ti) Cathodes for Lithium-Ion Batteries. *Electrochemistry* 85 (8), 472–477. doi:10.5796/electrochemistry.85.472

Ko, J., Kang, S. H., Cheong, H.-W., and Yoon, Y. S. (2019). Recent Progress in Cathode Materials for Thermal Batteries. *J. Korean Ceram. Soc.* 56 (3), 233–255. doi:10.4191/kcers.2019.56.3.05

Ko, J., Kim, I. Y., Jung, H. M., Cheong, H., and Yoon, Y. S. (2017). Thin Cathode for thermal Batteries Using a Tape-Casting Process. *Ceram. Int.* 43 (7), 5789–5793. doi:10.1016/j.ceramint.2017.01.126

Li, L., Meng, F., and Jin, S. (2012). High-capacity Lithium-Ion Battery Conversion Cathodes Based on Iron Fluoride Nanowires and Insights into the Conversion Mechanism. *Nano Lett.* 12 (11), 6030–6037. doi:10.1021/nl303630p

Li, X., Qian, K., He, Y., Liu, C., An, D., Li, Y., et al. (2017). A Dual-Functional Gel-Polymer Electrolyte for Lithium Ion Batteries with superior Rate and Safety Performances. *J. Mater. Chem. A, Mater. Energ. sustainability* 5 (35), 18888–18895. doi:10.1039/C7TA04415A

Li, X., Sun, Y., Xu, X., Wang, Y., Chou, S., Cao, A., et al. (2019). Lotus Rhizome-like S/N–C with Embedded WS_2 for superior Sodium Storage. *J. Mater. Chem. A.* 7 (45), 25932–25943. doi:10.1039/C9TA09373G

Li, Y., Hu, Y., Titirici, M., Chen, L., and Huang, X. (2016). Hard Carbon Microtubes Made from Renewable Cotton as High-Performance Anode Material for Sodium-Ion Batteries. *Adv. Energ. Mater.* 6 (18), 1600659. doi:10.1002/aenm.201600659

Liang, J., Ma, S., Li, J., Wang, Y., Wu, J., Zhang, Q., et al. (2020). Boosting the Acidic Electrocatalytic Nitrogen Reduction Performance of MoS_2 by Strain Engineering. *J. Mater. Chem. A.* 8 (20), 10426–10432. doi:10.1039/D0TA03622F

Liu, W., Liu, H., Bi, S., Cao, L., and Sun, Y. (2017). Variable-temperature Preparation and Performance of $NiCl_2$ as a Cathode Material for thermal Batteries. *Sci. China Mater.* 60 (3), 251–257. doi:10.1007/s40843-016-9003-x

Liu, X., Huang, J. Q., Zhang, Q., and Mai, L. (2017). Nanostructured Metal Oxides and Sulfides for Lithium-Sulfur Batteries. *Adv. Mater.* 29 (20). doi:10.1002/adma.201601759

Liu, Z., Lu, T., Song, T., Yu, X., Lou, X. W. D., and Paik, U. (2017). Structure-designed Synthesis of FeS_2@C Yolk–Shell Nanoboxes as a High-Performance Anode for Sodium-Ion Batteries. *Energ. Environ. Sci.* 10 (7), 1576–1580. doi:10.1039/C7EE01100H

Masset, P. J., and Guidotti, R. A. (2008). Thermal Activated ("thermal") Battery Technology. *J. Power Sourc.* 177 (2), 595–609. doi:10.1016/j.jpowsour.2007.11.017

Masset, P. J., and Guidotti, R. A. (2008). Thermal Activated ("thermal") Battery Technology. *J. Power Sourc.* 178 (1), 456–466. doi:10.1016/j.jpowsour.2007.11.073

Masset, P., Schoeffert, S., Poinso, J., and Poignet, J. (2005). LiF-LiCl-LiI vs. LiF-LiBr-KBr as Molten Salt Electrolyte in Thermal Batteries. *J. Electrochem. Soc.* 152 (2), A405. doi:10.1149/1.1850861

Oh, S. W., Myung, S., Oh, S., Oh, K. H., Amine, K., Scrosati, B., et al. (2010). Double Carbon Coating of $LiFePO_4$ as High Rate Electrode for Rechargeable Lithium Batteries. *Adv. Mater.* 22 (43), 4842–4845. doi:10.1002/adma.200904027

Park, J., Lee, S., Han, Y., Hwang, H., and Ryu, S. (2016). Effects of Debinding Atmosphere on Properties of Sintered Reaction-Bonded Si_3N_4 Prepared by Tape Casting Method. *J. Korean Ceram. Soc.* 53 (6), 622–627. doi:10.4191/kcers.2016.53.6.622

Payne, J. L., Percival, J. D., Giagloglou, K., Crouch, C. J., Carins, G. M., Smith, R. I., et al. (2017). In-Situ Thermal Battery Discharge Using NiS_2 as a Cathode Material. *ChemElectroChem* 4 (8), 1916–1923. doi:10.1002/celc.201700095

Payne, J. L., Percival, J. D., Giagloglou, K., Crouch, C. J., Carins, G. M., Smith, R. I., et al. (2019). *In Situ* Thermal Battery Discharge Using CoS_2 as a Cathode Material. *J. Electrochem. Soc.* 166 (12), A2660–A2664. doi:10.1149/2.1431912jes

Preto, S. K., Tomczuk, Z., Von Winbush, S., and Roche, M. F. (1983). Reactions of FeS_2, CoS_2, and NiS_2 Electrodes in Molten LiCl-KCl Electrolytes. *J. Electrochem. Soc.* 130 (2), 264–273. doi:10.1149/1.2119692

Read, W. K. B. A. (2012). A Study of Cobalt and Manganese Fluorides as Cathode Materials for Rechargeable Lithium Cells. *Electrochem. Soc.* 41 (41), 97–106. doi:10.1149/1.4717967

Sarma, P. V., Vineesh, T. V., Kumar, R., Sreepal, V., Prasannachandran, R., Singh, A. K., et al. (2020). Nanostructured Tungsten Oxysulfide as an Efficient Electrocatalyst for Hydrogen Evolution Reaction. *ACS Catal.* 10 (12), 6753–6762. doi:10.1021/acscatal.9b04177

Sen, U. K., and Mitra, S. (2013). High-Rate and High-Energy-Density Lithium-Ion Battery Anode Containing 2D MoS_2 Nanowall and Cellulose Binder. *ACS Appl. Mater. Inter.* 5 (4), 1240–1247. doi:10.1021/am3022015

Shan, J., Liu, Y., Su, Y., Liu, P., Zhuang, X., Wu, D., et al. (2016). Graphene-directed Two-Dimensional Porous Carbon Frameworks for High-Performance Lithium–Sulfur Battery Cathodes. *J. Mater. Chem. A, Mater. Energ. sustainability* 4 (1), 314–320. doi:10.1039/C5TA08109B

Sheng Nan Guo, H. G. X. W., and Wang, L. Z. A. J. (2019). Iron Trifluoride as a High Voltage Cathode Material for Thermal Batteries. *J. Electrochem. Soc.* 166 (15), 3599–3605. doi:10.1149/2.0371915jes

Tan, R., Yang, J., Hu, J., Wang, K., Zhao, Y., and Pan, F. (2016). Core-shell Nano-FeS_2@N-Doped Graphene as an Advanced Cathode Material for Rechargeable Li-Ion Batteries. *Chem. Commun. (Camb)* 52 (5), 986–989. doi:10.1039/c5cc08002a

Thu, T. T., Thu, T. T., Manh, T. D., Tan, T., and Chang, J. (2021). An Assessment of Pyrite Thin-Film Cathode Characteristics for thermal Batteries by the Doctor Blade Coating Method. *J. Mater. Res. Tech.* 13, 1139–1149. doi:10.1016/j.jmrt.2021.05.014

Tian, Q., Wang, J., Xiang, W., Zhao, J., Guo, H., Hu, J., et al. (2021). Fabrication of the Ni-$NiCl_2$ Composite Cathode Material for Fast-Response Thermal Batteries. *Front. Chem.* 9, 679231. doi:10.3389/fchem.2021.679231

Tomczuk, Z., Tani, B., Otto, N. C., Roche, M. F., and Vissers, D. R. (1982). Phase Relationships in Positive Electrodes of High Temperature Li - Al/LiCl - KCl/FeS_2 Cells. *J. Electrochem. Soc.* 129 (5), 925–931. doi:10.1149/1.2124067

Wang, F., Robert, R., Chernova, N. A., Pereira, N., Omenya, F., Badway, F., et al. (2011). Conversion Reaction Mechanisms in Lithium Ion Batteries: Study of the Binary Metal Fluoride Electrodes. *J. Am. Chem. Soc.* 133 (46), 18828–18836. doi:10.1021/ja206268a

Wang, X., Gu, W., Lee, J. T., Nitta, N., Benson, J., Magasinski, A., et al. (2015). Carbon Nanotube-CoF_2 Multifunctional Cathode for Lithium Ion Batteries: Effect of Electrolyte on Cycle Stability. *Small* 11 (38), 5164–5173. doi:10.1002/smll.201501139

Wang, X., Li, R., Yang, H., Zheng, J., Li, Y., Zhu, P., et al. (2021). Epitaxial Growth of Atomically Thick WSe_2 Nanoribbons. *Vacuum* 189, 110254. doi:10.1016/j.vacuum.2021.110254

Wang, X., Wang, G., Chen, J., Zhu, X., Tian, J., Jiang, C., et al. (2013). Pyrite Thin Films Prepared for thermal Batteries via Sulfuring Electrodeposited Iron Sulfide Films: Structure and Physical Properties. *Mater. Lett.* 110, 144–147. doi:10.1016/j.matlet.2013.07.107

Wu, F., and Yushin, G. (2017). Conversion Cathodes for Rechargeable Lithium and Lithium-Ion Batteries. *Energ. Environ. Sci.* 10 (2), 435–459. doi:10.1039/C6EE02326F

Xie, S., Deng, Y., Mei, J., Yang, Z., Lau, W., and Liu, H. (2017). Carbon Coated CoS_2 thermal Battery Electrode Material with Enhanced Discharge Performances and Air Stability. *Electrochim. Acta* 231, 287–293. doi:10.1016/j.electacta.2017.02.068

Xie, S., Deng, Y., Mei, J., Yang, Z., Lau, W., and Liu, H. (2016). Facile Synthesis of CoS_2/CNTs Composite and its Exploitation in thermal Battery Fabrication. *Composites B: Eng.* 93, 203–209. doi:10.1016/j.compositesb.2016.03.038

Xie, Y., Liu, Z., Ning, H., Huang, H., and Chen, L. (2018). Suppressing Self-Discharge of Li–B/CoS_2 thermal Batteries by Using a Carbon-Coated CoS_2 Cathode. *RSC Adv.* 8 (13), 7173–7178. doi:10.1039/C7RA13071F

Xu, X., Liu, W., Kim, Y., and Cho, J. (2014). Nanostructured Transition Metal Sulfides for Lithium Ion Batteries: Progress and Challenges. *Nano Today* 9 (5), 604–630. doi:10.1016/j.nantod.2014.09.005

Xu, X., Tian, X., Sun, B., Liang, Z., Cui, H., Tian, J., et al. (2020). 1 T-phase Molybdenum Sulfide Nanodots Enable Efficient Electrocatalytic Nitrogen Fixation under Ambient Conditions. *Appl. Catal. B: Environ.* 272, 118984. doi:10.1016/j.apcatb.2020.118984

Yamakawa, N., Jiang, M., and Grey, C. P. (2009). Investigation of the Conversion Reaction Mechanisms for Binary Copper(II) Compounds by Solid-State NMR Spectroscopy and X-ray Diffraction. *Chem. Mater.* 21 (14), 3162–3176. doi:10.1021/cm900581b

Yang, Z., Liu, X., Feng, X., Cui, Y., and Yang, X. (2014). Hydrothermal Synthesized Micro/nano-Sized Pyrite Used as Cathode Material to Improve the Electrochemical Performance of thermal Battery. *J. Appl. Electrochem.* 44 (10), 1075–1080. doi:10.1007/s10800-014-0724-9

Ying, C., Yun-Wei, L., Qi-Bing, W., Jing, H., Qian-Qiu, T., and He-Long, H. (2016). *In-situ* Synthesis and Discharge Performance of Ni-NiCl$lt;inf$gt;2$lt;/inf$gt; Composite as Cathode Materials for Thermal Batteries. *J. Inorg. Mater.* 31 (9), 992–996. doi:10.15541/jim20160085

Yu, L., Hu, H., Wu, H. B., and Lou, X. W. (2017). Complex Hollow Nanostructures: Synthesis and Energy-Related Applications. *Adv. Mater.* 29 (15). doi:10.1002/adma.201604563

Yu, X., Yu, L., and Lou, X. W. D. (2016). Metal Sulfide Hollow Nanostructures for Electrochemical Energy Storage. *Adv. Energ. Mater.* 6 (3), 1501333. doi:10.1002/aenm.201501333

Yusong Choi, T. A. S. H. (2019). Hydrothermally Synthesized Homogeneous Ni–Mo–S Structures on Ni-Foam Cathodes for thermal Batteries. *Chem. Commun.* 55, 7300. doi:10.1039/c9cc03388b

Zeng, L., Li, X., Chen, S., Wen, J., Huang, W., and Chen, A. (2020). Unique Hollow Ni–Fe@MoS_2 Nanocubes with Boosted Electrocatalytic Activity for N_2 Reduction to NH_3. *J. Mater. Chem. A.* 8 (15), 7339–7349. doi:10.1039/C9TA13336D

Zhang, S. S., and Tran, D. T. (2018). Pyrite FeS_2 as an *In-Situ* Oxygen Remover for Rechargeable Batteries with Layered Cathode Materials. *J. Power Sourc.* 403, 167–172. doi:10.1016/j.jpowsour.2018.09.079

Zhang, X., Lai, Z., Ma, Q., and Zhang, H. (2018). Novel Structured Transition Metal Dichalcogenide Nanosheets. *Chem. Soc. Rev.* 47 (9), 331–3338. doi:10.1039/c8cs00094h

Zhang, X., Zhang, X., Wang, X., Xie, Z., and Zhou, Z. (2016). $NiFe_2O_4$–CNT Composite: an Efficient Electrocatalyst for Oxygen Evolution Reactions in Li–O_2 Batteries Guided by Computations. *J. Mater. Chem. A.* 4 (24), 9390–9393. doi:10.1039/C6TA02779B

Zheng, X., Zhu, Y., Sun, Y., and Jiao, Q. (2018). Hydrothermal Synthesis of MoS_2 with Different Morphology and its Performance in thermal Battery. *J. Power Sourc.* 395, 318–327. doi:10.1016/j.jpowsour.2018.05.092

Zou, J., Zhao, J., Wang, B., Chen, S., Chen, P., Ran, Q., et al. (2020). Unraveling the Reaction Mechanism of FeS_2 as a Li-Ion Battery Cathode. *ACS Appl. Mater. Inter.* 12 (40), 44850–44857. doi:10.1021/acsami.0c14082

Conflict of Interest: The authors declare that the research was conducted in the absence of any commercial or financial relationships that could be construed as a potential conflict of interest.

ORIGINAL RESEARCH
published: 10 March 2022
doi: 10.3389/fchem.2022.845742

Hollow CoS/C Structures for High-Performance Li, Na, K Ion Batteries

Yan Liu[1]†, Xiangkun Li[1]†, Fengling Zhang[1], Leqing Zhang[1], Tao Zhang[1], Changshuan Li[1], Zhicheng Jin[1], Yueying Wu[1], Zhongyu Du[1], Huiwen Jiao[1], Ying Jiang[1], Yuliang Yan[1], Qiang Li[1,2]* and Weijin Kong[1]*

[1]College of Physics, University-Industry Joint Center for Ocean Observation and Broadband Communication, Qingdao, China, [2]Weihai Innovation Institute, Qingdao University, Weihai, China

Alkali ion (Li, Na, and K) batteries as a new generation of energy storage devices are widely applied in portable electronic devices and large-scale energy storage equipment. The recent focus has been devoted to develop universal anodes for these alkali ion batteries with superior performance. Transition metal sulfides can accommodate alkaline ions with large radius to travel freely between layers due to its large interlayer spacing. Moreover, the composite with carbon material can further improve electrical conductivity of transition metal sulfides and reduce the electron transfer resistance, which is beneficial for the transport of alkali ions. Herein, we designed zeolitic imidazolate framework (ZIF)–derived hollow structures CoS/C for excellent alkali ion (Li, Na, and K) battery anodes. The porous carbon framework can improve the conductivity and effectively buffer the stress-induced structural damage. The ZIF-derived CoS/C anodes maintain a reversible capacity of 648.9, and 373.2, 224.8 mAh g^{-1} for Li, Na, and K ion batteries after 100 cycles, respectively. Its outstanding electrochemical performance is considered as a universal anode material for Li, Na, and K ion batteries.

Keywords: CoS, porous carbon, Li ion batteries, Na ion batteries, K ion batteries

Edited by:
Jun Zhang,
Zhejiang University of Technology, China

Reviewed by:
Qinghua Tian,
Zhejiang Sci-Tech University, China
Xiaohua Huang,
Taizhou University, China

***Correspondence:**
Qiang Li
liqiang@qdu.edu.cn
Weijin Kong
kwjsd@163.com

†These authors have contributed equally to this work

Specialty section:
This article was submitted to Electrochemistry, a section of the journal Frontiers in Chemistry

Received: *30 December 2021*
Accepted: *24 January 2022*
Published: *10 March 2022*

Citation:
Liu Y, Li X, Zhang F, Zhang L, Zhang T, Li C, Jin Z, Wu Y, Du Z, Jiao H, Jiang Y, Yan Y, Li Q and Kong W (2022) Hollow CoS/C Structures for High-Performance Li, Na, K Ion Batteries. Front. Chem. 10:845742. doi: 10.3389/fchem.2022.845742

INTRODUCTION

Energy storage devices such as rechargeable batteries are the cornerstone of sustainable energy. With the rapid demand for large industrial devices, such as aerospace, national grid, electric vehicles, and so on, novel rechargeable batteries with high density and long cycle need to meet the supply comprehensively (Tarascon and Armand, 2001; Armand and Tarascon, 2008; Huang et al., 2020; Hongsen Li et al., 2021; Qiang Li et al., 2021; Zhang et al., 2021). Among them, lithium ion batteries (LIBs) are used as the source of hybrid electric vehicles at the earliest stage (Hosaka et al., 2020). The long-term use of lithium has made it expensive and scarce in the earth's crust (Vaalma et al., 2018). Therefore, sodium ion batteries (SIBs) and potassium ion batteries (PIBs) have gradually developed into high-quality alternatives to novel rechargeable batteries (Geng et al., 2018; Loaiza et al., 2019; Zhaohui Li et al., 2021). Sodium and potassium ions are abundant and inexpensive, and the lower standard electrode potentials of Na/Na^{+} and K/K^{+} can reduce the cutoff potential of the available negative electrode in the absence of metal sodium or potassium deposition (Mao et al., 2018; Liu et al., 2021).

However, the commercial graphite anode cannot ensure high density because of its low theoretical capacity, which cannot meet the application of LIBs in large-scale energy storage devices. Moreover,

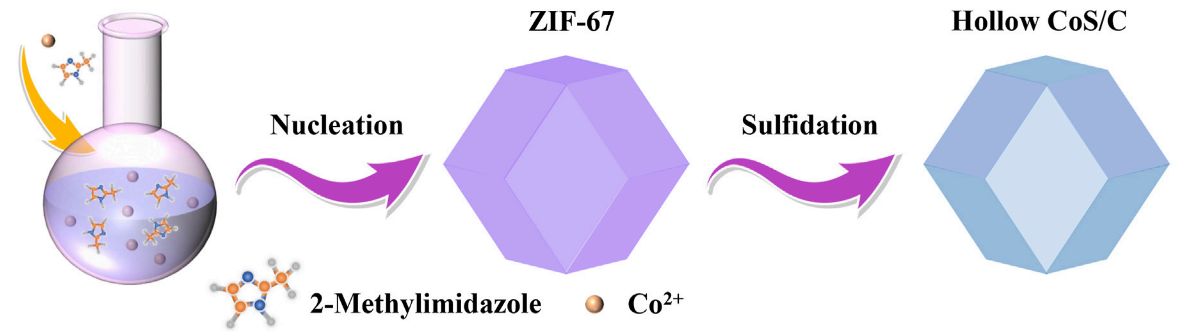

FIGURE 1 | Illustrations of the fabrication processes of ZIF-derived hollow CoS/C sample.

the large radius and heavier weight of sodium ions and potassium ions also make it impossible to shuttle freely and reversibly in the graphite lattice (Xu et al., 2017; Mao et al., 2018; Hongkang Wang et al., 2020). Therefore, the current exploration of potential anode materials with superior reversible capacity and excellent cycle/rate performances is an urgent need for rechargeable batteries including LIBs, SIBs and PIBs. Transition metal sulfides have attracted numerous attentions as anode materials in electrochemical energy storage due to the high specific capacities (Peng et al., 2016; Geng et al., 2018). Among them, cobalt sulfide has been widely studied in catalysis, capacitors, and LIBs by virtue of its unique physical, chemical, and electronic properties (Xie et al., 2013; Peng et al., 2014; Chen et al., 2016; Xu et al., 2018; Song and Yao, 2020), but the application of this electrode material to the negative electrode of SIBs and PIBs is rarely reported. In order to meet the large-scale application of high-performance alkaline ion batteries, it is necessary to design the structure of cobalt sulfide to avoid the structural damage in the cycle process. As an excellent precursor for constructing nanostructures and hollow structures, zeolitic imidazolate framework (ZIF-67) has adjustable physical and chemical properties and large specific surface area (Wang et al., 2016; Zhao et al., 2017; Lu et al., 2020; Yi et al., 2020). ZIF-derived cobalt sulfide hollow structure can effectively alleviate the structural damage caused by stress. The carbon layer framework greatly improves the conductivity of the electrode, and this structure has a huge cavity and porous carbon wall, which makes electrolyte and ions easy to enter, reduces the electron transfer resistance, and shortens the ion diffusion path (Xia et al., 2015; Liu et al., 2017).

Combined with the advantages of the above structural design, we designed a hollow ZIF-derived cobalt sulfide anode material. CoS was uniformly dispersed in the carbon layer of the ZIF framework in the form of nanocrystals. This kind of anode material has excellent electrochemical performance in LIBs, SIBs, and PIBs. The long-term cycling stability and rate capability are benefited from the integrated favorable structural characteristics of electrode. The carbon framework ensures the full penetration of electrolyte and shortens the diffusion path of ions. The porous hollow structure can also be well maintained upon the insertion/extraction of ions with large radius, which lays an effective foundation for the design of anode materials for the next generation of high-performance rechargeable batteries.

EXPERIMENTAL DETAILS

Synthesis Procedure of ZIF-67 Template

In a typical process, 0.873 g of cobalt nitrate hexahydrate ($Co(NO_3)_2·6H_2O$) was first dissolved in 30 mL methanol to form homogeneous solution. And another transparent solution can be obtained through dissolving 0.984 g of 2-methylimidazole into 10 mL of methanol. Afterward, these two solutions were mixed and shaken vigorously for 3 min, and the resulted mixed solutions were aged for 12 h at room temperature. After precipitation, centrifugation, and carefully washing with methanol, the corresponding precipitates were finally collected and dried overnight in an oven at 80°C.

Preparation of Hollow CoS/C Nanoparticles

In order to obtain hollow CoS/C nanoparticles, 25 mg ZIF-67 powder was first dispersed in 6 mL of ethanol with ultrasonication for 30 min to form a homogenous suspension. Then, 0.1875 mM of thioacetamide (dissolved in 2 mL ethanol) was added into the suspension and stirring in an oil bath for 1 h at 90°C. After that, the suspension was cooled down to room temperature and purified with deionized (DI) water and ethanol for several purification cycles. Finally, black products can be obtained under 50°C drying condition.

Preparation of CoS Nanoparticles

The pure CoS was prepared to compare with CoS/C; 190.4 mg of cobaltous chloride hexahydrate ($CoCl_2·6H_2O$) and 134.4 mg of sulfourea ($CS(NH_2)_2$) were dissolved in 40 mL of ethylene glycol. The obtained solution was then transformed into a Teflon-lined autoclave and kept at 180°C for 12 h. The precipitation was collected by centrifugation and washed with water and then dried in the vacuum oven at 70°C for 12 h.

Material Characterizations

The crystal structure was determined through X-ray diffraction (XRD) measurement with a high-intensity Cu Kα radiation (λ = 1.5406 Å). Scanning electron microscopy (SEM) images were

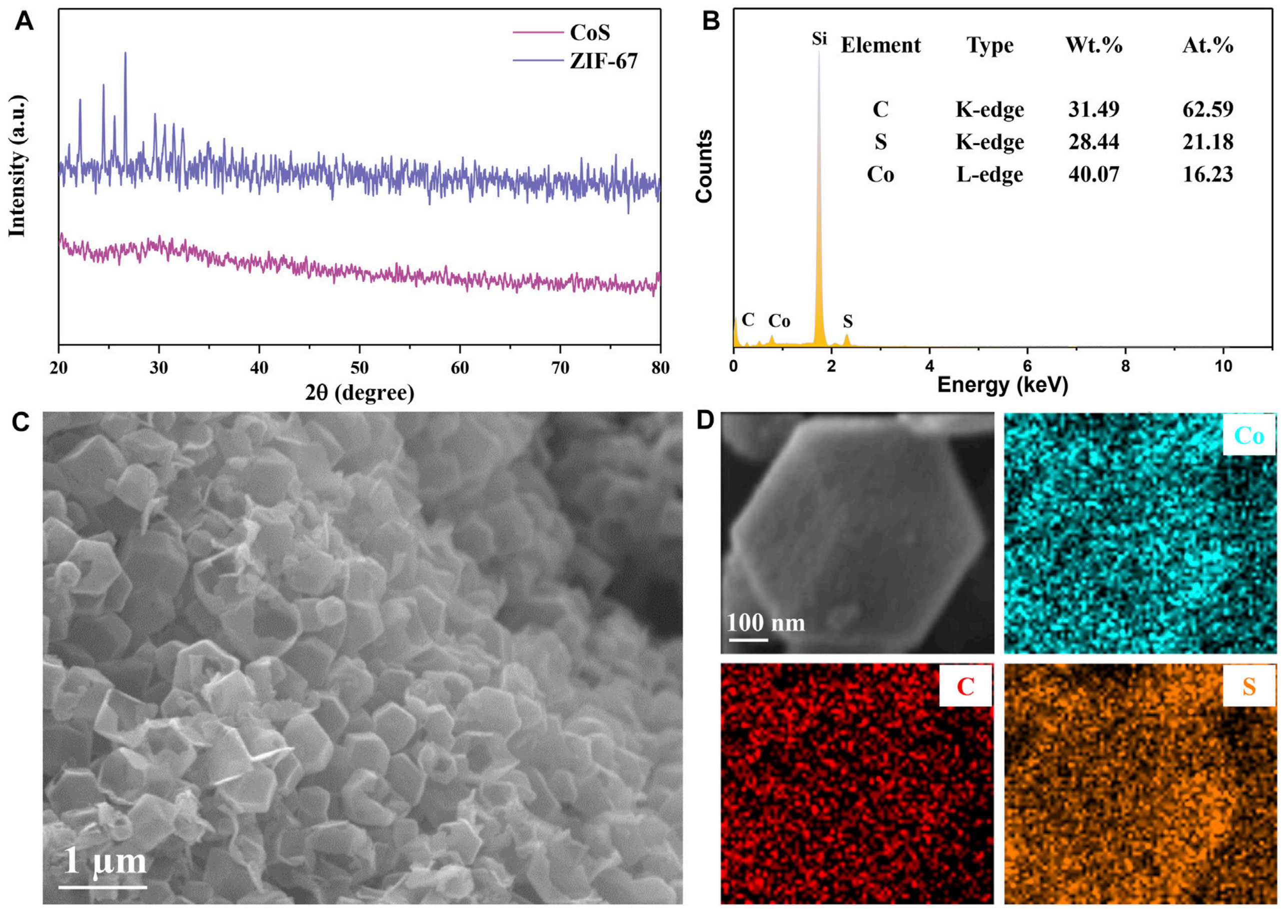

Element	Type	Wt.%	At.%
C	K-edge	31.49	62.59
S	K-edge	28.44	21.18
Co	L-edge	40.07	16.23

FIGURE 2 | (A) X-ray patterns of as-prepared ZIF-67 precursor and ZIF-derived hollow CoS/C. **(B)** EDS spectrum of ZIF-derived CoS/C. The Si element comes from the Si substrate used for SEM characterizations. **(C)** SEM images and **(D)** EDS mapping of ZIF-derived CoS/C, confirming the presence of Co, C, and S without any impurities.

used to observe the surface morphology through JSM-6700F microscope. High-resolution transmission electron microscopy (HR-TEM) and selected area electron diffraction (SAED) results were obtained through JEOL 100 CX microscope. X-ray photoelectron spectroscopy (XPS; Thermo ESCALAB 250XI) was used to analyze the chemical bonding of hollow CoS/C nanoparticles, and the corresponding spectrum was collected by a Kratos-Axis spectrometer under monochromatic Al Kα (1,486.6 eV) x-ray radiation (15 kV, 10 mA) with an energy resolution of 0.45 eV/(Ag $3d_{5/2}$) and C 1 s (284.5 eV) band correction. Thermogravimetric analysis (TGA; Pyris Diamond6000 TG/DTA; PerkinElmer Co., USA) can analyze the thermal properties of samples in air over a temperature range of 20°C–700°C with a heating rate of 10°C min^{-1}. N_2 adsorption/desorption isotherms were performed on a Micromeritics ASAP 2020 instrument to test the Brunauer–Emmett–Teller (BET) surface areas and porosity for as-prepared sample. The Raman test was performed on a LabRAM HR Evolution spectrograph (form France; Horiba Scientific, Longjumeau, France) with a laser at λ = 532 nm (He/Ne laser, <10 mW) at the range of 600–1,800 cm^{-1}.

Electrochemical Measurements

The electrochemical performance of the CoS/C nanoparticles was measured by assembled LIBs. The electrode can be obtained by homogenously mixing the active material, super-p, and sodium carboxymethyl-cellulose in DI with a mass ratio of 7:2:1; the prepared slurry was uniformly coated onto a copper foil and then dried under vacuum at 60°C for 12 h. For half-cell, lithium metal was used as the counter and reference electrode; the electrolyte was 1 M $LiPF_6$ in 1:1 vol/vol mixture of ethylene carbonate and diethyl carbonate. Celgard 2,250 film was utilized as the separator (Whatman). All electrochemical measurements were carried out at room temperature. Cyclic voltammetry (CV) and electrochemical impedance spectroscopy were performed on a CHI660E electrochemical workstation. Galvanostatic charge–discharge measurements were performed under a LAND-CT2001A instrument.

RESULTS AND DISCUSSION

After natural nucleation of the mixed homogeneous solution, the formed ZIF-67 precursor shows a uniform nanocrystalline

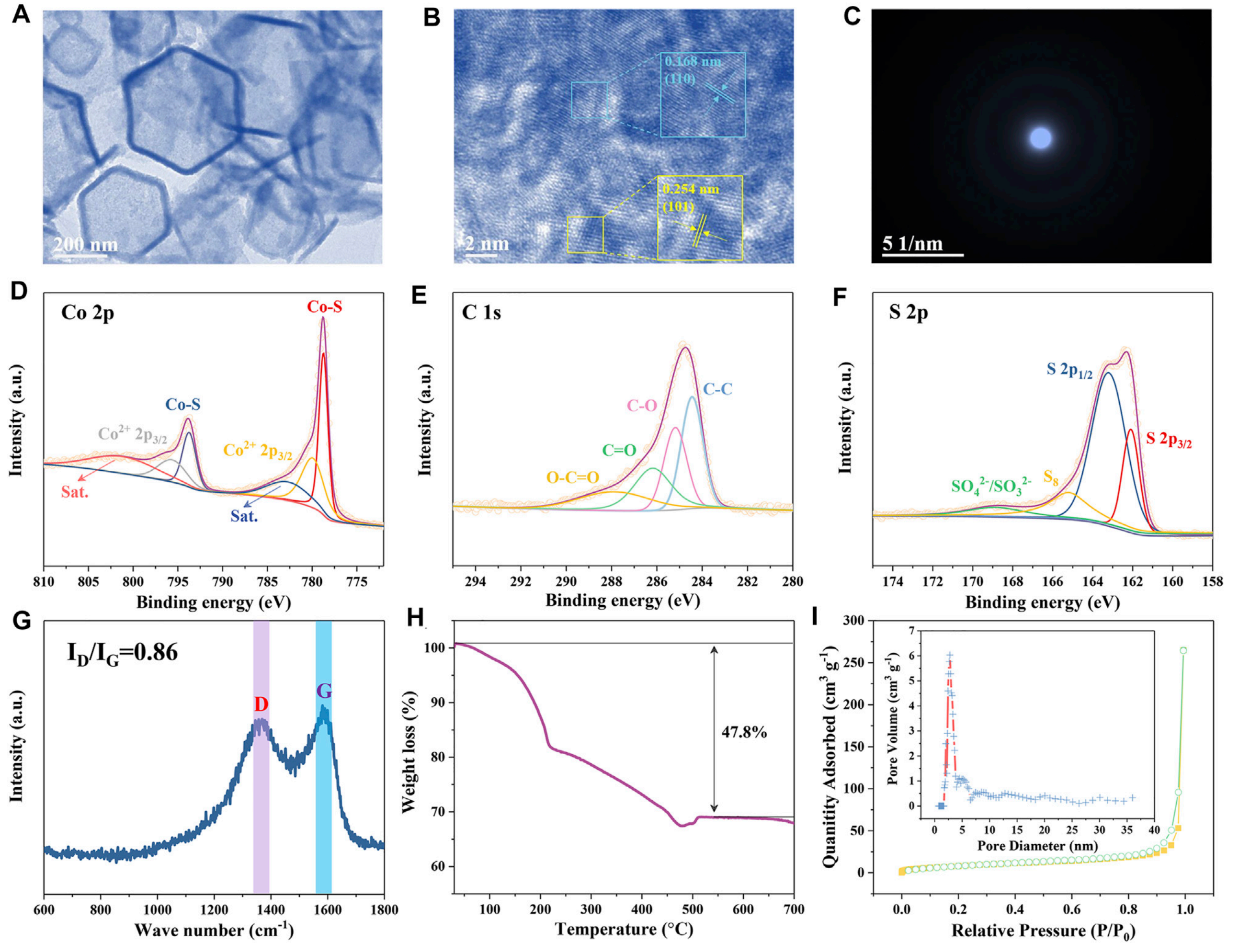

FIGURE 3 | TEM images **(A,B)** and SAED pattern **(C)** of CoS/C. **(D–F)** XPS results of CoS/C. **(G)** Raman spectrum, **(H)** TGA curve, and **(I)** N_2 absorption/desorption isotherms of CoS/C (inset: corresponding pore size distribution).

polyhedron structure. Hollow CoS/C nanocomposites with the same polyhedron structure can be obtained accompanied with the sulfidation process (**Figure 1**). The powder XRD results are shown in **Figure 2A**; it can be seen that there are obvious diffraction peaks in the diffraction patterns of ZIF-67 precursor (Zhou et al., 2017). By contrast, no obvious peaks can be observed in diffraction curves of CoS/C obtained by precursor after sulfidation, which is consistent with the previous reported results (Hu et al., 2016; Xu et al., 2018). This kind of phenomenon can be attributed to the amorphous nature of CoS/C materials; in other words, CoS/C nanoparticles exhibit small crystalline grains and poor crystallinity. And then, the chemical composition of CoS/C was analyzed through energy-dispersive X-ray spectroscopy (EDS), and the corresponding results are exhibited in **Figure 2B**. The EDS results show that the atomic ratio of Co and S is approximately ~1:1, suggesting the successful preparation of ZIF-derived hollow CoS/C samples. And the Si element comes from the Si substrate used for SEM characterizations. The surface morphology of CoS/C was characterized through SEM measurement; as can be seen from **Figure 2C**, the CoS/C samples show well-defined polyhedron structure with hollow core. In addition, the existence of Co, C, and S elements can be observed in the elemental mappings of as-prepared CoS/C sample shown in **Figure 2D**, demonstrating that all these elements are uniformly distributed in the hollow CoS/C sample.

The TEM image in **Figure 3A** further reveals that the ZIF-derived CoS/C sample is a hollow hexagonal structure. Moreover, from the HR-TEM as shown in **Figure 3B**, the lattice fringes of 0.168 and 0.254 nm can be assigned to the (110) and (101) plane of CoS, respectively (Peng et al., 2016; Pan et al., 2021). The HR-TEM results further confirmed the existence of CoS in the hollow hexagonal framework. Besides, the SAED was performed to characterize the crystallinity of obtained ZIF-derived CoS/C materials. As shown in **Figure 3C**, no diffraction spots or diffraction rings can be observed in SAED patterns, indicating

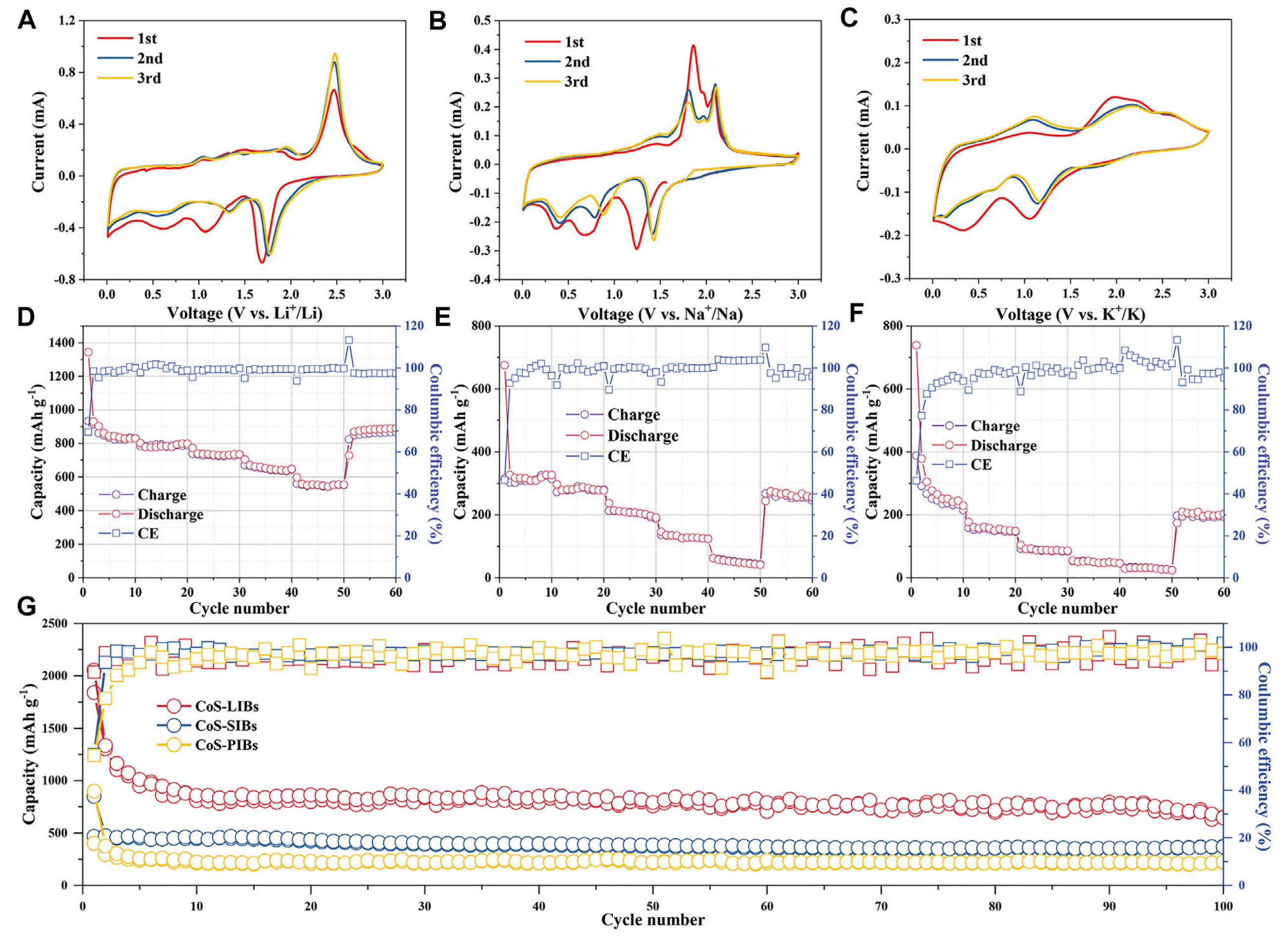

FIGURE 4 | CV measurement of ZIF-derived CoS/C electrode in **(A)** LIBs, **(B)** SIBs, and **(C)** PIBs for the first three cycles at a scan rate of 0.2 mV · s^{-1}. Rate performance of CoS/C electrode in **(D)** LIBs, **(E)** SIBs, and **(F)** PIBs. **(G)** Cycling capabilities for CoS/C–LIBs, CoS/C–SIBs, and CoS/C–PIBs at a current density of 0.2 A g^{-1}.

the obtained CoS/C featured in amorphous nature; this might be caused by the small particles and poor crystallinity (Cui et al., 2013).

Furthermore, the chemical composition of CoS/C and chemical valence states of Co, C, and S were analyzed by XPS measurements. **Figure 3D** presents the Co 2p XPS spectrum of the hollow CoS/C nanocomposite. Two main peaks at 778.7 and 793.7 eV can be assigned to the Co-S bond, whereas the peaks located at 780.0 and 795.7 eV can be attributed to the Co^{2+} $2p_{3/2}$ and Co^{2+} $2p_{1/2}$, respectively. In addition, peaks at 782.9 and 801.3 eV can be detected, indicating the existence of satellite peaks. The C 1s XPS spectrum is given in **Figure 3E**, where carboxylate carbon O–C=O, carbonyl carbon C=O, and C–O locates at 288.1, 286.2, and 285.2 eV, respectively, and the peak at 284.4 eV can be ascribed to C–C bonds. Peaks in XPS spectrum of S 2p shown in **Figure 3F** are located at approximately 162.1 and 163.2 eV, corresponding to S $2p_{3/2}$ and S $2p_{1/2}$, respectively. And the peak with 165.3 eV binging energy is assigned to S–S bond. Moreover, another peak at the 169.0 eV position is attributed to the surface sulfur in the high oxidation state (SO_4^{2-}/SO_3^{2-}) (Yu et al., 2019; Yun-Kai Wang et al., 2020). And then, Raman spectrum measurement was also carried out to investigate the nature of carbon. As shown in **Figure 3G**, two distinguished carbon bands can be identified from the Raman spectroscopy, which are related to the D and G bands. The D band can be attributed to the sp^2 hybridization of carbon, whereas the G band is related to the degree of graphitization. The peak intensity ratio of D/G band is 0.85; the disorder of carbon is beneficial to the alkali metal ion storage (Hu et al., 2020; Ruan et al., 2020).

The TGA result of CoS/C is displayed in **Figure 3H**. The carbon component will be burned out, and the CoS will be converted to Co_3O_4 through chemical reaction 3CoS (s) + $2O_2$ (g) = Co_3O_4 (s) + 3S (g). The calculated carbon content in ZIF-derived CoS/C is approximately 30 wt%, which is consistent with the above EDS spectrum. The BET-specific surface area of CoS/C was measured by N_2 adsorption–desorption measurement, and the pore size distribution was determined through quenched solid density functional theory. As can be seen from **Figure 3I**, the BET surface area is ~21.60 m^2 g^{-1} with micropore peaks at 3.5 nm. The

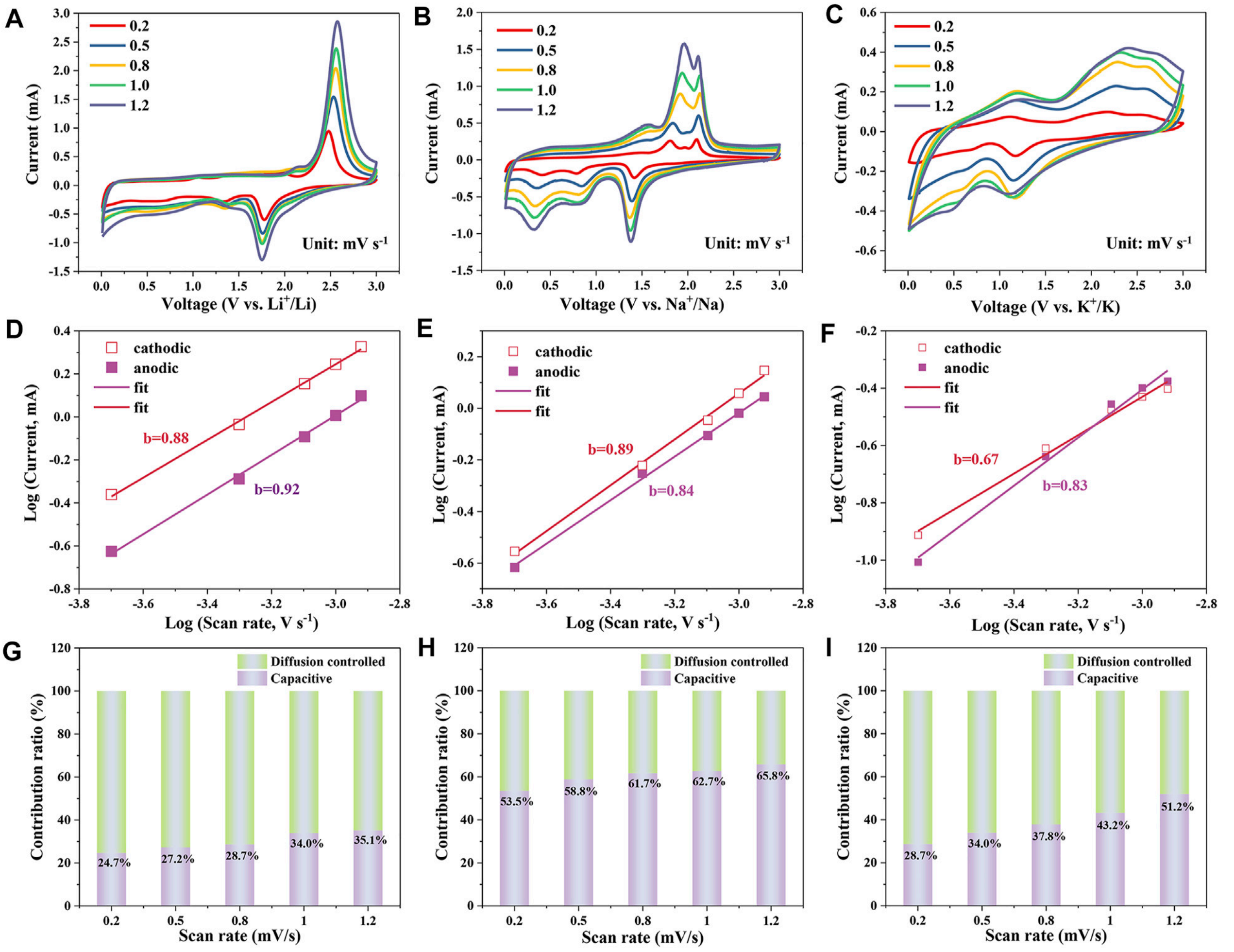

FIGURE 5 | CV measurements of CoS/C electrode in **(A)** LIBs, **(B)** SIBs, and **(C)** PIBs with various sweep rates. Log (current, mA)–log (sweep rate, mV s^{-1}) curves of CoS/C electrode in **(D)** LIBs, **(E)** SIBs, and **(F)** PIBs at the typical peaks. Normalized contribution ratio of diffusion-controlled and capacitive capacities for **(G)** CoS/C–LIBs, **(H)** CoS/C–SIBs, and **(I)** CoS/C–PIBs with various scan rates.

porous structure containing a large number of mesopores in ZIF-derived CoS/C is beneficial to the ionic adsorption, buffering the volume expansion during the electrochemical process and supporting high rate performance (Ruan et al., 2020).

The electrochemical performance of CoS/C was investigated in LIBs, SIBs, and PIBs for comparison. The CV measurements of CoS/C electrode in LIBs, SIBs, and PIBs for the first three cycles are presented in **Figures 4A–C**, respectively. The redox peaks in CV curves of all three batteries can well correspond to the platforms of discharge/charge curves (**Supplementary Figure S1**). For CoS/C–LIBs, a cathodic peak locates at 1.7 V in the first sweep cycle can be attributed to the initial insertion of lithium to form Li_xCoS_2 (Wu et al., 2015), whereas the peaks at approximately 1.1 V in the first cycle and then decreased in the following scans are due to the conversion reaction of CoS to metallic Co and the formation of Li_2S (Chen et al., 2016). Following the charging process, the oxidation peak at approximately 2.4 V can be attributed to the sulfidation of reduced Co nanoparticles. As for the CoS/C–SIBs, the peak at approximately 1.25 V in the first cathodic scan represents the initial insertion of sodium process, and the peak at 0.7 V is attributed to the formation of SEI film (Chen et al., 2016). For CoS/C–PIBs, the peak related to the initial insertion of potassium locates at 1.1 V and the peak attributed to SEI film formation are located at 0.4 V. For all three kinds of batteries, the peak intensity of the SEI film decreases with the increasing number of cycles, indicating that the side reactions such as electrolyte decomposition weaken gradually, which is consistent with the increase in Coulombic efficiency. Owing to different charge–discharge mode, the changes of Coulombic efficiency reflected by CV peak intensity variations are not as obvious as that under the galvanostatic charge–discharge mode (Ge et al., 2020). Besides, the intensity of redox peaks in LIBs is stronger than that in SIBs and PIBs, indicating that LIBs, SIBs, and PIBs show different reaction degrees based on different alkali metal ions. The storage behaviors of K and Na ions have lower absolute value changes of Gibbs energy, and the kinetics of charging and discharging process in PIBs are more sluggish than those in LIBs and SIBs, which can be ascribed to the larger ionic radius of K^+ than Na^+ and Li^+ (Loaiza et al., 2019).

Figure 4D shows the rate performance of the ZIF-CoS/C electrode in LIBs, which delivers discharge specific capacities of 834.9, 798.4, 734.6, 644.9, and 553.8 mAh g^{-1} at 0.1, 0.2, 0.5, 1 and 2 A g^{-1} current density, respectively. When the current density recovers to 0.1 A g^{-1}, the discharge capacity of 890.0 mAh g^{-1} can still be maintained, suggesting a superior rate capability. Moreover, the rate performance of ZIF-CoS/C electrode in SIBs and PIBs are also investigated, and the results are shown in **Figures 4E, F**, respectively. Compared with LIBs, specific capacity of CoS/C electrode in SIBs and PIBs decays rapidly, which is related to the larger radius of Na^+/K^+ than Li^+, and the result is consistent with the CV curves. Although the capacity is not as high as LIBs, the capacity still recovers well when the current density returns to 0.1 A g^{-1} in SIBs and PIBs. This phenomenon suggests that the unique structure of CoS/C nanoparticles and uniform hollow carbon framework ensure its excellent structural stability, which can well accommodate large radius ions to shuttle inside and buffer volume changes. Furthermore, the comparison of long-term cycling performance of ZIF-derived CoS/C electrode in corresponding ion batteries with the voltage range of 0.01–3 V is presented in **Figure 4G**. After 100 cycles, CoS/C anode can obtain a discharge capacity of 648.9, 373.2, and 224.8 mAh g^{-1} for LIBs, SIBs, and PIBs, respectively. The lower capacity of PIBs and SIBs compared with that in LIBs can be attributed to large alkali metal ions radius and incomplete conversion reaction of CoS/C nanoparticles. More importantly, after 100 cycles, the capacity remained stable without obvious attenuation. The superior cycling stability of both three kinds of alkali metal ion batteries further proved the robust structure stability of the electrode upon cycling as shown in **Supplementary Figure S2**. Compared with pure CoS (**Supplementary Figure S3**), CoS/C exhibits better cycling stability and higher capacity, which proves that the unique ZIF structure is beneficial to the structural stability of the electrode materials, and the introduction of carbon can increase the electrical conductivity, thus improving the capacity.

In order to investigate the reaction kinetics of the alkali metal ion storage, the CV curves of CoS/C-LIBs, CoS/C-SIBs and CoS/C-PIBs with different sweep rates ranging from 0.2 mV s^{-1}–1.2 mV s^{-1} were examined, and the corresponding results were provided in **Figures 5A–C**, respectively. It can be seen from the results that they displayed similar CV scan shape except that the peaks grow broader with increasing sweep rates. The electrochemical reaction kinetics can be further analyzed by the following equation:

$$i = av^b \tag{1}$$

where i is the peak current density, a and b are adjustable parameters, v is the scan rate, b = 0.5 implies the diffusion-controlled behavior, and b = 1 indicates surface-controlled capacitive behavior. As a consequence, the value of b obtained by the relation between $\log(v)$ and $\log(i)$ can be used to investigate the reaction kinetic behavior. For CoS/C-LIBs, the fitted b values of cathodic and anodic peaks were 0.88 and 0.92 (**Figure 5D**), respectively, which indicates the electrochemical reaction kinetics of CoS/C-LIBs is diffusion-controlled and surface-controlled capacitive behavior together. In the case of CoS/C-SIBs and CoS/C-PIBs (**Figures 5E, F**), the fitted b values from cathodic/anodic peaks are 0.89, 0.84, and 0.67, 0.83, respectively. These results indicate the electrochemical reaction kinetics of CoS/C-SIBs and CoS/C-PIBs is similar to CoS/C-LIBs, which dominated through diffusion-limited and surface-controlled capacitive behavior together. To further quantify the specific contribution of capacitive capacity and diffusion capacity, we conducted calculations through the following equation:

$$i(V) = k_1 v + k_2 v^{1/2} \tag{2}$$

$$i(V)/v^{1/2} = k_1 v^{1/2} v + k_2 \tag{3}$$

where i is the current at a fixed potential V, and v is the scan rate in the CV tests, whereas $k_1 v$ and $k_2 v^{1/2}$ indicate the surface capacitive and diffusion-controlled process, respectively. The k_1 and k_2 can be facilely obtained via plotting $i(V)/v^{1/2}$ (details are shown in **Supplementary Material S1**). The corresponding results are presented in **Figures 5G–I**. The capacitive contribution ratio is 24.7% at 0.5 mV s^{-1} for CoS/C-LIBs, the ratio increases with the increase in scan rates and finally reaches 35.1% at 1.2 mV s^{-1}. In the case of CoS/C-SIBs and CoS/C-PIBs, the capacitive contribution ratio also increases with the increase of scan rates. The corresponding capacitive ratio in CoS/C-SIBs ascends from 53.5% at 0.2 mV s^{-1} to 65.8% at 1.2 mV s^{-1}, whereas in CoS/C–PIBs, the capacitive contribution rises from 28.7% at 0.2 mV s^{-1} to 51.2% at 1.2 mV s^{-1}. Obviously, the capacity percentage of capacitive contribution generally shows a high value in SIBs. This phenomenon may be due to the unique pore size distribution of ZIF-derived CoS/C, which is beneficial to the surface adsorption of Na^+ and the insertion of Li^+ and K^+ to varying degrees. Besides, from the capacity comparison of LIBs and PIBs, the insertion of K^+ is limited to the surface of electrodes owning to its larger ionic radius, so the capacity caused by incomplete conversion reaction is lower than that of LIBs (Hosaka et al., 2020).

CONCLUSION

In this work, we successfully prepared ZIF-derived CoS/C electrodes and realized unprecedented performance for LIBs, SIBs, and PIBs. The CoS/C nanocomposite with hollow hexagon structure can be obtained through synthesis with ZIF-67 template. The large interlayer spacing in CoS/C is conducive to the migration of alkali metal ions, especially for Na^+ and K^+ with large ionic radius. The hollow structures provide a large number of active sites and thus improve the storage capability of alkali metal ions. Furthermore, the porous carbon framework improves the conductivity of electrodes and effectively buffers the volume expansion produced in electrochemical cycling. Therefore, for alkali ion batteries, the CoS/C electrodes exhibit superior electrochemical performance, including high specific capacity, long-cycle life, and fast rate ability. The electrochemical performance of designed CoS/C anode indicates that it has great application potential in advanced energy storage devices such as ion batteries or ion capacitors.

DATA AVAILABILITY STATEMENT

The original contributions presented in the study are included in the article/**Supplementary Material**, further inquiries can be directed to the corresponding authors.

AUTHOR CONTRIBUTIONS

YL and XL carried out experiments and wrote the manuscript. FZ, LZ and TZ performed and analyzed experimental results. CL, ZJ, YW, ZD and HJ carried out characterization of materials. YJ and YY contributed to writing the manuscript. QL and WK conceived the research and finalized the article. All authors contributed to the article and approved the submitted version.

FUNDING

This work was supported partly by the National Natural Science Foundation of China (22179066, 11674186, and 21975287); the National Science Foundation of Shandong Province (ZR2020MA073).

SUPPLEMENTARY MATERIAL

The Supplementary Material for this article can be found online at: https://www.frontiersin.org/articles/10.3389/fchem.2022.845742/full#supplementary-material

REFERENCES

Armand, M., and Tarascon, J.-M. (2008). Building Better Batteries. *Nature* 451, 652–657. doi:10.1038/451652a

Chen, Y., Li, X., Park, K., Zhou, L., Huang, H., Mai, Y.-W., et al. (2016). Hollow Nanotubes of N-Doped Carbon on CoS. *Angew. Chem. Int. Ed.* 55, 15831–15834. doi:10.1002/anie.201608489

Cui, Y.-H., Xue, M.-Z., Fu, Z.-W., Wang, X.-L., and Liu, X.-J. (2013). Nanocrystalline CoP Thin Film as a New Anode Material for Lithium Ion Battery. *J. Alloys Compd.* 555, 283–290. doi:10.1016/j.jallcom.2012.12.037

Ge, X., Di, H., Wang, P., Miao, X., Zhang, P., Wang, H., et al. (2020). Metal-Organic Framework-Derived Nitrogen-Doped Cobalt Nanocluster Inlaid Porous Carbon as High-Efficiency Catalyst for Advanced Potassium-Sulfur Batteries. *ACS Nano* 14, 16022–16035. doi:10.1021/acsnano.0c07658

Geng, P., Zheng, S., Tang, H., Zhu, R., Zhang, L., Cao, S., et al. (2018). Transition Metal Sulfides Based on Graphene for Electrochemical Energy Storage. *Adv. Energ. Mater.* 8, 1703259. doi:10.1002/aenm.201703259

Wang, H., Yao, T., Li, C., Meng, L., and Cheng, Y. (2020). Constructing Three-Dimensional Ordered Porous MoS2/C Hierarchies for Excellent High-Rate Long-Life Pseudocapacitive Sodium Storage. *Chem. Eng. J.* 397, 125385. doi:10.1016/j.cej.2020.125385

Li, H., Hu, Z., Xia, Q., Zhang, H., Li, Z., Wang, H., et al. (2021). Operando Magnetometry Probing the Charge Storage Mechanism of CoO Lithium-Ion Batteries. *Adv. Mater.* 33, 2006629. doi:10.1002/adma.202006629

Hosaka, T., Kubota, K., Hameed, A. S., and Komaba, S. (2020). Research Development on K-Ion Batteries. *Chem. Rev.* 120, 6358–6466. doi:10.1021/acs.chemrev.9b00463

Hu, H., Guan, B. Y., and Lou, X. W. (2016). Construction of Complex CoS Hollow Structures with Enhanced Electrochemical Properties for Hybrid Supercapacitors. *Chem* 1, 102–113. doi:10.1016/j.chempr.2016.06.001

Hu, X., Zhong, G., Li, J., Liu, Y., Yuan, J., Chen, J., et al. (2020). Hierarchical Porous Carbon Nanofibers for Compatible Anode and Cathode of Potassium-Ion Hybrid Capacitor. *Energy Environ. Sci.* 13, 2431–2440. doi:10.1039/d0ee00477d

Huang, J., Albero Blanquer, L., Bonefacino, J., Logan, E. R., Alves Dalla Corte, D., Delacourt, C., et al. (2020). Operando Decoding of Chemical and Thermal Events in Commercial Na(Li)-Ion Cells via Optical Sensors. *Nat. Energ.* 5, 674–683. doi:10.1038/s41560-020-0665-y

Liu, S., Wang, Z., Zhou, S., Yu, F., Yu, M., Chiang, C. Y., et al. (2017). Metal-Organic-Framework-Derived Hybrid Carbon Nanocages as a Bifunctional Electrocatalyst for Oxygen Reduction and Evolution. *Adv. Mater.* 29, 1700874. doi:10.1002/adma.201700874

Liu, T., Li, L., Yao, T., Li, Y., Zhu, L., Li, F., et al. (2021). Integrating Amorphous Vanadium Oxide into Carbon Nanofibers via Electrospinning as High-Performance Anodes for Alkaline Ion (Li+/Na+/K+) Batteries. *Electrochim. Acta* 369, 137711. doi:10.1016/j.electacta.2020.137711

Loaiza, L. C., Monconduit, L., and Seznec, V. (2019). Siloxene: A Potential Layered Silicon Intercalation Anode for Na, Li and K Ion Batteries. *J. Power Sourc.* 417, 99–107. doi:10.1016/j.jpowsour.2019.02.030

Lu, Y., Du, Y., and Li, H. (2020). Template-Sacrificing Synthesis of Ni-Co Layered Double Hydroxides Polyhedron as Advanced Anode for Lithium Ions Battery. *Front. Chem.* 8, 581653. doi:10.3389/fchem.2020.581653

Mao, M., Cui, C., Wu, M., Zhang, M., Gao, T., Fan, X., et al. (2018). Flexible ReS2 nanosheets/N-Doped Carbon Nanofibers-Based Paper as a Universal Anode for Alkali (Li, Na, K) Ion Battery. *Nano Energy* 45, 346–352. doi:10.1016/j.nanoen.2018.01.001

Pan, H., Huang, X., Lu, Z., Zhang, Z., An, B., Wu, D., et al. (2021). Dual Oxidation and Sulfurization Enabling Hybrid Co/Co3O4@CoS in S/N-doped Carbon Matrix for Bifunctional Oxygen Electrocatalysis and Rechargeable Zn-Air Batteries. *Chem. Eng. J.* 419, 129619. doi:10.1016/j.cej.2021.129619

Peng, S., Li, L., Han, X., Sun, W., Srinivasan, M., Mhaisalkar, S. G., et al. (2014). Cobalt Sulfide Nanosheet/Graphene/Carbon Nanotube Nanocomposites as Flexible Electrodes for Hydrogen Evolution. *Angew. Chem. Int. Ed.* 53, 12594–12599. doi:10.1002/anie.201408876

Peng, S., Han, X., Li, L., Zhu, Z., Cheng, F., Srinivansan, M., et al. (2016). Unique Cobalt Sulfide/Reduced Graphene Oxide Composite as an Anode for Sodium-Ion Batteries with Superior Rate Capability and Long Cycling Stability. *Small* 12, 1359–1368. doi:10.1002/smll.201502788

Li, Q., Li, H., Xia, Q., Hu, Z., Zhu, Y., Yan, S., et al. (2021). Extra Storage Capacity in Transition Metal Oxide Lithium-Ion Batteries Revealed by In Situ Magnetometry. *Nat. Mater.* 20, 76–83. doi:10.1038/s41563-020-0756-y

Ruan, J., Mo, F., Chen, Z., Liu, M., Zheng, S., Wu, R., et al. (2020). Rational Construction of Nitrogen-Doped Hierarchical Dual-Carbon for Advanced Potassium-Ion Hybrid Capacitors. *Adv. Energ. Mater.* 10, 1904045. doi:10.1002/aenm.201904045

Song, B.-Y., and Yao, S. (2020). Optimization of Sulfurization Process of Cobalt Sulfide and Nitrogen Doped Carbon Material for Boosting the Oxygen Reduction Reaction Catalytic Activity in Alkaline Medium. *Front. Chem.* 8, 314. doi:10.3389/fchem.2020.00314

Tarascon, J.-M., and Armand, M. (2001). Issues and Challenges Facing Rechargeable Lithium Batteries. *Nature* 414, 359–367. doi:10.1038/35104644

Vaalma, C., Buchholz, D., Weil, M., and Passerini, S. (2018). A Cost and Resource Analysis of Sodium-Ion Batteries. *Nat. Rev. Mater.* 3, 18013. doi:10.1038/natrevmats.2018.13

Wang, S., Chen, M., Xie, Y., Fan, Y., Wang, D., Jiang, J.-J., et al. (2016). Nanoparticle Cookies Derived from Metal-Organic Frameworks: Controlled Synthesis and Application in Anode Materials for Lithium-Ion Batteries. *Small* 12, 2365–2375. doi:10.1002/smll.201600106

Wu, R., Wang, D. P., Rui, X., Liu, B., Zhou, K., Law, A. W. K., et al. (2015). In-Situ Formation of Hollow Hybrids Composed of Cobalt Sulfides Embedded within Porous Carbon Polyhedra/Carbon Nanotubes for High-Performance Lithium-Ion Batteries. *Adv. Mater.* 27, 3038–3044. doi:10.1002/adma.201500783

Xia, W., Mahmood, A., Zou, R., and Xu, Q. (2015). Metal-organic Frameworks and Their Derived Nanostructures for Electrochemical Energy Storage and Conversion. *Energ. Environ. Sci.* 8, 1837–1866. doi:10.1039/c5ee00762c

Xie, J., Liu, S., Cao, G., Zhu, T., and Zhao, X. (2013). Self-assembly of CoS2/graphene Nanoarchitecture by a Facile One-Pot Route and its Improved Electrochemical Li-Storage Properties. *Nano Energy* 2, 49–56. doi:10.1016/j.nanoen.2012.07.010

Xu, J., Dou, Y., Wei, Z., Ma, J., Deng, Y., Li, Y., et al. (2017). Recent Progress in Graphite Intercalation Compounds for Rechargeable Metal (Li, Na, K, Al)-Ion Batteries. *Adv. Sci.* 4, 1700146. doi:10.1002/advs.201700146

Xu, H., Cao, J., Shan, C., Wang, B., Xi, P., Liu, W., et al. (2018). MOF-Derived Hollow CoS Decorated with CeO X Nanoparticles for Boosting Oxygen Evolution Reaction Electrocatalysis. *Angew. Chem. Int. Ed.* 57, 8654–8658. doi:10.1002/anie.201804673

Yi, Y., Zhao, W., Zeng, Z., Wei, C., Lu, C., Shao, Y., et al. (2020). ZIF-8@ZIF-67-Derived Nitrogen-Doped Porous Carbon Confined CoP Polyhedron Targeting Superior Potassium-Ion Storage. *Small* 16, 1906566. doi:10.1002/smll.201906566

Yu, Z., Zhang, N., Zhang, X., Li, Y., Xie, G., Ge, W., et al. (2019). Synthesis and Research of Layered CoS/graphene Nanoflakes as Sulfur Cathode for High-Energy Lithium Sulfur Batteries. *J. Electroanalytical Chem.* 854, 113524. doi:10.1016/j.jelechem.2019.113524

Wang, Y.-K., Liu, M.-C., Cao, J., Zhang, H.-J., Kong, L.-B., Trudgeon, D. P., et al. (2020). 3D Hierarchically Structured CoS Nanosheets: Li+ Storage Mechanism and Application of the High-Performance Lithium-Ion Capacitors. *ACS Appl. Mater. Inter.* 12, 3709–3718. doi:10.1021/acsami.9b10990

Zhang, F., Li, Z., Xia, Q., Zhang, Q., Ge, C., Chen, Y., et al. (2021). Li-Ionic Control of Magnetism through Spin Capacitance and Conversion. *Matter* 4, 3605–3620. doi:10.1016/j.matt.2021.09.006

Zhao, H., Wang, Y., and Zhao, L. (2017). Magnetic Nanocomposites Derived from Hollow ZIF-67 and Core-Shell ZIF-67@ZIF-8: Synthesis, Properties, and Adsorption of Rhodamine B. *Eur. J. Inorg. Chem.* 2017, 4110–4116. doi:10.1002/ejic.201700587

Li, Z., Zhang, Y., Li, X., Gu, F., Zhang, L., Liu, H., et al. (2021). Reacquainting the Electrochemical Conversion Mechanism of FeS_2 Sodium-Ion Batteries by Operando Magnetometry. *J. Am. Chem. Soc.* 143, 12800–12808. doi:10.1021/jacs.1c06115

Zhou, K., Mousavi, B., Luo, Z., Phatanasri, S., Chaemchuen, S., and Verpoort, F. (2017). Characterization and Properties of Zn/Co Zeolitic Imidazolate Frameworks vs. ZIF-8 and ZIF-67. *J. Mater. Chem. A.* 5, 952–957. doi:10.1039/c6ta07860e

Conflict of Interest: The authors declare that the research was conducted in the absence of any commercial or financial relationships that could be construed as a potential conflict of interest.

frontiers in Chemistry

ORIGINAL RESEARCH
published: 22 March 2022
doi: 10.3389/fchem.2022.851264

Synthesis and Modification of Tetrahedron $Li_{10.35}Si_{1.35}P_{1.65}S_{12}$ *via* Elemental Doping for All-Solid-State Lithium Batteries

*Yuanzhong Lin[1], Jian Chen[1], Jiawei Yan[1], Yanhua Zhuang[1], Hengyi Lu[2] and Chenyang Zhao[1]**

[1]College of Chemistry and Environmental Engineering, Shenzhen University, Shenzhen, China, [2]Walker Department of Mechanical Engineering, The University of Texas at Austin, Austin, TX, United States

Solid-state electrolyte (SSE), as the core component of solid-state batteries, plays a critical role in the performance of the batteries. Currently, the development of SSE is still hindered by its high price, low ionic conductivity, and poor interface stability. In this work, we report the tailored synthesis of a high ionic conductive and low cost sulfide SSE for all-solid-state lithium batteries. The $Li_{10.35}Si_{1.35}P_{1.65}S_{12}$ with favorable tetragonal structure was synthesis by increasing the concentration of Si^{4+}, which shows an ionic conductivity of 4.28×10^{-3} S cm^{-1} and a wide electrochemical stability window of up to 5 V. By further modifying the composition of the electrolyte *via* ionic doping, the ionic conductivity of $Li_{10.35}Si_{1.35}P_{1.65}S_{12}$ can be further enhanced. Among them, the 1% Co^{4+}-doped $Li_{10.35}Si_{1.35}P_{1.65}S_{12}$ shows the highest ionic conductivity of 6.91×10^{-3} S cm^{-1}, 40% higher than the undoped one. This can be attributed to the broadened MS_4^- tetrahedrons and increased Li^+ concentration. As a demonstration, an all-solid-state Li metal battery was assembled using TiS_2 as the cathode and 1% Co^{4+}-doped $Li_{10.35}Si_{1.35}P_{1.65}S_{12}$ as the electrolyte, showing capacity retention of 72% at the 110th cycle. This strategy is simple and can be easily extended for the construction of other high-performance sulfide SSEs.

Keywords: sulfide solid-state electrolyte, solid-state battery, $Li_{10.35}Si_{1.35}P_{1.65}S_{12}$, ionic conductivity, cation substitution

Edited by:
Yu Ding,
University of Maryland, United States

Reviewed by:
Wenwu Li,
Guangdong University of Technology, China
Yumin Qian,
Beijing Institute of Technology, China

****Correspondence:***
Chenyang Zhao
cyzhao@szu.edu.cn

Specialty section:
This article was submitted to Electrochemistry, a section of the journal Frontiers in Chemistry

Received: *09 January 2022*
Accepted: *21 February 2022*
Published: *22 March 2022*

Citation:
Lin Y, Chen J, Yan J, Zhuang Y, Lu H and Zhao C (2022) Synthesis and Modification of Tetrahedron $Li_{10.35}Si_{1.35}P_{1.65}S_{12}$ via Elemental Doping for All-Solid-State Lithium Batteries. Front. Chem. 10:851264. doi: 10.3389/fchem.2022.851264

INTRODUCTION

With the gradual popularity of electric vehicles, the safety issues of lithium-ion batteries and mileage anxiety have become the biggest obstacles that hinder their further development (Chen et al., 2021). Regarding these, solid-state batteries are considered as one of the most promising solutions. On the one hand, by using solid-state electrolyte (SSE), batteries can reduce or even completely avoid the use of flammable organic liquid electrolyte, which can effectively avoid the spontaneous combustion of batteries in special circumstances (Bates et al., 1992; Dudney et al., 1992; Manthiram et al., 2017); on the other hand, solid-state batteries can use lithium metal and high-voltage cathode materials as electrode materials, which increases the energy density of batteries and reduces mileage anxiety (De Luna et al., 2021). At present, the SSE still cannot meet the requirements of commercial applications. The major problems are low ion conductivity, high production cost, and poor stability with electrodes (Porz et al., 2017; Kim et al., 2021).

Since the discovery of 2011, $Li_{10}GeP_2S_{12}$ (LGPS) SSE has attracted increasing attention due to its extremely high ionic conductivity, which is comparable to commercial liquid electrolyte (Kanno and Murayama, 2001; Kamaya et al., 2011). However, its high production cost and poor stability with lithium metal restrict its large-scale applications (Wenzel et al., 2016; Chen et al., 2017; Madsen et al., 2020). As the same main group of Ge, Si is the second rich element in the Earth's crust. The replacement of Si to Ge will significantly reduce the cost of the electrolyte. More importantly, it is predicted that Si-substituted electrolyte (LiSiPS) has the same body-centered cubic-like anion framework as LGPS, which allows fast Li^+ hops along the c-axis (Wang et al., 2015; Harm et al., 2019). However, the preparation of phase-pure LGPS-type $Li_{10}SiP_2S_{12}$ was not successful due to the small ionic radius of Si^{4+} (Ong et al., 2013; Kuhn et al., 2014; Zhang et al., 2019). The ionic conductivity of LiSiPS is far lower than expected and needs to be further enhanced for battery applications (Kato et al., 2014; Kuhn et al., 2014; Kato et al., 2016; Sun et al., 2017; Chen et al., 2018; Wu et al., 2018).

In the LGPS-type electrolyte, the MS_4 tetrahedron center is occupied by metal cations and P^{5+} (De Luna et al., 2021). The radii of cations directly affect the size of the tetrahedron and the crystal structure stability. Because of the smaller radius of Si^{4+} (0.026 nm) compared to Ge^{4+} (0.039 nm), the structure of $Li_{10}SiP_2S_{12}$ changes to orthorhombic, which is less favorable for Li^+ transport (Shannon, 1976). On one hand, increasing the concentration of Si^{4+} can partially compensate the volume loss [P^{5+} (0.017 nm) is replaced by Si^{4+} (0.026 nm)] and is believed to enhance the stability of LiSiPS (Kondo et al., 1992; Murayama et al., 2002; Whiteley et al., 2014). The non-equivalent substitution can also increase the concentration of Li^+ due to charge compensation, which is beneficial for Li^+ transport. On the other, the introduction of other metal ions with ionic radius close to Ge^{4+} will largely expand the size of the tetrahedrons and reduce the Li^+ transport resistance. By further modifying the composition of the ionic framework, the interaction between Li^+ and the host may be even weakened (Adams and Rao, 2012; Bron et al., 2016; Kim and Martin, 2019).

On the basis of the above assumption, in this work, a low-cost and high ionic conductive LGPS-type LiSiPS was prepared through composition regulation and doping. The $Li_{10.35}Si_{1.35}P_{1.65}S_{12}$ obtained shows high ionic conductivity of 4.28×10^{-3} S cm^{-1} at room temperature and good electrochemical stability up to 5 V. Doping $Li_{10.35}Si_{1.35}P_{1.65}S_{12}$ with Co^{4+}, which is equivalent to Si^{4+} but has a larger radius than Si^{4+}, broadens the MS_4 tetrahedrons and reduces the Li^+ transmission resistance. The 1% Co^{4+}-doped $Li_{10.35}Si_{1.35}P_{1.65}S_{12}$ shows the best electrochemical performances. It has an ionic conductivity of 6.91×10^{-3} S cm^{-1} and a Li^+ migration number as high as 0.97. The ion conductivity is about 40% higher than that of undoped sample. The assembled Li/SSE/TiS_2 all-solid-state lithium battery shows stable lifespan of more than 100 cycles with a specific discharge capacity of 70 mAh g^{-1} (Li et al., 2016). Finally, to verify the effect of anion doping on the performance of the SSE, Se^{2-}, which has a larger radius than S^{2-}, was introduced and a $CoSe_2$-doped LiSiPS sulfide SSE was prepared. The enhanced ionic conductivity can be attributed to the large ion radius of Se^{2-}, which widens the migration channel for Li^+, and the larger polarization characteristics of Se^{2-} that effectively reduce the affinity to Li^+.

EXPERIMENTAL SECTION

Materials Synthesis

The LiSiPS SSEs were synthesized by high-energy ball milling process followed by thermal annealing. Stoichiometric proportion of Li_2S, SiS_2 and P_2S_5 and 10 zirconia balls (10 mm in diameter) were added to the ball mill tank in an Ar-filled glove box. The mixture was ball milled for 40 h at 500 rpm. A 15-min rest was set after 15-min ball milling to avoid overheat of the machine. The ground powder was put into a quartz tube and sealed under vacuum. The LiSiPS SSEs were finally obtained by heat treatment at 400°C–500°C for 3 days and naturally cooled to room temperature. The modification of the LiSiPS SSEs was carried out under the same conditions except the addition of a certain amount of CoS_2, TiS_2, and $CoSe_2$. The doping ratio (0%, 0.5%, 1%, 2%, and 3%) refers to the proportion of M^{4+}:Si^{4+} (M = Si^{4+}, Ti^{4+}).

Materials Characterization

The crystal structure was characterized by X-ray diffraction (XRD; D8ADVANCE) with a Cu Kα source between 10° and 80°. The morphology and microstructure of the samples were characterized by scanning electron microscope (SEM; JSM-7800F) with acceleration voltage of 30 kV. The molecular vibrations and rotations were characterized by Raman spectra with a wavelength of 532 nm in range of 200–4,000 cm^{-1}. The surface elements and chemical states of the samples were characterized by X-ray photoelectron spectroscopy (XPS; K-Alpha+).

Electrochemical Measurement

The ionic conductivity was measured by sandwiching the electrolyte pellets between two stainless steel sheets after hot-pressed at 380 MPa at 250°C. Electrochemical impedance spectroscopy (EIS) at frequencies from 1 MHz to 10 Hz was performed on the blocking cells with amplitude of 10 mV. The Li^+ migration number (t_{Li+}) was measured by Li/SSE/Li symmetric cell based on the following equation:

$$t_{Li^+} = \frac{I_{ss}R_{\mathrm{bss}}(V - I_0R_{i0})}{I_0R_{\mathrm{b0}}(V - I_{ss}R_{iss})} \tag{1}$$

where V is the voltage applied; I_0 is the initial current; R_{b0} is the initial bulk resistance of SSE; R_{i0} is the initial resistance of the passivation layer; and I_{ss}, R_{bss}, and R_{iss} are the current, bulk resistance of SSE, and the resistance of the passivation layer at steady state, respectively. The chemical stability to Li metal was measured using the same symmetric cell. The current density and duration time were set as 0.05 mA cm^{-2} and 1 h, respectively. The electrochemical window of electrolyte was estimated by Cyclic

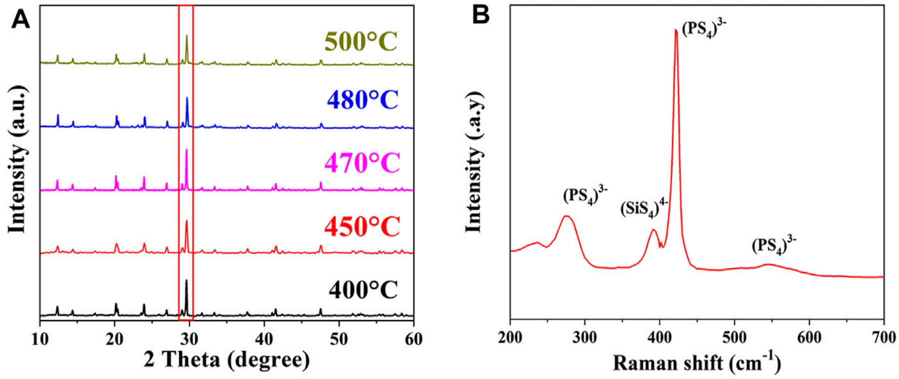

FIGURE 1 | XRD patterns of $Li_{10.35}Si_{1.35}P_{1.65}S_{12}$ synthesized at different temperatures **(A)** and typical Raman spectrum of the $Li_{10.35}Si_{1.35}P_{1.65}S_{12}$ **(B)**.

Voltammetry (CV) with stainless steel sheet and Li foil as the electrodes. The sample was scanned between –0.5 and 5 V with a scan rate of 1 mV s^{-1}.

Electrode Preparation and All-Solid-State Battery Assembly

To avoid the direct contact between the sulfide SSE and lithium metal, a fluorination of lithium metal was conducted (Fan et al., 2018). A certain amount of Lithiumbis (fluorosulfonyl)imide was added to anhydrous DME to get a 6 mol L^{-1} LiFSI-DME solution. The solution was then dropped on both sides of the lithium metal. The 10-mm lithium foil was then placed on the surface of the SSE pellets and dried overnight in a vacuum oven at 120°C. The cathode was prepared by mixing TiS_2, acetylene black, and SSE with a mass ratio of 5:1:4. They were first manually mixed in a mortar for 10 min and then ball-milled for 6 h at 500 rpm. The powder sample after ball milling was used as composite cathode material for all-solid-state lithium battery.

For the battery assembly, 60-mg SSE was added into a custom mold and pressed into pellets at 250 MPa. Then, the composite cathode material was added to the upper side of the electrolyte and pressed under a pressure of 375 MPa for 5 min. The areal density of TiS_2 was ca. 4 mg cm^{-2}. After compaction, the fluorinated lithium metal was put onto the other side of the SSE. The battery was cycled between 1.5 and 3 V at 0.1 C.

RESULTS AND DISCUSSION

Structure and Property of the $Li_{10.35}Si_{1.35}P_{1.65}S_{12}$ SSE

The structure of the synthesized $Li_{10.35}Si_{1.35}P_{1.65}S_{12}$ SSE was first analyzed by XRD and Raman. The normalized XRD patterns are shown in **Figure 1A**. All the diffraction peaks are in good consistent with LGPS, indicating the successful synthesis of phase-pure tetragonal $Li_{10.35}Si_{1.35}P_{1.65}S_{12}$ with a space group of P42/nmc (137). Compared to LGPS, the $Li_{10.35}Si_{1.35}P_{1.65}S_{12}$ has higher content of tetravalent center ions, which enhances the stability of the body-centered cubic-like anion framework (Kuhn et al., 2014). The sample synthesized between 400°C and 500°C exhibits identical XRD patterns. Among them, the sample at 470°C shows the highest crystallinity. The Raman spectrum of the $Li_{10.35}Si_{1.35}P_{1.65}S_{12}$ (470°C) is shown in **Figure 1B**. The peaks at 275, 420, 550, and 575 cm^{-1} are attributed to the characteristic signals of PS_4^{3-}, whereas the peak at 390 cm^{-1} comes from the stretching vibration of Si-S^- bond in SiS_4^{4-}(Pradel and Ribes, 1989). The above results confirmed the successful synthesis of the desirable LGPS-type $Li_{10.35}Si_{1.35}P_{1.65}S_{12}$ SSE.

The morphologies of $Li_{10.35}Si_{1.35}P_{1.65}S_{12}$ synthesized at different temperatures are shown in **Figure 2**. All the electrolyte powders are composed of micron-sized granules with irregular shape. From the high-resolution view, it can be seen that the electrolyte synthesized at 470°C has higher degree of particle agglomerations. This is beneficial to reduce the interface impedance of the electrolyte and promote Li^+ transfer across the grain boundaries. The ionic conductivity of $Li_{10.35}Si_{1.35}P_{1.65}S_{12}$ was then measured by EIS. To lower the interface impedance inside the electrolyte, the samples were hot presses to make the power more compact and denser. The impedances of $Li_{10.35}Si_{1.35}P_{1.65}S_{12}$ synthesized at 470°C were tested under different temperature and pressure, and the results are shown in **Supplementary Figure S8**. As shown in **Supplementary Figure S8**, the sample treated at 375 MPa and 250°C shows the lowest resistance. Therefore, they are chosen as the optimized hot pressing parameters unless otherwise specified. **Figure 3A** shows the Nyquist plots of the samples.

The detailed information is shown in **Supplementary Table S1**. As shown in **Figure 3A**, all the plots show the diagonal characteristics, indicating the ionic conductor nature of the electrolytes. The negligible semicircles at high-frequency region signify small grain boundary impedance of the electrolytes. The ionic conductivity of $Li_{10.35}Si_{1.35}P_{1.65}S_{12}$ increases first with the annealing temperature due to the enhanced crystallinity and reaches 4.28×10^{-3} S cm^{-1} at 470°C (**Figure 3B**). However, the ionic conductivity decreases with the further increase of the temperature. This may be attributed to the slight

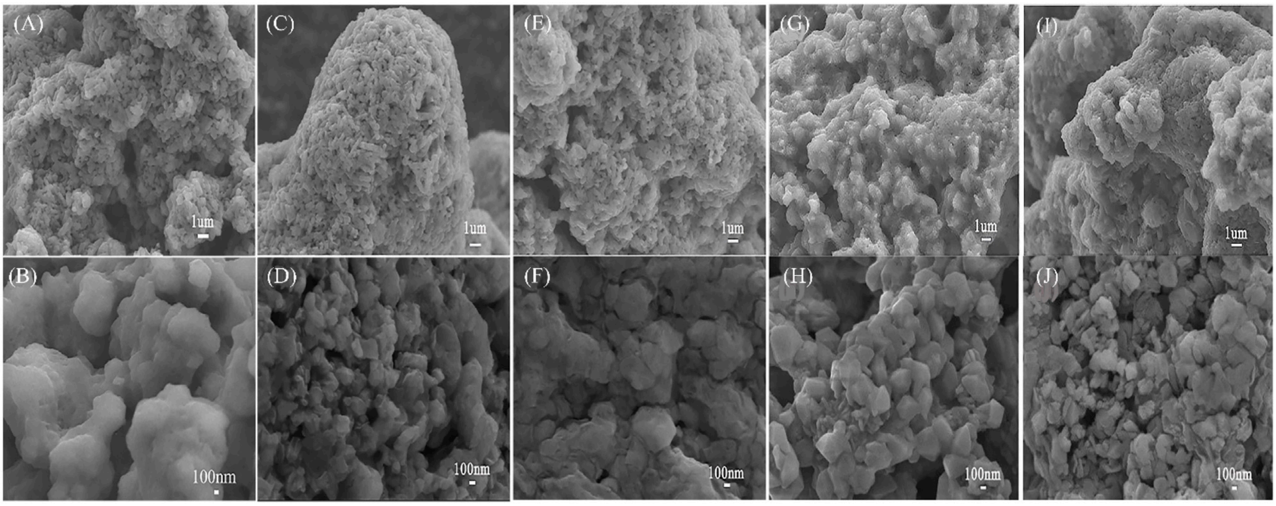

FIGURE 2 | SEM images of $Li_{10.35}Si_{1.35}P_{1.65}S_{12}$ synthesized at 400°C **(A,B)**, 450°C **(C,D)**, 470°C **(E,F)**, 480°C **(G,H)**, and 500°C **(I,J)**.

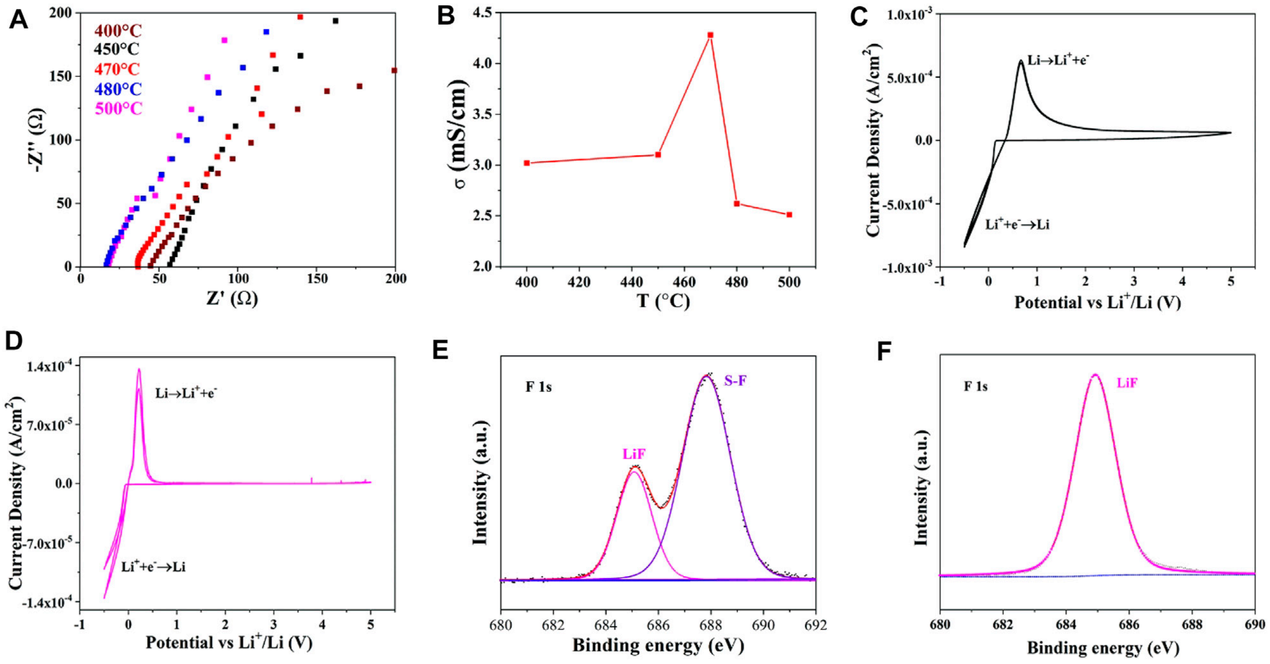

FIGURE 3 | Nyquist plots of $Li_{10.35}Si_{1.35}P_{1.65}S_{12}$ synthesized at different temperatures **(A)**, the corresponding ionic conductivities **(B)**, CV test of $Li_{10.35}Si_{1.35}P_{1.65}S_{12}$ with pristine lithium metal **(C)** and modified lithium metal **(D)** as electrodes, XPS of lithium metal before **(E)** and after **(F)** polarization test.

decomposition of $Li_{10.35}Si_{1.35}P_{1.65}S_{12}$, as indicated by the reduced peak intensity in XRD.

The electrochemical window of $Li_{10.35}Si_{1.35}P_{1.65}S_{12}$ (470°C) was investigated by CV. An asymmetric configuration was adopted using stainless steel and lithium metal as electrodes. As shown in **Figure 3C**, the sharp peak started at 0 V can be attributed to the Li^+ deposition on the lithium metal surface. Its dissolution is found at 0.5 V during the anodic scan. However, the anodic current lasts throughout the test window, indicating a continuous interface reaction between Li and $Li_{10.35}Si_{1.35}P_{1.65}S_{12}$. To avoid this, a thin layer of LiF was *in situ* deposited to prevent the direct contact between them (details seen in the experimental section) (Porz et al., 2017). The XPS spectrum of the modified lithium is shown in **Figure 3E**. The characteristic peak at 685 eV is assigned to LiF, confirming the successful formation of LiF protection layer. The peak that appears at 687.8 eV corresponds

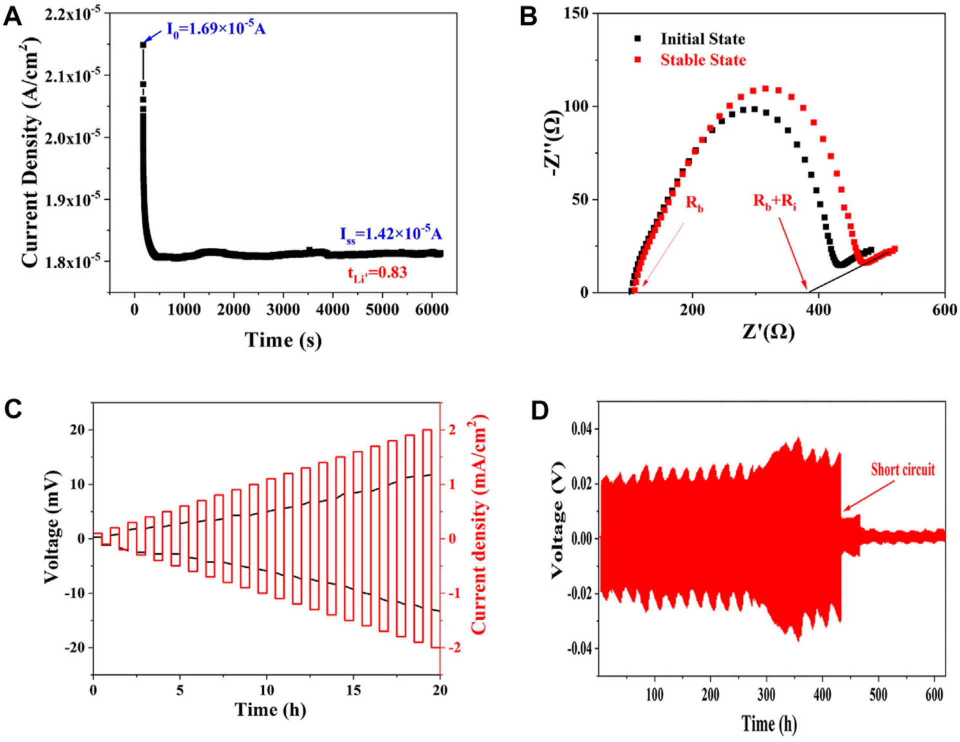

FIGURE 4 | The time-current curve of Li/SSE/Li symmetric cell under 10 mV **(A)**, the Nyquist plots of the cell at initial and steady states **(B)**, and polarization curves of the Li/SSE/Li symmetric cell under different current densities **(C,D)**.

to S-F bonds of LiFSI precursor, which further reacts with Li and converts to LiF during the following electrochemical reaction (**Figure 3F**). As a result, the interface side reaction is largely suppressed. As shown in **Figure 3D**, only one pair of redox peaks corresponding to $Li^+ + e^- \leftrightarrow Li$ is observed. The $Li_{10.35}Si_{1.35}P_{1.65}S_{12}$ is stable up to 5 V, showing potential to match with high voltage cathodes. In the following text, the Li metals are all modified using the same method unless otherwise specified.

The ionic migration number of $Li_{10.35}Si_{1.35}P_{1.65}S_{12}$ (470°C) was then measured to confirm the proportion of Li^+ transport in the electrolyte. As shown in **Figures 4A,B**, the total impedance increases from 363.4 to 384.2 Ω due to the space charge separation at the interface. The polarization current decreases from initial 1.69 × 10^{-5} A to steady state 1.42 × 10^{-5} A. The ionic migration number was calculated to be 0.83 according to **Eq. 1**. The high ionic migration number explains the high ionic conductivity of $Li_{10.35}Si_{1.35}P_{1.65}S_{12}$, especially compared with polymer and oxide SSEs. The ability of $Li_{10.35}Si_{1.35}P_{1.65}S_{12}$ to inhibit the growth of Li dendrites was evaluated using Li/SSE/Li symmetrical cell. As shown in **Figure 4C**, with the increase of current density from 0.1 mA cm^{-2} to 2 mA cm^{-2}, the overpotential increases from 0.3 to 13.3 mV without short circuit. This result indicates that the limiting current density of $Li_{10.35}Si_{1.35}P_{1.65}S_{12}$ is higher than 2 mA cm^{-2}. **Figure 4D** shows the constant-current polarization curve at an areal capacity of 0.05 mAh cm^{-2}. The cell is stable up to 432 h, showing good resistance to the growth of lithium dendrites.

Modification of the $Li_{10.35}Si_{1.35}P_{1.65}S_{12}$ SSE *via* Cation Doping

To further enhance the ionic conductivity of $Li_{10.35}Si_{1.35}P_{1.65}S_{12}$, Ti^{4+} (0.042 nm) and Co^{4+} (0.04 nm) were introduced into the lattice of $Li_{10.35}Si_{1.35}P_{1.65}S_{12}$ because of their comparable ionic radii with Ge^{4+} but much lower price. The XRD patterns of the synthesized CoS_2 and TiS_2 are shown in **Supplementary Figure S1**. After ball milling and thermal annealing, Co^{4+} and Ti4$^+$-doped $Li_{10.35}Si_{1.35}P_{1.65}S_{12}$ SSE were obtained.

Figure 5A shows the normalized XRD patterns of Co4$^+$-doped $Li_{10.35}Si_{1.35}P_{1.65}S_{12}$. The position of the peaks match well with $Li_{10.35}Si_{1.35}P_{1.65}S_{12}$, indicating that the doping of Co^{4+} does not change the initial tetragonal structure. The crystallinity decreases with the increase of Co^{4+} content, showing more defects are introduced which can promote the transport of Li^+. Unknown impurity appears (15.5°, 25.3°, and 32.3°) when the doping ratio of Co^{4+} is higher than 2%. The higher content of Co^{4+} exceeds the limit of the solid solution and leads to the emergence of new phase. It worth to note that peak shifts to higher angles are observed (14.4°, 17.4°, and 20.2°) at relatively low doping ratios (0.5% and 1%). This indicates a constriction of crystal lattice and

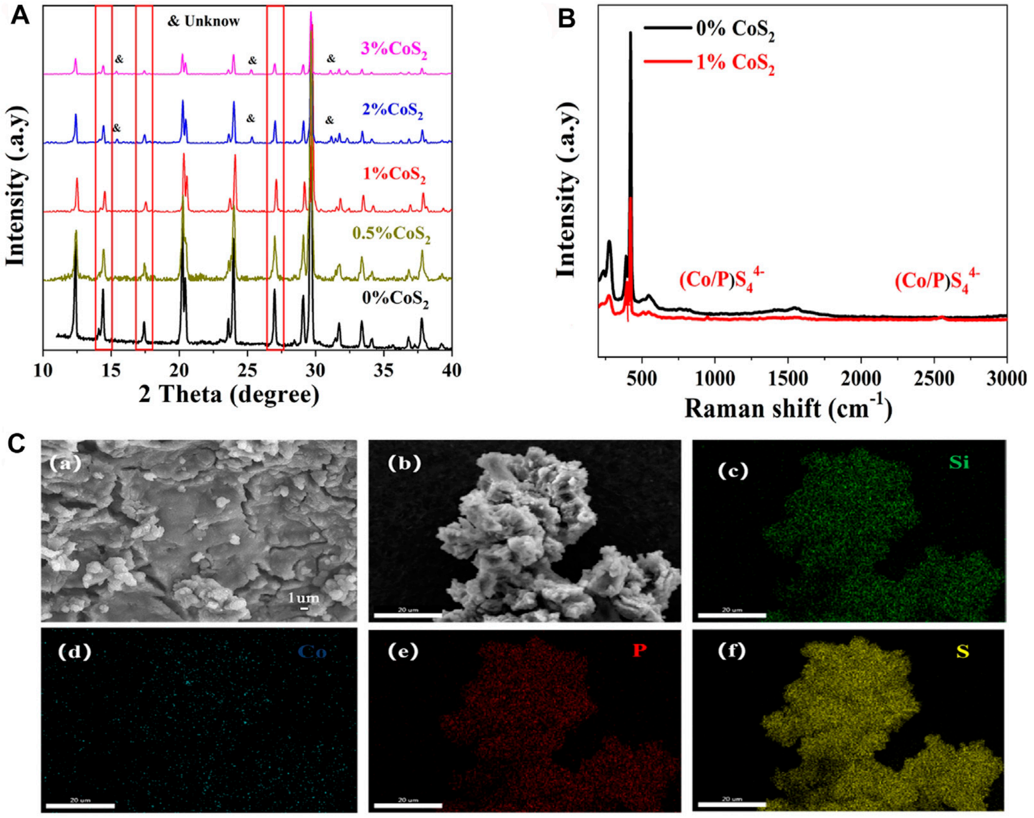

FIGURE 5 | XRD patterns of $Li_{10.35}Si_{1.35\text{-}x}Co_xP_{1.65}S_{12}$ with different Co^{4+} doping ratios **(A)**, Raman Spectra of pristine and 1% Co^{4+}-doped electrolytes **(B)**, and SEM and EDS images of 1% Co^{4+}-doped $Li_{10.35}Si_{1.35\text{-}x}Co_xP_{1.65}S_{12}$ **(C)**.

contradicts with the previous prediction. To explore the crystal parameters after doping, the Rietveld refinement for 1% Co^{4+}-doped $Li_{10.35}Si_{1.35}P_{1.65}S_{12}$ was carried out. The results are shown in **Supplementary Table S2** and **Supplementary Figure S2**. The 1% $Co4^+$-doped $Li_{10.35}Si_{1.35}P_{1.65}S_{12}$ shows a $P4_2/nmc$ space group with lattice constants of a = 8.6731 Å and c = 12.5331 Å. Compared to original $Li_{10.35}Si_{1.35}P_{1.65}S_{12}$ (a = 8.6708 Å and c = 12.5396 Å), the unit cell expands along the a-direction but shrinks slightly in the c-direction due to the Co^{4+} doping, resulting in an expansion of the cell volume. This broadens the channels of Li^+ transport, which further enhances the ionic conductivity of electrolytes. The XRD patterns of Ti^{4+}-doped $Li_{10.35}Si_{1.35}P_{1.65}S_{12}$ show similarly characteristics (**Supplementary Figure S3**). The Raman spectrum of 1% Co-doped $Li_{10.35}Si_{1.35}P_{1.65}S_{124}$ is shown in **Figure 5B**. Compared to $Li_{10.35}Si_{1.35}P_{1.65}S_{12}$, two new peaks emerge at 950 and 2,550 cm^{-1}, which are related to $(Co./P)S_4{}^{4-}$ structure. The morphology of the 1% Co^{4+}-doped $Li_{10.35}Si_{1.35}P_{1.65}S_{12}$ is shown in **Figure 5C**. It can be seen that most of the electrolyte granules melt together during the thermal treatment, and some are clearly visible on the surface. All the elements are uniformly distributed within the electrolyte, again confirming the successful doping of Co^{4+}.

The ionic conductivity of Co^{4+}-doped $Li_{10.35}Si_{1.35}P_{1.65}S_{12}$ was measured by blocking cell. The testing parameters are summarized in **Supplementary Table S3**. As shown in **Figures 6A,B**, the ionic conductivity of $Li_{10.35}Si_{1.35}P_{1.65}S_{12}$ is effectively enhanced by Co^{4+} doping, and 1% Co^{4+}-doped sample shows the highest ionic conductivity of 6.91 mS cm^{-1}, 40% higher than the undoped one. The enhanced ionic conductivity could be attributed to the LGPS-type anion packing, the higher concentration of Li^+ induced by M^{4+} substitution, and the broadened Li^+ transport path. Compared to Co^{4+}, the doping of Ti^{4+} can also enhance the ionic conductivity of $Li_{10.35}Si_{1.35}P_{1.65}S_{12}$ by 15% (5.69 mS cm^{-1}) when 0.5% TiS_2 was added, showing the effectiveness of the doping strategy (**Suplementary Figure S4**). The slightly difference may be attributed to the limited doping ratio of Ti^{4+}. The electrochemical windows of the Co^{4+}-doped samples were studied using asymmetrical cell. **Figure 6C** and **Suplementary Figure S5** show the CV curves of 0.5%, 1%, and 2% Co^{4+}-doped $Li_{10.35}Si_{1.35}P_{1.65}S_{12}$. Only one pair of redox peak at around 0 V is observed for all the samples, indicating that they are electrochemically stable between 0 and 5 V. The ionic migration number of 1% Co^{4+}-doped $Li_{10.35}Si_{1.35}P_{1.65}S_{12}$ is calculated to be 0.97. The much increased value shows that Co^{4+} doping can promote the migration of Li^+. As a demonstration, a solid-state Li battery was assembled using the 1% Co^{4+}-doped $Li_{10.35}Si_{1.35}P_{1.65}S_{12}$ as electrolyte and TiS_2 as the active material. As shown in **Figure 6D**, the specific charge capacity of the first cycle is

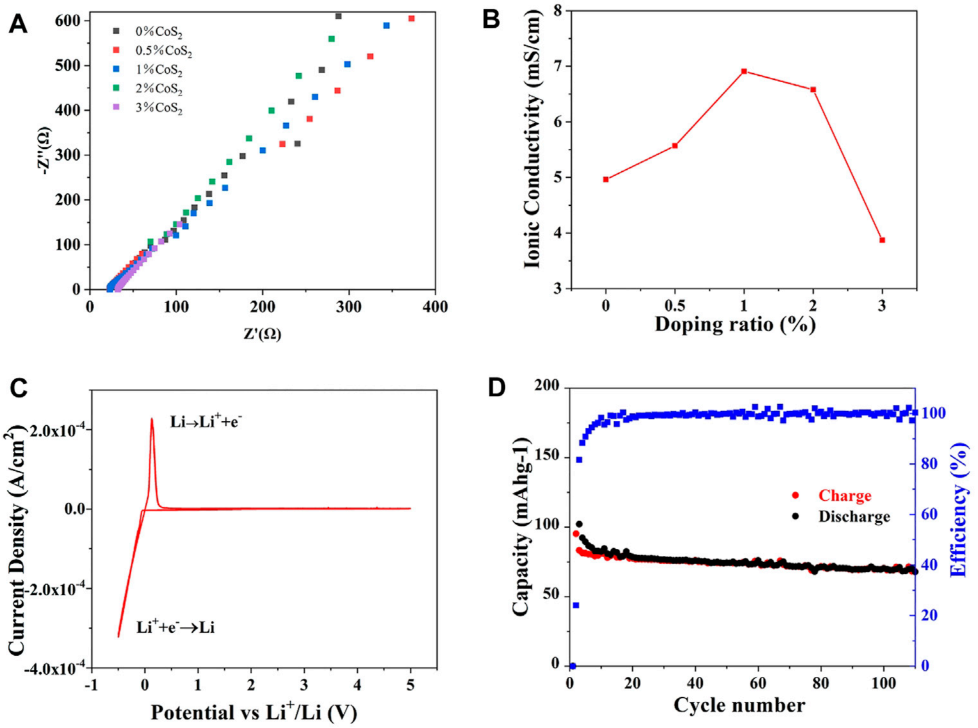

FIGURE 6 | Ionic conductivity of Co^{4+}-doped $Li_{10.35}Si_{1.35}P_{1.65}S_{12}$ **(A,B)**, CV curve of 1% Co^{4+}-doped electrolyte **(C)**, and cycling stability of the all-solid-state lithium battery **(D)**.

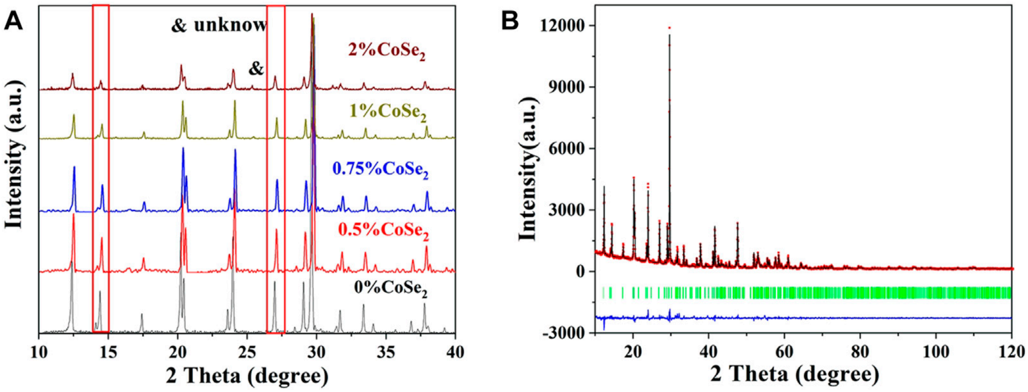

FIGURE 7 | XRD pattern of the $CoSe_2$ doping $Li_{10.35}Si_{1.35}P_{1.65}S_{12}$ **(A)** and the Rietveld refinement of 1% $CoSe_2$-doped sample **(B)**.

95.2 mAh g^{-1}, and 72% of the initial capacity can be retained after 110 cycles, showing stable performance in practical use. The low Coulombic efficiency of the first cycle can be attributed to the decomposition of LiFSI precursor, as shown in **Figure 3F**.

Further Attempt for the Performance Improvement of $Li_{10.35}Si_{1.35}P_{1.65}S_{12}$

The above results have inspired us to further improve the ionic conductivity of $Li_{10.35}Si_{1.35}P_{1.65}S_{12}$ through dual doping. The Se^{2-} (0.198 nm) has a large ionic radius than S^{2-} (0.184 nm). Similar to Co^{4+}, the proper Se^{2-} anion substitution may also enlarge the diffusion channel of Li^+. What is more, the higher polarizability of Se^{2-} can further weaken the binding between Li^+ and the anion framework, thus improving the ionic conductivity of $Li_{10.35}Si_{1.35}P_{1.65}S_{12}$.

$CoSe_2$ was first synthesized by solid-phase reaction. The $CoSe_2$ consists of cubic-shaped particles with size of ca. 1 μm (**Supplementary Figure S6**), and its XRD is shown in **Supplementary Figure S7**. After ball milling and thermal

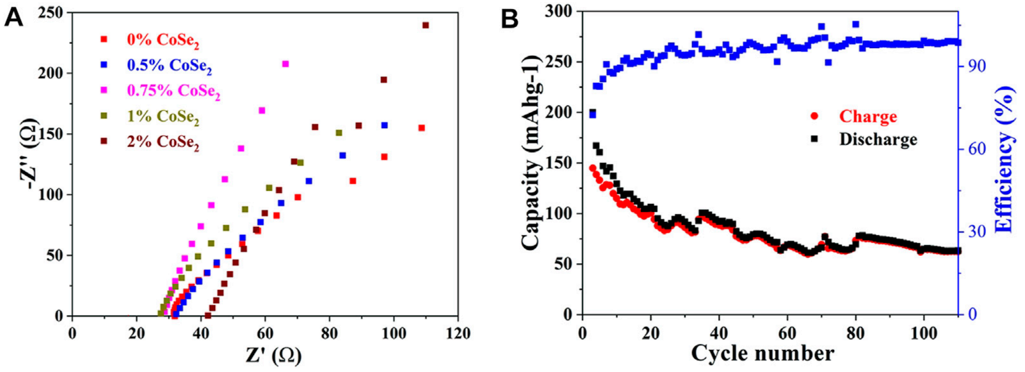

FIGURE 8 | (A) Nyquist plots of $CoSe_2$-doped $Li_{10.35}Si_{1.35}P_{1.65}S_{12}$ **(B)** Cycling stability of the all-solid-state lithium battery assembled with 1% $CoSe_2$ doped SSE.

treatment, sintered irregular particles are obtained. The normalized XRD patterns of $CoSe_2$-doped $Li_{10.35}Si_{1.35}P_{1.65}S_{12}$ SSEs are shown in **Figure 7A**. All the samples exhibit the same LGPS-type structure. With the increase of doping ratio, the peak intensity decreases gradually and some peaks shift to lower angles, similar to the case of CoS_2. When the doping ratio of $CoSe_2$ exceeds 1%, the saturation of $CoSe_2$ is reached and impurity phase appears at 26°. The cell parameters of the 1% $CoSe_2$-doped $Li_{10.35}Si_{1.35}P_{1.65}S_{12}$ were analyzed by Rietveld refinement. The results are shown in **Figure 7B** and **Supplementary Table S4**. The dual-doped sample maintains the same tetragonal structure. The lattice parameters are a = 8.677 Å and c = 12.535 Å with a cell volume of 943.835 Å^3. These values are larger than that of 1% $Co4^+$-doped sample, indicating the successful doping of Co^{4+} and Se^{2-} into the lattice of $Li_{10.35}Si_{1.35}P_{1.65}S_{12}$. The incorporation of Co^{4+} and Se^{2-} mainly induces the lattice expansion along the *a*-axis.

The ionic conductivities of the $CoSe_2$-doped samples were measured by EIS. As shown in **Figure 8A**, all the samples show negligible grain boundary resistances. With the increase of $CoSe_2$ doping ratio, the impedance first decreases and then increases, and 1% $CoSe_2$-doped sample has the highest ionic conductivity of 6.07×10^{-3} S cm^{-1}, slight lower than that of 1% Co^{4+}-doped one. The electronic conductivity of the 1% CoSe2-doped sample was added in **Supplementary Figure S9**. The electronic conductivity of 1% $CoSe_2$-doped electrolyte was measured to be 1.89×10^{-7} S cm^{-1}, four orders of magnitude lower than its ionic conductivity. The results show that the doping of Co and Se in the LSiPS system can greatly enhance the ionic conductivity. The ionic conductivity obtained in this work is comparable or even better than the previous reports as shown in **Supplementary Table S5**.

An all-solid-state Li battery was then assembled using the 1% $CoSe_2$-doped sample as SSE. The cell shows an initial specific charge capacity 160 mAh g^{-1} and the reversible specific capacity decreases gradually to 65 mAh g^{-1} at the end of 100th (**Figure 8B**). This result shows that, although the incorporation of Se^{2+} can enlarge the $MS_{4-x}{}^{2-}/Se_x{}^{2-}$ tetrahedrons, the conductivity of doped $Li_{10.35}Si_{1.35}P_{1.65}S_{12}$ strongly related to its purity and composition. Further research is still underway and will be reported elsewhere.

CONCLUSION

In summary, a low-cost and high-quality sulfide SSE $Li_{10.35}Si_{1.35}P_{1.65}S_{12}$ with favorable tetrahedron structure was synthesized, which was further modified by elemental doping. The 1% Co^{4+}-doped $Li_{10.35}Si_{1.35}P_{1.65}S_{12}$ maintained body-centered cubic-like anion framework and shows a high ionic conductivity of 6.91×10^{-3} S cm^{-1} due to easy Li^+ transport between enlarged tetrahedral sites. A high Li^+ transport number of 0.97 and wide electrochemical stability window of up to 5 V are also reached. These interesting characteristics endow the sample with good electrochemical performance when assembled into all-solid-state Li batteries.

DATA AVAILABILITY STATEMENT

The original contributions presented in the study are included in the article/**Supplementary Material**; further inquiries can be directed to the corresponding author.

AUTHOR CONTRIBUTIONS

YL, JC, and JY contributed to conception and design of the study. YZ and HL performed the data collection. JC performed the analysis. YL wrote the first draft of the manuscript. All authors contributed to manuscript revision, read, and approved the submitted version.

FUNDING

This work is supported by the Overseas High-level Talents Foundation of Shenzhen.

SUPPLEMENTARY MATERIAL

The Supplementary Material for this article can be found online at: https://www.frontiersin.org/articles/10.3389/fchem.2022.851264/full#supplementary-material

REFERENCES

Adams, S., and Rao, R. P. (2012). Structural Requirements for Fast Lithium Ion Migration in Li10GeP2S12. *J. Mater. Chem.* 22, 7687–7691. doi:10.1039/c2jm16688g

Bates, J., Dudney, N. J., Gruzalski, G. R., Zuhr, R. A., Choudhury, A., Luck, C. F., et al. (1992). Electrical Properties of Amorphous Lithium Electrolyte Thin Films. *Solid State Ionics* 53-56, 647–654. doi:10.1016/0167-2738(92)90442-r

Bron, P., Dehnen, S., and Roling, B. (2016). Li10Si0.3Sn0.7P2S12 - A Low-Cost and Low-Grain-Boundary-Resistance Lithium Superionic Conductor. *J. Power Sourc.* 329, 530–535. doi:10.1016/j.jpowsour.2016.08.115

Chen, B., Ju, J., Ma, J., Zhang, J., Xiao, R., Cui, G., et al. (2017). An Insight into Intrinsic Interfacial Properties between Li Metals and Li10GeP2S12 Solid Electrolytes. *Phys. Chem. Chem. Phys.* 19, 31436–31442. doi:10.1039/c7cp05253g

Chen, S., Xie, D., Liu, G., Mwizerwa, J. P., Zhang, Q., Zhao, Y., et al. (2018). Sulfide Solid Electrolytes for All-Solid-State Lithium Batteries: Structure, Conductivity, Stability and Application. *Energ. Storage Mater.* 14, 58–74. doi:10.1016/j.ensm.2018.02.020

Chen, Y., Kang, Y., Zhao, Y., Wang, L., Liu, J., Li, Y., et al. (2021). A Review of Lithium-Ion Battery Safety Concerns: The Issues, Strategies, and Testing Standards. *J. Energ. Chem.* 59, 83–99. doi:10.1016/j.jechem.2020.10.017

De Luna, Y., Abdullah, M., Dimassi, S. N., and Bensalah, N. (2021). All-Solid Lithium-Sulfur Batteries: Present Situation and Future Progress. *Ionics* 27, 4937–4960. doi:10.1007/s11581-021-04284-7

Dudney, N., Bates, J. B., Zuhr, R. A., Luck, C. F., and Robertson, J. D. (1992). Sputtering of Lithium Compounds for Preparation of Electrolyte Thin Films. *Solid State Ionics* 53-56, 655–661. doi:10.1016/0167-2738(92)90443-s

Fan, X., Ji, X., Han, F., Yue, J., Chen, J., Chen, L., et al. (2018). Fluorinated Solid Electrolyte Interphase Enables Highly Reversible Solid-State Li Metal Battery. *Sci. Adv.* 4 (12), eaau9245. doi:10.1126/sciadv.aau9245

Harm, S., Hatz, A.-K., Moudrakovski, I., Eger, R., Kuhn, A., Hoch, C., et al. (2019). Lesson Learned from NMR: Characterization and Ionic Conductivity of LGPS-Like Li7SiPS8. *Chem. Mater.* 31, 1280–1288. doi:10.1021/acs.chemmater.8b04051

Kamaya, N., Homma, K., Yamakawa, Y., Hirayama, M., Kanno, R., Yonemura, M., et al. (2011). A Lithium Superionic Conductor. *Nat. Mater* 10, 682–686. doi:10.1038/nmat3066

Kanno, R., and Murayama, M. (2001). Lithium Ionic Conductor Thio-LISICON - The Li2S-GeS2-P2S5 System. *J. Electrochem. Soc.* 148, A742–A746. doi:10.1149/1.1379028

Kato, Y., Hori, S., Saito, T., Suzuki, K., Hirayama, M., Mitsui, A., et al. (2016). High-Power All-Solid-State Batteries Using Sulfide Superionic Conductors. *Nat. Energ.* 1, 16030. doi:10.1038/nenergy.2016.30

Kato, Y., Saito, R., Sakano, M., Mitsui, A., Hirayama, M., and Kanno, R. (2014). Synthesis, Structure and Lithium Ionic Conductivity of Solid Solutions of Li10(Ge1−M)P2S12 (M = Si, Sn). *J. Power Sourc.* 271, 60–64. doi:10.1016/j.jpowsour.2014.07.159

Kim, K.-H., and Martin, S. W. (2019). Structures and Properties of Oxygen-Substituted Li10SiP2S12-xOx Solid-State Electrolytes. *Chem. Mater.* 31, 3984–3991. doi:10.1021/acs.chemmater.9b00505

Kim, K. J., Balaish, M., Wadaguchi, M., Kong, L., and Rupp, J. L. M. (2021). Solid-State Li-Metal Batteries: Challenges and Horizons of Oxide and Sulfide Solid Electrolytes and Their Interfaces. *Adv. Energ. Mater.* 11, 2002689. doi:10.1002/aenm.202002689

Kondo, S., Takada, K., and Yamamura, Y. (1992). New Lithium Ion Conductors Based on Li2s-Sis2 System. *Solid State Ionics* 53-56, 1183–1186. doi:10.1016/0167-2738(92)90310-l

Kuhn, A., Gerbig, O., Zhu, C., Falkenberg, F., Maier, J., and Lotsch, B. V. (2014). A New Ultrafast Superionic Li-Conductor: Ion Dynamics in Li11Si2PS12 and Comparison with Other Tetragonal LGPS-type Electrolytes. *Phys. Chem. Chem. Phys.* 16, 14669–14674. doi:10.1039/c4cp02046d

Li, W. J., Hirayama, M., Suzuki, K., and Kanno, R. (2016). Fabrication and All Solid-State Battery Performance of TiS2/Li10GeP2S12 Composite Electrodes. *Mater. Trans.* 57, 549–552. doi:10.2320/matertrans.Y-M2016804

Madsen, K. E., Bassett, K. L., Ta, K., Sforzo, B. A., Matusik, K. E., Kastengren, A. L., et al. (2020). Direct Observation of Interfacial Mechanical Failure in Thiophosphate Solid Electrolytes with Operando X-Ray Tomography. *Adv. Mater. Inter.* 7, 2000751. doi:10.1002/admi.202000751

Manthiram, A., Yu, X., and Wang, S. (2017). Lithium Battery Chemistries Enabled by Solid-State Electrolytes. *Nat. Rev. Mater.* 2, 16103. doi:10.1038/natrevmats.2016.103

Murayama, M., Kanno, R., Irie, M., Ito, S., Hata, T., Sonoyama, N., et al. (2002). Synthesis of New Lithium Ionic Conductor Thio-LISICON-Lithium Silicon Sulfides System. *J. Solid State. Chem.* 168, 140–148. doi:10.1006/jssc.2002.9701

Ong, S. P., Mo, Y., Richards, W. D., Miara, L., Lee, H. S., and Ceder, G. (2013). Phase Stability, Electrochemical Stability and Ionic Conductivity of the Li10±1MP2X12 (M = Ge, Si, Sn, Al or P, and X = O, S or Se) Family of Superionic Conductors. *Energy Environ. Sci.* 6, 148–156. doi:10.1039/c2ee23355j

Porz, L., Swamy, T., Sheldon, B. W., Rettenwander, D., Frömling, T., Thaman, H. L., et al. (2017). Mechanism of Lithium Metal Penetration through Inorganic Solid Electrolytes. *Adv. Energ. Mater.* 7, 1701003. doi:10.1002/aenm.201701003

Pradel, A., and Ribes, M. (1989). Lithium Chalcogenide Conductive Glasses. *Mater. Chem. Phys.* 23, 121–142. doi:10.1016/0254-0584(89)90021-7

Shannon, R. D. (1976). Revised Effective Ionic Radii and Systematic Studies of Interatomic Distances in Halides and Chalcogenides. *Acta Cryst. Sect A.* 32, 751–767. doi:10.1107/s0567739476001551

Sun, Y., Suzuki, K., Hori, S., Hirayama, M., and Kanno, R. (2017). Superionic Conductors: Li10+δ[SnySi1-y]1+δP2−δS12 with a Li10GeP2S12-type Structure in the Li3PS4-Li4SnS4-Li4SiS4 Quasi-Ternary System. *Chem. Mater.* 29, 5858–5864. doi:10.1021/acs.chemmater.7b00886

Wang, Y., Richards, W. D., Ong, S. P., Miara, L. J., Kim, J. C., Mo, Y., et al. (2015). Design Principles for Solid-State Lithium Superionic Conductors. *Nat. Mater* 14, 1026–1031. doi:10.1038/nmat4369

Wenzel, S., Randau, S., Leichtweiss, T., Weber, D. A., Sann, J., Zeier, W. G., et al. (2016). Direct Observation of the Interfacial Instability of the Fast Ionic Conductor Li10GeP2S12 at the Lithium Metal Anode. *Chem. Mater.* 28, 2400–2407. doi:10.1021/acs.chemmater.6b00610

Whiteley, J. M., Woo, J. H., Hu, E., Nam, K.-W., and Lee, S.-H. (2014). Empowering the Lithium Metal Battery through a Silicon-Based Superionic Conductor. *J. Electrochem. Soc.* 161, A1812–A1817. doi:10.1149/2.0501412jes

Wu, F., Fitzhugh, W., Ye, L., Ning, J., and Li, X. (2018). Advanced Sulfide Solid Electrolyte by Core-Shell Structural Design. *Nat. Commun.* 9, 4037. doi:10.1038/s41467-018-06123-2

Zhang, Q., Cao, D., Ma, Y., Natan, A., Aurora, P., and Zhu, H. (2019). Sulfide-Based Solid-State Electrolytes: Synthesis, Stability, and Potential for All-Solid-State Batteries. *Adv. Mater.* 31, 1901131. doi:10.1002/adma.201901131

Conflict of Interest: The authors declare that the research was conducted in the absence of any commercial or financial relationships that could be construed as a potential conflict of interest.

Advantages of publishing in Frontiers

OPEN ACCESS

Articles are free to read
for greatest visibility
and readership

FAST PUBLICATION

Around 90 days
from submission
to decision

HIGH QUALITY PEER-REVIEW

Rigorous, collaborative,
and constructive
peer-review

TRANSPARENT PEER-REVIEW

Editors and reviewers
acknowledged by name
on published articles

Frontiers
Avenue du Tribunal-Fédéral 34
1005 Lausanne | Switzerland

Visit us: www.frontiersin.org
Contact us: frontiersin.org/about/contact

REPRODUCIBILITY OF RESEARCH

Support open data
and methods to enhance
research reproducibility

DIGITAL PUBLISHING

Articles designed
for optimal readership
across devices

FOLLOW US

@frontiersin

IMPACT METRICS

Advanced article metrics
track visibility across
digital media

EXTENSIVE PROMOTION

Marketing
and promotion
of impactful research

LOOP RESEARCH NETWORK

Our network
increases your
article's readership